INVESTIGATION OF PLASMONIC PROPERTIES IN OXIDE AND NITRIDE THIN FILMS

Thesis submitted
In Partial Fulfillment of the Requirements

for the Degree of

Doctor of Philosophy
In Physics
Under the Faculty of Science
University of Calicut, Kerala, India

by

SOUMYA K

Senior research fellow, CSIR

Under the guidance of

Dr S. Sankara Narayanan Potty

CENTRE FOR MATERIALS FOR ELECTRONICS TECHNOLOGY (C-MET)

Scientific Society, Ministry of Electronics and Information Technology, (MeitY)

Government of India, MG Kavu, Athani PO, Thrissur, India

www.cmet.gov.in

August 2021

Declaration

I hereby declare that the dissertation entitled “Investigation of plasmonic properties in oxide and nitride thin films” submitted to University of Calicut in partial fulfillment of the requirement for the award of the degree of Doctor of Philosophy in Physics is a record of original work done by me under the supervision and guidance of Dr S Sankara Narayanan Potty, Scientist, C-MET Thrissur and it has not formed the basis for the award of any Degree/ Diploma/ Associateship/ Fellowship or any other similar title to any candidate of any university.

Thrissur Soumya K

Certificate

This is to certify that the thesis titled “Investigation of plasmonic properties in oxide and nitride thin films ” submitted to University of Calicut in partial fulfilment of the requirements for the award of the degree of Doctor of Philosophy in Physics under the Faculty of Science, University of Calicut, is a record of the authentic work carried out by Ms Soumya K, at Centre for M aterials for Electronics Technology (C-M ET), Thrissur, under my guidance. The work presented in this thesis has not been submitted for any other degree or diploma of this or any other University and has been found to have no plagiarism using the software approved by the UGC/University.

Thrissur
Dr S. Sankara Narayanan Potty
Research Guide

Acknowledgements

I am deeply indebted to my guide Dr S Sankara Narayanan Potty, Thin Film and Plasmonic Division, C-MET Thrissur for giving me the confidence and inspiration to pursue research work. I also express my sincere gratitude to him for the support, invaluable advice, encouraging words, positive attitude and sincere concern given throughout the period of research. I am extremely grateful to him for his patience, immense help, guidance, encouragement and persistent efforts rendered on me.

I owe my gratitude to Dr N Raghu, Director, C-MET Thrissur for the support to do research with legacy. I express my sincere thanks to Dr Sandip Dhara, Head, surface and Nanoscience Division, IGCAR, Homi Bhabha National institute Kalpakkam and also grateful to Dr Vinod C Prabhakaran, Principal scientist and Assoc Professor(AcSIR), NCL Pune for collaborating work with us and also for constant encouragement and support. I am always thankful to Dr K Muraleedharan, CSIR Scientist Emeritus and Dr V Kumar, Scientist, CMET, for guiding me to analyse EDAX results.

I express my sincere gratitude to all the members in the C-MET Thrissur for their sincere concern, valuable advices and encouragement. I thank to all technical staff especially Mr Packia Selvam, Mr Arun, Ms Priyadarshini who have helped me to do various characterisation during the period of study. I gratefully acknowledge, the financial support from CSIR in the form of junior research fellowship.

The successful completion of this research work would not have been possible without the generous help, support and encouragement from my labmates Mr Sajeesh, Mr Sumesh, Ms Sridevi, Ms Liya tony, and Mr Vishnu. I am grateful to Dr Prabeesh P for his kind support and constant encouragement to complete my research work. I am very much indebted to my C-MET friends especially Mr Ranjith KR and Ms Anju for their insightful comments and advice. My heartfelt thanks to Dr.Suresh EK, Dr Manoj, Mr Navaneeth, Ms Lekshmi, Ms Merin, Ms Arathi for their continuous support and concern. I express my sincere thanks to Mr C Mohanan for Solving my stipend issues with CSIR. I owe my deep sense of gratitude to Mr Suseel Rahul, Dr Devadas K M, Dr Akhil K Nair, Mr Unnikrishnan M S, Dept of Physics, Sri Vyasa NSS college, Wadakkanchery for their encouragement and support. I like to express my gratitude to each and everyone who have worked with me at different stages of this work. I also thank all the research scholars and Project staffs of the C-MET Thrissur for their support.

And finally I would like to express my sincere gratitude to my family members. I am deeply indebted to my parents(amma, achan, susheelamma, muraliachan, beenamma), my siblings(echu, maha, remya) and to all who live close to my heart. It would have been impossible for me to pursue this research work without the whole hearted support and constant encouragement of my life companion Mr Unnikrishnan MS. With all respect, I would like to express my sincere gratitude toward him for making my research life enjoyable. Once again I convey my gratitude to all those persons who had direct or indirect influence on my work. There are many people who have helped me during these years and I apologize for not mentioning all of them here.

Soumya k

Preface

History of plasmonics shows that its effects have been known for ages. The vibrant colour of Lycurgus cup and its colour changes in reflected and transmitted light is due to plasmonic resonance of metal nanoparticles present in the glass. The interaction of electromagnetic field with the free electrons in a metal-dielectric interface or in small metallic nanostructures will result in near field enhancement at subwavelength dimensions. Plasmonics became an active field in nanotechnology and explored to various applications such as biological and chemical sensors, solar cells, super resolution imaging, surface enhanced Raman spectroscopy etc. When an electromagnetic field interact with cloud of free electrons, they can support a wave of charge density fluctuations along a metal-dielectric interface. This creates a mode, which is called surface plasmon. This non-radiative optical mode can enhance light-matter interaction considerably because it can couple electromagnetic wave more effectively to the metal surface. The excitation of surface plasmon is achieved using an evanescent field by the momentum match of resonant interaction. The fields of surface plasmon resonance can propagate along the metal surfaces in metal-dielectric interface. The enhancement is associated with strong reduction of the reflected intensity when the incoming field is completely transformed into surface plasmons. This property is extensively used to study the changes in refractive index of thin films, and hence widely used for sensing applications. In this phenomenon, light can be confined to an area below the diffraction limit. Enhancement of the local field intensity by many orders of magnitude is also taking place. The field of plasmonics open a new horizon in modern communication system, which could impact the daily lives. The optical communication systems, which are widely using now offers high bandwidth and fastest method for high-speed information processing. However, due to the diffraction limit, the photonic components cannot be arranged in a compact form like nanoscale electronic devices. This issue can be addressed in plasmonics, where the problem of diffraction limit is eliminated. Plasmonics thus promises miniaturisation of optical components by sustaining the large band width of light.

Metals such as silver and gold having carrier density ($10^{23}/\text{cm}^3$) were the primary choices for plasmonics. However, they suffer from the main disadvantages of large loss, especially in the infrared spectral range, due to the interband electronic transitions, or optical absorption by free carriers. These losses are seriously affecting the plasmonic performance of these materials. The optical response of a material is given by permittivity, where the real part ϵ_1 describes the ability of the material to get polarised, and the imaginary part ϵ_2 describes the loss came across while polarising it. Thus, for a low loss material, the imaginary permittivity should have small values. In addition, metals also possess large negative values for the real permittivity in near infrared, which introduce device fabrication difficulties. The polarisation responses from dielectric and metallic components in devices are to be of the same order; in such cases the geometric fill fraction of the metal and dielectric can be tuned to match the design requirements. Due to these reasons, metals are not ideal for NIR plasmonics. Since the losses are inherent to the constituent materials, new plasmonic materials with lower losses are required. The low-loss plasmonic materials must be characterized by a larger bandgap and plasma frequency than the frequency range with interest. Another condition required for NIR plasmonic material is the free carrier concentration (n), which has to be of the order of $10^{20}/\text{cm}^3$. This can be achieved using doped metal oxides such as tin doped indium oxide (ITO), aluminium doped zinc oxide (AZO), gallium doped zinc oxide (GZO) and fluorine doped tin oxide (FTO) etc. These materials can be promising low-loss alternatives in NIR by doping, by controlling the number oxygen vacancies and interstitial metal dopants. In order to exhibit plasmonics in visible region, the material should have carrier concentration of $10^{21-22}/\text{cm}^3$. However, oxides cannot be used for this; high doping for enhancing carrier concentration may cross the solid solubility limits. Transition metal nitrides can be prepared with such high carrier concentrations and can be explored as plasmonic materials for the visible frequencies. Deposition parameters and dopant concentrations have to be optimized in order to achieve required carrier densities and low losses.

By engineering the material properties, oxides and nitrides can have high free carrier density required for exhibiting metal like properties in the near-infrared and visible regions, respectively. Due to the presence of free as well as bound electrons in these materials, the Drude-Lorentz (D-L) approach is the accurate method for understanding their optical responses. The important criteria for a material to exhibit plasmonic properties is the negative real permittivity at the operating wavelength range. The wavelength at which the real permittivity turns negative is defined as the cross-over wavelength (ω_c). This is directly related to the plasma wavelength (ω_p), which limit the wavelength region for plasmonic properties of the materials. The plasma wavelength is directly proportional to the carrier density of the films and the material exhibit plasmonic properties only beyond the plasma wavelength.

The thesis entitled “Investigation of plasmonic properties in oxide and nitride thin films” focusses a detailed investigation in the plasmonic behaviour of oxides and nitrides. For NIR plasmonic studies, among various transparent conducting oxides, zinc oxide has been chosen as the host material due to its low cost as well as high stability. From various transition metal nitrides, titanium nitride was chosen for plasmonic study in visible region. For the deposition of oxide films, thin film preparation techniques such as physical and chemical methods were used. In chemical deposition techniques, spin and spray coating roues were utilised. Physical deposition method is adopted for the fabrication of transition metal nitrides. In this work, co-doping has been attempted to modify the material properties of ZnO. Aluminium and Indium were selected as the dopants. The strain in the lattice due to ionic radius mismatch of a dopant with the host material can be reduced by using co-dopants with relatively large and small ionic radii with the host lattice. In addition, co-doping also helps to reduce the usage of costly material like In when using along with cost effective material like Al. The studies included in the thesis are divided into six chapters and the contents of each chapter are summarised as follows.

Chapter 1 is a general introduction to plasmonics including a brief history and review of literature on transparent conducting oxides and transition metal nitrides deposited by various groups using different techniques. The objectives of the work carried out are briefed at the end of the chapter 1.

Chapter 2 describes the experimental and characterization techniques used to fabricate and characterize co-doped ZnO and TiN thin films. Details of solution-based routes, such as, spin and spray coatings, and vacuum based routes such as RF and DC sputtering are also discussed in detail. Structural characterisation using x-ray diffractometer is also discussed in this chapter along with the description of the Rietveld technique used to refine the structural parameters of the films. The basics of analysis of elemental compositions by energy dispersive x-ray spectroscopy, and optical properties by UV-visible spectroscopy are explained. In addition, working of scanning electron microscope and field emission scanning electron microscope are included in this chapter. The importance of Hall Effect measurement system for investigating the electrical properties were also described. The Kretschmann configuration used to generate surface plasmon resonance is discussed in detail at the end of this chapter.

Chapter 3, the first working chapter discusses the deposition of Al and In co-doped ZnO thin films by cost effective spin coating technique. By fixing total doping percentage to 3, doping ratios of aluminium and indium were varied. The films were annealed at 400°C or 450°C in air atmosphere followed by annealing at 300°C in reduced atmosphere. Films showed better electrical properties when annealed at 400°C were considered for further studies. The films fabricated with particular a ratio of aluminium and indium (A_3I_7) exhibited better electrical, structural, morphological properties as well as optical behaviour. This was further verified by XRD, which showed relatively higher stress and strain for the films A_1I_9 and A_5I_5. SEM image revealed wrinkle network structure for the co-doped films. Optical properties along with Urbach energy calculations showed variation in the bandgap of all films. Films with higher Urbach energy had less bandgap because of the additional localized states created near the conduction band minimum. Finally, the films were sorted according to carrier concentration ($n=10^{20}/cm^3$) and investigated their plasmonic behaviour. The dielectric functions of the films were retrieved by fitting Drude-Lorentz oscillator model to the reflectance spectra. Plasma frequency calculated from reflectance-transmittance spectra showed direct dependence with cross-over frequency extracted from fitting, and hence confirmed the plasmonic behaviour in the near IR range. The loss (ϵ_2) of these films were very low in the range from 1500nm to 2500nm compared with conventional metallic plasmonic materials. The studies revealed metal like behaviour with low loss for AZO, AIZO (A_3I_7), IZO films in the NIR frequency region. The novelty of this work is the adoption of a simple technique for fabricating TCO based plasmonic materials and the properties obtained were in consistent with those fabricated by vacuum routes such as sputtering, PLD etc.

Chapter 4 describes the preparation of Al and In doped and co-doped ZnO films with different Al:In ratios by simple spray coating technique using water as solvent. The effect of ionic radii of dopants as well as their concentrations (Al:In) while substituting in Zn site were studied using x-ray diffraction. The Rietveld refinement studies revealed wurtzite structure for the films and showed the dependence of the ionic radii of the dopants on lattice constants, cell volume and bond length. SEM images were recorded and analysed to understand how the doping or co-doping and their ratios affect the grain shape, size and uniformity of films. The electrical properties of the films before and after annealing in the reduced atmosphere were studied. Enhancement in carrier concentrations was observed for all the films due to the additional oxygen vacancies created during reduced atmosphere annealing. The differences in carrier densities of these films were validated using Raman line shape analysis with Fano and Lorentz fittings. The quantification of the dopants present in the ZnO was analysed using XPS. The variation in the bandgap energies of the films was estimated using Tauc's relation with respect to the carrier densities was in analogy with the findings from the Fano and Lorentz fitting, and thus confirmed a large number of free carriers for the films A_5I_5, $A_{2.5}I_{7.5}$ and A_0I_{10}. The absence of deep defects in the bandgap of films was confirmed from the photoluminescence spectra of these films. Theoretical fitting using the Drude-Lorentz model was utilized to extract the real and imaginary parts of the permittivity of the films. Films

A_5I_5, $A_{2.5}I_{7.5}$ and A_0I_{10} having carrier density $10^{20}/cm^3$ showed negative permittivity in near infrared. Tuning of cross-over the frequency with carrier density in the NIR region was observed for these films. The surface plasmon resonance simulated using the permittivity values extracted from the D-L model showed the influence of mobility of the films on the broadening of the dip. The low loss exhibited by the films in the NIR region compared with conventional plasmonic material suggests the suitability of the films for plasmonic applications.

Chapter 5 focusses on the plasmonic properties of Al and In co-doped ZnO thin films fabricated by RF sputtering using powder target prepared by solid state route. The Rietveld refinement studies revealed wurtzite structure for the films. The free carrier densities of all films were of the order of $10^{20}/cm^3$, required to exhibit plasmonic properties in NIR wavelength. The Fano resonance fitting of A_1(LO) mode confirmed Raman active inter-conduction band transitions occurring for heavily doped n type materials. The near band and visible emissions due to oxygen vacancies further confirmed the n type doping in these films. The bandgap variations of the thin films were according to the band renormalization (BR) effect. The real and imaginary parts of the permittivity extracted from the D-L equation predicted SPR in these film for wavelengths beyond 1350nm with relatively small loss comparing to conventional metals. SPR has been successfully generated in these films using the Kretschmann type prism configuration. The tuning of SPR wavelength in the telecommunication wavelength has been done by wavelength interrogation method. Co-doping of ZnO resulted in wide range of SPR behaviour for wavelengths from 1360nm to 1830nm when the angle of incidence was changed from 45^o to 55^o.

Chapter 6 discusses the plasmonic studies carried out on titanium nitride thin films. The TiN thin films were fabricated by DC reactive sputtering by varying the Ar-N_2 ratio. Structural confirmation of the films was done by x-ray diffraction. The non-stoichiometric nature of the films were studied using the EDAX spectra. The bandgap of the TiN films calculated using the Tauc relation showed a increasing trend with increase in nitrogen content in the films. The real and imaginary parts of the permittivity extracted from the D-L equation revealed SPR in these film for wavelengths near to 470nm with loss comparable to the conventional plasmonic metals. The SPR has been successfully generated in these films using the Kretschmann configuration in wavelength interrogation method. The shift in SPR wavelength by changing the incident angle was studied in detail. The variation in the Ar-N_2 ratio resulted in wide range of SPR behaviour, for wavelengths from 550nm to 650nm, when the incident angle is changed from 51^o to 53^o.

List of Publications

Parts of the work presented in this thesis were published in the following reputed international journals

i K. Soumya, Selvam I.P, Potty S.N. Study on the doping effect of spin coated Al and In doped and (Al/In) co-doped ZnO thin films for near-infrared plasmonic applications. Thin Solid Films 687 (2019) 137482.

ii K. Soumya, Irulappan P S, Dhara S, Potty S N. Wide Band Gap Al and In Co-doped ZnO Films for Near-Infrared Plasmonic Application. Plasmonics 27 (2021) 1-12.

Parts of the work presented in this thesis were published in the following proceedings

i K. Soumya, I Packia Selvam, S N Potty "Structural, electrical and optical properties of spray coated indium doped zinc oxide films for nanophotonic applications in near IR, National Photonics Symposium proceedings, (2019).

ii K. Soumya, I Packia Selvam, S N Potty "Investigation of Plasmonic Properties of Spin Coated And Spray Coated IZO Thin Film, AIP proceedings, (2020)

iii K. Soumya, I Packia Selvam, S N Potty "Effect of RF power on structural, electrical,optical properties and surface plasmon resonance of sputtered AZO thin films, IEEE, (2020)

Parts of the work were presented or accepted for presentation in the following seminars/conferences

i Delivered an oral presentation entitled " Structural optical and electrical properties of IZO thin film by Spray coating technique for NIR applications"on National Photonics Symposium (NPS) 2019 organised by International School of Photonics,CUSAT during 27 Feb to 1 March, 2019 ii Presented a poster entitled “sol gel derived aluminium and indium codoped zinc oxide film by spray coating for nanophotonics applications” on the International Conference on Advanced Materials (ICAM 2019) organised by Dept of Physics, Nirmalagiri College, Kannur during June 12-14, 2019

iii Delivered an oral presentation entitled “Investigation of plasmonic properties in spin coated and spray coated IZO thin films” on 5th National Conference on Advanced Materials and Radiation Physics organized by Department of Physics Sant Longowal Institute of Engg. & Technology Longowal, Distt. Sangrur (Punjab) during 9 -11 November, 2020 .

iv Delivered an oral presentation entitled “Effect of RF power on structural, electrical, optical properties and surface plasmon resonance of sputtered AZO thin films” on 5th International Conference on Emerging electronics (ICEE 2020) organized by IEEE and hosted by IIT, Delhi during 26-28 November, 2020

Contents

List of Figures

List of Tables

Chapter 1

Introduction

1.1 Overview

Researchers have developed technologies for advanced materials for many decades, enabling new applications and providing opportunities for the exploration of new science. New scientific concepts are allowing us to further strengthen advanced materials technology. In addition, choice of material has equal importance in deciding the confluence of science and technology. Semiconductor technology and optical communication already enlightened their importance in processing information. Today the technology has grown worldwide in such a way that miniaturized materials give the best property[1]. Modern communication system needs to transport huge amount of data with ever increasing speed. Electronic circuits with size $<$100nm are able to achieve our demands; however, its operational speed is limited by RC delay[2]. With the advent of photonics, high speed is attained, but miniaturisation of component to $<1\mu$m is not possible because of the diffraction limit[3, 4]. As a result of these challenges, researchers developed an alternative solution, called plasmonics. Plasmonics exploits the interaction of electromagnetic wave and free electrons in a material. It also deals with excitation, interaction, manipulation and utilisation of quantum excitation of oscillatory electrons, known as surface plasmon[5]. How well a material will interact with electromagnetic field is given by their dielectric permittivity and magnetic permeability[6]. The weak interaction of magnetic field at the optical frequency neglects the contribution of permeability, and hence permittivity alone is used to define the behaviour of material interacting with the photon[6, 7]. The complex permittivity is defined as $\epsilon = \epsilon_1 + i\epsilon_2$, in which real part defines polarisation response and imaginary part defines the loss encountered while polarising the material. Practically, the imaginary part is zero for dielectrics; however, metals have significant values for the loss[6]. Plasmons enduring in a material having sufficient free electrons due to their weak interaction to atom[8]. Since availability of free electrons have paramount importance in the generation of plasmons as well as its studies, metals such as gold, silver, copper, aluminium, etc are used as conventional plasmonic materials[6, 8]. High DC conductivity and small ohmic loss make of a material make it absolute for plasmonic applications such as chemical sensing[9] and information processing[10]. The advent of field such as metamaterials[11, 12] and transformation optics[13] again strengthened the applications of plasmonic materials, and thus many new prototypes and physical phenomena were established in the field of plasmonics. However, to convert such novel concepts into real as well as practical technologies, new materials are required. Large loss in metals when used in the near IR region creates the necessity of alternative materials to metals. Therefore, this study has been focused more on searching of new materials that have small loss in the near IR region. Such materials can be used for sensing or optical communication purposes.

1.2 Motivation

Plasmonics applications have been known for ages. The vibrant colour of Lycurgus cup, and the different reflected and transmitted colours coming from due to optical plasmonic resonance of metal nanoparticles present in the glass[14]. The interaction of electromagnetic field with the free electrons in a metal-dielectric interface or in small metallic nanostructures will result in enhanced optical near field at subwavelength dimensions[15]. Plasmonics became an active field in nanotechnology and used successfully in various applications such as biological and chemical sensors, solar cells, super-resolution imaging, surface enhanced Raman spectroscopy etc[16–18]. When an electromagnetic field interact with cloud of free electrons, there will be a wave of charge density fluctuations on the surface of the metal. This wave is called surface plasmon, and at resonance condition, these wave couple with the incoming electromagnetic wave, which result in surface plasmon polariton (SPP). The resonance condition at which this occurs is called surface plasmon resonance (SPR)[15].

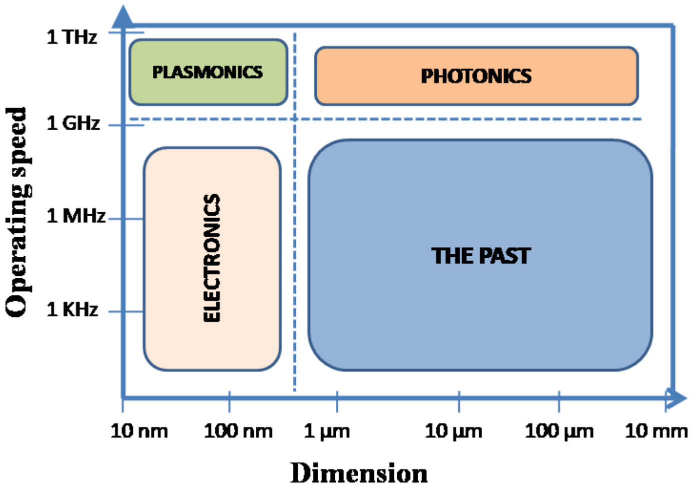

Figure 1.1: Trade-off between device dimension and operating speed[10]

The important consequences of this interaction are, incoming light can be confined to a small area, which overcomes the diffraction limit observed in photonic devices, and the other is enhancement in the field intensity by many orders of magnitude. This enhancement helps to amplify the minute change in the environment, and thus helps in sensing applications. As described, in modern communication system, the field of plasmonics open a new horizon that could revolutionize our daily lives. Optical communication system has been widely used now due to its high bandwidth and fastest method for high speed information processing. However, due to the diffraction limit, optical components cannot be arranged in a compact form like nanoelectric devices[6, 19]. This issue can be addressed in plasmonics, and the problem of diffraction limit can be eliminated in plasmonic devices. Plasmonics promises miniaturisation of the optical components by sustaining large band width of light. Fig.1.1 shows the trade-off between device integration and operating speed during the journey from electronics to photonics then to plasmonics[10].

1.3 Theory of surface plasmon resonance

The beginning of the surface plasmon resonance was in 1902, from Wood's experiment on observation of anomalous behaviour in the reflected beam from diffraction grating[20]. In 1968, Otto and Kretschmann excited the surface plasmon of silver using attenuated total reflection coupler[21, 22]. Later in 1977, the SPR method was used for the determination of optical constants of the organic monolayer on the surface of gold. It was then used for biosensing and gas sensing in 1983 by Liedberg et al.[23].

A surface plasmon is defined as a transverse magnetic (TM) wave, which travels along the interface of the two media, metal and dielectric. If the phase velocity $\frac{\omega}{k}$ < velocity of light(c), then surface plasmon waves cannot decay in to photons. This mode of surface plasmon waves is called non-radioactive mode. If velocity $\frac{\omega}{k}$ > c, it corresponds to radioactive modes, which decay directly in to photon[21]. The non-radioactive surface plasmon is considered here; the dispersion relation for such plasmon is given by [23]

$$k_{sp} = \frac{\omega}{c}(\frac{1}{\epsilon_d} + \frac{1}{\epsilon_m})^{-\frac{1}{2}} \tag{1.1}$$

Where ϵ_d and ϵ_m are the dielectric constants of the air and the metal, respectively. Only those frequencies, where ϵ_m of the metal is negative, are interested. For an incident light falling on a metal at an angle θ, the wave vector of light that is parallel to the metal surface is given by,

$$k_x = \frac{\omega}{c}\sqrt{\epsilon} sin\theta \tag{1.2}$$

For obtaining negative value of ϵ_m, eqn (1.1) and eqn (1.2) indicates that the parallel wave vectors for the incident light and the surface plasmons are not equal for any ω and θ values. However, if it is thin film on a substrate, the dielectric constants on both sides of the metal will be different. This makes ϵ in eqn (1.2) different and there exist an angle of incidence where eqn (1.1) and eqn (1.2) are equal. This angle is defined as resonance angle for surface plasmon resonance[23]. Hence, the interaction of light with the metal at resonant condition results in coherent electron oscillation on the surface of the plasmonic material. This wave of charge density fluctuation is called surface plasmon wave as shown in Fig.1.2[24]

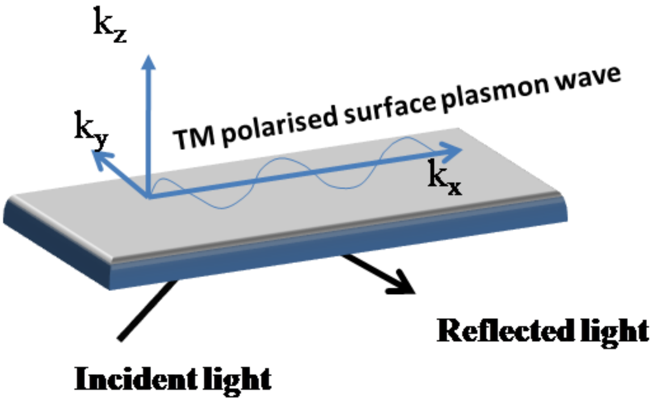

Figure 1.2: Excitation of surface plasmon wave when coupled with incoming electromagnetic wave at resonance condition[24]

The experimental observation of SPR is done by observing a sharp dip in the reflectance spectra by varying the angle of incidence or wavelength. Measuring SPR by varying angle is called angular interrogation method, and if by wavelength-based measurement, it is termed as wavelength interrogation method [25]. The resonance angle(θ_{SPR}) is very sensitive to the refractive index because,

$$\theta_{SPR} = sin^{-1}(\frac{1}{n_p}\sqrt{\frac{n_d^2 n_m^2}{n_d^2 + n_m^2}}) \tag{1.3}$$

Where n_p, n_d, n_m, are the refractive indices of the prism, dielectric media and metal film. For a fixed n_p, and n_m, θ_{SPR}, is related to the change in the refractive index of the dielectric medium[26].

1.3.1 Surface plasmon polariton (SPP)

The resonant interaction between electromagnetic field and surface plasmon results in a wave at the metal dielectric interface. This wave is SPP, which offers a promising approach to control and manipulate dispersion as well as propagation of light at nanoscale[27]. In 1956, Pines observed an energy loss in fast electrons while travelling through the metal[28] due to the collective oscillation of electron, which was termed as plasmon. Fano introduced the name polariton for the coupled oscillation of bound electrons and light at transparent media, in the same year[29]. Theoretical description for surface plasmons was given by Ritchie[30], and later Otto and Kretschmann[21, 22] experimentally proved optical excitation in metal films due to surface plasmons. Cunningham et al[31] later introduced the term surface plasmon polariton; representing the coupled state between a plasmon and photon.

The main reason for the increasing peculiar interest in SPP related structures is due to its applications in optics, data storage, sensors, solar cells, surface enhanced Raman spectroscopy etc[32]. In addition, a near field enhancement having resolution of 3nm was able to achieve in near field plasmon microscope, due to excitation of SPP during resonant interaction with metal tip and electromagnetic field[32]. The magnitude of this enhancement is estimated to be 100-200 times the incident electromagnetic field, indicating the high detection capacity in near field spectroscopy[33]. The excitation of surface plasmons is done using p polarised light, that is, in TM mode, where the electric field vector is parallel to the incident plane. The p polarised light will create surface charges to undergo collective oscillations. Even though the incident wave is totally reflected, there will be oscillating charge penetrating through the metals. These wave decays spatially perpendicular to the interface, and is defined as evanescent field[27]. The schematic illustration of electromagnetic field and the surface charges at the plasmonic metal-dielectric interface is shown in the Fig.1.3a[27].

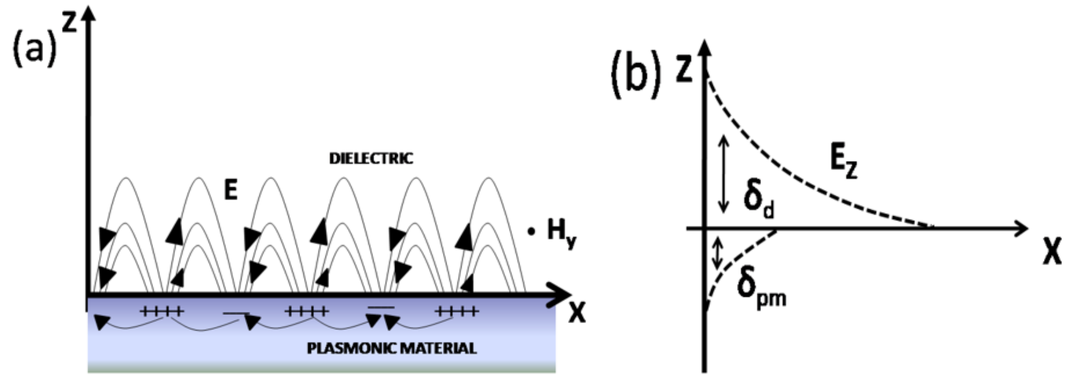

Figure 1.3: (a) represents geometric representation of surface plasmon polariton at the metal –dielectric interface,(b) represents the decay length of the evanescent wave in to dielectric and plasmonic material[27]

The enhancement of electric field component near the surface and decaying field exponentially with distance normal to the interface is represented in Fig.1.3b. Exponential decay of SPP in dielectric (d) and plasmonic metal (pm) are represented as δ_d and δ_{pm}, respectively. The x component of electric field (E_x) is conserved in x direction, since there is no boundary. However, the z component is forced to change due to the different values of ϵ for metal and dielectric. This discontinuity makes changes in the polarisation in the interface. In view of this, s polarised light is not suitable to excite surface plasmons[27]. The resulting surface plasmons have momentum ($\hbar k_{sp}$) greater than that of the electromagnetic field ($\hbar k_o$) in free space. Considering the wave equation of electromagnetic field at metal and dielectric media, and solving with Maxwell's equation under appropriate boundary conditions, the SP dispersion relation can be written as[34]

$$k_{SP} = k_o\sqrt{\frac{\epsilon_m \epsilon_d}{\epsilon_m + \epsilon_d}} \tag{1.4}$$

Where ϵ_m and ϵ_d are the permittivities of metal and dielectric, respectively and k_o is the free space wave vector. The dispersion relation of SPP is shown in Fig.1.4.

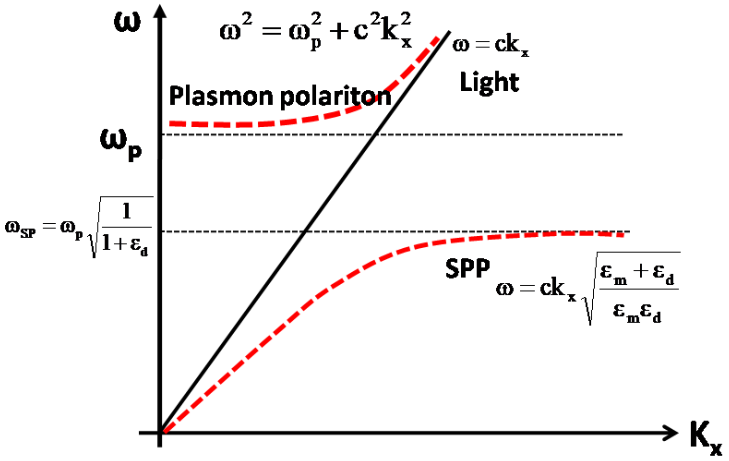

Figure 1.4: Dispersion relation of SPP, light and plasmon polariton[35]

It is evident from the figure that for low wave vectors the dispersion approaches, but remains less than that of light; at high wave vectors it approaches the frequency, $\omega_{SP}= \frac{\omega_p}{2}$. The dispersion curve lines of surface plasmon polariton always appear in the right side of the light line. Hence, in order to excite SPP of certain frequency up to limiting value of ω_{SP}, the wave vector of plasmon should be greater than the wave vector of light line, so that it cannot be excited using the direct illumination light[34–36]. This is clear from the mismatches of momenta described earlier for these two cases. The techniques for the condition, $k_{SP} = k_{light}$ will be discussed in the next section.

1.3.2 Generation of surface plasmon polariton(SPP)

As described, the momentum mismatch between photon and electron makes it impossible to generate SPR through direct interaction. Hence, the excitation of surface plasmons is achieved by the following methods,

- Prism-coupler based SPR
- Grating coupler based SPR
- Optical waveguide based SPR

1.3.2.1 Prism-coupler based SPR system

Fig.1.5a and Fig.1.5b shows the two different methods for the excitation of surface plasmons, such as Kretschmann[22] and Otto configurations[21], respectively. Kretschmann configuration is one of the most popular set up for generating surface plasmons. In this case, plasmonic material is deposited on the base of a dielectric prism. A beam of p polarised light (direction of vibration parallel to the plane of incidence) is allowed to incident on the prism as shown in Fig.1.5a.

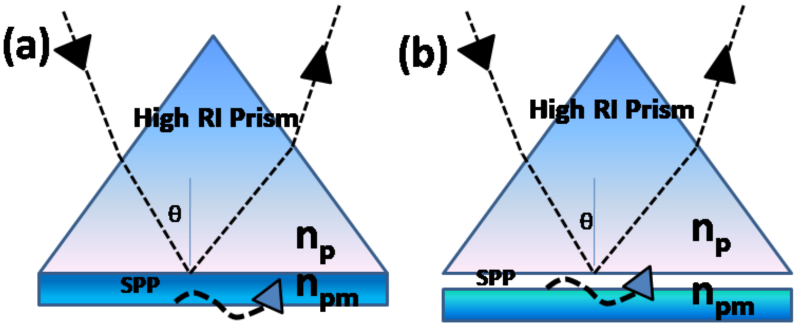

Figure 1.5: Representation of two methods for generating SPR using coupling (a) Kretschmann configuration (b) Otto configuration[36]

The total internal reflection at the prism-metal interface will result in generation of evanescent field, which will pass through the metal and thus interact with electrons at metal-dielectric (air) interface. The energy coupling of evanescent wave and electrons at metal-dielectric occurs when momentum of evanescent wave and surface plasmons are equal. At a particular incident angle θ, resonance occurs, which leads to the coupling between evanescent field and generates surface plasmons. Under this resonant condition, there will be a sharp dip in the reflectance spectra of the light coming from the prism. The thickness of the plasmonic film in the prism should be minimum to travel the evanescent field in to metal-dielectric interface. In addition, the coupling strength of SPR depends on skin depth of material and film thickness. When the skin depth is greater than thickness, surface plasmons can easily couple and generate SPP[37]. In the Otto configuration, metal thin film is not directly deposited on to the prism. Instead, the evanescent field is allowed to move through dielectric medium and thus reach the metal surface, as seen in Fig.1.5b. When the momenta of evanescent field and surface plasmons are equal, coupling takes place and thus SPP propagates [21, 38]. The coupling strength is determined by the width of air gap; optimum coupling take place when width of air gap is in the order of incoming wavelength. However, one of the main disadvantages of this configuration is that when the size of the dust particles is greater than the air gap, the accuracy of the SPR measurement will be compromised. Unlike Kretschmann configuration, thick film can also be used to generate SPR in this configuration[39].

1.3.2.2 Grating coupler based SPR

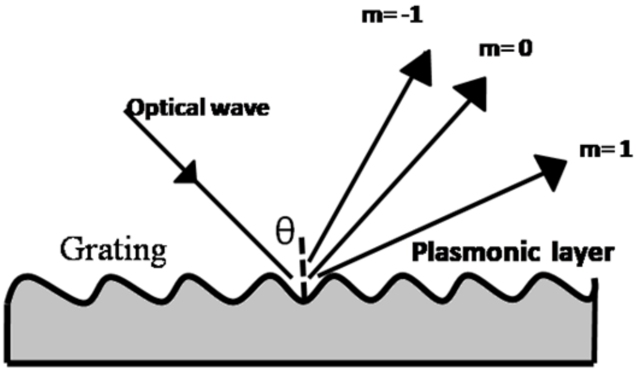

Figure 1.6: SPR Coupling using grating method[42]

Grating structures in the metals are utilised as dispersive elements in monochromator and spectrometers[40]. The same gratings can be used to obtain momentum matching between electron and photon. A schematic representation of SPR grating coupler is shown in Fig.1.6.[41]. Incoming photon at an angle θ with respect to normal to the surface of the metal can undergo scattering due to grating, which will increase or decrease the component of its wave vector of incident wavelength by integral multiples of grating wave vector k_g result in diffracted orders lead to the formation of surface plasmons[42]. Generation of evanescent wave occurs when the wave vector of diffracted order is greater than that of incident light wave vector[40,43].The coupling condition is given by

$$K_{sp} = n_d k_o sin\theta \pm N k_g \tag{1.5}$$

where N is an integer and n_d is the refractive index of the dielectric medium(air). The period and the amplitude of the grating determine the resonance frequency [40,43].

1.3.2.3 Optical waveguide based SPR

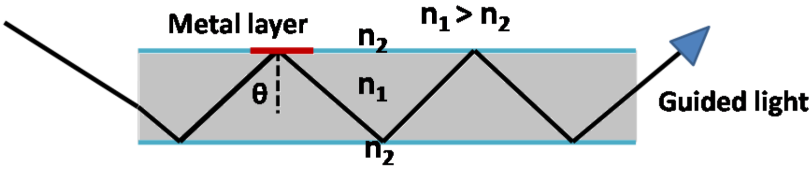

Figure 1.7: SPR generation using fibre optic waveguide

An optical fibre consists of high index core, low index cladding and the mechanical jacket. The light propagates undergoes many total internal reflections while traversing through the fibre, as shown in Fig.1.7. In this case, a small portion of the cladding was removed and coated with plasmonic material. The evanescent wave penetrates through the plasmonic metal film and reach at plasmonic metal-dielectric interface and results in the generation of SPP [44].

In the present study, Kretschmann configuration has been utilized for SPR generation. The plasmonic material which usually deposit in the prism should have negative permittivity in the concerned wavelength region. As described, p polarised light is allowed to fall on the prism, at this polarisation electric field is oscillating normal to the surface of the film. The amplitude of the SPP decrease in the direction of propagation and increase away from the interface. This property differentiates SPP from the reflected plane wave in Kretschmann configuration. The SPR is detected by observing the intensity of reflected light with respect to change in wavelength for a fixed angle (or change in angle of incidence for a monochromatic light source). A sharp fall in the intensity as shown in Fig.1.8. indicates the generation of SPR. Any change in the refractive index, and hence permittivity of the dielectric will change the surface plasmon wavelength(or angle). This property of the plasmonic materials is being used for sensing applications.

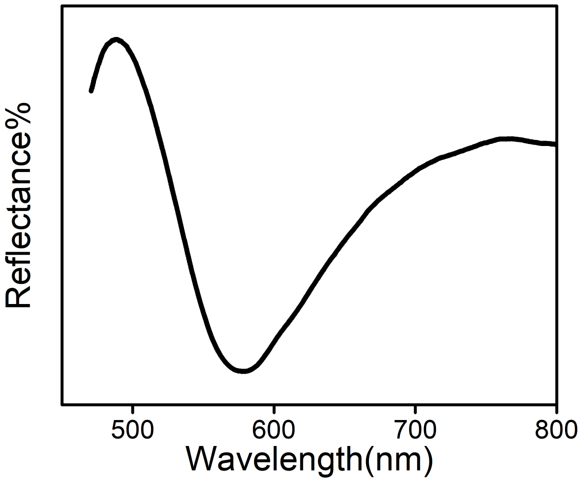

Figure 1.8: Experimental observation of SPR in the reflectance spectra

1.3.3 Drude-Lorentz model

Polarisation is based on the interaction of electromagnetic wave with materials and it can be described using dielectric function. Classical Drude theory of metals explains the behaviour of free electrons interacting with electromagnetic wave. Drude assumed free electrons in the metal to behave like gas molecules obeying the kinetic theory of gases. Due to the presence of free as well as bound electrons in doped semiconductors (the material developed in this work), the interaction of bound electrons with the electromagnetic wave is also to be considered along with Drude model, and thus formed the Drude-Lorentz (D-L) equation. The D-L model is defined as[6, 45],

$$\epsilon(\omega) = \epsilon_\infty - \frac{\omega_p^2}{\omega^2 + \gamma^2} + i\frac{\omega_p^2\gamma}{(\omega^2 + \gamma^2)\omega} \tag{1.6}$$

Here ϵ_∞ is the high frequency dielectric constant, ω_p is the plasma frequency and γ is the Drude relaxation, which quantifies the loss and hence ϵ_2. To make ϵ_2 small, either ω_p or γ should be small. The large fixed carrier concentration $10^{23}/\mathrm{cm}^3$ of metals thus fix the ω_p because of the direct relation between these, defined as[15],

$$\omega_p = \sqrt{\frac{ne^2}{m\epsilon_o}} \tag{1.7}$$

Where n is the free carrier concentration, e is charge of electron, m is effective mass and ϵ_o is permittivity at vacuum. The real part of the permittivity ϵ_1 describes the polarisation strength induced by the electric field and the imaginary part ϵ_2 describes the loss induced by the polarisation. In a simple plasmonic configuration, the permittivity of the prism ϵ_p should be greater than permittivity of air to generate the surface plasmons. When the light beam incident at an angle greater than the critical angle, it will undergo total internal reflection. The critical angle is defined as $\theta_c = sin^{-1}\sqrt{\frac{\epsilon_m}{\epsilon_p}}$ [46]. Due to total internal reflection, an evanescent wave is generated at prism-film interface in the Kretschmann configuration will couple with surface plasmon and generate SPP at the resonant condition.

The incoming electric field incident on the prism have the form $E = E_o e^{i(k_x x + k_z z - \omega t)}$, where x, z directions are as shown in Fig.1.9, where k = $(k_x, 0, k_z)$ is the wave vector and ω is the angular frequency. The electromagnetic wave should satisfy Maxwell's equation so that $k^2 = k_x^2 + k_z^2 = (\frac{\omega}{c})^2\ \epsilon_p$, c represents the light velocity. The wave vector of the incident electromagnetic wave inside the prism in the x direction will be k_x = k sinθ and this is same for all three layers since they are parallel and k_x is parallel to them. To measure the SPP generation, the reflectance in the two interfaces such as prism-film and film-dielectric have to be considered. For this, one can use the Fresnel equation, which in general is used to describe the the reflection and transmission of light incident on the interface of the two media[47]. A three-layer model consisting of prism, plasmonic film and dielectric represented as p, m, d, respectively are showed in Fig.1.9. The reflectance at the first interface such as prism-film (r_{pm}) and film - dielectric (r_{md}) can be find out from Fresnel equation given as[48].

$$r_{pm} = \frac{\frac{cos\theta}{n_p} - \frac{\sqrt{\epsilon_m - n_p^2 sin^2\theta}}{\epsilon_m}}{\frac{cos\theta}{n_p} + \frac{\sqrt{\epsilon_m - n_p^2 sin^2\theta}}{\epsilon_m}} \tag{1.8}$$

$$r_{md} = \frac{\frac{\sqrt{\epsilon_m - n_p^2 sin^2\theta}}{\epsilon_m} - \frac{\sqrt{\epsilon_d - n_p^2 sin^2\theta}}{\epsilon_d}}{\frac{\sqrt{\epsilon_m - n_p^2 sin^2\theta}}{\epsilon_m} + \frac{\sqrt{\epsilon_d - n_p^2 sin^2\theta}}{\epsilon_d}} \tag{1.9}$$

And the final Fresnel reflectance equation is

$$r_{pmd} = \frac{r_{pm} + r_{md}e^{2ik_{zm}d_m}}{1 + r_{pm} + r_{md}e^{2ik_{zm}d_m}} \tag{1.10}$$

Where d_m is the thickness of the film and k_{zm} is the wave vector in the film.

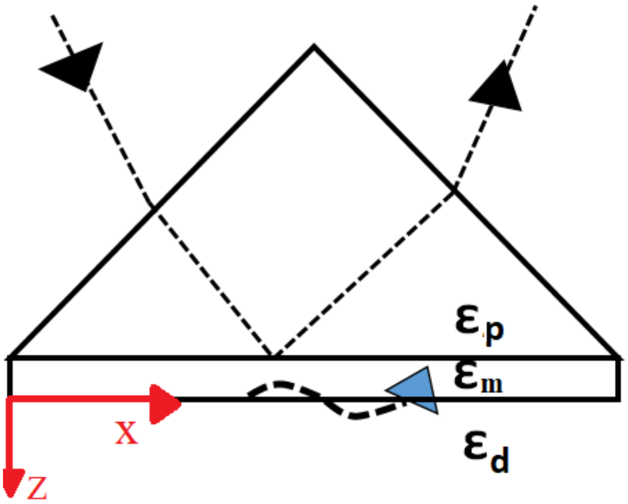

Figure 1.9: Three layer model consisting of prism, film and air.

1.4 Plasmonic materials

1.4.1 Problems with conventional plasmonic materials

Metals, which is the granary of free electrons, are considered as conventional plasmonic materials. When a photon having energy, E is allowed to fall on a metal, free electrons absorb this energy and move near to fermi level. On the other hand, electrons at the fermi surface utilize this energy to move to next higher conduction band, if the energy is sufficient for transition. Thus, there generated a loss corresponding to transition of electron between the bands, and is described as interband transition loss. Similar losses are reported in metals at high frequency end of visible range[49]. If the energy of incoming photon is not sufficient to make transition between bands, then it will increase the chances for intraband transition and hence losses. Low frequency photons usually suffer this intraband loss or Drude loss[8]. In a conventional plasmonic material like gold, interband transitions cause loss in visible region and intraband transitions in NIR. The higher magnitude of loss ϵ_2 in NIR of gold thus make it unsuitable for NIR plasmonic applications[8]. Besides intra-inter band transitions, scattering due to defects in the material also contribute to ϵ_2 [50]. The loss mechanism can be understood properly using the free electron response of metal, defined by Drude-Lorentz(eqn 1.6)[51]. Along with this, the large negative real part of permittivity of metals in near infrared region including telecommunication wavelength of 1550nm made it unsuitable for device fabrication in this field. The large negative value demands different dimensions to metal and dielectric components, which introduce device fabrication difficulties. The polarisation responses from dielectric and metallic components are to be of the same order, so that the geometric fill fraction of the metal and dielectric can be tuned to match the design requirements[49].

Despite of all these issues, metals also have nanofabrication challenges, especially in the thin film form. The integration of noble metals into silicon manufacturing process will result in deep traps, which affects the nanoelectronics performance of the material[6]. These kinds of traps can be additionally added if they are grown as thin films; while comparing with bulk material, metal thin film pose different morphology, which will result in loss due to grain-boundary scattering[6]. In addition, nanoscale patterning in metal leads to rough surface and edge, which also increase the scattering and hence loss[52, 53]. Regarding the chemical stability of the metals, gold is more stable than silver and copper. Copper is sensitive in air to form oxide [54, 55], and silver undergoes sulphidation in sulphur atmosphere[56, 57]. Both these have direct consequences in optical properties and thus increase the loss. Based on the aforementioned drawbacks of conventional plasmonic materials, researches have been searching better plasmonic materials. The significance of this work is also to develop a better low loss plasmonic material for NIR and visible applications.

1.4.2 Alternative plasmonic material

Necessity of an alternative solution is evident because of the issues discussed in the previous section related to conventional plasmonic device applications[58–60]. The introduction of new materials in this area will open up possibilities of new devices and also improves the performance of many existing plasmonic devices. As discussed earlier, material performance depends on both real and imaginary part of permittivity values, hence both these factors need to be considered critically when developing alternate materials. Ideally, for plasmonic applications, $\epsilon_1 < 0$ and $\epsilon_2 = 0$. However, it is not possible because of the loss mechanisms in the material. To control the loss, a number of strategies have been pursued.

One of the methods is to dope the semiconductors, which result in increase in free electron concentration up to $10^{21}/\text{cm}^3$, and such a carrier density will provide negative permittivity in NIR [62–64]. Other method is to reduce the number of free electrons to the required value, for example, by making metal alloys[65]. Fig.1.10. shows the various plasmonic materials with their carrier density and mobility[61]. Since availability of free electron is an important parameter for plasmonic application, doped semiconductor is a good approach. The optical response of free electrons can be described by Drude model[66]. By varying doping concentration, it is possible to alter the carrier concentration and hence one can tune the plasma frequency. This property of semiconductor makes it differ from the metals. However, sorting of desired semiconductor is utmost importance.

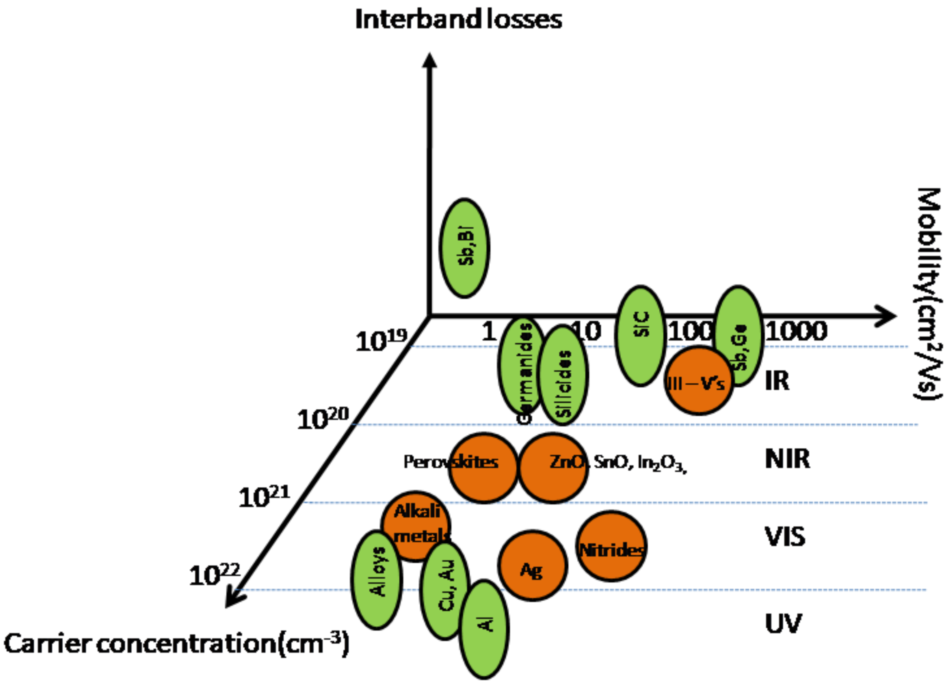

Figure 1.10: Variation of carrier density, mobility and interband loss of various plasmonic material in UV-VIS-IR range[61]

Conventional semiconductor such as silicon and germanium are not able to exceed carrier concentration to $10^{20}/\mathrm{cm}^3$. However, transparent conducting oxides such as Al:ZnO (AZO), Ga:ZnO (GZO), In:ZnO (IZO) have been reported with carrier concentration upto $10^{21}/\mathrm{cm}^3$, which promised as a good plasmonic material[67–69]. According to West et al[8], loss reported by AZO, IZO, ITO is four times lesser than that of silver in the near infrared. Moreover, the metal-like behaviour of these doped semiconducting materials in NIR helps to understand the optical response by combined effect of Drude-Lorentz model, where the real part of the dielectric permittivity ϵ_1

decides the optical response of a material, and optical loss by the imaginary part(ϵ_2)[6, 65].

1.4.3 Transparent conducting oxides

It was in 1907, Badeker[70] reported the first transparent conducting oxide (TCO). The first reported TCO film was thermally oxidized vacuum sputtered CdO thin film. The high mobility because of its low effective mass attracted the researchers initially; however, this material remained as theoretical interest due to its high toxicity. The deposition of metals in their oxide form was done through the post oxidation method of evaporated metal films[71]. The significant development of TCO materials started in 1957, as seen in most of the everyday applications, ranging from digital watches to computer screens, or any other types of displays[72, 73].

The simultaneous behaviour of optical transparency and electrical conductivity in a material has been utilized before long years. This behaviour defines the material class of TCOs, such as zinc oxide (ZnO), tin oxide (SnO_2) and indium oxide (In_2O_3), which have large band gap near to 3.3 eV. Considering these materials as host lattices, and doping these by higher valent atom results in generation of free electrons[74–79]. The pronounced nonstoichiometry of the materials and oxygen deficiency up to 1% results in intrinsic defects and hence act as source of free electrons[80–82]. The wide band gap of the materials avoids the transition between conduction and valence bands, and hence appropriate as low loss plasmonic materials[83]. Most of the researchers use ZnO as the host lattice for TCO applications. This is mainly due to its unique chemical and physical properties such as high electrochemical coupling coefficient, high chemical stability, broad range of radiation absorption and high photo stability[83–89]. ZnO has wide bandgap (3.37 eV), and high bond energy of nearly 60 meV with high thermal and mechanical stability attracted researchers to use in electronics, optoelectronics and laser technology[90–92]. Doping with trivalent atoms such as, aluminium, indium or gallium in zinc lattice results in increasing free electron concentration[93–95]. Theoretical studies indicate that dopants having comparable ionic radii with that of the host zinc ion will substitute well in the lattice. The dopants use only two of its valence electrons among three and the remaining one will go to the conduction band, and results in introducing a shallow donor level in the oxide[96].

Solid solubility limit of a material is defined as the capacity of the host lattice for substitution of dopants. These have direct dependence with charge and ionic radii of dopants and host atom[97]. Excessive doping results in moving dopants to the interstitial site, thus forming oxide which entirely distorts the lattice[98, 99]. Below solubility limit, the carrier density of the material can be tuned according to doping percentage and thus become more attractive than metals[97]. Direct dependence of carrier density with plasma frequency results in tuning plasmonic behaviour of these materials[15]. Also there are reports on decreasing the stress and strain induced by a dopant by adding another dopant; for example, in ZnO, doping with Al atom having ionic radii less than Zn leads to compression and this can be balanced by adding In, which has higher ionic radii than Zn[100].

TCOs can be grown in to thin films with polycrystalline structures. They can be integrated with standard technologies, and hence can be considered as obvious choices for alternative plasmonic materials in NIR. Among the TCOs, ITO and doped zinc oxide are preferred by most of the researchers[6, 8, 62, 64, 65]. Different methods such as laser ablation[101], sputtering[102], solution processing[103], evaporation[104], chemical vapour deposition[105] etc were used to deposit TCO thin films. Since non-stoichiometric, their properties will depend upon the deposition conditions. Sputtering method was widely used to control the stochiometry of the TCOs[6].

In this study, ZnO has been considered as the host lattice and it is co-doped with Al and In. These co-dopants have large and small ionic radii compared to the host, and thus can balance the elongation or contraction developed in ZnO lattice, formed due to the mismatch in the ionic radii between the dopants and host ion. Thin films are prepared using simple solution-based techniques such as spin and spray coatings, and also by sputtering technique. Factors such as cheap, versatile and uniform film coating etc. gave priorities to opt methods such as spin and spray coatings compared to other vacuum methods.

1.4.4 Transition metal nitrides

The recent development in alternative metallic materials other than gold or silver has been due to the distinct advantages of these materials compared with the conventional metals [64, 106–108]. TiN along with other transition metal nitrides like zirconium nitride (ZrN), tantalum nitride (TaN) are also projected as promising plasmonic materials in visible and NIR wavelength[109, 110]. These materials are known for their refractory properties; these are chemically stable even at temperature >2000^{o}C. They can exhibit metallic properties also[109]. In addition, non-stoichiometry allows them for tuning the optical properties[111]. There are other remarkable properties, such as, excellent adhesion to the substrate, high toughness, oxidative resistance etc., which make themselves to have wide range of applications[112]. Recent studies in TiN revealed its comparable plasmonic performance to the conventional plasmonic metal, gold. Hence, TiN is also promised to be a good candidate for hyperbolic metamaterial application, transformation optics, etc.[113–116].

The titanium nitride contains both Ti-Ti bond and Ti-N bond in which former is metallic bond and the latter is covalent bond. The combined metallic properties such as metallic reflectance and electrical conductivity, the covalent properties such as high melting point, and extreme hardness and brittleness, along with excellent thermal and chemical stabilities make these materials unique for plasmonic applications[117]. During the formation of TiN, nitrogen atom whose outer shell having five valence electrons will make covalent bond with the three electrons in the outer shell of titanium atom. Remaining one electron in titanium atom, which is not involved in the covalent bond formation thus contribute one free electron to the material. These electrons occupy in the shallow donor levels and a very small energy is needed to activate this electron in to the conduction band. TiN possesses high free carrier concentration this way; the number of carriers is proportional to the concentration of titanium in the material. By giving an electron to the lattice, Ti atom become positively charged, reside in the lattice and forms metallic bonding with other Ti ions[118]. In an overstoichiometric TiN_x thin films with $x > 1$, possessing the rocksalt structure, point defects such as Ti vacancies or N interstitials were already reported[119, 120]. Both these point defects together with grain boundaries modify the electron interactions with N and Ti atoms.

The varying electrical properties with non-stoichiometry was studied by Schmid et al[121]. According to them, carrier concentration decreases with increase in nitrogen content in the thin film. The band structure of TiN reveals the presence of three bands located between 3 eV and 8 eV below the fermi energy derived from the '2p' nitrogen orbital and one from 'd' titanium orbital[121,122]. The charge corresponding to N 2p amounts to four electrons and Ti d orbital corresponds to 2 electrons. Thus, charge transfer of roughly one electron to the nitrogen ion will take place. When nitrogen is removed from the stoichiometric TiN, there is no charge transfer take place, and thus the corresponding electron will return to the fermi level. Hence, the removal of nitrogen atom results in loss of hybridization energy of Ti 3d orbital. If the nitrogen is inserted into an interstitial position, it is likely to bind to the extra electron, and remove one electron from fermi level[122]. If titanium vacancy is created, it will deteriorate the conduction electrons in TiN. The one electron, which normally transferred to nitrogen ion, will miss with Ti vacancy. Hence, an electron from the conduction band will be transferred to nitrogen ion. The second electron lost by the conduction band is the one that normally contribute while making covalent bond with nitrogen. For non-stoichiometric TiN_x, free carrier concentration will vary like $N_o g(1\text{-}x)$, where N_o is the free carrier concentration in the stoichiometric compound, and $g = 1$ for nitrogen defects and $g = 2$ for titanium defects[120–123]. Thus, the present work is focussed on the deposition of TiN films on glass substrates, and on the study of their electrical, structural and optical properties in the context of plasmonic properties.

1.5 Plasmonic materials- a review

It is common to treat metals such as gold and silver as conventional plasmonic materials in visible region due to their low ohmic losses or high DC conductivity[6]. Michael Faraday first observed colour changes when metal nanoparticles, mainly gold (Au) and silver (Ag), were dispersed in dielectric body[124]. Colloidal assembly methods extensively studied over the years is another reason for the widespread use and application of metal nanoparticles[125, 126]. As a result of these two fundamental advantages, the use of Au and Ag in plasmonics research has been flourished in recent decades. However, problems in a wide range of fields await a solution in the field of plasmonics, which cannot be addressed with a few materials. One of the major drawbacks of metals is its large absorption loss in IR region. As such, alternative materials that provide a 'golden mean' are required to provide solutions to problems, such as operating within specific window of the electromagnetic spectrum, and operating under different ambient conditions[109, 125, 126]. Apart from the absorption losses, metals often suffer high transition losses because their interband transitions are very close to the resonance regions. Despite the fact that high carrier concentrations are necessary for plasmonic response, large values are not always the best[61]. Plasmonic materials are usually used in applications where their physical and chemical properties are equally important as their optical properties[127]. Getting stable Ag nanoparticles is still a challenge in the plasmonics community [128]. In the same way, other metals such as copper, aluminum, and alkali metals also show good plasmonic responses, but are chemically unstable[55, 129, 130]. Even if gold has shown to be chemically stable, they possess high thermal instability at high temperature, and hence a poor material for temperature based applications[131].

Transparent conducting oxides (TCOs) have recently been proposed as an alternative plasmonic material especially in NIR region.Indium oxide, zinc oxide, and cadmium oxide are some of the oxide semiconductors that can be highly doped to generate free electrons. In 2013, kim et al[62] demonstrated TCO materials like AZO, GZO and ITO nanostructures, which can support surface plasmon polariton at the telecommunication wavelength. When patterning these films using standard nanofabrication techniques, TCOs can exhibit localised surface plasmon like gold and silver. Jin et al[132] used TCO to incorporate Ag particles with AZO film, and which greatly influenced the surface morphology, size distribution and surface plasmon resonance of Ag particle. Another study using AZO has been done by Guske et al[133] by making a sandwich thin film of AZO-Ag-AZO on BK7 substrate, and showed that the optical properties of the silver are substantially different from bulk silver, when it is in the sandwich configuration. A comparative study on the excitation and propagation of the surface polariton wave of AZO and ITO thin film was done using a mathematical simulation by Rajak et al[134]. They observed a resonant frequency shift from 7586 to 7798 cm^{-1} for ITO when the thickness is increased and for AZO the observed shift is from 3926 to 4668 cm^{-1}.

In this work, the plasmonic properties of the co-doped films, which have not been explored before have been studied. The research involved the preparation of Al and In co-doped ZnO films by vacuum and solution based methods, and the analysis of the results in detail.

Transition metal nitrides are another class of materials exhibiting plasmonic resonances in visible and NIR regions [135]. Optical properties of TiN thin films were studied numerically by Steinmüller-Nethl et al[136] in 1994 and Hibbins et al[137] in 1998 in which excitation of surface plasmon wave on a corrugated TiN surface using grating based coupling was reported. The relation connecting the stoichiometry and the plasma frequency was studied by logothetidis et al[138] using the in situ spectroscopic elliposometry measurement. The optical properties of TiN films deposited on Si substrates were studied using the Drude-lorentz approach by adachi et al[139].

Later Cortie et al in 2010[140] fabricated nanostructured TiN thin films and showed that their structure has tunable plasmonic properties with light. In 2011 Chen et al[141] excited surface plasmon wave in TiN thin film coated on a sapphire substrate using Kretschmann configuration. In 2018 Chen et al[142] demonstrated the surface plasmon polariton of ITO-TiN-ITO thin films at the telecommunication window using the Kretschmann configuration. The room temperature deposition of TiN thin films and their dependence on processing parameter like substrate choice, reactive gas flow ratio and film thickness were reported by chang et al[143]. Recently Chen et al[144] studied the tunable plasmonic properties of ternary (Ti,Zr)N_x thin films by varying the nitrogen gas flow ratio.In this work the focus was on fabricating non-stoichiometric TiN_x films on glass substrates, where the deposition was done at room temperature by varying $Ar:N_2$ ratio, and finally excited surface plasmon resonance in these films using the Kretschmann configuration.

1.6 Objectives of the present work

The main objectives of the proposed work are

- To develop semiconductor oxide and nitride thin films with carrier density in the range 10^{20} to 10^{22}/cc on glass substrates by solution and vacuum based techniques
- To study the structural, electrical, optical properties and to extract the dielectric function
- To study the surface plasmon resonance in semiconductor oxide or nitride thin films in the context of applications in the visible and near-IR frequencies

References

[1] P. S. Peercy, “The drive to miniaturization,” *Nature*, vol. 406, no. 6799, pp. 1023–1026, 2000.

[2] K. Liu, S. Sun, A. Majumdar, and V. J. Sorger, “Fundamental scaling laws in nanophotonics,” *Sci. Rep*, vol. 6, no. 1, pp. 1–12, 2016.

[3] S. Sun, V. K. Narayana, M. Miscuglio, L. C. Kimerling, T. El-Ghazawi, and V. J. Sorger, “clear: a holistic figure-of-merit for post-and predicting electronic and photonic-based compute-system evolution,” *Sci. Rep*, vol. 10, no. 1, pp. 1–9, 2020.

[4] C. Lee, F. Dieleman, J. Lee, C. Rockstuhl, S. A. Maier, and M. Tame, “Quantum plasmonic sensing: beyond the shot-noise and diffraction limit,” *ACS Photonics*, vol. 3, no. 6, pp. 992–999, 2016.

[5] M. Tame and K. McEnery, “O? zdemir, s.. k., lee, j., maier, sa, and kim, ms,“,” *Quantum plasmonics. Nat Phys*, vol. 9, p. 32940, 2013.

[6] G. V. Naik, V. M. Shalaev, and A. Boltasseva, “Alternative plasmonic materials: beyond gold and silver,” *Adv. Mater.*, vol. 25, no. 24, pp. 3264–3294, 2013.

[7] L. Landau and E. Lifshits, “Electrodynamics of solid media,” *Izd. Nauka, Moscow*, 1982.

[8] P. R. West, S. Ishii, G. V. Naik, N. K. Emani, V. M. Shalaev, and A. Boltasseva, “Searching for better plasmonic materials,” *Laser Photonics Rev.*, vol. 4, no. 6, pp. 795–808, 2010.

[9] S. Lal, S. Link, and N. J. Halas, "Nano-optics from sensing to waveguiding," *Nanosci. Nanotechnol.*, pp. 213–220, 2010.

[10] M. L. Brongersma and V. M. Shalaev, "The case for plasmonics," *science*, vol. 328, no. 5977, pp. 440–441, 2010.

[11] D. R. Smith, J. B. Pendry, and M. C. Wiltshire, "Metamaterials and negative refractive index," *Science*, vol. 305, no. 5685, pp. 788–792, 2004.

[12] W. Cai and V. M. Shalaev, *Optical metamaterials*, vol. 10. Springer, 2010.

[13] J. B. Pendry, D. Schurig, and D. R. Smith, "Controlling electromagnetic fields," *science*, vol. 312, no. 5781, pp. 1780–1782, 2006.

[14] H. A. Atwater, "The promise of plasmonics," *Sci. Am.*, vol. 296, no. 4, pp. 56–63, 2007.

[15] S. A. Maier, *Plasmonics: fundamentals and applications.* Springer Science & Business Media, 2007.

[16] L. Jauffred, A. Samadi, H. Klingberg, P. M. Bendix, and L. B. Oddershede, "Plasmonic heating of nanostructures," *Chem. Rev.*, vol. 119, no. 13, pp. 8087–8130, 2019.

[17] S. Zeng, D. Baillargeat, H.-P. Ho, and K.-T. Yong, "Nanomaterials enhanced surface plasmon resonance for biological and chemical sensing applications," *Chem. Soc. Rev.*, vol. 43, no. 10, pp. 3426–3452, 2014.

[18] O. Tokel, F. Inci, and U. Demirci, "Advances in plasmonic technologies for point of care applications," *Chem. Rev.*, vol. 114, no. 11, pp. 5728–5752, 2014.

[19] J. A. Schuller, E. S. Barnard, W. Cai, Y. C. Jun, J. S. White, and M. L. Brongersma, "Plasmonics for extreme light concentration and manipulation," *Nat. Mater.*, vol. 9, no. 3, pp. 193–204, 2010.

[20] R. W. Wood, “Xlii. on a remarkable case of uneven distribution of light in a diffraction grating spectrum,” *London, Edinburgh Dublin Philos. Mag. J. Sci.*, vol. 4, no. 21, pp. 396–402, 1902.

[21] A. Otto, “Excitation of nonradiative surface plasma waves in silver by the method of frustrated total reflection,” *Zeitschrift für Physik A Hadrons and nuclei*, vol. 216, no. 4, pp. 398–410, 1968.

[22] E. Kretschmann and H. Raether, “Radiative decay of non radiative surface plasmons excited by light,” *Zeitschrift für Naturforschung A*, vol. 23, no. 12, pp. 2135–2136, 1968.

[23] B. Liedberg, C. Nylander, and I. Lunström, “Surface plasmon resonance for gas detection and biosensing,” *Sens. Actuators*, vol. 4, pp. 299–304, 1983.

[24] M. Couture, S. S. Zhao, and J.-F. Masson, “Modern surface plasmon resonance for bioanalytics and biophysics,” *Phys. Chem. Chem. Phys.*, vol. 15, no. 27, pp. 11190–11216, 2013.

[25] M. Yamamoto, “Surface plasmon resonance (spr) theory: tutorial,” *Rev. Polarogr.*, vol. 48, no. 3, pp. 209–237, 2002.

[26] Y. Tang, X. Zeng, and J. Liang, “Surface plasmon resonance: an introduction to a surface spectroscopy technique,” *J. Chem. Educ.*, vol. 87, no. 7, pp. 742–746, 2010.

[27] J. Zhang, L. Zhang, and W. Xu, “Surface plasmon polaritons: physics and applications,” *J. Phys. D: Appl. Phys.*, vol. 45, no. 11, p. 113001, 2012.

[28] D. Pines, “Collective energy losses in solids,” *Rev. Mod. Phys.*, vol. 28, no. 3, p. 184, 1956.

[29] U. Fano, “Atomic theory of electromagnetic interactions in dense materials,” *Phys. Rev.*, vol. 103, no. 5, p. 1202, 1956.

[30] R. H. Ritchie, “Plasma losses by fast electrons in thin films,” *Phys. Rev.*, vol. 106, no. 5, p. 874, 1957.

[31] S. Cunningham, A. Maradudin, and R. Wallis, “Effect of a charge layer on the surface-plasmon-polariton dispersion curve,” *Phys. Rev. B*, vol. 10, no. 8, p. 3342, 1974.

[32] J. Pedarnig, M. Specht, W. Heckl, and T. Hänsch, “Scanning plasmon near-field microscope,” in *Near Field Optics*, pp. 273–280, Springer, 1993.

[33] M. Ashino and M. Ohtsu, “Fabrication and evaluation of a localized plasmon resonance probe for near-field optical microscopy/spectroscopy,” *Appl. Phys. Lett.*, vol. 72, no. 11, pp. 1299–1301, 1998.

[34] J. Sambles, G. Bradbery, and F. Yang, “Optical excitation of surface plasmons: an introduction,” *Contemp. Phys.*, vol. 32, no. 3, pp. 173–183, 1991.

[35] W. L. Barnes, A. Dereux, and T. W. Ebbesen, “Surface plasmon subwavelength optics,” *nature*, vol. 424, no. 6950, pp. 824–830, 2003.

[36] A. Sato, “Surface plasmon fluorescence spectroscopy and optical waveguide fluorescence spectroscopy in limit of detection studies,” *Max Planck Institute for Polymer Research, Johannes Gutenberg University of Mainz, Mainz. Master thesis*, 2006.

[37] Y. Suzuki, M. Osawa, A. Hatta, and W. Suëtaka, “Mechanism of absorption enhancement in infrared atr spectra observed in the kretschmann configuration,” *Appl. Surf. Sci.*, vol. 33, pp. 875–881, 1988.

[38] E. K. Akowuah, T. Gorman, and S. Haxha, “Design and optimization of a novel surface plasmon resonance biosensor based on otto configuration,” *Opt. Express*, vol. 17, no. 26, pp. 23511–23521, 2009.

[39] G. Bradberry and J. Sambles, "The excitation of infra-red surface plasmon-polaritons on refractory metals," *Opt. Commun.*, vol. 67, no. 6, pp. 404–408, 1988.

[40] G. Ruffato, G. Zacco, and F. Romanato, "Innovative exploitation of grating-coupled surface plasmon resonance for sensing," *Plasmonics-Principles Appl*, vol. 2012, pp. 419–444, 2012.

[41] K. Lin, Y. Lu, J. Chen, R. Zheng, P. Wang, and H. Ming, "Surface plasmon resonance hydrogen sensor based on metallic grating with high sensitivity," *Opt. Express*, vol. 16, no. 23, pp. 18599–18604, 2008.

[42] B. A. Prabowo, A. Purwidyantri, and K.-C. Liu, "Surface plasmon resonance optical sensor: A review on light source technology," *Biosensors*, vol. 8, no. 3, p. 80, 2018.

[43] M. Barberoglou, D. Gray, E. Magoulakis, C. Fotakis, P. Loukakos, and E. Stratakis, "Controlling ripples' periodicity using temporally delayed femtosecond laser double pulses," *Opt. Express*, vol. 21, no. 15, pp. 18501–18508, 2013.

[44] J. Čtyroký, J. Homola, P. Lambeck, S. Musa, H. Hoekstra, R. Harris, J. Wilkinson, B. Usievich, and N. Lyndin, "Theory and modelling of optical waveguide sensors utilising surface plasmon resonance," *Sens. Actuators B Chem.*, vol. 54, no. 1-2, pp. 66–73, 1999.

[45] R. Onaka, "F. wooten: Optical properties of solids, academic press, new york and london, 1972, 260 , 23.5× 16cm, 4,660 ," *J. Phys. Soc. Jpn.*, vol. 28, no. 9, pp. 803–804, 1973.

[46] S. Rajak, J. Banerjee, and M. Ray, "Parametric influence of film thickness and incident angle on resonance spectra of pre-and post-annealed ga doped zno," *J. Appl. Phys.*, vol. 125, no. 24, p. 243105, 2019.

[47] R. Azzam, "Relationship between the p and s fresnel reflection coefficients of an interface independent of angle of incidence," *JOSA A*, vol. 3, no. 7, pp. 928–929, 1986.

[48] M. Born *et al.*, “E. wolf principles of optics,” *Pergamon Press*, vol. 6, no. 188, pp. 36–111, 1980.

[49] P. B. Johnson and R.-W. Christy, “Optical constants of the noble metals,” *Phys. Rev. B*, vol. 6, no. 12, p. 4370, 1972.

[50] J. B. Khurgin and A. Boltasseva, “Reflecting upon the losses in plasmonics and metamaterials,” *MRS Bull.*, vol. 37, no. 8, pp. 768–779, 2012.

[51] S. Schubin and S. Wonsowsky, “On the electron theory of metals,” *Proc. R. Soc. London A.*, vol. 145, no. 854, pp. 159–180, 1934.

[52] E. Kretschmann, “Decay of non radiative surface plasmons into light on rough silver films. comparison of experimental and theoretical results,” *Opt. Commun.*, vol. 6, no. 2, pp. 185–187, 1972.

[53] D.-L. Hornauer, “Light scattering experiments on silver films of different roughness using surface plasmon excitation,” *Opt. Commun.*, vol. 16, no. 1, pp. 76–79, 1976.

[54] W. Campbell and U. Thomas, “Films on freshly abraded copper surfaces,” *Nature*, vol. 142, no. 3588, pp. 253–254, 1938.

[55] G. H. Chan, J. Zhao, E. M. Hicks, G. C. Schatz, and R. P. Van Duyne, “Plasmonic properties of copper nanoparticles fabricated by nanosphere lithography,” *Nano Lett.*, vol. 7, no. 7, pp. 1947–1952, 2007.

[56] H. Bennett, R. Peck, D. Burge, and J. Bennett, “Formation and growth of tarnish on evaporated silver films,” *J. Appl. Phys.*, vol. 40, no. 8, pp. 3351–3360, 1969.

[57] D. Burge, J. Bennett, R. Peck, and H. Bennett, “Growth of surface films on silver,” *Surf. Sci.*, vol. 16, pp. 303–320, 1969.

[58] E. Bacaksiz, M. Parlak, M. Tomakin, A. Özçelik, M. Karakız, and M. Altunbaş, “The effects of zinc nitrate, zinc acetate and zinc chloride precursors on investigation of structural and optical properties of zno thin films,” *J. Alloys. Compd*, vol. 466, no. 1-2, pp. 447–450, 2008.

[59] J. Wang, J. Cao, B. Fang, P. Lu, S. Deng, and H. Wang, “Synthesis and characterization of multipod, flower-like, and shuttle-like zno frameworks in ionic liquids,” *Mater. Lett.*, vol. 59, no. 11, pp. 1405–1408, 2005.

[60] A. Pradhan, R. Mundle, K. Santiago, J. Skuza, B. Xiao, K. Song, M. Bahoura, R. Cheaito, and P. E. Hopkins, “Extreme tunability in aluminum doped zinc oxide plasmonic materials for near-infrared applications,” *Sci. Rep.*, vol. 4, no. 1, pp. 1–6, 2014.

[61] A. Boltasseva and H. A. Atwater, “Low-loss plasmonic metamaterials,” *Science*, vol. 331, no. 6015, pp. 290–291, 2011.

[62] J. Kim, G. V. Naik, N. K. Emani, U. Guler, and A. Boltasseva, “Plasmonic resonances in nanostructured transparent conducting oxide films,” *IEEE J. Sel. Top. Quantum Electron.*, vol. 19, no. 3, pp. 4601907–4601907, 2013.

[63] H. Kim, M. Osofsky, S. Prokes, O. Glembocki, and A. Piqué, “Optimization of al-doped zno films for low loss plasmonic materials at telecommunication wavelengths,” *Appl. Phys. Lett.*, vol. 102, no. 17, p. 171103, 2013.

[64] J. Kim, G. V. Naik, A. V. Gavrilenko, K. Dondapati, V. I. Gavrilenko, S. Prokes, O. J. Glembocki, V. M. Shalaev, and A. Boltasseva, “Optical properties of gallium-doped zinc oxide—a low-loss plasmonic material: first-principles theory and experiment,” *Phys. Rev. X*, vol. 3, no. 4, p. 041037, 2013.

[65] G. V. Naik, J. Kim, and A. Boltasseva, “Oxides and nitrides as alternative plasmonic materials in the optical range,” *Opt. Mater. Express*, vol. 1, no. 6, pp. 1090–1099, 2011.

[66] K. Fuchs, "The conductivity of thin metallic films according to the electron theory of metals," in *Mathematical Proceedings of the Cambridge Philosophical Society*, vol. 34, pp. 100–108, Cambridge University Press, 1938.

[67] C. Muiva, T. Sathiaraj, and K. Maabong, "Effect of doping concentration on the properties of aluminium doped zinc oxide thin films prepared by spray pyrolysis for transparent electrode applications," *Ceram. Int.*, vol. 37, no. 2, pp. 555–560, 2011.

[68] G. Hirata, J. McKittrick, T. Cheeks, J. Siqueiros, J. Diaz, O. Contreras, and O. Lopez, "Synthesis and optelectronic characterization of gallium doped zinc oxide transparent electrodes," *Thin solid films*, vol. 288, no. 1-2, pp. 29–31, 1996.

[69] S. Major, A. Banerjee, and K. Chopra, "Highly transparent and conducting indium-doped zinc oxide films by spray pyrolysis," *Thin solid films*, vol. 108, no. 3, pp. 333–340, 1983.

[70] K. Badeker, "Concerning the electricity conductibility and the thermoelectric energy of several heavy metal bonds," *Ann. Phys. (Berlin)*, vol. 22, p. 749, 1907.

[71] G. Rupprecht, "Investigations of the electrical and photoelectric conductivity of thin indium oxide layers. z phys 139: 504–517," 1954.

[72] D. Mattox and V. Mattox, "Review of transparent conductive oxides (tco)," in *Society of Vacuum Coaters*, 2007.

[73] S. Wakeham, M. Thwaites, B. Holton, C. Tsakonas, W. Cranton, D. Koutsogeorgis, and R. Ranson, "Low temperature remote plasma sputtering of indium tin oxide for flexible display applications," *Thin Solid Films*, vol. 518, no. 4, pp. 1355–1358, 2009.

[74] K. Chopra, S. Major, and D. Pandya, "Transparent conductors—a status review," *Thin solid films*, vol. 102, no. 1, pp. 1–46, 1983.

[75] A. Stadler, “Transparent conducting oxides—an up-to-date overview,” *Materials*, vol. 5, no. 4, pp. 661–683, 2012.

[76] S. Laux, N. Kaiser, A. Zöller, R. Götzelmann, H. Lauth, and H. Bernitzki, “Room-temperature deposition of indium tin oxide thin films with plasma ion-assisted evaporation,” *Thin Solid Films*, vol. 335, no. 1-2, pp. 1–5, 1998.

[77] D. C. Paine, T. Whitson, D. Janiac, R. Beresford, C. O. Yang, and B. Lewis, “A study of low temperature crystallization of amorphous thin film indium–tin–oxide,” *J. Appl. Phys.*, vol. 85, no. 12, pp. 8445–8450, 1999.

[78] J.-M. Ting and B. Tsai, “Dc reactive sputter deposition of zno: Al thin film on glass,” *Mater. Chem. Phys.*, vol. 72, no. 2, pp. 273–277, 2001.

[79] D. Dimova-Malinovska, N. Tzenov, M. Tzolov, and L. Vassilev, “Optical and electrical properties of rf magnetron sputtered zno: Al thin films,” *Mat.Sci.Eng. B*, vol. 52, no. 1, pp. 59–62, 1998.

[80] P. Ágoston, P. Erhart, A. Klein, and K. Albe, “Geometry, electronic structure and thermodynamic stability of intrinsic point defects in indium oxide,” *J. Phys.: Condens. Matter*, vol. 21, no. 45, p. 455801, 2009.

[81] Ç. Kılıç and A. Zunger, “Origins of coexistence of conductivity and transparency in sno 2,” *Physical review letters*, vol. 88, no. 9, p. 095501, 2002.

[82] L. Liu, Z. Mei, A. Tang, A. Azarov, A. Kuznetsov, Q.-K. Xue, and X. Du, “Oxygen vacancies: The origin of n-type conductivity in zno,” *Phys. Rev. B*, vol. 93, no. 23, p. 235305, 2016.

[83] J. B. Khurgin and G. Sun, “In search of the elusive lossless metal,” *Appl. Phys. Lett.*, vol. 96, no. 18, p. 181102, 2010.

[84] C. Jagadish and S. J. Pearton, *Zinc oxide bulk, thin films and nanostructures: processing, properties, and applications.* Elsevier, 2011.

[85] M. Chen, Z. Pei, C. Sun, L. Wen, and X. Wang, "Formation of al-doped zno films by dc magnetron reactive sputtering," *Mater. Lett.*, vol. 48, no. 3-4, pp. 194–198, 2001.

[86] J. Hu and R. G. Gordon, "Atmospheric pressure chemical vapor deposition of gallium doped zinc oxide thin films from diethyl zinc, water, and triethyl gallium," *J. Appl. Phys.*, vol. 72, no. 11, pp. 5381–5392, 1992.

[87] V. Fathollahi and M. M. Amini, "Sol–gel preparation of highly oriented gallium-doped zinc oxide thin films," *Mater. Lett.*, vol. 50, no. 4, pp. 235–239, 2001.

[88] S. Major and K. Chopra, "Indium-doped zinc oxide films as transparent electrodes for solar cells," *Sol Energ Mater*, vol. 17, no. 5, pp. 319–327, 1988.

[89] G. Machado, D. Guerra, D. Leinen, J. Ramos-Barrado, R. Marotti, and E. Dalchiele, "Indium doped zinc oxide thin films obtained by electrodeposition," *Thin Solid Films*, vol. 490, no. 2, pp. 124–131, 2005.

[90] P. Capper, S. Kasap, and A. Willoughby, *Zinc oxide materials for electronic and optoelectronic device applications.* John Wiley & Sons, 2011.

[91] M.-F. Chen, Y.-P. Chen, W.-T. Hsiao, and Z.-P. Gu, "Laser direct write patterning technique of indium tin oxide film," *Thin Solid Films*, vol. 515, no. 24, pp. 8515–8518, 2007.

[92] S. Fay, J. Steinhauser, N. Oliveira, E. Vallat-Sauvain, and C. Ballif, "Opto-electronic properties of rough lp-cvd zno: B for use as tco in thin-film silicon solar cells," *Thin solid films*, vol. 515, no. 24, pp. 8558–8561, 2007.

[93] E. Fortunato, L. Raniero, L. Silva, A. Goncalves, A. Pimentel, P. Barquinha, H. Aguas, L. Pereira, G. Goncalves, I. Ferreira, *et al.*, "Highly stable transparent and conducting gallium-doped zinc oxide thin films for photovoltaic applications," *Sol Energ Mat Sol C*, vol. 92, no. 12, pp. 1605–1610, 2008.

[94] A. Singh, R. Mehra, N. Buthrath, A. Wakahara, and A. Yoshida, "Highly conductive and transparent aluminum-doped zinc oxide thin films prepared by pulsed laser deposition in oxygen ambient," *J. Appl. Phys.*, vol. 90, no. 11, pp. 5661–5665, 2001.

[95] A. Maldonado, R. Asomoza, S. Tirado-Guerra, *et al.*, "Highly conductive and transparent in-doped zinc oxide thin films deposited by chemical spray using zn (c 5 h 7 o 2) 2," *J. Mater. Sci. Mater. Electron.*, vol. 12, no. 11, pp. 623–627, 2001.

[96] D. P. Norton, Y. Heo, M. Ivill, K. Ip, S. Pearton, M. F. Chisholm, and T. Steiner, "Zno: growth, doping & processing," *Mater. Today*, vol. 7, no. 6, pp. 34–40, 2004.

[97] B. Efafi, M. S. Ghamsari, M. Aberoumand, M. M. Ara, A. S. Ghamsari, and H. H. Rad, "Aluminum doped zno sol–gel derived nanocrystals: Raman spectroscopy and solid solubility characterization," *Phys. Status Solidi A*, vol. 211, no. 10, pp. 2426–2430, 2014.

[98] C. Richard A áCatlow, G. NevilleáGreaves, *et al.*, "Studies of cation dopant sites in metal oxides by exafs and computer-simulation techniques," *J. Mater. Chem.*, vol. 2, no. 3, pp. 309–316, 1992.

[99] V. K. Jayaraman, A. M. Álvarez, Y. M. Kuwabara, Y. Koudriavstev, *et al.*, "Effect of co-doping concentration on structural, morphological, optical and electrical properties of aluminium and indium co-doped zno thin films deposited by ultrasonic spray pyrolysis," *Mater. Sci. Semicond. Process.*, vol. 47, pp. 32–36, 2016.

[100] S. Kirby and R. Van Dover, “Improved conductivity of zno through codoping with in and al,” *Thin Solid Films*, vol. 517, no. 6, pp. 1958–1960, 2009.

[101] S. Krause, P. Miclea, F. Steudel, S. Schweizer, and G. Seifert, “Precise microstructuring of indium-tin oxide thin films on glass by selective femtosecond laser ablation,” *EPJ Photovolt.*, vol. 4, p. 40601, 2013.

[102] C. May, R. Menner, J. Strümpfel, M. Oertel, and B. Sprecher, “Deposition of tco films by reactive magnetron sputtering from metallic zn: Al alloy targets,” *Surf. Coat. Technol.*, vol. 169, pp. 512–516, 2003.

[103] R. M. Pasquarelli, D. S. Ginley, and R. O’Hayre, “Solution processing of transparent conductors: from flask to film,” *Chem. Soc. Rev.*, vol. 40, no. 11, pp. 5406–5441, 2011.

[104] T. Minami, S. Ida, and T. Miyata, “High rate deposition of transparent conducting oxide thin films by vacuum arc plasma evaporation,” *Thin Solid Films*, vol. 416, no. 1-2, pp. 92–96, 2002.

[105] Ü. Dagkaldiran, A. Gordijn, F. Finger, H. Yates, P. Evans, D. Sheel, Z. Remes, and M. Vanecek, “Amorphous silicon solar cells made with sno2: F tco films deposited by atmospheric pressure cvd,” *Mat.Sci.Eng.B*, vol. 159, pp. 6–9, 2009.

[106] U. Guler, A. V. Kildishev, A. Boltasseva, and V. M. Shalaev, “Plasmonics on the slope of enlightenment: the role of transition metal nitrides,” *Faraday Discuss.*, vol. 178, pp. 71–86, 2015.

[107] J. A. Dionne and H. A. Atwater, “Plasmonics: metal-worthy methods and materials in nanophotonics,” *Mrs Bull*, vol. 37, no. 8, pp. 717–724, 2012.

[108] F. H. Koppens, D. E. Chang, and F. J. García de Abajo, “Graphene plasmonics: a platform for strong light–matter interactions,” *Nano lett.*, vol. 11, no. 8, pp. 3370–3377, 2011.

[109] U. Guler, V. M. Shalaev, and A. Boltasseva, “Nanoparticle plasmonics: going practical with transition metal nitrides,” *Mater. Today*, vol. 18, no. 4, pp. 227–237, 2015.

[110] G. Abadias, C.-H. Li, L. Belliard, Q. M. Hu, N. Greneèche, and P. Djemia, “Large influence of vacancies on the elastic constants of cubic epitaxial tantalum nitride layers grown by reactive magnetron sputtering,” *Acta Mater.*, vol. 184, pp. 254–266, 2020.

[111] C. M. Zgrabik and E. L. Hu, “Optimization of sputtered titanium nitride as a tunable metal for plasmonic applications,” *Opt. Mater. Express*, vol. 5, no. 12, pp. 2786–2797, 2015.

[112] S. Yu, Q. Zeng, A. R. Oganov, G. Frapper, and L. Zhang, “Phase stability, chemical bonding and mechanical properties of titanium nitrides: a first-principles study,” *Phys. Chem. Chem. Phys.*, vol. 17, no. 17, pp. 11763–11769, 2015.

[113] G. V. Naik, J. L. Schroeder, X. Ni, A. V. Kildishev, T. D. Sands, and A. Boltasseva, “Titanium nitride as a plasmonic material for visible and near-infrared wavelengths,” *Opt. Mater. Express*, vol. 2, no. 4, pp. 478–489, 2012.

[114] G. V. Naik, B. Saha, J. Liu, S. M. Saber, E. A. Stach, J. M. Irudayaraj, T. D. Sands, V. M. Shalaev, and A. Boltasseva, “Epitaxial superlattices with titanium nitride as a plasmonic component for optical hyperbolic metamaterials,” *Proc. Natl. Acad. Sci.*, vol. 111, no. 21, pp. 7546–7551, 2014.

[115] M. Kumar, N. Umezawa, S. Ishii, and T. Nagao, “Examining the performance of refractory conductive ceramics as plasmonic materials: a theoretical approach,” *ACS Photonics*, vol. 3, no. 1, pp. 43–50, 2016.

[116] A. Lalisse, G. Tessier, J. Plain, and G. Baffou, “Quantifying the efficiency of plasmonic materials for near-field enhancement and photothermal conversion,” *J. Phys. Chem. C*, vol. 119, no. 45, pp. 25518–25528, 2015.

[117] Y. Jeyachandran, S. K. Narayandass, D. Mangalaraj, S. Areva, and J. Mielczarski, “Properties of titanium nitride films prepared by direct current magnetron sputtering,” *Mat.Sci.Eng.A*, vol. 445, pp. 223–236, 2007.

[118] M. Solovan, V. Brus, E. Maistruk, and P. Maryanchuk, “Electrical and optical properties of tin thin films,” *Inorg. Mater.*, vol. 50, no. 1, pp. 40–45, 2014.

[119] J. Hojo, O. Iwamoto, Y. Maruyama, and A. Kato, “Defect structure, thermal and electrical properties of ti nitride and v nitride powders,” *J. Less-Common Met.*, vol. 53, no. 2, pp. 265–276, 1977.

[120] M. Delfino, J. Fair, and D. Hodul, “X-ray photoemission spectra of reactively sputtered tin,” *J. Appl. Phys.*, vol. 71, no. 12, pp. 6079–6085, 1992.

[121] P. E. Schmid, M. Sato Sunaga, and F. Lévy, “Optical and electronic properties of sputtered tin x thin films,” *J. Vac. Sci. Technol. A: Vac. Surf. Films*, vol. 16, no. 5, pp. 2870–2875, 1998.

[122] A. Neckel, P. Rastl, R. Eibler, P. Weinberger, and K. Schwarz, “Results of self-consistent band-structure calculations for scn, sco, tic, tin, tio, vc, vn and vo,” *J. Phys. C: Solid State Phys.*, vol. 9, no. 4, p. 579, 1975.

[123] L. Porte, L. Roux, and J. Hanus, “Vacancy effects in the x-ray photoelectron spectra of ti n x,” *Phys. Rev. B*, vol. 28, no. 6, p. 3214, 1983.

[124] M. Faraday, “X. the bakerian lecture.—experimental relations of gold (and other metals) to light,” *Philos. Trans. R. Soc. Lond.*, no. 147, pp. 145–181, 1857.

[125] J. M. Romo-Herrera, R. A. Alvarez-Puebla, and L. M. Liz-Marzán, “Controlled assembly of plasmonic colloidal nanoparticle clusters,” *Nanoscale*, vol. 3, no. 4, pp. 1304–1315, 2011.

[126] X. Ye, L. Jin, H. Caglayan, J. Chen, G. Xing, C. Zheng, V. Doan-Nguyen, Y. Kang, N. Engheta, C. R. Kagan, *et al.*, "Improved size-tunable synthesis of monodisperse gold nanorods through the use of aromatic additives," *ACS nano*, vol. 6, no. 3, pp. 2804–2817, 2012.

[127] W. Cao and H. E. Elsayed-Ali, "Stability of ag nanoparticles fabricated by electron beam lithography," *Mater. Lett.*, vol. 63, no. 26, pp. 2263–2266, 2009.

[128] A. Desireddy, B. E. Conn, J. Guo, B. Yoon, R. N. Barnett, B. M. Monahan, K. Kirschbaum, W. P. Griffith, R. L. Whetten, U. Landman, *et al.*, "Ultrastable silver nanoparticles," *Nature*, vol. 501, no. 7467, pp. 399–402, 2013.

[129] G. H. Chan, J. Zhao, G. C. Schatz, and R. P. Van Duyne, "Localized surface plasmon resonance spectroscopy of triangular aluminum nanoparticles," *J. Phys. Chem. C*, vol. 112, no. 36, pp. 13958–13963, 2008.

[130] M. G. Blaber, M. D. Arnold, and M. J. Ford, "Search for the ideal plasmonic nanoshell: the effects of surface scattering and alternatives to gold and silver," *J. Phys. Chem. C*, vol. 113, no. 8, pp. 3041–3045, 2009.

[131] A. Tittl, X. Yin, H. Giessen, X.-D. Tian, Z.-Q. Tian, C. Kremers, D. N. Chigrin, and N. Liu, "Plasmonic smart dust for probing local chemical reactions," *Nano lett.*, vol. 13, no. 4, pp. 1816–1821, 2013.

[132] J. Jin, C. Liu, Z.-j. Yang, and L. Wang, "The influence of azo films on morphology and surface plasmon resonance properties of ag particles," *Surf. Coat. Technol.*, vol. 363, pp. 135–141, 2019.

[133] J. T. Guske, J. Brown, A. Welsh, and S. Franzen, "Infrared surface plasmon resonance of azo-ag-azo sandwich thin films," *Opt. Express*, vol. 20, no. 21, pp. 23215–23226, 2012.

[134] S. Rajak and M. Ray, "Comparative study of plasmonic resonance in transparent conducting oxides: Ito and azo," *J. Opt.*, vol. 43, no. 3, pp. 231–238, 2014.

[135] M. Wittmer, "Properties and microelectronic applications of thin films of refractory metal nitrides," *J. Vac. Sci. Technol. A: Vac. Surf. Films*, vol. 3, no. 4, pp. 1797–1803, 1985.

[136] D. Steinmüller-Nethl, R. Kovacs, E. Gornik, and P. Rödhammer, "Excitation of surface plasmons on titanium nitride films: determination of the dielectric function," *Thin Solid Films*, vol. 237, no. 1-2, pp. 277–281, 1994.

[137] A. P. Hibbins, J. R. Sambles, and C. R. Lawrence, "Surface plasmon-polariton study of the optical dielectric function of titanium nitride," *J. Mod. Opt.*, vol. 45, no. 10, pp. 2051–2062, 1998.

[138] S. Logothetidis, I. Alexandrou, and A. Papadopoulos, "In situ spectroscopic ellipsometry to monitor the process of tin x thin films deposited by reactive sputtering," *J. Appl. Phys*, vol. 77, no. 3, pp. 1043–1047, 1995.

[139] S. Adachi and M. Takahashi, "Optical properties of tin films deposited by direct current reactive sputtering," *J. Appl. Phys.*, vol. 87, no. 3, pp. 1264–1269, 2000.

[140] M. Cortie, J. Giddings, and A. Dowd, "Optical properties and plasmon resonances of titanium nitride nanostructures," *Nanotechnology*, vol. 21, no. 11, p. 115201, 2010.

[141] N. Chen, W. Lien, C. Liu, Y. Huang, Y. Lin, C. Chou, S. Chang, and C. Ho, "Excitation of surface plasma wave at tin/air interface in the kretschmann geometry," *J. Appl. Phys.*, vol. 109, no. 4, pp. 043104–043104, 2011.

[142] C. Chen, Z. Wang, K. Wu, H. Chong, Z. Xu, and H. Ye, "Ito–tin–ito sandwiches for near-infrared plasmonic materials," *ACS Appl Mater Inter*, vol. 10, no. 17, pp. 14886–14893, 2018.

[143] C.-C. Chang, J. Nogan, Z.-P. Yang, W. J. Kort-Kamp, W. Ross, T. S. Luk, D. A. Dalvit, A. K. Azad, and H.-T. Chen, "Highly plasmonic titanium nitride by room-temperature sputtering," *Sci. Rep.*, vol. 9, no. 1, pp. 1–9, 2019.

[144] L. Chen, Y. Ran, Z. Jiang, Y. Li, and Z. Wang, "Structural, compositional, and plasmonic characteristics of ti–zr ternary nitride thin films tuned by the nitrogen flow ratio in magnetron sputtering," *Nanomaterials*, vol. 10, no. 5, p. 829, 2020.

Chapter 2

Experimental and characterisation techniques

2.1 Introduction

This chapter includes brief descriptions of the experimental techniques used for the coating of co-doped zinc oxide and titanium nitride thin films and the characterisation studies carried out to investigate their structural, electrical, optical as well as plasmonic properties. The thin metal oxide films were developed by using both simple solution based and vacuum based RF magnetron sputtering techniques, while DC magnetron sputtering was used for fabricating TiN films. The structural and morphological studies of the films deposited by the above routes were carried out by x-ray diffraction (XRD), Raman spectroscopy and scanning electron microscope (SEM). In addition, x-ray photo electron spectroscopy (XPS) and energy dispersive X-ray (EDAX) were used for the elemental analysis of the films. The shifting of fermi level with dopants in doped ZnO thin film was also investigated with the help of XPS. The electrical properties of these films were investigated by hall measurement system. The optical properties such as, transmittance and reflectance, and also the energy bandgap of the films were investigated by UV-VIS-NIR spectrophotometer. In addition, photoluminescence spectroscopy (PL) was used to understand the defect states present in the thin films. To study the plasmonic properties of the films, a theoretical approach was adopted initially to estimate the crossover frequency and surface plasmon resonance (SPR), based on fresnel and Drude-Lorentz formula with the help of standard programs such as RefFIT and Winspall software. The SPR was finally generated in the optimised films with the help of prism based Kretschmann configuration.

2.2 Films fabrication techniques

2.2.1 Chemical solution deposition

2.2.1.1 Spin coating

Spin coating is one of the predominant techniques used for the coating of uniform thin films, and this route is capable of coating films with various thicknesses, from micrometre to nanometre. More than 50 years ago, Emsile et al[1] coated a thin asymmetric film of newtonian fluid on a plane substrate rotating in a constant angular frequency, which is considered as a pioneering experiment in the history of spin coating. This route has become popular thereafter and researchers used it widely for the applications such as integrated circuits[2], optical mirrors, magnetic disk for data storage[3], photolithography, deposition of photoresist materials, etc [4]. Fig.2.1 shows the spin coating set up used for this study. The typical processes include dispensing of solution to the centre of the substrate, allow the spin coater to rotate initially in medium spinning speed (300 rpm) followed by a high speed rotation (3000 rpm). The centrifugal force will spread the viscous fluid and drive the liquid outward leaving a thin film on the surface of the substrate, and removes the excess solution[5]. The film thickness and all other properties will depend on solution properties such as it's viscosity, drying rate, solution concentration, solution stability etc and also for spinning parameters like spinning speed, spinning time[6]. The solvent used for dissolving the precursor salts were usually volatile and thus small drying temperature is enough to evaporate them[6].The process of spin coating continuous until the desired thickness achieves.

Figure 2.1: Spin coating system

Spin coating consist of four distinct stages as shown in Fig 2.2[2, 7]

- Dispense stage
  The initial stage of the spin coating, the fluid is deposited onto the substrate using the spin coater shown in Fig.2.2a. If the solution is simply dropped on the substrate in rest position, then it is called static dispense. Dynamic dispense occurs when the substrate is rotated in a low speed; this results in spreading the fluid all over the substrate. Researchers identified this as an advantageous method when the fluid has less wetting capability with the substrate surface.

- Substrate acceleration stage (spin up)
  The rotational motion of the substrate cause expulsion of solution from the substrate. The solution has some depth in the initial stage and the twisting motion caused by the inertia at the top layer of the fluid results in spiral vortices. The film will finally become thin and uniform. The combined effects of spin speed and time selected for this process define the thickness of the thin film coated(Fig.2.2b)

- Fluid viscous force (Spin off)
  The thickness of the film coated by this technique depends upon the

viscosity, surface tension and fluid force. If the liquid exhibits Newtonian viscosity and the fluid is initially uniform across the substrate, the fluid thickness at any following time also will be equal and finally ends in uniform film coating(Fig.2.2c).

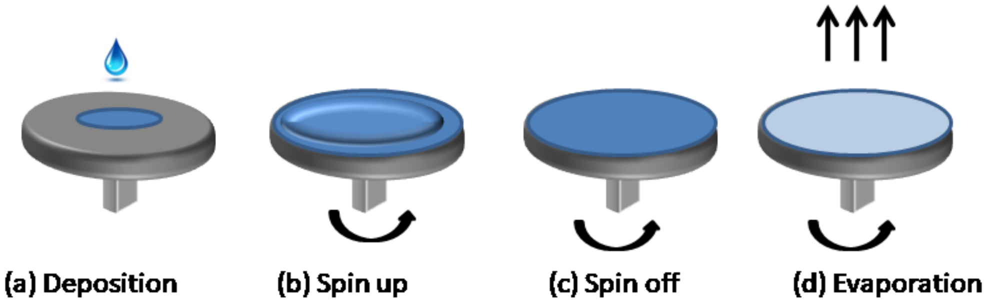

Figure 2.2: Four stages of spin coating

- Solvent evaporation
  Evaporation of solvent is also a dominant process while coating uniform film using spin coating method. This is usually done by a heat treatment at a temperature where the solvent is evaporated off(Fig.2.2d).

The major drawbacks of spin coating are (i) deposition of one single film at a time, and (ii) the wastage of solution which are spin off .

In this work, a Chemat KW-4A spin coater (Fig.2.1) was used to coat Al and In co-doped ZnO thin films for different doping ratio. The KW-4A is a compact spin coater and it also helps for precise and uniform deposition of thin films.

2.2.1.2 Spray coating

Spray coating includes the dynamic collection of droplets generated by a fluid mechanism of atomisation of solution with an atomizer or spray nozzle[8]. Even though this method is facile, versatile, scalable and low-cost, the complexity comes in the multistep solution dynamics processes. The process of thin film synthesis using spray coating can be classified as,

- Atomization of the precursor solution.
- Aerosol transport of droplet.
- Decomposition of precursor.

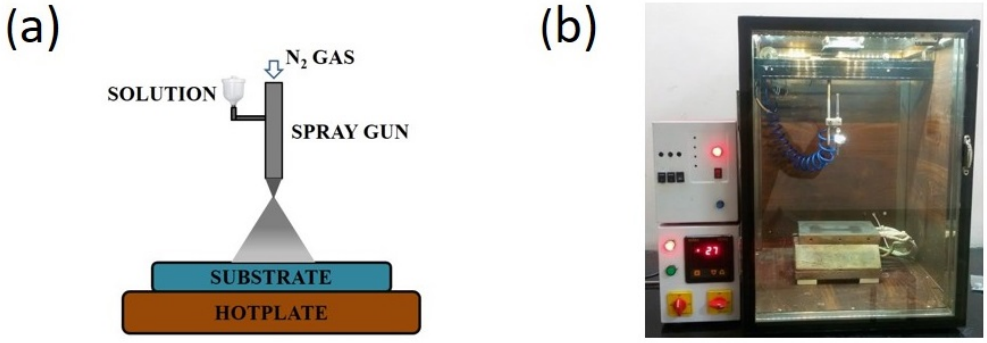

Figure 2.3: (a) Schematic diagram of spray coating and (b) image of the spray coater used

In spray coating technique, the thermal decomposition to fine droplets of spraying solution using a sharp spray nozzle helps to provide a uniform thin film[9, 10]. Generally, for atomization, an air blast or ultrasonic waves or electrostatic field are used. In air blast, the liquid is exposed to the flowing air[11], whereas in ultrasonicator, ultrasonic waves will help for fine atomization[12]. These can also be done by exposing the liquid to the high electric field [13]. The different routes differ in the rate of atomization droplet size and droplet velocity. The velocity of the droplet when it leaves atomizer is also important. In addition, the characteristics of the droplet from an atomizer is also dependent on surface tension, solution density and solution viscosity [9, 10, 14]. Precursor solution gets atomized through the nozzle and forms small droplets known as aerosols. These aerosols are allowed to fall on the preheated substrate and create thin film through pyrolytic decomposition. The dynamics contains spreading, splashing or coalescence of droplets on the substrate surface. When a liquid droplet having moderate momentum reaches the substrate, the initial wetting of substrate is dominated by inertia. It is then followed by rapid and dynamic spreading in a few order of millisecond. The droplet may then vibrate, recede and finally will pin to the surface, achieving an equilibrium state for longer time [8,15,16]. During this transportation, the droplet generally experiences the forces such as gravitational force, stokes force, thermophoretic force, and electrical force [9,10,14]. These four forces control the trajectory of the solution droplet. As it moves through the heated ambient, the precursor undergoes various changes such as evaporation, precipitate formation and vaporization, depending on the droplet size and ambient temperature. For better dense films, the solvent has to be evaporated before it reaches the substrate[17].

Fig.2.3a shows the schematic diagram of a simple spray coater consisting of spraying solution, carrying gas (nitrogen), substrate and hotplate, and Fig.2.3b shows the image of the spray coating unit used in the present work. The nitrogen gas carries the solution from the spray gun in the downward direction and thus the film forms on the hot substrate. Unlike spin coating, film formation is simultaneously occurring in this technique, when the solution falls on the hot substrate. Therefore further drying and annealing are not needed in this technique. The main advantages of spray coating are

- Simple and cost-effective
- Capability to produce uniform films over a large area
- No need of high-quality targets or vacuum
- Can be operated over moderate temperatures

2.2.2 Physical deposition

2.2.2.1 DC/RF Magnetron Sputtering

Sputtering refers to a process of ejecting particles from a material surface due to the momentum transfer between the energetic particles, usually an ion and the surface[18]. The surface bombardment is due to the discharge of inert gas like argon, which is confined between two oppositely charged electrodes. The continuous current glow discharge starts by the application of highly energetic particles, which initiates the sputtering process. This is achieved by applying potential difference between two electrodes in the presence of argon gas. A continuous current power supply is also needed for providing required volts depending on the configuration of the equipment[19, 20].

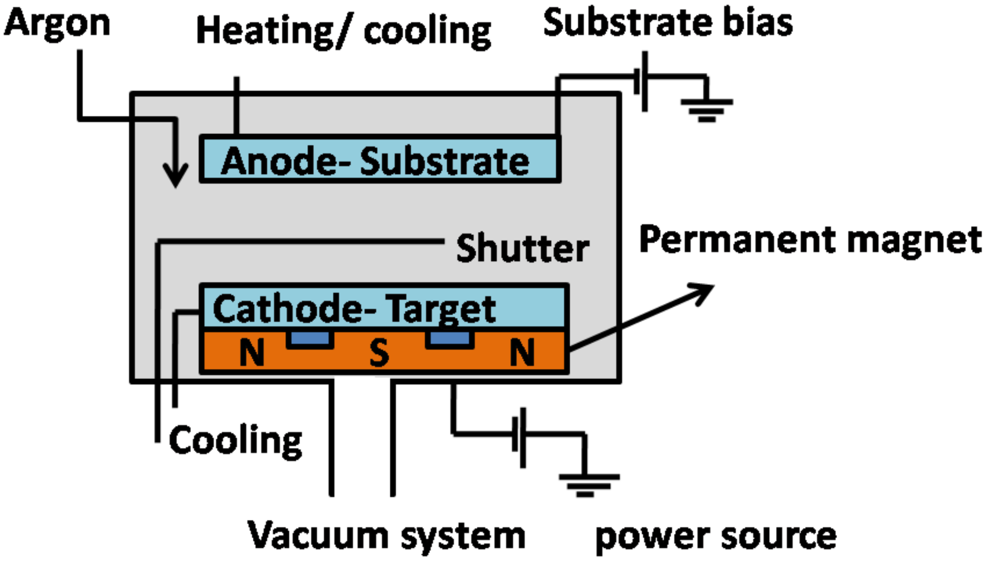

Figure 2.4: Schematic diagram of sputtering chamber[21, 22]

Based on the power sources, that is, DC and AC voltages, sputtering can be classified into DC and radio frequency (RF) sputtering techniques, respectively. A target is needed for sputtering process, which is made up of the material to be coated onto the substrates. DC sputtering requires conducting metal targets, as insulating targets result in accumulation of charges on the target surface leading to prevention of ion bombardment. However, both conducting and non-conducting targets can be used in RF sputtering for depositing films[23–25].

Sputtering yield is an important parameter in sputtering, which is the ratio of the number of particles ejected to particles incident. As mentioned in the previous paragraph, a continuous current glow discharge is needed to produce energetic particles to support the sputtering process. This is achieved by applying a potential difference between two electrodes in the presence of a gas (argon) kept inside a vacuum chamber maintained at low pressure[18, 26]. A schematic diagram of a sputtering chamber is shown in Fig.2.4. Depending on the equipment design, the power supply can deliver voltage up to thousands of volts. The electrodes separated by a distance will have the potential difference, which generates a plasma in the rarefied gas. Argon atoms lose electrons inside the plasma and forms positively charged ions. The ion accelerates towards the cathode, which is the target, and the electrons move towards the anode due to the electric field. Before reaching the anode, these electrons will also produce new ionization or excitation of argon [18, 26]. In order to allow collisions between the electron and argon atom before the electron hits the anode, the gas pressure inside the chamber should not be very small. However, large pressure inside the chamber also will result in increased collisions, and this will not have enough energy to form new ions or excited species in the collisions. The ions accelerated by the electric field can reach the cathode with energy to cause the emission of secondary electrons along with the sputtered atoms. These secondary electrons move towards the anode and thus generate new collisions, causing a cascade effect, establishing a stable discharge, and keeping the plasma in an equilibrium condition[18, 26, 27].

Plasma will not sustain when insulating targets are used. This is due to the formation of positively charged surface on the exposed face of the insulator material. In this case, to maintain glow discharge using an insulator target, a radio frequency (RF) power supply has to be used; this is known as RF sputtering process. When an RF potential with a high peak-to-peak voltage is coupled to an electrode, an alternating positive-negative voltage is generated at the electrode surface. During each part of the half-cycle, the potential is accelerating the ions towards the surface with enough energy for sputtering. In the other half cycle, the electrons that reach the target surface prevent the charge barrier. For this, this system requires an impedance-matching network between the chamber and the power supply. Here, the current density is defined as,

$$I_s = C\frac{dV}{dt} \tag{2.1}$$

Where C represents the capacitance between the plasma and the target and dV/dt is the variation of surface potential of the target with time.The ion current increases with frequency as per above equation. The frequency used in commercial system is 13.56 MHz[18, 26, 27].

In normal sputtering, ions are produced away from the target; there are chances to lose before reaching into the anode. This leads to low deposition rate due the low overall ionization efficiency[26]. To overcome this issue, a magnetic field is applied at right angles to the electric field by placing large magnets behind the target (Fig 2.4). The cathode surface is thus bounded in a magnetic field, and electron traps are formed near to cathode. This increases the rate of ionization near the cathode, which further increases the sputtering yield[18, 27]. Magnetron sputtering is used both in DC and RF sputtering system[18, 26, 27]. The advantages of the sputtering technique are[22, 27, 28],

- A wide variety of materials, such as metals, insulators, alloys, composites can be deposited
- Better film quality
- Reproducibility

However, there are a few disadvantages also,

- High energy ion bombardment or UV generated by plasma may damage substrates.
- To avoid contamination, ultra-clean gases and targets are required
- Deposition rate depends on the material type

- Heating due to ion bombardment may damage the target.

In the present work, RF magnetron sputtering (Hind High Vacuum, Bangalore) was employed for coating Al and In codoped ZnO thin films using powder target prepared by solid state ceramic process. The deposition of ZnO thin films using the powder targets were already reported[29–31]. Titanium metal target was used for coating titanium nitride films by DC magnetron sputtering.

2.3 Characterisation techniques

2.3.1 X-ray diffraction (XRD)

The pioneer experiment on x-ray diffraction was done by W. Friedrich, P. Knipping, and M.Von Laue in 1912, and the Braggs law was derived in 1913[32]. They showed that materials having similar dimension of x-ray wavelength and spacing of planes in the crystal lattice can act as three dimensional diffraction grating. This technique now becomes a common method to investigate crystal structure and atomic spacing of materials. In a x ray diffractometer, x-rays are produced by a cathode ray tube and filtered to produce the monochromatic radiation. The collimator will concentrate and direct x-rays towards the sample. X-ray diffraction is based on the constructive interference of monochromatic x-rays from parallel planes of the substance. The condition for constructive interference is,

$$n\lambda = 2dsin\theta \tag{2.2}$$

Where ‘n’ is an integer, λ is the wavelength of x-rays, and d is the interplanar spacing and θ is the diffraction angle[33, 34]. If the material has random orientations, all possible diffraction directions of the lattice can be attained by scanning the sample through a range of 2θ degree. Since each compound has unique d spacing, the peaks also will be unique, this helps to identify the material. Schematic representation of diffraction was showed in Fig.2.5.

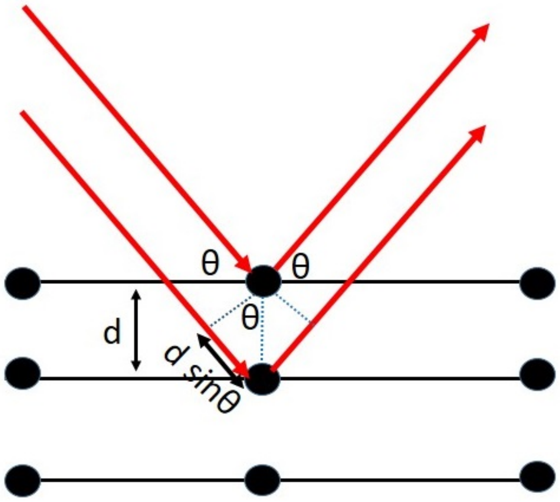

Figure 2.5: (a)Schematic diagram indicating the Bragg reflection from a crystal plane

Typical XRD consist of three basic elements; an x-ray tube, a sample holder and a detector as showed in Fig.2.6. Heating filament will produce electrons and these can be accelerate towards the target by applying voltage and thus bombard the target material with electrons. When the energy of electron is sufficient to knock inner shell electron, x-rays are produced. This consist of several components such as K_α and K_β. K_α can again split as $K_{\alpha1}$ and $K_{\alpha2}$ such that $K_{\alpha1}$ has twice the intensity compared with $K_{\alpha2}$. Copper is the most common target material used for single crystal diffraction(Cu K_α=1.541 A^o). During the rotations of the sample and detector, the intensity of the reflected intensity are measured accurately. There will be a constructive interference when the incident x-ray satisfies the Bragg's law, and thus a intensity in peak occurs. The detector record, process and converts the signal to count rate[35]. XRD is mostly used by the researchers to identify the crystal structure of material. This is crucial for researchers in material science, geology, environmental science and biology[33]. Identification of fine grained minerals such as clays and mixed layer clays are also done by XRD[36,37]. Crystal structure calculation using Rietveld refinement helps to get accurate refined structural parameters like lattice parameter, cell volume, bond length etc.[38, 39].

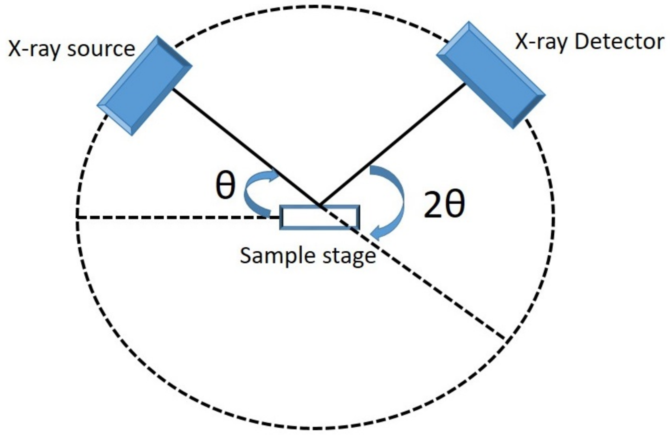

Figure 2.6: Schematic arrangement of XRD.

The scherrer equation gives the average size of the crystallites which is defined as[40, 41],

$$D = \frac{k\lambda}{\beta cos\theta} \tag{2.3}$$

Where k is the constant depending on crystallite shape, λ is the wave length of X-rays, β is the full-width half maximum (FWHM), and θ represents the Bragg angle. For hexagonal lattice, d_{hkl} (obtained from XRD pattern) in terms of lattice parameter (a=b, c) can be written as[41].

$$\frac{1}{d_{hkl}^2} = \frac{4}{3a^2}[h^2 + k^2 + hk] + \frac{l^2}{c^2} \tag{2.4}$$

Moreover, the effect of lattice distortion in the film can induce strain (S) (strain is represented by the symbol ϵ by convention, but S is used here not to confuse with dielectric constant, described below) and stress (σ) along the c axis and can be estimated by

$$S = \frac{c_{film} - c_{bulk}}{c_{bulk}} \tag{2.5}$$

and

$$\sigma = -2.33 \times 10^{11} S \tag{2.6}$$

Where c_{film} represents the lattice parameter of film and c_{bulk} $(= 5.206A^0)$ is that for unstrained ZnO film[42, 43].

Another method to calculate the strain and the crystallite was introduced by G K Williamson and his student[45, 46]. According to them, broadenings due to size (β_D) and strain (β_e) vary quite differently with the Bragg angle, θ;

$$\beta_D = \frac{k\lambda}{Dcos\theta} \tag{2.7}$$

$$\beta_e = 4Stan\theta \tag{2.8}$$

where S is the induced strain

$$\beta_{total} = \beta_D + \beta_e$$

$$\beta_{total} = \frac{k\lambda}{Dcos\theta} + 4Stan\theta \tag{2.9}$$

multiplying with cosθ we get,

$$\beta_{total}cos\theta = \frac{k\lambda}{D} + 4Ssin\theta \tag{2.10}$$

This equation represents a straight line for βcosθ in Y axis and 4sinθ in X axis. Thus slope of the straight line gives the strain(S) and Y intercept gives the crystallite size.

The major limitations of XRD are as follows[33],

- The detection limit of dopants in material is limited upto 2%
- For high angle reflection, peak overlay may occur.
- Difficulty in identifying the unknown material

2.3.1.1 Rietveld refinement using GSAS software

The extraction of structural information quantitatively from the XRD data can be done using Rietveld refinement technique. Hugo Rietveld[47, 48] introduced this novel idea in 1969 to extract structural information from neutron diffraction data. Now this technique has been used for extracting other structural studies, such as bond angle, bond length, atom position, accurate lattice parameter, occupancies, etc.[49–54]. A wide variety of licensed and free software like FullProf[55], Rietan [56], Topas [57], JANA [58], GSAS/EXPGUI[47, 48] etc. are available for structural refinement. In the present study, EXPGUI, the graphical user interface version of General Structure Analysis System (GSAS) was used for structural refinement [47,48]. A high-resolution x-ray diffraction data and standard crystallographic information file (CIF) are required for carrying out the refinement process. The refining parameters includes scale factor, lattice parameters, occupancy, preferred orientation correction, isotropic atomic displacement parameters, peak width, and shape functions. The fitting will continue until the goodness of fit (χ^2) becomes an acceptable value (ideally 1), or a good fit between observed and calculated x-ray diffraction patterns is observed [45–48]. In the refinement, pseudo-Voigt profile shape is assumed [51–54, 59].

$$\chi^2 = \sum \frac{(\sigma_{ip}^2 - \sigma_{ib}^2)^{-1} \times (y_{io} - y_{ic})^2}{N - P} \tag{2.11}$$

Where σ_{ip} and σ_{ib} are the standard deviation associated with peak and background intensity respectively. The y_{io}, y_{ib} and y_{ic} and are the observed intensity, background intensity and the calculated intensity. N is the total number of observations and P is the number of variables in least square refinement. The calculated intensity y_{ic} is obtained using

$$y_{ic} = s \sum_j M_j PL_j |F_j|^2 G(\delta\theta_i j) + y_{ib} \tag{2.12}$$

Where, M_j is multiplicity factor, PL_j is Lorentz polarization factor, F_j is structure factor, s is scale factor, G is reflection factor and $\delta\theta_{ij}$ is calculated Bragg peak position. After refinement process, the structural informations were extracted by running the program DISAGL in GSAS software[47, 48]. In the present study, Rigaku Miniflex 600 XRD using CuK_α radiation was used for the structural studies. The 2θ range used was from 10-80 degrees, and 0.001 degree/min was the scanning rate used for the measurements.

2.3.2 Scanning electron microscope (SEM)/Field emission scanning electron microscope(FESEM)

Scanning electron microscope is used for the examination and analysis of morphology of microstructure and characterisation of chemical compounds. The limit of optical microscopy corresponding to resolution of $2000A^o$ was surmounted by electron microscopy[60]. The limit of resolution based on wavelength illuminated was studied by Ernst Abbe [61]. The magnified image blurs at certain wavelengths when the resolution exceeds the limit [60,61]. In a light source, due to the diffraction and interference, focussing like a perfect dot is not possible [60]. In a perfect optical system, the resolution can be defined mathematically by Abbe's equation as

$$d = \frac{0.612\lambda}{nsin\alpha} \tag{2.13}$$

Where d is resolution, λ is the wavelength of imaging radiation and n is the refractive index of medium between lens and point source and α is the half aperture angle in radians.

Image development in the SEM depends on acquisition of interacting signals between electron and the specimen. The possible interactions are elastic and inelastic, where elastic interaction is due to the deflection of the incident electron of similar energy by atomic nucleus or by outer shell electrons. When the incident electrons are elastically back scattered at an angle greater than 90^o, then these are called backscattered electrons (BSE). Inelastic scattering occurs due to the variety of interactions between incident electrons and electrons in the sample. The amount of energy loss depends on single or collective excitation of specimen electron and also on the binding energy of the electron to the atom. When the incident electron ionise the specimen atom leading to excitation of electron, which results in generation of

secondary electrons having energy less than 50 eV, and these are used for imaging the specimen. In addition to secondary electrons, other possible emissions are x-rays, auger electrons and cathodoluminescence. Secondary electrons are used principally for the topographic image formation and this depends on the number of secondary electrons reached into the detector. The elastic collision between the incident electron and specimen electron causes the electron to bounce back in a wide-angle having energy greater than 50 eV. Elements with higher atomic number have more number of positive charges on the nuclei, and thus more electrons will be back scattered. The spatial resolution of backscattered electron images varies between 50 and 100 nm for beam energies of 10–20 keV and this is directly related to the large volume within the specimen from where the backscattered electrons will form the image. At low beam energy (1keV), the information volume of SE and BSE becomes comparable. For high-resolution microscopy, low-loss BSE are used which are ejected from the area immediately surrounding the point of beam incidence. These electrons undergo single or lesser number of scattering events and represent high-resolution signal.
Fig.2.7 shows the schematic representation of SEM. The major parts include[60–62],

- Electron gun

  Role of the electron gun is to produce a stable electron beam having high current, adjustable energy, small spot size and small energy dispersion. The first SEM used tungsten or lanthanum hexaboride cathode as electron source, but in modern SEM, field emission sources are used because of current enhancement properties and low energy dispersion. Thus, it is named as Field emission scanning electron microscope (FE-SEM). The higher resolution and magnified image can be obtained in FESEM.

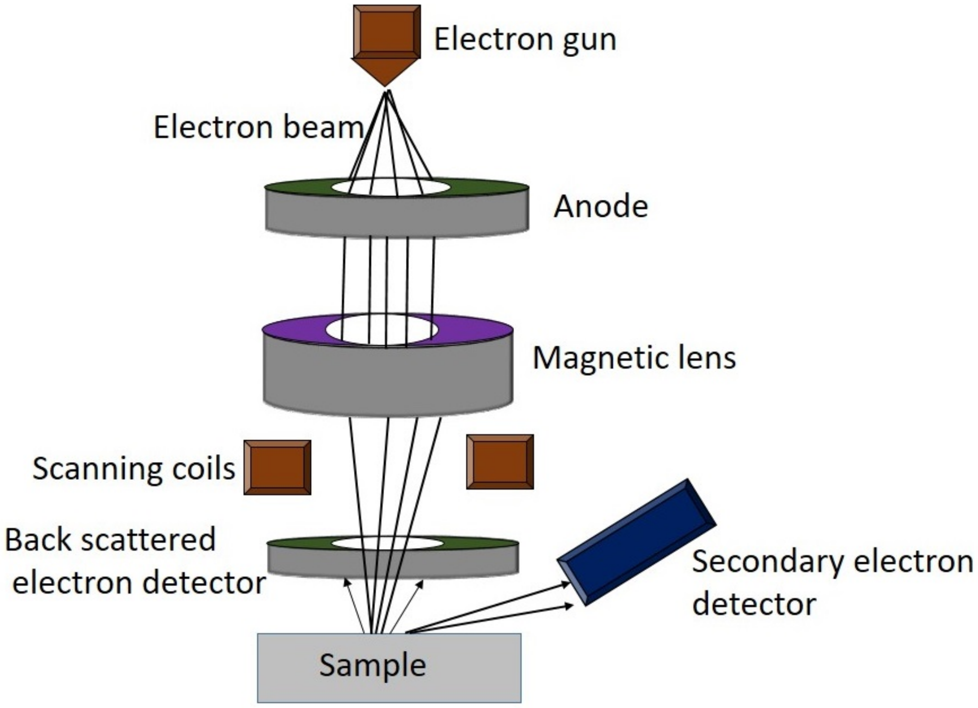

Figure 2.7: Schematic representation of SEM/FESEM

- Electron lenses

  Though the electron beam can be focussed by electrostatic or magnetic fields, the beam control of magnetic field has small aberration, and because of this, in SEM/FESEM electron beam focussing is usually done by magnetic field. Trajectory of the electron is controlled by current in the electromagnets. The electron lenses can demagnify/magnify the electron beam diameter because of their variable strength, and thus have variable focal length. SEM use electron lenses to demagnify the image of the emission source so that narrow probe can be formed on the surface. To converge and collimate the electron beam in a parallel stream, a condenser lens is also used. By adjusting the position of the condenser lens current, the position of the focal point can be adjusted. By choosing the appropriate aperture size, the inhomogenous/scattered electrons also can be excluded. Below the condenser aperture, electron beam are focussed in to the probe point at the specimen surface using a objective lens.

- Column parameters
  Along with small spot size and beam convergence, other parameters related to the resolution and depth of focus are electron beam energy, lens current, working distance, aperture size etc. Aperture also helps to avoid spherical aberration in the final lens. For same working distance, decreasing aperture size will reduce beam angle, which thus result in enhancement of the depth of field.

- Image formation
  Interaction of electron beam with specimen will occur within an excitation volume, and the depth of interaction depends on the composition of specimen, energy and incident angle of electron beam. By recording the magnitude of the emitted signal with suitable detectors, information of the sample will be obtained. However, the information come from one single spot, and the probe should be scanned in vertical and horizontal directions to form an image. The morphology of the image is obtained from SE detectors because of low energy of secondary electrons. As the atomic number of samples increases, production of SEs and BSEs also will be increased. Therefore, the contrast of SE and BSE signals can also give information about the specimen composition.

Thus the main difference between SEM and FESEM lies in the electron generation system. In FESEM, a field-emission cathode in the electron gun provides narrower probing beams at low as well as high electron energies resulting in both improved spatial resolution and minimized sample charging and damage. Thus FESEM provides excellent magnification and low voltage[62]. In this work, both SEM (Zeiss Evo18, USA) and FESEM (CARL ZEISS, Gemini SEM 300) were used for the surface morphological studies and for obtaining cross-sectional images of films.

2.3.3 Energy Dispersive analysis of X Rays (EDAX)

EDAX is an analytical method that involves the chemical characterisation or elemental analysis of a sample. Each element has a unique atomic structure that allows interaction of x-rays with materials to be characteristic of an element's atomic structure. In an atom, ground state electrons distributed across discrete energies or electron shells bound to the nucleus[63]. When x-rays fall on the material, electron in the inner shell will be excited and ejects from the shell, creating a hole. Eventually, the vacated position by an ejected electron from an inner shell is occupied by a higher energy electron from an outer shell. The difference in energy between the higher and the lower shells is released in the form of an x-ray[63]., as shown in Fig.2.8.

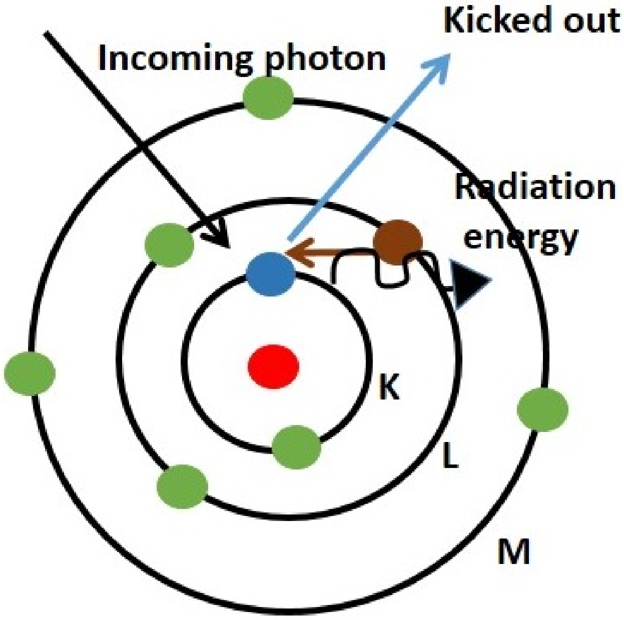

Figure 2.8: Principle of EDAX

Identifying the position of the EDAX peak with appropriate energies will give information on the quantitative composition of the sample. The number of the x-ray quanta is the measure of the concentration of the elements (peak height). Quantitative analysis of lighter elements from an EDAX is usually effected by it's strong absorption before it reaches to the detector[64]. This is eliminated by adding suitable mass absorption correction given by cliff & lorimer[65] and philbert [66]. For a binary system having elements A and B, the weight percentage of elements A and B represented as C_A and C_B respectively, are related to the intensities I_A and I_B as

$$\frac{C_A}{C_B} = (k_{AB} \times ACF)\frac{I_A}{I_B} \tag{2.14}$$

Where K_{AB} is the sensitivity factor depend on ZAF correction(Z: Atomic number, A: Absorption of x-rays within the specimen, F: Fluorescence of x-rays within specimen)[65], and absorption correction factor(ACF) is defined as

$$f(\chi) = (1 + 1.2 \times 10^{-6}\gamma\chi)^{-2} \tag{2.15}$$

Where, $\chi = \frac{\mu}{\rho}cosec\alpha$ and $\gamma = (E_0^{(1.65)} - E_x^{(1.65)})$, E_0 is accelerating (gun) voltage,(thus the energy of the primary electrons), E_x is the critical ionization energy of the level of the atom and α is the take off angle.

EDAX systems are commonly available in SEM/FESEM. As described in the section (2.3.3), these are equipped with a cathode to create electrons and magnetic lenses to focus the beam of electrons. The x-ray excited in the specimen is analysed by EDAX detectors by measuring the relative intensity of emitted x-rays versus their corresponding energy. Typically, the detectors used are lithium drifted silicon or solid state device[67, 68]. Charge pulses are generated when the x rays strike on the detector in proportion to their energy. The conversion of charge pulse to a voltage pulse was done by a charge sensitive pre-amplifier. These signals are then send to a multichannel analyzer, where these pulses will sort according to the voltage. This energy (determined from the voltage measurement), for each incident x-rays will send to the computer for display and then for further data evaluation. The spectrum of x-ray energy versus counts is used to determine the elemental composition of the sample[67, 68]. In this work, Zeiss Evo18, USA EDAX was used for quantitative analysis of elements present in the films.

2.3.4 Raman Spectroscopy

The basic principle of Raman spectroscopy lies in the inelastic scattering of monochromatic light inside the sample, which is then followed by the generation or annihilation of elementary excitations. The elementary excitations are vibrations, particularly phonons (lattice vibrations). Raman spectroscopy thus provides information on structural properties like chemical composition, orientation, and crystalline quality. These were done by analyzing the frequency position, intensity, and line shape and FWHM of Raman signals in the Raman spectra.

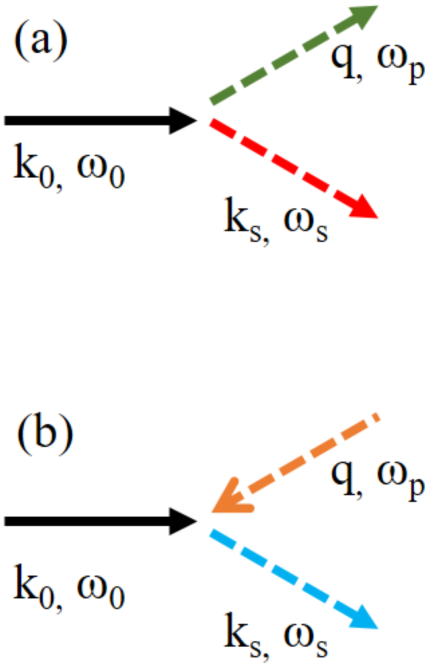

Figure 2.9: Schematic representation of (a) Stoke and (b) anti-Stoke process

The typical Raman spectrum is intensity versus the Raman shift, where intensity is directly related to the photon numbers reaching at the detector. Any frequency difference between the monochromatic excitation source and the scattered light gives the Raman shift[69]. This shift denotes the energy annihilated or generated during elementary excitation. Raman shift is usually represented in wavenumber $\bar{\nu} = \nu/\mathrm{c}$ [67–71].

Conventionally, if the inelastic light scattering generates an elementary excitation, the frequency of the scattered light exhibits a lower frequency, then the Raman shift will denote as positive, indicating stokes Raman scattering. For annihilated elementary excitation, the Raman shift will becomes negative defined as anti-stokes Raman scattering. According to Maxwell-Boltzmann distribution law, the population of phonons in a solid at ground state is higher than the excited state. Therefore, the stokes lines are stronger than the anti-stoke lines. Since both Stokes and anti-Stokes lines provide the same information, in general practice the stoke lines are measured experimentally because of its higher intensity than that of the anti-stoke lines. When an incident photon with energy $\hbar\omega_0$ and momentum $\hbar k_0$ undergoes inelastic scattering, a phonon of energy $\hbar\omega_p$ and momentum $\hbar\omega_q$ is either created or annihilated. However, the total energy and momentum before and after the scattering will be conserved. During phonon creation(Fig.2.9a), the lattice will go to an excited vibrational state from the ground state by absorbing energy from the incident photon. while, in the phonon annihilation process (Fig.2.9b), lattice returns to the ground state from the excited state by releasing energy[69]. For the above-mentioned light scattering processes, the energy and momentum conservation demand the condition such as,

$$\hbar\omega_s = \hbar\omega_o \pm \hbar\omega_p \tag{2.16}$$

$$\hbar k_s = \hbar k_o - \hbar q \tag{2.17}$$

where, $\hbar\omega_s$ and $\hbar k_s$ are the scattered photon energy and momentum, respectively. In eqn (2.16), the +ve sign represents anti-stokes lines (phonon annihilation) and -ve sign represents stoke lines (creation of a phonon). The magnitude of the scattering vector q depends on the scattering angle. The wave vector of the photon is directly proportional to its frequency q=ω/c. Since the maximum phonon energy is less than the UV-visible-IR photon energy, the scattered photon energy (wave vector) is nearly the same as that of the incident photon. Therefore, one can make the approximation $k_0 = k_s$.

From the vector diagram (Fig.2.9),for a scattering angle θ, the phonon momentum can be written as, q= $2k_0$ sin($\theta/2$). In the backscattering configuration θ is 180 and thus q is $2k_0$. Therefore, the maximum value of q can be achieved in the Raman scattering in UV-Visible and IR region is of the order of 10^{-5} cm^{-1}, which is very small as compared to the Brillouin zone boundary in a typical crystal[69]. The schematic block diagram of the micro-Raman spectrometer used for the present study is depicted in Fig.2.10. The major component and their working principle are briefly discussed below

- Laser

  An Ar+ laser of wavelength of 514.5 nm was used as the light source for the Raman scattering measurement.

- Optical unit

  The laser entering the optical unit was first aligned by the mirror B and it is then followed by convergence lens C to converge it to 10 μm pinhole. Another objective lens D was used to make a well collimated parallel beam. Using the mirror E and F, the collimated parallel laser beam was then reflected to the holographic filter. The angle of the holographic filter was adjusted so that the laser beam can pass into the optical path of the microscope,located outside of the spectrometer unit.

- Microscope unit

  The microscope unit helped in positioning and focusing the sample for the measurement. The microscope in the micro Raman system was facilitated with objective lenses of 5X, 20X, 50X and 100X for visible light and 15X and 40X for UV light.

- Monochromator

  In the Raman spectrometer the back scattered photons are dispersed through the single monochromator with gratings. The spectral resolution of the measurement is decided by the number of groves in the grating. In the present study, 1800 groves/mm gratings were used for 514.5nm excitation source.

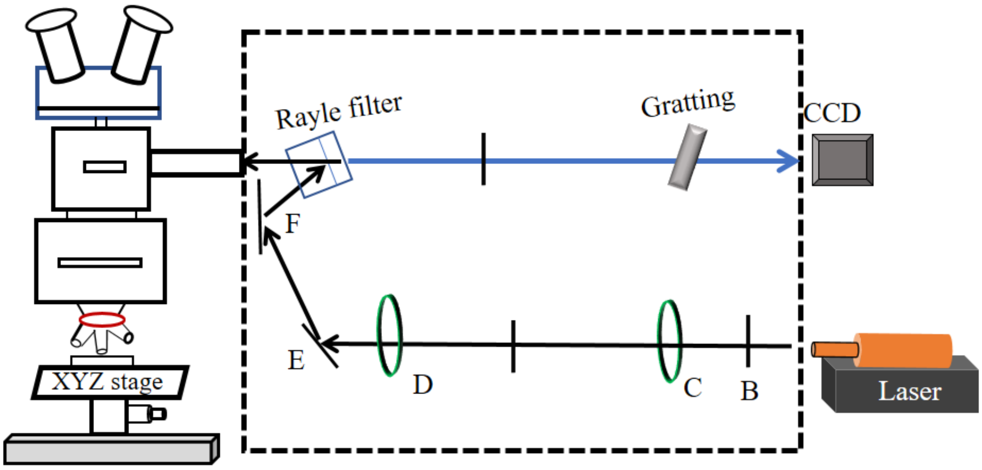

Figure 2.10: Schematic block diagram of the micro-Raman spectrometer

- Detector

  The dispersed light from the monochromator was focused on a charged coupled device (CCD), which served as a detector for spectra acquisition of the scattered photons.

The wurtzite ZnO lattice structure contains four atoms in the unit cell. Thus the number of phonons amounts to 3n = 12, with 3 acoustic modes (1-LA, 2-TA) and 3n - 3 = 9 optical phonons (3-LO, 6-TO). The group theory predicts the irreducible representation of optical phonon as γ_{opt} = A1+2B1+E1+2E2. The E modes are two fold degenerate and the B1 modes are silent, i.e. IR and Raman inactive, and the E2 modes are Raman active only. Since the Raman and IR active modes A1 and E1 are polar and due to the macroscopic electric fields of the LO phonons, each splits into LO and TO modes with different frequencies[67–71]. In the present work, a micro-Raman spectrometer in the backscattering geometry with laser excitation of 532nm (inVia, Renishaw;UK) was used for investigating vibrational properties of the films.

2.3.5 Photoluminescence (PL)

PL spectroscopy is a non destructive technique used widely to yield valuable information about intrinsic as well as extrinsic transitions in the sample. Since ZnO exhibit both defect related and near band emissions, both these transitions are important in our study. PL comprised of fluorescence and phosphorescence which originates from the absorption/emission process between different electronic energy levels and type/intensity of PL depends mainly on the material and wavelength of source which we used. By choosing an appropriate laser wavelength unwanted interference due to fluorescence can be avoided[72]. In Photoluminescence spectroscopy, light illuminated onto the sample will absorb and excess energy will be imparted into the material through photoexcitation. This excess energy released by the sample through the emission of light is called luminescence[73]. If the photons are involved in this excitation, then this luminescence is called photoluminescence. Hence, photoluminescence occurs when a material exhibit spontaneous emission of light from a material during optical excitation. This light is then collected and analysed further spatially, temporally and also spectrally. Various important material property are measured directly using this intensity and spectral content of the photoluminescence. Photo excitation causes electrons within the material to move into allowed excited states. When these electrons return to their ground states, the excess energy will be released and results in the emission of light . This process is a radiative process and if radiation is not emitted, then it is non radiative process, as shown in Fig.2.11. The emitted radiation is photoluminescence and its energy is related to the difference in energy levels between the two electron states involved in the transition between the excited state and the equilibrium state. This method only provides information on the lower lying energy levels of the system under investigation. In a semiconductor, the radiative transition occurs commonly between the conduction and valence bands. This difference in energy is called the bandgap. The measurement of PL spectroscopy is usually done by laser light or with xenon lamp having an energy much larger than the optical band gap. This wavelength is called excitation wavelength. In this study, since zinc oxide has bandgap near to 3.3eV, excitation wavelength selected was 325nm[73, 74].

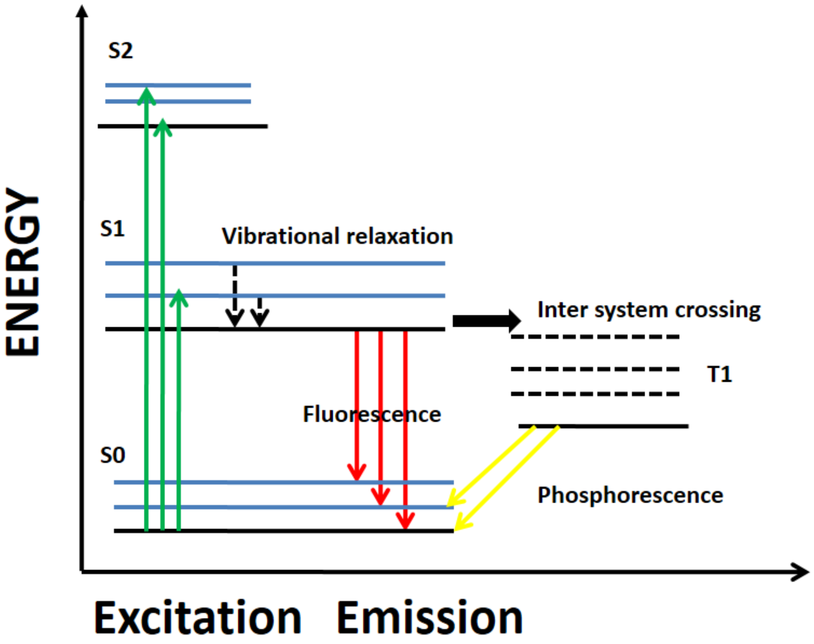

Figure 2.11: Principle of photoluminescence spectroscopy

The carriers that are excited by light includes electrons and holes that relax towards to their respective band edges (bandgap), and then recombine by emitting light. It is also possible that radiative transitions in semiconductors involve localised defects or impurities. Thus, PL analysis also can be used to understand the defect states within the sample, and the magnitude of the PL signal can be used to understand their concentration[75]. The PL studies reported in this thesis were carried out using the same setup used for micro raman measurements (inVia Renishaw)(Fig.2.10) by excitating the films with the He-Cd laser source having excitation wavelength of 325nm.The emission spectra were recorded by using a grating (2400gr/mm) as a monochromator and a CCD detector.

2.3.6 Hall effect measurement

American physicist Edwin Herbert Hall observed in 1979 that when an electric current passed through sample placed in a magnetic field B, a voltage later known as Hall voltage perpendicular to current and magnetic field will be developed across the material. This effect is known as hall effect and using this carrier density, mobility and resistivity of the material can be determined. The first understanding about the sign of the charge carriers was done using this technique. Hall measurements are widely used today for investigating the electrical transport of semiconductors and metals.

Consider a conductor as shown in Fig.2.12 in which current I_x is flowing in x direction. Let the charge inside the conductor is ‘q’ and the charge carrier density is ‘n’ and charge drift velocity is v_x. The current I_x is the current density times the cross sectional area of the conductor. If t and w are the thickness and width of the conductor respectively, then,

$$I_x = J_x wt = nqv_x wt \tag{2.18}$$

Thus carrier density is defined as

$$n = \frac{I_x}{qv_x wt} \tag{2.19}$$

The carrier density related to mobility(μ) and resistivity(ρ) as

$$n = \frac{1}{\rho q \mu} \tag{2.20}$$

The Hall voltage(VH) developed in the conductor related to Hall field as

,

$$V_H = -\int_0^w E_y dy = -E_y w \tag{2.21}$$

Where E_y is the Hall field defined as

$$E_y = B_x V_z$$

Thus

$$V_H = -\frac{1}{nq}\frac{I_x B_z}{t} = -R_H \frac{I_x B_z}{t} \tag{2.22}$$

Where R_H is the Hall coefficient. For n type material, the Hall coefficient will be negative and for p type material it will be positive. Using the Hall voltage, the mobility can be found as,

$$\mu = \frac{V_H}{R_s I B} \tag{2.23}$$

And Rs is the sheet resistance can be determined from the van der pauw equation,

$$e^{-\pi\frac{R_A}{R_s}} + e^{-\pi\frac{R_B}{R_s}} = 1 \tag{2.24}$$

$$R_A = \frac{V_{43}}{I_{12}}$$

$$R_B = \frac{V_{14}}{I_{23}}$$

I_{12} is the DC current entering through contact 1 and leaves through contact 2 of the sample, and I_{23} is the DC current entering through contact 2 and leaving through contact 3 as showed in Fig.2.12. Voltage between contact 4 and 3 is V_{43} and V_{14} is the voltage between contact 1 and 4[76–78].

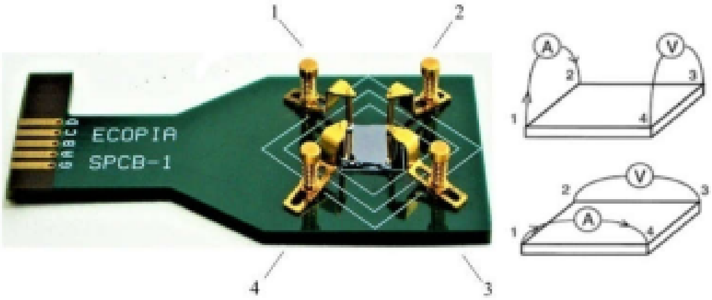

Figure 2.12: Image of the sample holder along with the schematic diagram of sample with four leads numbered as 1,2,3 and 4

The plasmonic property of the plasmonic thin film at the desired wavelength is dependent on the free carrier density of the films. Hence, the study of electrical property of the oxide and nitride thin films are utmost important. For the present work, Ecopia HMS 3000 Hall measurement system was used with a magnetic field of 0.54T. The measurements were done at room temperature.

2.3.7 X-Ray Photoelectron spectroscopy

X-ray photoelectron spectroscopy (XPS), also named as electron spectroscopy for chemical analysis (ESCA), is a technique used for analyzing the surface chemistry of the material. It can measure the elemental composition, chemical state, empirical formula, and electronic state of the elements within a material.

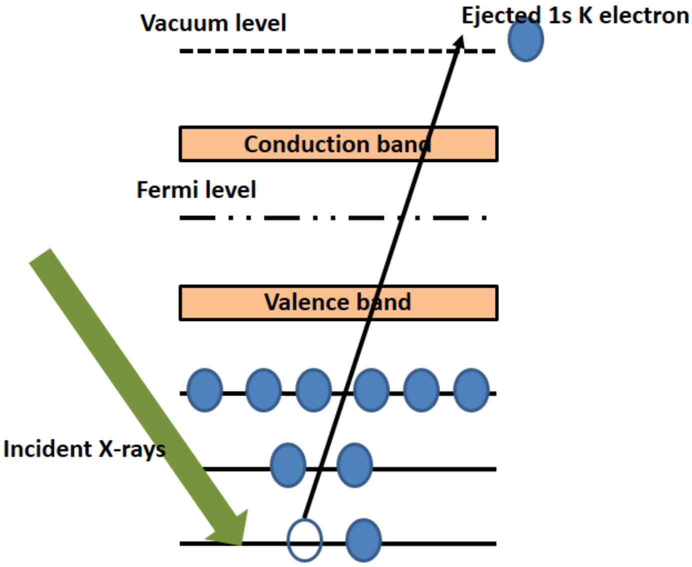

Figure 2.13: The photoemission process involved for XPS surface analysis

The spectra are obtained when a beam of x-rays are irradiating on a solid surface and simultaneously measuring the kinetic energy of electrons that are emitted from the top 1-10 nm of the material being analyzed. A photoelectron spectra are recorded by counting the ejected electrons over a range of kinetic energies of electrons. Since each atom have particular binding energy, peaks appear in the spectrum will correspond to a particular element. The energies and intensities of the photoelectron peaks enable identification and quantification of all surface elements (except hydrogen)[79]. When the x-ray beam hits the sample surface, the electron in the surface absorbs photon energy and thus be excited as shown in Fig.2.13. In some cases, due to ionization the electrons can escape from the host material. The energy of the emitted photon can be analysed using a spectrometer and the results can be plotted as a graph with intensity/counts per second versus electron energy. The kinetic energy of the escaped electron related to the binding energy of the material as,

$$KE = h\nu - BE - \phi \tag{2.25}$$

Where hν is the incident photon energy. BE is the binding energy of the electron and ϕ is the work function of the material.

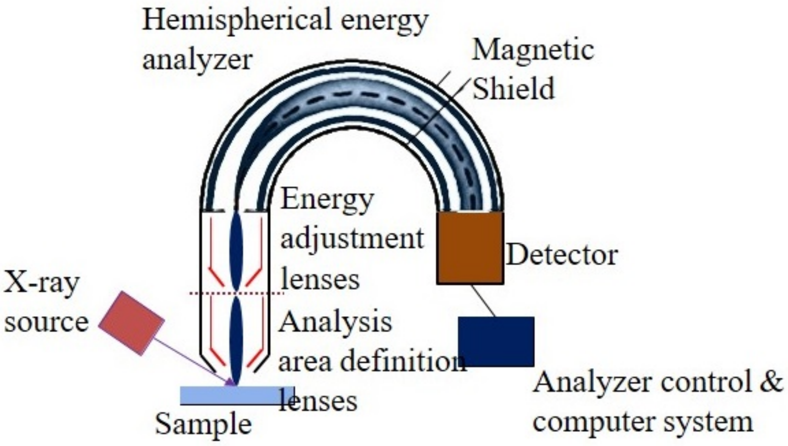

Figure 2.14: The schematic representation of XPS[80]

This equation is known as Einstein's Photoelectric equation. This kinetic energy is the fingerprint of the electrons on specific subshell of the electronic levels of the elements. And any variation in the type of elements or their valancy can alter the XPS peak position and hence can be identified. The absorption of photon by a material is an instantaneous process and take place within a time range of 10-16s. For absorption to take place hν should be greater than BE+ϕ and the remaining energy will be used for the kinetic part of the electron. Thus as the intensity of the incident photon increases the intensity of the emitted photoelectron also will increases[81].

The major components of the XPS system are x-ray source, analyser and detector as showed in Fig.2.14. XPS usually use Al K_α and Mg K_α as the excitation source. In our work we used monochromated Al K_α of energy 1486.6eV and the BE were measured by referencing with respect to the C1s peak. A hemispherical electron analyser was usually used in XPS instrumentation. The electrons which are dispersed through the hemispherical analyzer having different energy arrive at different positions in the radial direction and also they are spatially dispersed around the circumference of the sphere. To allow the photoelectrons a longer electron path, an ultra high vacuum is always maintained in XPS. In addition it also prevents the contamination to produce the x-ray signals.For the deconvolution of peaks we used Shirley type background and curve fitted with a mixture of Gaussian and Lorentzian line shape[81].

2.3.8 UV-VIS-NIR spectrophotometer

The incidence of an electromagnetic wave on a material will result in phenomena such as transmission, absorption, reflection or scattering due to the interaction of wavelength with objects of discrete dimension like atoms/molecules. Depending upon the wavelength used, this spectroscopy can be divided into three. The UV region is measured from 180 to 400nm, the visible is from 400 to 800nm and near infrared region ranges 700 to 2500nm. A UV-VIS-NIR spectrophotometer measures the amount of light transmitted/ transmittance through a sample by taking the ratio of intensity of incident light(I_0) to the ratio of intensity of transmitted light (I)(after eliminating the background light). The relationship between the transmittance and the absorbance(A) can be described as

$$A = -log_{10}T \tag{2.26}$$

where $T = \frac{I}{I_O}$.The absorption coefficient α of the thin film sample can be calculated as,

$$\alpha = -\frac{ln(\%T)}{d} \tag{2.27}$$

Where'd' is the thickness of the film. Bandgap of the thin films (E_g) was calculated in the present work using the Tauc relation

$$\alpha h\nu = A(h\nu - E_g)^n \tag{2.28}$$

where hν is the incident photon energy, A is a constant and n =1/2 for allowed direct transitions. The optical band gap energies were calculated by extrapolating the linear portion of $(\alpha h\nu)^2$ versus hν curve at α=0[82, 83].

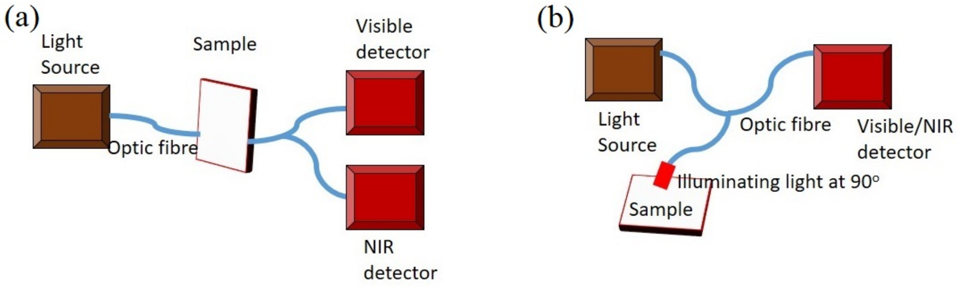

Figure 2.15: shows fibre based (a)transmission measurement and (b) reflection measurement.

In this work, a fibre based UV-VIS NIR spectroscopy (Ocean optics) was used for transmission and reflection measurements. The schematic diagram of the device used is shown in Fig 2.15 a and b. The principle of measurement for the fibre based UV VIS NIR spectrophotometer is relatively simple and it consist of a light source, sample holder, fibre and a spectrophotometer (Fig.2.15). The light source used here is tungsten halogen lamp. The working principle inside the spectrophotometer is shown in Fig.2.16. Light from the optical fibre enters inside the detector using a SMA connector. The light then passes through the slit, which act as the entrance aperture. It is then reflected by a collimating mirror and move towards grating, which splits the photons by wavelength. The grating spreads the light across the focussing mirror, which direct light of each wavelength into detector. In the UV-VIS region, CCD arrays are used as detectors and in NIR region, InGaAs detector is used. Using the spectroscopic software, data from the detector were analysed.

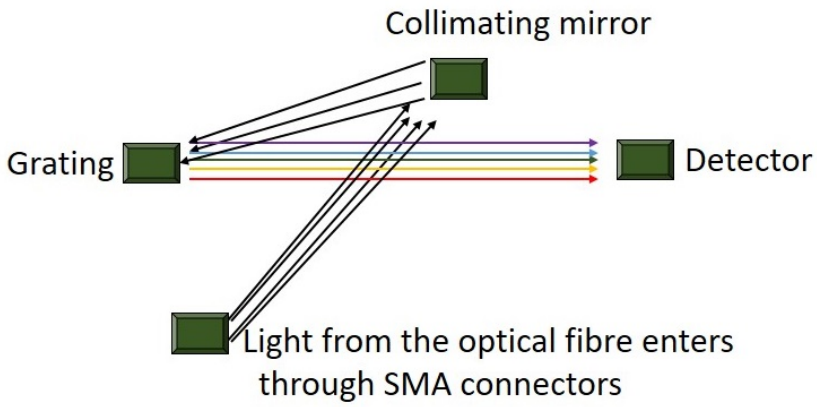

Figure 2.16: Schematic diagram of light from optical fibre reaches the detector.

2.3.9 Analysis of SPR using kretschmann configuration

Surface plasmons can be excited on plasmonic film using incident photons using certain experimental methods. The resonance condition at which coupling of photon and surface plasmon excitation is called surface plasmon resonance[84, 85]. A detailed description of methods of generating SPR was discussed in the section (1.3.2) of Chapter 1. In the present study, we used Kretschmann configuration for exciting SPR, as shown in Fig 2.17. The light source used is tungsten halogen lamp having wavelength region ranging from 300 to 2200 nm. The incident light are allowed to pass through a collimator and then through a p polariser. The p polarised light have electric field components in the x and z direction, as seen in figure. The plasmonic film was coated on the hypotenuse side of the right angled prism and lights are allowed to fall on one side of the prism. In this study, BK7 prism (n =1.57 at NIR) has been used for the measurement. The plasmonic films were coated on glass substrates. The light reaches at the prism- film interface undergoes total internal reflection and the evanescent wave generated at this interface will move through the film and reaches at film-air interface. At resonance condition, this evanescent wave will couple with surface plasmons and generate SPR.The coupling thus result in decreasing the reflected light intensity. The generation of SPR can be done in wavelength interrogation and angular interrogation methods. The angle is fixed in the former case and the wavelength is fixed in latter[84–87].

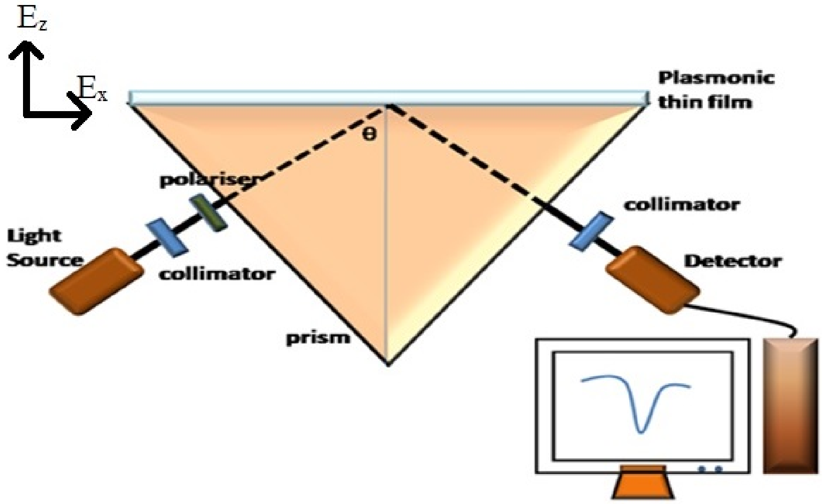

Figure 2.17: Schematic diagram of generation of SPR using Kretschmann configuration

2.4 Summary

In this chapter, major experimental techniques used for coating of co-doped zinc oxide films and titanium nitride films were discussed. In addition, basic principles, major components along with schematic diagram of thin film deposition techniques were also described. The characterization equipment and techniques used for probing electrical, structural, surface morphological and optical properties of the co-doped oxide and nitride thin films were discussed. The details of surface plasmon resonance measurements of the plasmonic films using Kretschmann configuration were also described in detail.

References

[1] A. G. Emslie, F. T. Bonner, and L. G. Peck, “Flow of a viscous liquid on a rotating disk,” *J. Appl. Phys.*, vol. 29, no. 5, pp. 858–862, 1958.

[2] D. Bornside, C. Macosko, and L. Scriven, “Modeling of spin coating.,” *J. Imaging Technol.*, vol. 13, no. 4, pp. 122–130, 1987.

[3] R. Yonkoski and D. Soane, “Model for spin coating in microelectronic applications,” *J. Appl. Phys.*, vol. 72, no. 2, pp. 725–740, 1992.

[4] D. Hanaor, G. Triani, and C. Sorrell, “Morphology and photocatalytic activity of highly oriented mixed phase titanium dioxide thin films,” *Surf Coat Tech*, vol. 205, no. 12, pp. 3658–3664, 2011.

[5] N. Sahu, B. Parija, and S. Panigrahi, “Fundamental understanding and modeling of spin coating process: A review,” *Indian J. Phys.*, vol. 83, no. 4, pp. 493–502, 2009.

[6] M. Tyona, “A theoritical study on spin coating technique,” *Adv. Mater. Res.*, vol. 2, no. 4, p. 195, 2013.

[7] C. Lawrence, “The mechanics of spin coating of polymer films,” *Phys. Fluids*, vol. 31, no. 10, pp. 2786–2795, 1988.

[8] N. Ashgriz, *Handbook of atomization and sprays: theory and applications.* Springer Science & Business Media, 2011.

[9] C. Chen, E. Kelder, and J. Schoonman, “Effects of additives in electrospraying for materials preparation,” *J. Eur. Ceram. Soc.*, vol. 18, no. 10, pp. 1439–1443, 1998.

[10] F. Caillaud, A. Smith, and J.-F. Baumard, "Effect of ph of the solution on the deposition of zinc oxide films by spray pyrolysis," *J. Am. Ceram. Soc.*, vol. 76, no. 4, pp. 998–1002, 1993.

[11] A. Balkenende, A. Bogaerts, J. Scholtz, R. Tijburg, and H. Willems, "Thin mgo layers for effective hopping transport of electrons," *Philips J. Res.*, vol. 50, no. 3-4, pp. 365–373, 1996.

[12] b. S. Arya and H. Hintermann, "Growth of yba cu o superconducting thin films by ultrasonic spray pyrolysis," *Thin Solid Films*, vol. 193, pp. 841–846, 1990.

[13] P. J. ávan der Put *et al.*, "Morphology control of thin licoo 2 films fabricated using the electrostatic spray deposition (esd) technique," *J. Mater. Chem.*, vol. 6, no. 5, pp. 765–771, 1996.

[14] C. Girotto, B. P. Rand, J. Genoe, and P. Heremans, "Exploring spray coating as a deposition technique for the fabrication of solution-processed solar cells," *Sol. Energy Mater. Sol. Cells*, vol. 93, no. 4, pp. 454–458, 2009.

[15] J. Huang, Z. Yuan, S. Gao, J. Liao, and M. Eslamian, "Understanding spray coating process: Visual observation of impingement of multiple droplets on a substrate," *J.Shanghai Jiaotong University (Science)*, vol. 23, no. 1, pp. 97–105, 2018.

[16] A. L. Yarin, "Drop impact dynamics: splashing, spreading, receding, bouncing…," *Annu. Rev. Fluid Mech.*, vol. 38, pp. 159–192, 2006.

[17] M. Espindola-Rodriguez, M. Placidi, O. Vigil-Galán, V. Izquierdo-Roca, X. Fontané, A. Fairbrother, D. Sylla, E. Saucedo, and A. Pérez-Rodríguez, "Compositional optimization of photovoltaic grade cu2znsns4 films grown by pneumatic spray pyrolysis," *Thin solid films*, vol. 535, pp. 67–72, 2013.

[18] M. Braun, “Magnetron sputtering technique,” *Handbook of Manufacturing Engineering Technology; Springer: Berlin, Germany*, pp. 2929–2957, 2015.

[19] P. Sigmund, “Theory of sputtering. i. sputtering yield of amorphous and polycrystalline targets,” *Phys. Rev.*, vol. 184, no. 2, p. 383, 1969.

[20] N. Matsunami, Y. Yamamura, Y. Itikawa, N. Itoh, Y. Kazumata, S. Miyagawa, K. Morita, R. Shimizu, and H. Tawara, “Energy dependence of the ion-induced sputtering yields of monatomic solids,” *At. Data Nucl. Data Tables*, vol. 31, no. 1, pp. 1–80, 1984.

[21] G. Vijaya, M. Krupashankara, B. Sridhara, T. Shridhar, *et al.*, “Studies on nanostructure aluminium thin film coatings deposited using dc magnetron sputtering process,” in *IOP Conference Series: Materials Science and Engineering*, vol. 149, p. 012071, IOP Publishing, 2016.

[22] S. Berg and T. Nyberg, “Fundamental understanding and modeling of reactive sputtering processes,” *Thin solid films*, vol. 476, no. 2, pp. 215–230, 2005.

[23] S. Sivaram, “Thin film phenomena,” in *Chemical Vapor Deposition*, pp. 8–40, Springer, 1995.

[24] K. Chopra, “Thin film phenomena mcgraw-hill,” *New York*, vol. 19692, p. 196, 1969.

[25] D. L. Smith and D. W. Hoffman, “Thin-film deposition: principles and practice,” *Phys. Today*, vol. 49, no. 4, p. 60, 1996.

[26] H. H. Andersen and H. L. Bay, “Sputtering yield measurements,” in *Sputtering by particle bombardment I*, pp. 145–218, Springer, 1981.

[27] S. Swann, “Magnetron sputtering,” *Phys.Technol.*, vol. 19, no. 2, p. 67, 1988.

[28] J. J. Cuomo, S. M. Rossnagel, H. Haufman, and R. Komanduri, “Handbook of ion beam processing technology: principles, deposition, film modification, and synthesis,” 1990.

[29] T. Minami, S. Suzuki, and T. Miyata, “Transparent conducting impurity-co-doped zno: Al thin films prepared by magnetron sputtering,” *Thin solid films*, vol. 398, pp. 53–58, 2001.

[30] N. Neves, R. Barros, E. Antunes, I. Ferreira, J. Calado, E. Fortunato, and R. Martins, “Sintering behavior of nano-and micro-sized zno powder targets for rf magnetron sputtering applications,” *J. Am. Ceram. Soc.*, vol. 95, no. 1, pp. 204–210, 2012.

[31] W. Lan, Y. Liu, M. Zhang, B. Wang, H. Yan, and Y. Wang, “Structural and optical properties of la-doped zno films prepared by magnetron sputtering,” *Mater. Lett.*, vol. 61, no. 11-12, pp. 2262–2265, 2007.

[32] A. Authier, *Dynamical theory of X-ray diffraction*, vol. 11. Oxford University Press on Demand, 2004.

[33] A. A. Bunaciu, E. G. Udri§Tioiu, and H. Y. Aboul-Enein, “X-ray diffraction: instrumentation and applications,” *Crit. Rev. Anal. Chem.*, vol. 45, no. 4, pp. 289–299, 2015.

[34] B. D. Cullity, *Elements of X-ray Diffraction.* Addison-Wesley Publishing, 1956.

[35] J. R. Connolly, “Elementary crystallography for x-ray diffraction,” *Introduction to X-Ray powder diffraction, Spring*, 2012.

[36] G. Brown, *Crystal structures of clay minerals and their X-ray identification*, vol. 5. The Mineralogical Society of Great Britain and Ireland, 1982.

[37] G. W. Brindley, “Identification of clay minerals by x-ray diffraction analysis,” *Clays Clay Miner.*, vol. 1, no. 1, pp. 119–129, 1952.

[38] V. Kumar, S. Kumari, P. Kumar, M. Kar, and L. Kumar, "Structural analysis by rietveld method and its correlation with optical propertis of nanocrystalline zinc oxide," *Adv Mater Lett*, vol. 6, no. 2, pp. 139–147, 2015.

[39] P. Prabeesh, I. P. Selvam, and S. Potty, "Structural properties of czts thin films on glass and mo coated glass substrates: a rietveld refinement study," *Appl. Phys. A*, vol. 124, no. 3, pp. 1–6, 2018.

[40] Y. T. Prabhu, K. V. Rao, V. S. S. Kumar, and B. S. Kumari, "X-ray analysis by williamson-hall and size-strain plot methods of zno nanoparticles with fuel variation," *World J. Nano Sci. Eng.*, vol. 2014, 2014.

[41] S. Pati, P. Banerji, and S. Majumder, "Properties of indium doped nanocrystalline zno thin films and their enhanced gas sensing performance," *RSC Adv.*, vol. 5, no. 75, pp. 61230–61238, 2015.

[42] E. Ş. Tüzemen, H. Kavak, and R. Esen, "Influence of oxygen pressure of zno/glass substrate produced by pulsed filtered cathodic vacuum arc deposition," *Phys. B: Condens. Matter*, vol. 390, no. 1-2, pp. 366–372, 2007.

[43] Y. Wang, S. P. Lau, H. Lee, S. F. Yu, B. Tay, X. Zhang, K. Tse, and H. Hng, "Comprehensive study of zno films prepared by filtered cathodic vacuum arc at room temperature," *J. Appl. Phys.*, vol. 94, no. 3, pp. 1597–1604, 2003.

[44] G. H. Jo, S.-H. Kim, and J.-H. Koh, "Enhanced electrical and optical properties based on stress reduced graded structure of al-doped zno thin films," *Ceram. Int.*, vol. 44, no. 1, pp. 735–741, 2018.

[45] V. Mote, Y. Purushotham, and B. Dole, "Williamson-hall analysis in estimation of lattice strain in nanometer-sized zno particles," *J. Theor. Appl. Phys.*, vol. 6, no. 1, pp. 1–8, 2012.

[46] K. Venkateswarlu, A. C. Bose, and N. Rameshbabu, “X-ray peak broadening studies of nanocrystalline hydroxyapatite by williamson–hall analysis,” *Phys. B: Condens. Matter*, vol. 405, no. 20, pp. 4256–4261, 2010.

[47] A. C. Larson and R. B. Von Dreele, “Gsas,” *Report lAUR*, pp. 86–748, 1994.

[48] B. H. Toby, “Expgui, a graphical user interface for gsas,” *J. Appl. Crystallogr.*, vol. 34, no. 2, pp. 210–213, 2001.

[49] A. Fischereder, T. Rath, W. Haas, H. Amenitsch, J. Albering, D. Meischler, S. Larissegger, M. Edler, R. Saf, F. Hofer, *et al.*, “Investigation of cu2znsns4 formation from metal salts and thioacetamide,” *Chem. Mater.*, vol. 22, no. 11, pp. 3399–3406, 2010.

[50] S. C. Vogel, “gsaslanguage: a gsas script language for automated rietveld refinements of diffraction data,” *J. Appl. Crystallogr.*, vol. 44, no. 4, pp. 873–877, 2011.

[51] R. Young, “The rietveld method oxford univ,” 1995.

[52] F. Izumi, “Applications of synchrotron radiation to materials analysis,” *by H. Saisho and Y. Gohshi, Elsevier, Amsterdam*, p. 405, 1996.

[53] H. M. Rietveld and R. Young, “The early days: a retrospective view,” *The Rietveld Method, Oxford University Press, Oxford*, pp. 39–42, 1993.

[54] J. C. Taylor and I. Hinczak, *Rietveld made easy: a practical guide to the understanding of the method and successful phase quantifications.* Sietronics Pty Limited, 2006.

[55] J. Rodriguez-Carvajal and T. Roisnel, “Fullprof. 98 and winplotr: new windows 95/nt applications for diffraction,” *Commission for Powder Diffraction, International Union of Crystallography, Newsletter*, vol. 20, pp. May–August, 1998.

[56] F. Izumi and T. Ikeda, “A rietveld-analysis programm rietan-98 and its applications to zeolites,” in *Mater. Sci. Forum*, vol. 321, pp. 198–205, Trans Tech Publ, 2000.

[57] A. Bruker, “Topas v4. 2: General profile and structure analysis software for powder diffraction data,” *Bruker AXS, Karlsruhe, Germany*, 2009.

[58] M. Dušek, V. Petříček, M. Wunschel, R. Dinnebier, and S. v. Smaalen, “Refinement of modulated structures against x-ray powder diffraction data with jana2000,” *J. Appl. Crystallogr.*, vol. 34, no. 3, pp. 398–404, 2001.

[59] M. Quaas, C. Eggs, and H. Wulff, “Structural studies of ito thin films with the rietveld method,” *Thin Solid Films*, vol. 332, no. 1-2, pp. 277–281, 1998.

[60] W. Zhou, R. Apkarian, Z. L. Wang, and D. Joy, “Fundamentals of scanning electron microscopy (sem),” in *Scanning microscopy for nanotechnology*, pp. 1–40, Springer, 2006.

[61] T. Ichinokawa, “Oc wells, a. boyde, e. lifshin and a. rezanowich: Scanning electron microscopy, mcgraw-hill, new york and st. louis, 1974, xviii+ 421 23.5× 16.5 cm, 8,490 ,” *J. Phys. Soc. Jpn.*, vol. 31, no. 1, pp. 85–86, 1976.

[62] W. A. High, R. A. Ayers, J. Chandler, G. Zito, and S. E. Cowper, “Gadolinium is detectable within the tissue of patients with nephrogenic systemic fibrosis,” *J. Am. Acad. Dermatol.*, vol. 56, no. 1, pp. 21–26, 2007.

[63] S. Nasrazadani and S. Hassani, “Modern analytical techniques in failure analysis of aerospace, chemical, and oil and gas industries,” *Handbook of Materials Failure Analysis with Case Studies from the Oil and Gas Industry*, pp. 39–54, 2016.

[64] K. Muraleedharan and D. Banerjee, "Alloy partitioning in ti-24al-11 nb by analytical electron microscopy," *Metall. Trans. A*, vol. 20, no. 6, pp. 1139–1142, 1989.

[65] D. B. Williams, "Practical analytical electron microscopy in materials science," in *Analytical Proceedings*, vol. 23, p. 41, 1986.

[66] J. Small, D. Newbury, R. Myklebust, C. Fiori, A. Bell, and K. Heinrich, "The f (χ) machine: An experimental bench for the measurement of electron probe parameters," in *Electron Probe Quantitation*, pp. 317–334, Springer, 1991.

[67] C.-C. Chen, C.-C. Yeh, C.-H. Chen, M.-Y. Yu, H.-L. Liu, J.-J. Wu, K.-H. Chen, L.-C. Chen, J.-Y. Peng, and Y.-F. Chen, "Catalytic growth and characterization of gallium nitride nanowires," *J. Am. Chem. Soc.*, vol. 123, no. 12, pp. 2791–2798, 2001.

[68] P. Sahoo, J. Basu, S. Dhara, H. C. Fang, C.-P. Liu, T. Ravindran, S. Dash, and A. K. Tyagi, "Single-step growth dynamics of core–shell gan on ga 2 o 3 freestanding nanoprotruded microbelts," *J. Mater. Sci.*, vol. 47, no. 7, pp. 3447–3453, 2012.

[69] J. R. Ferraro, *Introductory raman spectroscopy.* Elsevier, 2003.

[70] H.-J. Choi, "Vapor–liquid–solid growth of semiconductor nanowires," in *Semiconductor nanostructures for optoelectronic devices*, pp. 1–36, Springer, 2012.

[71] S. Parida, P. Magudapathy, A. Sivadasan, R. Pandian, and S. Dhara, "Optical properties of algan nanowires synthesized via ion beam techniques," *J. Appl. Phys.*, vol. 121, no. 20, p. 205901, 2017.

[72] Renishaw, "Pl spectroscopy." `https://www.renishaw.com/en/photoluminescence-explained--25809`, May 2001.

[73] D. Zhang, Q. Wang, and Z. Xue, “Photoluminescence of zno films excited with light of different wavelength,” *Appl. Surf. Sci.*, vol. 207, no. 1-4, pp. 20–25, 2003.

[74] L. Wu, Y. Wu, X. Pan, and F. Kong, “Synthesis of zno nanorod and the annealing effect on its photoluminescence property,” *Opt. Mater.*, vol. 28, no. 4, pp. 418–422, 2006.

[75] S. Eaton-Magaña and C. M. Breeding, “An introduction to photoluminescence spectroscopy for diamond and its applications in gemology.,” *Gems & Gemology*, vol. 52, no. 1, 2016.

[76] O. Philips’Gloeilampenfabrieken, “A method of measuring specific resistivity and hall effect of discs of arbitrary shape,” *Philips Res. Rep*, vol. 13, no. 1, pp. 1–9, 1958.

[77] K. Ellmer, “Hall effect and conductivity measurements in semiconductor crystals and thin films,” *Charact. Mater.*, pp. 1–16, 2012.

[78] L. J. van der Pauw, “A method of measuring the resistivity and hall coefficient on lamellae of arbitrary shape,” *Philips Techn. Rev.*, vol. 20, pp. 220–224, 1958.

[79] D. R. Baer, K. Artyushkova, C. Richard Brundle, J. E. Castle, M. H. Engelhard, K. J. Gaskell, J. T. Grant, R. T. Haasch, M. R. Linford, C. J. Powell, *et al.*, “Practical guides for x-ray photoelectron spectroscopy: First steps in planning, conducting, and reporting xps measurements,” *J. Vac. Sci. Technol. A: Vac. Surf. Films*, vol. 37, no. 3, p. 031401, 2019.

[80] G. Greczynski and L. Hultman, “X-ray photoelectron spectroscopy: towards reliable binding energy referencing,” *Prog. Mater Sci.*, vol. 107, p. 100591, 2020.

[81] P. Van der Heide, *X-ray photoelectron spectroscopy: an introduction to principles and practices.* John Wiley & Sons, 2011.

[82] G. Patonay, G. Beckford, and P. Hänninen, "Uv–vis and nir fluorescence spectroscopy," *Handbook of Spectroscopy: Second, Enlarged Edition*, pp. 999–1036, 2014.

[83] A. Singh, M. Kumar, R. Mehra, A. Wakahara, and A. Yoshida, "Al-doped zinc oxide (zno: Al) thin films by pulsed laser ablation.," *J. Indian Inst. Sci.*, vol. 81, no. 5, p. 527, 2001.

[84] J. Homola, S. S. Yee, and G. Gauglitz, "Surface plasmon resonance sensors," *Sens. Actuators, B*, vol. 54, no. 1-2, pp. 3–15, 1999.

[85] R. B. Schasfoort, *Handbook of surface plasmon resonance.* Royal Society of Chemistry, 2017.

[86] P. Pattnaik, "Surface plasmon resonance," *Appl. Biochem. Biotechnol.*, vol. 126, no. 2, pp. 79–92, 2005.

[87] Y. Chen and H. Ming, "Review of surface plasmon resonance and localized surface plasmon resonance sensor," *Photonic Sens.*, vol. 2, no. 1, pp. 37–49, 2012.

Chapter 3

Investigation of plasmonic properties of spin coated oxide co-doped ZnO thin films

3.1 Overview

Material research plays an essential role in making a breakthrough in the scientific community. An understanding of proper material has a great influence, especially in the field of plasmonics. Currently, research in this field lacks an excellent and a cost-effective material for potential device fabrication. Since plasmonics deals with electron-photon coupling, availability of free electrons is essential for a material. Hence, importance has been given to materials research in this work. This chapter investigates the plasmonic properties in Al and In co-doped ZnO thin films fabricated by spin coating technique. Doping in ZnO usually results in expansion or contraction of the lattice due to the difference in ionic radius of dopants and host material. Thus, expansion or contraction can be balanced when co-doped with two atoms having larger and smaller ionic radii than host atoms, for a particular co-doping ratio. The co-doping ratio of Al:In was varied sequentially from 100:0 to 0:100 (in percentage). Crystallinity of the films were studied by x-ray diffraction using CuKα radiation in 2θ range 20-60^o at a scanning rate of 3 degree/min. For the study of surface morphology, scanning electron microscope at an operating voltage of 20 kV was used. UV-Vis-NIR reflectance spectra were recorded in the range 300-2500 nm using a spectrophotometer. Electrical properties were measured using Ecopia HMS-3000 hall measurement system having magnetic field of 0.54T at 300K. Dielectric functions of films were retrieved by fitting the reflectance data with theoretical values according to the Drude-Lorentz model using RefFit, a standard software. As discussed in Chapter 1, section (1.3.3), of this thesis, the optical response of free electrons in metals can be described by the Drude model[1]. However, in doped or co-doped semiconductors having free as well as bound electrons, Drude theory alone is not sufficient to explain the optical response. Thus, this model is extended to Drude+Lorentz model where Lorentz approach treat bound electrons as a spring-like system that always experience a restoring force.

3.2 Sample preparation

3.2.1 Preparation of Al and In doped/co-doped ZnO solution

Precursor solutions for coating AZO, AIZO,IZO films were prepared from analytical grade zinc acetate dihydrate (Merck), aluminium nitrate (Merck), and indium chloride (Alfa Aesar). Zinc acetate dihydrate was dissolved in 2 methoxy ethanol and monoethanolamine (MEA), and the Al and In dopants dissolved in 2 methoxy ethanol were added to prepare a solution with atomic ratio (Al+In) of 3%. MEA was used as stabilizer for obtaining a homogeneous solution without precipitation. The molar ratio MEA/Zn was fixed as 1 and the solution concentration was fixed at 0.6M. A total of 11 solutions were prepared with various Al: In ratios (from 100: 0, 90: 10, 80: 20 to 10: 90, 0: 100). The solution as well as the films were named according to their co-dopant ratio (Al: In) as, A_0I_{10}, A_1I_9, A_5I_5, A_2I_8 etc. The resulting solution was stirred with a magnetic stirrer at room temperature for two hours. The clear and transparent solution obtained was aged for 24 h.

3.2.2 Substrate cleaning

In thin film preparation, substrate cleaning is very important as it will affect the smoothness, uniformity and repeatability of the films coated. Therefore, the soda lime glass substrates used for spin coating were cleaned using soap water, distilled water, acetone and isopropyl alcohol successively in an ultrasonic bath for 15 minutes each and then dried in nitrogen flow, before coating.

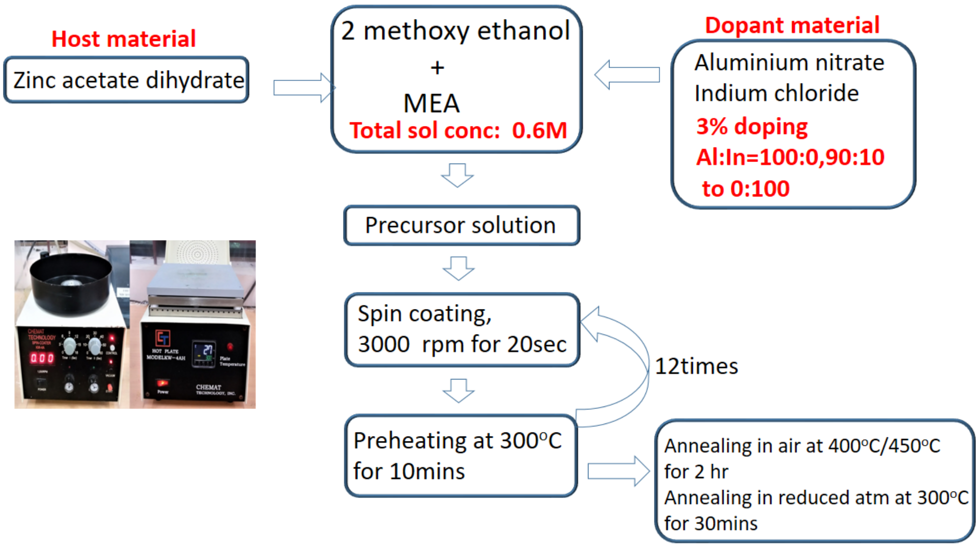

Figure 3.1: Flow chart of coating of Al and In doped/co-doped thin films by spin coating

3.2.3 Thin film preparation using spin coater

Thin films were coated on to the cleaned substrates having dimension of 1 inch × 1 inch using a Chemat KW-4A spin coater at 3000 rpm for 20s. The as coated films were dried at 300°C in air on a hot plate (Chemat) for 10 min to remove solvents and other organics. Fig.3.1 shows the flow chart adopted for the coating process in the present study. The spin coating procedure was repeated 12 times to achieve desired thickness for the film. The films were finally annealed in air at two temperatures, 400°C and 450°C, for 2 hr to study the effect of annealing temperature on the properties of the films. In ZnO, apart from extrinsic doping, the other method that helps for improving electrical properties is its non-stoichiometry. For that a second post deposition annealing was carried out in reduced atmosphere for another 30 min at 300°C to create more oxygen vacancies and hence to improve the electrical properties. A gas mixture of N_2 and H_2 in the ratio of 95: 5 was used for this purpose. The ramping is set to 5°C/min upto 300°C and the dwell time is set to 30 mins at 300°C. The furnace was cooled naturally to room temperature. The films were subjected to structural, electrical, optical, and plasmonic studies after the completion of annealing processes.

3.3 Electrical Properties

The carrier concentrations of the spin coated co-doped films are plotted in Fig.3.2. It is clear from the figure that the post deposition annealing in reduced atmosphere improved the free electron concentrations of the films. This is due to the additional oxygen vacancies created due to the desorption of oxygen by hydrogen[2, 3]. Annealing in air atmosphere may result in the chemisorption of oxygen and hence trapping of free electrons on grain boundaries and surface[2–4]. As seen, the maximum carrier concentration was obtained for the film annealed initially in air at 400°C. The study on the effect of annealing temperature on carrier density were done by Jeon et al[5]. They observed a sharp decrease in free carrier concentration when the annealing temperature was increased from 100°C to 200°C and then to 300°C[5]. According to them, annealing in air atmosphere annihilates the intrinsic oxygen vacancies(V_O) and zinc interstitials(Zn_i) possess dominant role in the n-type behaviour of the films. Yim et al[6] reported a sharp decrease in carrier density in GZO for annealing temperature beyond 400°C, and attributed the same as decreasing V_O and Zn_i using the following equation,

$$Zn_{Zn} + V_O + \frac{1}{2}O_2 \longrightarrow ZnO \tag{3.1}$$

$$Zn_i + \frac{1}{2}O_2 \longrightarrow ZnO \tag{3.2}$$

Similarly, in our study also the carrier density decreased when annealing temperature was increased from 400°C to 450°C. However, it was further increased when annealed in reduced atmosphere, as shown in Fig.3.2. As discussed, the annihilation of intrinsic defects during annealing in air atmosphere might have nullified by creating the oxygen vacancies during the annealing in a reduced atmosphere[6]. During the annealing, the hydrogen passivates grain boundary surface and removes the depletion region near the grain boundary. This in turn increases the free carrier density of the films[7]. The post-heating in reduced atmosphere resulted in thin film with better carrier density [3, 8].

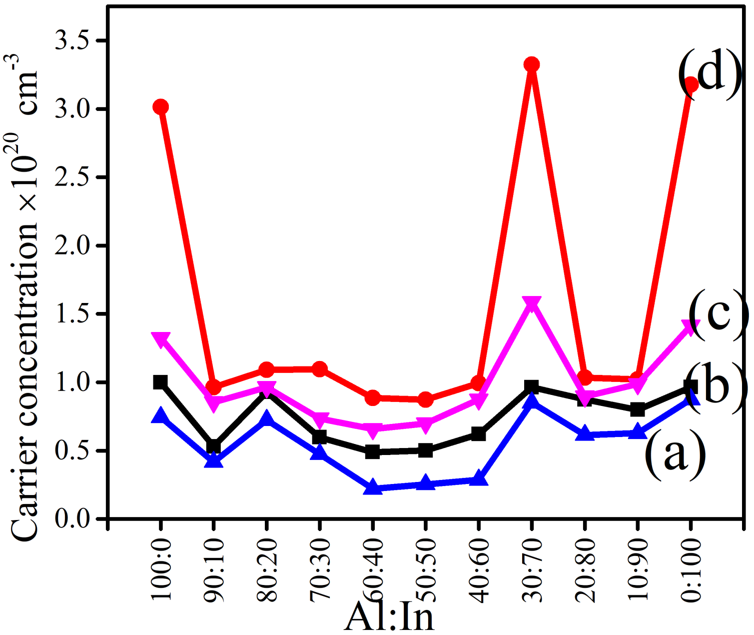

Figure 3.2: Variations in carrier concentration with dopant ratio; before hydrogen annealing [(a) and (c) annealed in air at 450°C and 400°C respectively], and after hydrogen annealing[(b) and (d) corresponding to the films (a) and (c) respectively]

As seen, the maximum carrier concentration was obtained for the film annealed initially in air at 400°C. In this study, the In doped ZnO films exhibited better carrier concentration than the Al doped ZnO films. Analyzing the co-doped samples, films with equal doping percentage of aluminium and indium showed poor metallic behaviour compared to those with Al/In ratio of <1 (especially forA_3I_7). Equal concentrations of aluminium and indium may form non-conducting Al_2O_3/ln_2O_3 clusters at grain boundaries[9]. Here, a favourable change was observed for the film with 70% indium in its overall doping of 3%. The study indicates that the carrier concentrations in the Al/In co-doped films did not improve with further increase of the In dopant. This is evident from the results obtained for the films with Al/In ratios of 20:80 and 10:90. Even though co-doping has the advantage of exploiting the two dopants simultaneously, high reactivity of aluminium sometimes results in other side reaction[10, 11]. The present study also revealed reduction in carrier concentration from 3.323×10^{20} / cm^3 (for the film A_3I_7) to 1.092×10^{20} /cm^3 (A_8I_2). This is further clear in the case of the film A_0I_{10}, which shows an improvement in the carrier density compared with $A_{10}I_0$, and this may be due to the absence of the other side reactions due to aluminium. The carrier density of films was not improved further in the film A_1I_9, thus suggested a compatible co-doping ratio for the films. Kirby et al also reported a specific ratio for Al and In in co-doped films due to their different ionic radii from the host zinc atom[12]. The structural studies of the films with better carrier concentrations were carried out further to study more about this behaviour of co-doped films.

3.4 Structural properties

The films were selected according to their carrier concentration for studying structural properties. IZO, AZO and AIZO (A_3I_7) films, annealed initially in air at 400°C and subsequently treated in reduced atmosphere, showed better carrier concentrations were selected for further studies.

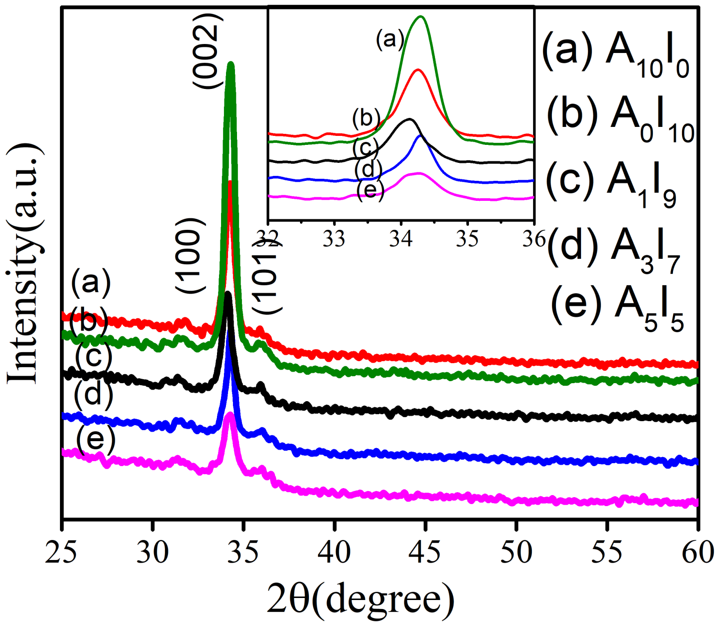

Figure 3.3: XRD patterns of doped(A_0I_{10}, $A_{10}I_0$) and co-doped film(A_1I_9, A_3I_7, A_5I_5). Inset shows enlarged portion of (002) peak

In addition, two more samples with dopant ratios close to the above (A_1I_9 and A_5I_5) were also considered for the analysis. Structural properties of these samples were studied with x-ray diffraction and the patterns are plotted in Fig.3.3. The films exhibited hexagonal wurtzite structure, irrespective of the dopant concentration. The peaks observed between 2θ values 34.24^o and 34.35^o identified as the (002) plane, indicated growth of films along the c axis. The underlying mechanism for the c axis growth of the film was not clearly understood. However, growth along this plane can be predominant due to minimum surface energy of wurtzite structure and highest atomic density of Zn on this plane[10]. No peaks corresponding to secondary phases such as for Al_2O_3 and In_2O_3 or any ternary phases were observed, which confirmed that the Al and In were well substituted with zinc atoms.

Pati et al[13] observed a decrease in intensity of the (002) peak and increase in the FWHM of the same with increase in the In dopant concentration in the films. According to them, this was mainly due to the substitution of In in Zn site which altered the growth of film along (002) plane. In the present study, the film A_0I_{10} exhibited an intense and sharp peak than that of the film $A_{10}I_0$, which indicates the high crystallinity of the indium doped ZnO film. In the case of co-doped films, as indicated earlier, incorporation of equal amounts of Al and In may result in cluster formation, which could lead to a deterioration in crystal quality[9]. This behaviour can be seen for A_5I_5 film. Jayaraman et al.[9] also noted the change in the intensity of (002) diffraction peak, when ZnO is co-doped with metals such as aluminium and indium. Unlike powder, for thin films, their growth is restricted in specific directions and this may result in strain[14].

To further investigate the structural behaviour of co-doped (especially for A_3I_7 and A_1I_9) and doped films, parameters such as lattice constants, lattice stress, strain and full width at half maximum (FWHM) were calculated and shown in Table.3.1.

In addition, average crystallite size (D) of the films were determined using Debye-Scherrer formula [13]

$$D = \frac{0.9\lambda}{\beta cos\theta} \tag{3.3}$$

λ (=1.54060A^o), the wavelength of x-ray used, β is FWHM of diffraction peaks in radian and θ is the incident angle expressed in degree. For hexagonal lattice, interplanar distance(d_{hkl}) in terms of lattice parameter (a=b, c) can be written as

$$\frac{1}{d_{hkl}^2} = \frac{4}{3a^2}[h^2 + k^2 + hk] + \frac{l^2}{c^2} \tag{3.4}$$

The structural behaviour of co-doped and doped films can be attributed to the distortion in the ZnO lattice due to the substitution of In^{3+} and Al^{3+} ions[15]. The ionic radius of In^{3+} (0.080nm) is larger and Al^{3+}(0.057nm) is

Table 3.1: Structural parameters of doped and co-doped ZnO thin films, estimated from XRD data

Sample	d A^o		Lattice parameters		FWHM	Crystallite size	Lattice strain	Lattice stress
	(002)	(100)	c	a	radian	(nm)	S(x10^{-2})	σ(Gpa)
$A_{10}I_0$	2.601	2.81	5.202	3.24	0.0088	20	-0.07683	0.1790
A_1I_9	2.615	2.84	5.230	3.28	0.0086	20	0.461	-1.0741
A_3I_7	2.608	2.83	5.216	3.26	0.0080	21	0.19	-0.442
A_5I_5	2.622	2.85	5.244	3.29	0.0115	15	0.729	-1.698
A_0I_{10}	2.610	2.82	5.220	3.25	0.0082	20	0.26	-0.605

less than that of Zn^{2+} (0.074nm), and this causes distortion in ZnO lattice [16, 17]. The distortion can be understood from the changes of the lattice parameters (c and a) with respect to the ICDD data (powder diffraction file # 36-1451) and the same is shown in Fig.3.4 (values of lattice parameters are given in Table.3.1). As seen in the figure, the maximum change in the lattice constants is observed for the samples A_1I_9 and A_5I_5. Comparing with A_3I_7, it shows that a particular ratio of Al and In is favourable for less distorted films and this behaviour was reflected in their electrical properties. The shifting of lattice parameter as a function of dopant composition or any other parameter like temperature variation or structural phase transformation will result in development of local stress or strain[17]. The minimum shift in the lattice constants of A_3I_7 indicates that this ratio of Al and In is favoured for less distortion. The importance of less stress or strain in thin films for their better electrical performance was also studied by Alsaad et al[18]. The behaviour of specific dopant ratio in co-doped films was reported by Le et al[19].

The ionic mismatch of -32% and +9%, when aluminium and indium[12] respectively are doped in ZnO lattice, can be compensated if doped them together in a particular ratio. From the present investigation, the film A_3I_7 provides less distorted film, exhibits improved electrical properties. The negative values of Δa and Δc for the film $A_{10}I_0$ further confirms the shrink in the structure, when a metal with high ionic radius (Zn) is replaced with that of smaller one (Al), in accordance with Vegard's law [20, 21]. The distortion of lattice parameters (positive for indium doped and negative for aluminium doped) itself indicates that the dopants are substituted in the Zn lattice and not in the interstitial site[20].

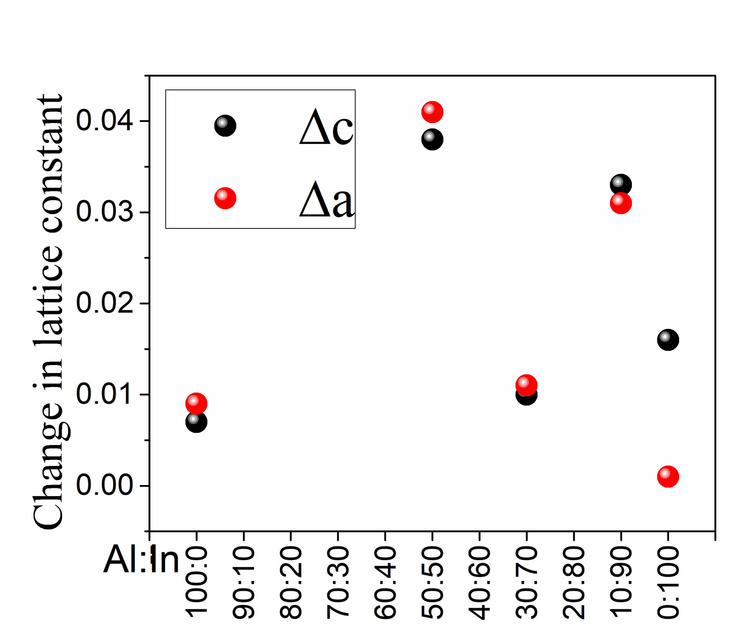

Figure 3.4: Deviation of lattice constants a (red) and c (black) for doped and co-doped films

The slightly large positive Δa, Δc values of A_1I_9 and A_5I_5 may be due to movement of more Al/In ions or both to the interstitial site[20, 21]. The effect of lattice distortion in the film can induce strain (S) (strain is represented by the symbol ϵ by convention; but S is used here not to confuse with dielectric constant, described below) and stress (σ) along the c axis and can be estimated by

$$S = \frac{c_{film} - c_{bulk}}{c_b ulk} \tag{3.5}$$

$$\sigma = -2.33 \times 10^{11} S \tag{3.6}$$

Where c_{film} represents the lattice parameter of film and $c_{bulk}(= 5.206A^0)$ is that for unstrained ZnO film[22, 23]. Maximum stress, strain and FWHM were observed for the films A_5I_5 and A_1I_9. The negative value for stress indicates that it is compressive stress[24].

3.5 Morphological studies

3.5.1 Surface morphology

Fig.3.5 (a-e) show the SEM images of the films A_1I_9, A_3I_7 and A_5I_5. The changes in the film morphology with dopant concentration can be well understood from the SEM images.

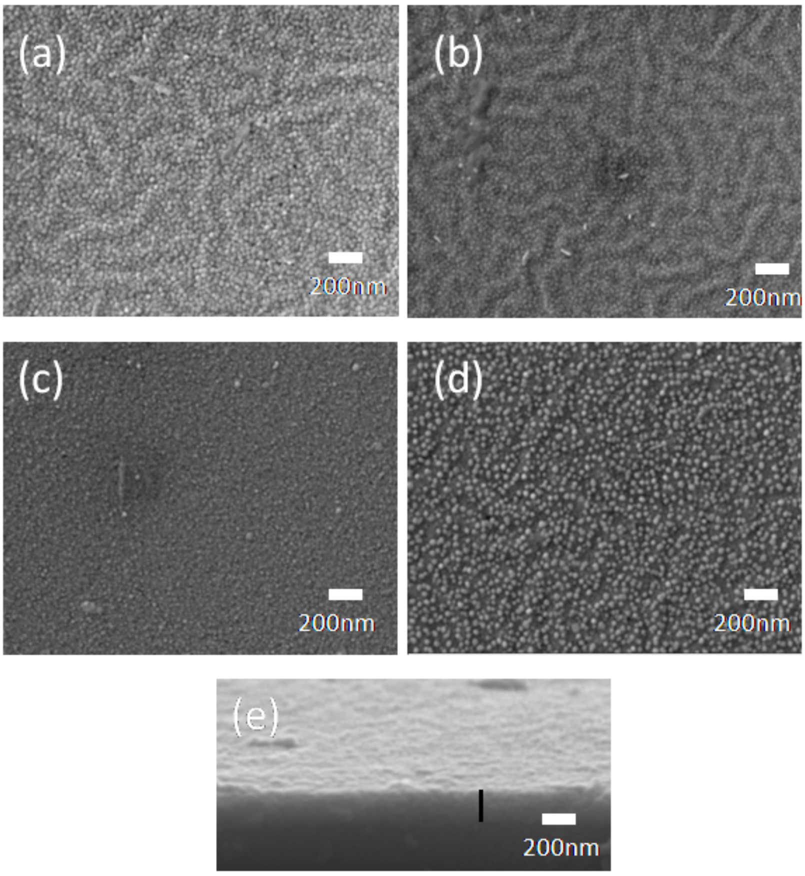

Figure 3.5: SEM images of the films (a)A_3I_7 (**62nm**), (b)A_1I_9 (**50nm**), (c) A_5I_5 (**44nm**) annealed at 400°C and (d)A_3I_7 annealed at 450°C in oxidised atmosphere (grain size are given in bold), (e)Cross-section of the film A_3I_7 air annealed at 400°C

In the case of the films A_3I_7 and A_1I_9, densely packed wrinkle-like network structure was observed with average crystallite sizes of 62nm and 50nm, respectively (Fig.3.5a and Fig.3.5b). While for the film A_5I_5, the average particle size reduced to 44nm and the wrinkle network structure was diminished along with uneven appearance in the surface, as depicted in the Fig.3.5c. The average crystallite sizes of the films obtained here were almost three times higher than those estimated from XRD (Table.3.1). The average size evaluated from SEM may be from a grain consisting of two or more crystallites, and this may be the reason for the difference in sizes. Basyooni et al.[25] also noticed similar results for the spin coated ZnO films doped with Na. The thicknesses of the films determined from the SEM images were found to be nearly equal, around 290 nm; cross section of A_3I_7 is shown in Fig.3.5e. To understand the effect of air annealing temperature in these films, A_3I_7, which got a better result at 400°C was subjected to SEM analysis. As the annealing temperature was increased from 400°C to 450°C, more voids appeared, as seen in Fig.3.5d. The study indicates that annealing at 400°C is more suitable for co-doped films.

3.5.2 Elemental compositional analysis

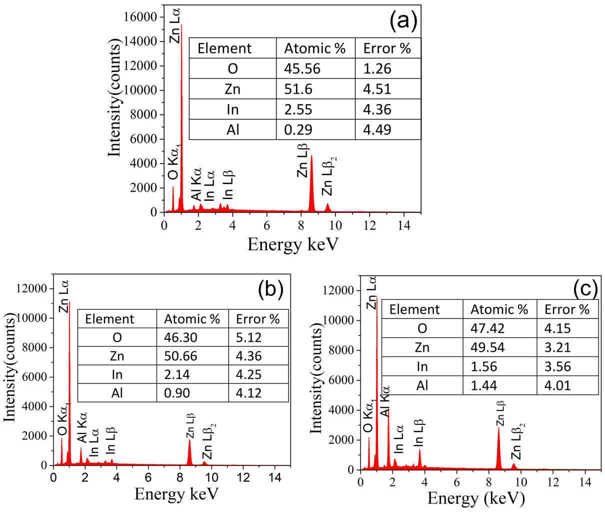

(a)

Element	Atomic %	Error %
O	45.56	1.26
Zn	51.6	4.51
In	2.55	4.36
Al	0.29	4.49

(b)

Element	Atomic %	Error %
O	46.30	5.12
Zn	50.66	4.36
In	2.14	4.25
Al	0.90	4.12

(c)

Element	Atomic %	Error %
O	47.42	4.15
Zn	49.54	3.21
In	1.56	3.56
Al	1.44	4.01

Figure 3.6: EDAX spectra of co-doped ZnO films (a)A_1I_9 (b) A_3I_7 (c) A_5I_5.

Fig.3.6 shows the Energy Dispersive X-Ray spectra (EDAX) of co-doped ZnO thin films. The peaks in the patterns were well agreed with Zn, Al, In and O. The inset tables in Fig.3.6a, Fig.3.6b, Fig.3.6c respectively shows the quantitative analysis of the atomic composition of Al:In for A_1I_9, A_3I_7, and A_5I_5 thin films and were close to 1:9, 3:7, and 5:5.

3.6 Optical properties

3.6.1 Band gap determination

Fig.3.7(a) shows the transmittance spectra of $A_{10}I_0$, A_5I_5, A_3I_7, A_1I_9, and A_0I_{10} films in the visible region. For most of the TCO applications, average optical transmittance greater than 80% is preferred[10, 26]. In the present study, all films except $A_{10}I_0$ exhibited average optical transmittance of >90% in the visible region. The band gap energies of the films were estimated from the transmittance spectra shown in Fig.3.7(b), using the well known Tauc's relation[27],

$$\alpha h\nu = A(h\nu - E_g)^n \tag{3.7}$$

Where h ν is the incident photon energy, A is a constant and n is $\frac{1}{2}$ for allowed direct transitions. The optical band gap energies were calculated by extrapolating the linear portion of $(\alpha h\nu)^2$ versus hν curve at α is 0, as shown in Fig.3.7(b).

The bandgap of the films showed a blue-shift with respect to carrier density as seen in Fig.3.8. Increase in band gap with respect to carrier density is usually observed in doped ZnO [10,28,29]. The donor electrons in the film occupy the states which are at the bottom of the conduction band. For an electron to make a vertical transition from the valence band to states with fermi momentum in the conduction band, higher energy is needed. This bandgap widening is generally seen in heavily doped wide bandgap semiconductors and is called Burstein-Moss (BM) band filling effect[30]. In this study, the BM effect is found to be valid for the samples from A_5I_5 to $A_{10}I_0$, as shown in Fig.3.8.

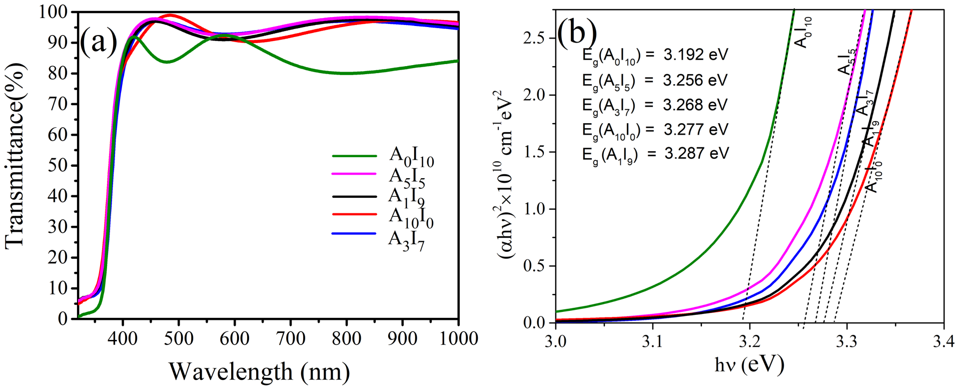

Figure 3.7: (a) Optical transmittance spectra (b) squared absorption coefficients of doped and co-doped films

However, the blue-shift was then changed to red shift; the sudden bandgap narrowing (BN) effect after a specific carrier density was studied by Kim et al[31]. The BN effect is due to the merging of donor and conduction bands, and indicates the transition from semiconductor to metal[32, 33]. The free carrier density at which the BN effect starts is called as the Mott critical density(n_o), which is inversely proportional to the Bohr radius of dopant[32, 33]. The observed Mott critical density n_o by Kim et al[31] and Sernelius et al[33] were beyond n= 4.5 $\times 10^{20}/\text{cm}^3$ for AZO and 5 $\times 10^{19}/\text{cm}^3$ for IZO. In this work, the Mott critical density was observed to be at n=$3.178\times 10^{20}/\text{cm}^3$ for the $A_{10}I_0$ film. According to Lu et al[30], a wide band gap semiconductor upon doping will result in increase in free electron density, and the increase in bandgap with carrier density obeying the BM effect will undergo the BN effect later, consistent with the Mott criterion (n_o), but again shows blue-shift in bandgap due to band renormalisation (BR) in a different rate. The effects of these three process can be seen in the samples under study, in such a way that the films from A_5I_5 to $A_{10}I_0$ obey BM effect, the films from $A_{10}I_0$ to A_0I_{10} exhibit BN effect and the films from A_0I_{10} to A_3I_7 shows BR effect.

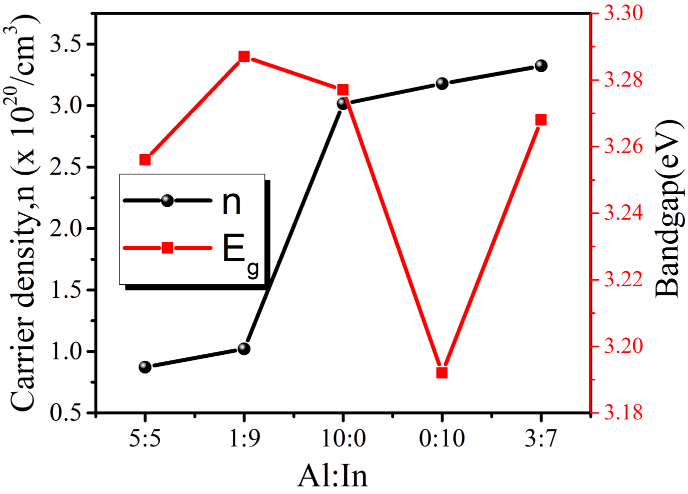

Figure 3.8: Variation of bandgap with carrier density of doped and co-doped films

3.6.2 Urbach energy calculation

The lower average transmittance in indium doped films may be attributed to the optical absorption due to the formation of localized states near the conduction band minimum[26]. As discussed, the large ionic radius of indium can cause disorder in film structure and can result in band tail width known as urbach energy. Hence, calculating urbach energy of these films will give a clear idea about the structural disorder due to formation of new states[34,35]. The urbach energy, governed by structural disorder or imperfection in stoichiometric or passivation on the film surface, is found below the absorption edge of the compound. It calculates the degree of smearing absorption edge due to lattice crystal disordering caused by external factors[25, 34, 35]. Urbach tail energy is determined using the following equation[36].

$$\alpha_E = \alpha_0 e^{\frac{E-E_0}{E_u(T,X)}}, where E < E_g \tag{3.8}$$

After taking natural logarithm of both sides of the equation, we have,

$$\ln(\alpha) = \ln(\alpha_0 - \frac{E_0}{E_u}) + \frac{E}{E_u} \tag{3.9}$$

where α is the absorption coefficient, E_g is the bandgap energy, and α_0 and E_0 are constants. The urbach energy, represented as E_u, is dependent on defects and disorder induced by temperature(T) and structure(X), and will result in the formation of additional states in conduction band minimum[36, 37]. Since temperature is fixed in this case, the main contribution of E_u will be from the structure. Considering the following equation (3.9) and using the linear least square fit of the experimental absorption data, E_u was calculated and is tabulated in Table.3.2. As seen in the table, the film A_0I_{10} possesses large E_u, in turn represents localized states created within bandgap, and this may be the reason for the relatively low average transmission in the optical range.

Table 3.2: Fitting parameters of ln $(\alpha) = b_0 + (h\nu)b_1$ together with R^2 value of linear regression analysis(reciprocal of b_1 is E_u)

Sample	b_0	b_1	E_u (eV)	R^2
$A_{10}I_0$	8.11	0.961	1.040	0.68
A_1I_9	6.88	0.867	1.153	0.57
A_3I_7	7.19	0.822	1.216	0.58
A_5I_5	7.17	0.817	1.223	0.54
A_0I_{10}	7.27	0.796	1.255	0.55

3.7 Investigation of plasmonic properties in the films

3.7.1 Drude-Lorentz approach on doped -semiconductors

Interaction of electromagnetic field with thin films has utmost importance to study their plasmonic behaviour. As in the case of metals, the optical response of transparent conducting films can be described by dielectric permittivity (ϵ) as,

$$\epsilon(\omega) = \epsilon_1 + \epsilon_2 \tag{3.10}$$

Where ϵ_1 describes strength of polarisation and ϵ_2 denotes the losses due to the interaction between electrons as well as between electron and phonon, or due to scattering because of lattice defects and grain boundaries[38]. Drude-Lorentz (DL) approach was used for obtaining physically meaningful plasmonic characteristics of the films from experimental data[1, 38]. For doped semiconductors, we have free electrons (Drude model) as well as bound electrons (Lorentz model) and hence this model is ideal to explain and extract the real and imaginary parts of dielectric constant. Treating electrons in a spring like system and considering harmonic potential, DL model can be described as[4],

$$\epsilon(\omega) = \epsilon_\infty - \sum_j \frac{\omega_{pj}^2}{\omega_{0j}^2 + \omega^2 + i\gamma_j\omega} \tag{3.11}$$

where ω_{0j} is the resonant frequency of oscillation of the j^{th}oscillator, ω is the frequency of the incident electromagnetic wave, ω_p is the plasma frequency and γ_j is the damping factor. ω_{0j} is zero for the Drude term because it describes response of bound electrons

3.7.2 Estimation of plasma frequency of the thin films

Plasma frequency is an important material property in the field of plasmonics. An electromagnetic radiation having frequency less than plasma frequency will be reflected, while with higher frequency will be transmitted [40]. Plasma frequency is directly related to the carrier concentration (n) as

$$\omega_p^2 = \frac{ne^2}{m\epsilon_0} \tag{3.12}$$

where e, m and ϵ_0 are the electronic charge, effective mass of the free carrier and the permittivity of vacuum, respectively[39].

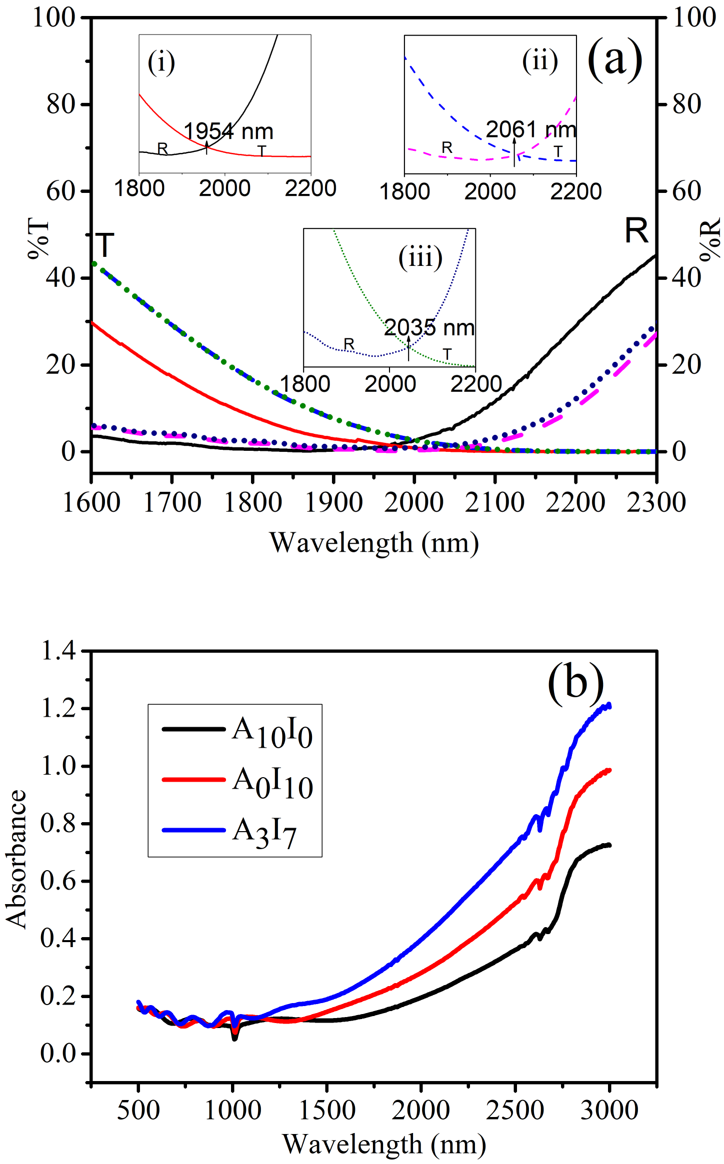

Figure 3.9: (a)Estimation of plasma frequency (ω_p). Inset images show ω_p of (i) A_3I_7 (ii) $A_{10}I_0$ and (iii) A_0I_{10} thin films (b) absorbance spectra of films from visible to infrared wavelength.

Due to the direct dependence of plasma frequency with carrier concentration, the films $A_{10}I_0$, A_3I_7, A_0I_{10}, which showed carrier densities $10^{20}/\mathrm{cm}^3$

were selected for further study to understand their plasmonic behaviour. The plasma frequency of materials can be estimated from the reflectance-transmittance (R-T) spectra. The frequency at which the R-T spectra intersect is considered to estimate plasma frequency[31]. The films of the present study were observed to behave like metals in the region between 1950nm to 2070nm. The plasma frequency, in terms of wavelength, of the films are described in Fig.3.9(a); the values are 1954 nm, 2061 nm, 2035nm respectively for the films A_3I_7, $A_{10}I_0$ and A_0I_{10}. The A_3I_7 film with higher carrier concentration exhibited small plasma wavelength, which is as per the eqn (3.12). Fig.3.9(b) shows the absorbance spectra of these films. Buonsanti et al[40] and Ghosh et al[41] reported similar absorbance in the near infrared for AZO and IZO films respectively and has been attributed to surface plasmon absorption. Here, strong absorbance from 1500nm to 3000nm of $A_{10}I_0$, A_3I_7, A_0I_{10} can also be considered as the suitability of these films for plasmonic applications in the infrared region.

3.7.3 Comparison of plasma frequency and cross over frequency of the thin films.

The dielectric functions were extracted from optical reflection spectra to understand the plasmonic behaviour of these three films, using a standard program RefFit[42]. This was done by fitting the optical spectra using the model of dielectric function with set of values for oscillators as per the Drude-Lorentz model (eqn 3.11). The parameters varied in order to obtain the best match between experimental and calculated data points are given in Table.3.3.

Table 3.3: Drude- Lorentz parameters fitted according to eqn (3.11) using RefFit

	$A_{10}I_0$	A_3I_7	A_0I_{10}
ϵ_∞	4.7	5.03	5.08
ω_p(eV)	1.19	1.30	1.28
ω_0(eV)	0.0006	0.0004	0.0001
γ((eV)	0.059	0.066	0.060

Fig.3.10(a-c) show the experimental and fitted data of reflectance spectra, where the theoretical calculations were done using the Fresnel formula [42,43].

$$R = |\frac{1-\sqrt{\epsilon}}{1+\sqrt{\epsilon}}|^2 \tag{3.13}$$

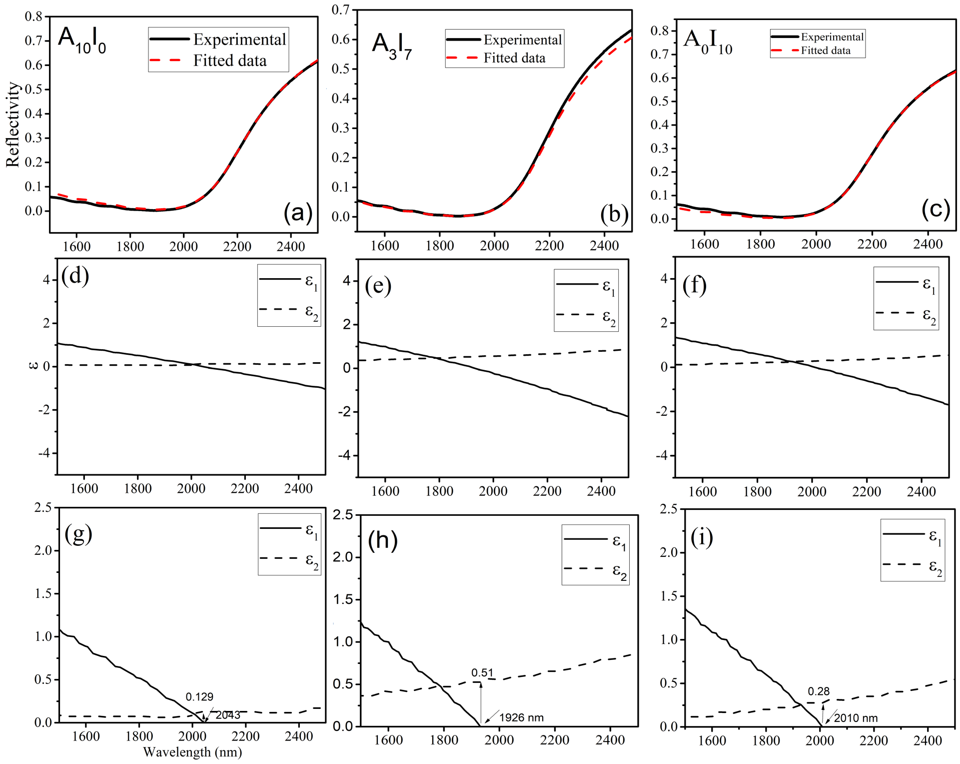

Figure 3.10: Fitted reflectance spectra of (a) $A_{10}I_0$, (b) A_3I_7, (c) A_0I_{10} and (d) to (f) their real and imaginary parts of dielectric constant (ϵ), and (g) to (i) represent the enlarged portion of cross over wavelength of these films respectively.

The corresponding dielectric functions are plotted and the curves are shown in Fig.3.10(d-f), where real and imaginary parts of the dielectric constant are presented. Plasmonic behaviour of thin films was well understood from the fitted data, which revealed negative values for the real part of permittivity below 2100 nm. The crossover wavelength (ω_c) of $A_{10}I_0$, A_3I_7 and

A_0I_{10} were found to be 2042nm, 1926nm, 2010nm respectively, which are very close to the plasma frequencies (ω_p) 2061nm, 1954nm and 2035nm, obtained from the R-T spectra. Since cross over frequency (ω_c) and plasma frequency (ω_p) represent the transformation of a material from metallic to dielectric or vice versa, these values might have a direct dependence as noted by Naik et al.[44]. The difference in these values may be due to the difference in accounting of losses, or due to the fact that the value of ω_c is calculated theoretically while that of ω_p is from experimental analysis. It can be seen that the A_3I_7 film with higher carrier concentration exhibited shorter crossover wavelength, which emphasize the direct dependence of these two values. The ϵ_2 values obtained for the films were very small and comparable with those reported in previous studies[45]. Nevertheless, the loss in the films may be due to the additional states created in the film due to urbach energy, which results in increase of interband transition losses along with free carrier absorption losses. According to Noginov et. al[45], large free carriers will result in maximum absorption and hence exhibits loss. This may be the reason for slightly higher value of ϵ_2 for A_3I_7 film compared to the other two films, as shown in Fig.3.10(g-i). Comparing the loss obtained in the present study with the values reported for gold and silver [46,47], these semiconductor films promise to be good plasmonic materials in the near IR range, and the same can be prepared using low cost spin coating technique.

3.8 Summary

AZO, AIZO, IZO transparent conducting oxide films were prepared by cost effective spin coating for plasmonic applications in NIR region. By fixing total doping percentage to 3, doping ratios of aluminium and indium were varied for fabricating AIZO films. The films were annealed at 400°C or 450°C in air atmosphere followed by annealing at 300°C in reduced atmosphere. Films showed better electrical properties when annealed at 400°C and these films were considered for further studies. The films fabricated with particular ratio of aluminium and indium (A_3I_7) exhibited better electrical, structural, morphological properties as well as optical behaviour. This was further verified by XRD, which showed relatively higher stress and strain for the films A_1I_9 and A_5I_5. SEM image revealed wrinkle network structure for the co-doped films. Optical properties along with urbach energy calculations revealed variation in the bandgap of all films. Films with higher urbach energy had less bandgap due to the additional localized states created near the conduction band minimum. Finally, the films were sorted according to carrier concentration ($n=10^{20}/cm^3$) and investigated their plasmonic behaviour. The dielectric functions of the films were retrieved by fitting Drude-Lorentz oscillator model to the reflectance spectra. Plasma frequency calculated from reflectance-transmittance spectra showed direct dependence with crossover frequency extracted from fitting, and hence confirmed the plasmonic behaviour in the near IR range. The loss(ϵ_2) of these films were very low in the range from 1500nm to 2500nm compared with conventional metallic plasmonic materials. The studies revealed metal like behaviour with low loss for AZO, AIZO (A_3I_7),IZO films in the near infrared frequency region and the properties obtained were in consistent with those fabricated by vacuum routes such as sputtering, PLD etc.

References

[1] G. V. Naik, V. M. Shalaev, and A. Boltasseva, “Alternative plasmonic materials: beyond gold and silver,” *Adv. Mater.*, vol. 25, no. 24, pp. 3264–3294, 2013.

[2] J. Chang, W. Lin, and M.-H. Hon, “Effects of post-annealing on the structure and properties of al-doped zinc oxide films,” *Appl. Surf. Sci.*, vol. 183, no. 1-2, pp. 18–25, 2001.

[3] P. Nunes, E. Fortunato, and R. Martins, “Influence of the post-treatment on the properties of zno thin films,” *Thin Solid Films*, vol. 383, no. 1-2, pp. 277–280, 2001.

[4] B.-Y. Oh, M.-C. Jeong, D.-S. Kim, W. Lee, and J.-M. Myoung, “Post-annealing of al-doped zno films in hydrogen atmosphere,” *J. Cryst. Growth*, vol. 281, no. 2-4, pp. 475–480, 2005.

[5] J.-W. Jeon, D.-W. Jeon, T. Sahoo, M. Kim, J.-H. Baek, J. L. Hoffman, N. S. Kim, and I.-H. Lee, “Effect of annealing temperature on optical band-gap of amorphous indium zinc oxide film,” *J. Alloys*, vol. 509, no. 41, pp. 10062–10065, 2011.

[6] K. Yim and C. Lee, “Dependence of the electrical and optical properties of sputter-deposited zno: Ga films on the annealing temperature, time, and atmosphere,” *J. Mater. Sci. Mater. Electron.*, vol. 18, no. 4, pp. 385–390, 2007.

[7] M. Addonizio, A. Antonaia, G. Cantele, and C. Privato, “Transport mechanisms of rf sputtered al-doped zno films by h2 process gas dilution,” *Thin solid films*, vol. 349, no. 1-2, pp. 93–99, 1999.

[8] M. H. Habibi and M. K. Sardashti, “Effect of annealing temperatures and pre-heating on the characteristics of a nanocrystalline zno thin film prepared by the sol-gel dip-coating method,” *Zeitschrift für Naturforschung A*, vol. 63, no. 7-8, pp. 440–444, 2008.

[9] V. K. Jayaraman, A. M. Álvarez, Y. M. Kuwabara, Y. Koudriavstev, *et al.*, “Effect of co-doping concentration on structural, morphological, optical and electrical properties of aluminium and indium co-doped zno thin films deposited by ultrasonic spray pyrolysis,” *Mater. Sci. Semicond. Process.*, vol. 47, pp. 32–36, 2016.

[10] D. B. Potter, M. J. Powell, I. P. Parkin, and C. J. Carmalt, “Aluminium/gallium, indium/gallium, and aluminium/indium co-doped zno thin films deposited via aerosol assisted cvd,” *J. Mater. Chem. C*, vol. 6, no. 3, pp. 588–597, 2018.

[11] B. Onwona-Agyeman, M. Nakao, T. Kohno, D. Liyanage, K. Murakami, and T. Kitaoka, “Preparation and characterization of sputtered aluminum and gallium co-doped zno films as conductive substrates in dye-sensitized solar cells,” *Chem. Eng. Sci.*, vol. 219, pp. 273–277, 2013.

[12] S. Kirby and R. Van Dover, “Improved conductivity of zno through codoping with in and al,” *Thin Solid Films*, vol. 517, no. 6, pp. 1958–1960, 2009.

[13] S. Pati, P. Banerji, and S. Majumder, “Properties of indium doped nanocrystalline zno thin films and their enhanced gas sensing performance,” *RSC Adv.*, vol. 5, no. 75, pp. 61230–61238, 2015.

[14] M.-C. Jun, S.-U. Park, and J.-H. Koh, “Comparative studies of al-doped zno and ga-doped zno transparent conducting oxide thin films,” *Nanoscale Res. Lett.*, vol. 7, no. 1, pp. 1–6, 2012.

[15] S. Kim, G. Nam, H. Park, H. Yoon, S.-h. Lee, J. S. Kim, J. S. Kim, D. Y. Kim, S.-O. Kim, and J.-Y. Leem, "Effects of doping with al, ga, and in on structural and optical properties of zno nanorods grown by hydrothermal method," *Bull. Korean Chem. Soc.*, vol. 34, no. 4, pp. 1205–1211, 2013.

[16] S. Luo, J. Zou, H. Luo, J. Feng, and K. M. Ng, "Synthesis of highly dispersible izo and ito nanocrystals for the fabrication of transparent nanocomposites in uv-and near ir-blocking," *J. Nanoparticle Res. Interdiscip. Forum Nanoscale Sci. Technol.*, vol. 20, no. 4, pp. 1–12, 2018.

[17] L.-Q. Chen and Y. Gu, "Computational metallurgy," in *Physical Metallurgy*, pp. 2807–2835, Elsevier, 2014.

[18] A. M. Alsaad, A. A. Ahmad, Q. M. Al-Bataineh, A. A. Bani-Salameh, H. S. Abdullah, I. A. Qattan, Z. M. Albataineh, and A. D. Telfah, "Optical, structural, and crystal defects characterizations of dip synthesized (fe-ni) co-doped zno thin films," *Materials*, vol. 13, no. 7, p. 1737, 2020.

[19] H. Q. Le and S. J. Chua, "Gallium and indium co-doping of epitaxial zinc oxide thin films grown in water at 90 c," *J. Phys. D: Appl. Phys.*, vol. 44, no. 12, p. 125104, 2011.

[20] A. Nakrela, N. Benramdane, A. Bouzidi, Z. Kebbab, M. Medles, and C. Mathieu, "Site location of al-dopant in zno lattice by exploiting the structural and optical characterisation of zno: Al thin films," *Results Phys.*, vol. 6, pp. 133–138, 2016.

[21] N. Ashcroft and A. Denton, "Vegard's law," *Phys. Rev. A*, vol. 43, no. 6, pp. 3161–3164, 1991.

[22] E. Ş. Tüzemen, H. Kavak, and R. Esen, "Influence of oxygen pressure of zno/glass substrate produced by pulsed filtered cathodic vacuum arc deposition," *Phys. B: Condens. Matter*, vol. 390, no. 1-2, pp. 366–372, 2007.

[23] Y. Wang, S. P. Lau, H. Lee, S. F. Yu, B. Tay, X. Zhang, K. Tse, and H. Hng, “Comprehensive study of zno films prepared by filtered cathodic vacuum arc at room temperature,” *J. Appl. Phys.*, vol. 94, no. 3, pp. 1597–1604, 2003.

[24] G. H. Jo, S.-H. Kim, and J.-H. Koh, “Enhanced electrical and optical properties based on stress reduced graded structure of al-doped zno thin films,” *Ceram. Int.*, vol. 44, no. 1, pp. 735–741, 2018.

[25] M. A. Basyooni, M. Shaban, and A. M. El Sayed, “Enhanced gas sensing properties of spin-coated na-doped zno nanostructured films,” *Sci.Rep.*, vol. 7, no. 1, pp. 1–12, 2017.

[26] D. S. Bhachu, M. R. Waugh, K. Zeissler, W. R. Branford, and I. P. Parkin, “Textured fluorine-doped tin dioxide films formed by chemical vapour deposition,” *Chem.–Eur. J.*, vol. 17, no. 41, pp. 11613–11621, 2011.

[27] A. Singh, M. Kumar, R. Mehra, A. Wakahara, and A. Yoshida, “Al-doped zinc oxide (zno: Al) thin films by pulsed laser ablation.,” *J. Indian Inst. Sci.*, vol. 81, no. 5, p. 527, 2001.

[28] S. Major, A. Banerjee, and K. Chopra, “Electrical and optical transport in undoped and indium-doped zinc oxide films,” *J. Mater. Res.*, vol. 1, no. 2, pp. 300–310, 1986.

[29] C.-F. Yu, S.-H. Chen, S.-J. Sun, and H. Chou, “Influence of the grain boundary barrier height on the electrical properties of gallium doped zno thin films,” *Appl. Surf. Sci.*, vol. 257, no. 15, pp. 6498–6502, 2011.

[30] J. Lu, S. Fujita, T. Kawaharamura, H. Nishinaka, Y. Kamada, T. Ohshima, Z. Ye, Y. Zeng, Y. Zhang, L. Zhu, *et al.*, “Carrier concentration dependence of band gap shift in n-type zno: Al films,” *J. Appl. Phys.*, vol. 101, no. 8, p. 083705, 2007.

[31] K. J. Kim and Y. R. Park, “Large and abrupt optical band gap variation in in-doped zno,” *Appl. Phys. Lett.*, vol. 78, no. 4, pp. 475–477, 2001.

[32] A. P. Roth, J. B. Webb, and D. F. Williams, “Band-gap narrowing in heavily defect-doped zno,” *Phys. Rev. B*, vol. 25, no. 12, p. 7836, 1982.

[33] B. E. Sernelius, K.-F. Berggren, Z.-C. Jin, I. Hamberg, and C. G. Granqvist, “Band-gap tailoring of zno by means of heavy al doping,” *Phys. Rev. B*, vol. 37, no. 17, p. 10244, 1988.

[34] F. Anyaegbunam and C. Augustine, “A study of optical band gap and associated urbach energy tail of chemically deposited metal oxides binary thin films,” *Dig. J. Nanomater. Biostructures*, vol. 13, pp. 847–856, 2018.

[35] S. Schönau, F. Ruske, S. Neubert, and B. Rech, “Analysis of urbach-like absorption tails in thermally treated zno: Al thin films,” *Appl. Phys. Lett.*, vol. 103, no. 19, p. 192108, 2013.

[36] B. Pejova, “The urbach–martienssen absorption tails in the optical spectra of semiconducting variable-sized zinc selenide and cadmium selenide quantum dots in thin film form,” *Mater. Chem. Phys.*, vol. 119, no. 3, pp. 367–376, 2010.

[37] S. Edinger, N. Bansal, M. Bauch, R. Wibowo, R. Hamid, G. Trimmel, and T. Dimopoulos, “Comparison of chemical bath-deposited zno films doped with al, ga and in,” *J. Mater. Sci.*, vol. 52, no. 16, pp. 9410–9423, 2017.

[38] A. Pradhan, R. Mundle, K. Santiago, J. Skuza, B. Xiao, K. Song, M. Bahoura, R. Cheaito, and P. E. Hopkins, “Extreme tunability in aluminum doped zinc oxide plasmonic materials for near-infrared applications,” *Sci.Rep.*, vol. 4, no. 1, pp. 1–6, 2014.

[39] S. A. Maier, *Plasmonics: fundamentals and applications.* Springer Science & Business Media, 2007.

[40] R. Buonsanti, A. Llordes, S. Aloni, B. A. Helms, and D. J. Milliron, “Tunable infrared absorption and visible transparency of colloidal

aluminum-doped zinc oxide nanocrystals," *Nano lett.*, vol. 11, no. 11, pp. 4706–4710, 2011.

[41] S. Ghosh, M. Saha, and S. K. De, "Tunable surface plasmon resonance and enhanced electrical conductivity of in doped zno colloidal nanocrystals," *Nanoscale*, vol. 6, no. 12, pp. 7039–7051, 2014.

[42] A. Kuzmenko, "Kramers–kronig constrained variational analysis of optical spectra," *Review of scientific instruments*, vol. 76, no. 8, p. 083108, 2005.

[43] H. Berrezoug, A. Merad, M. Aillerie, and Z. S. Hassoun, "Ab-initio study of the structural, electronic and optical properties of zno co-doped gallium aluminum zn1- x- ygaxalyo," *Mater. Res. Express*, vol. 6, no. 6, p. 065909, 2019.

[44] G. V. Naik, J. Kim, and A. Boltasseva, "Oxides and nitrides as alternative plasmonic materials in the optical range," *Opt. Mater. Express*, vol. 1, no. 6, pp. 1090–1099, 2011.

[45] M. Noginov, L. Gu, J. Livenere, G. Zhu, A. Pradhan, R. Mundle, M. Bahoura, Y. A. Barnakov, and V. Podolskiy, "Transparent conductive oxides: Plasmonic materials for telecom wavelengths," *Appl. Phys. Lett.*, vol. 99, no. 2, p. 021101, 2011.

[46] J.-Y. Lin, K.-D. Zhong, and P.-T. Lee, "Plasmonic behaviors of metallic azo thin film and azo nanodisk array," *Opt. Express*, vol. 24, no. 5, pp. 5125–5135, 2016.

[47] G. V. Naik, J. L. Schroeder, X. Ni, A. V. Kildishev, T. D. Sands, and A. Boltasseva, "Titanium nitride as a plasmonic material for visible and near-infrared wavelengths," *Opt. Mater. Express*, vol. 2, no. 4, pp. 478–489, 2012.

Chapter 4

Investigation of plasmonic property in Spray coated co-doped ZnO thin films

4.1 Overview

This chapter investigates the plasmonic properties in Al and In co-doped ZnO thin films fabricated by spray coating technique. In spray coating, simultaneous temperature treatment while spraying solution on substrate will lead to formation of uniform and crystalline films compared with film coated by spin coating technique. In this work, water was used as solvent for preparing solution for coating Al and In doped and (Al/In) co-doped zinc oxide thin films. The effect of Al/In dopant ratio on the structural, electrical, optical and plasmonic properties of spray coated films were investigated. Structural properties were studied by x-ray diffraction. Electrical properties were investigated at 300K using a Hall measurement system. The elemental studies were done using the XPS. The electron charge correction was calibrated using 284.6 eV as reference. A micro-Raman spectrometer in the backscattering geometry with laser excitation of 532nm was used for investigating vibrational properties of the films. Scanning electron microscope was used for surface morphological studies. Ultraviolet-visible-NIR (UV-Vis-NIR) reflectance spectra were recorded in the range 400-2200nm using a spectrophotometer. Photoluminescence (PL) experiments were performed using Xe lamp with an excitation wavelength of 320nm. Extraction of dielectric functions of the films were done using RefFIT software as described in chapter 3 (section 3.7.3). Winspall software based on Fresnel equation developed at the Max-Plank-Institute Germany, is used for SPR simulation studies.

4.2 Sample preparation

4.2.1 Preparation of Al and In doped/co-doped ZnO solution

The $Al_xIn_yZn_{1-x-y}O$ films with x = 0, 0.0225, 0.015, 0.0075, 0.03 were deposited on 3× 1cm soda lime glass substrates by using a custom fabricated spray coating system, keeping the overall In and Al concentrations (x+y) equal to 3mol%. The films were named according to the Al:In doping ratio, that is A_0I_{10}, $A_{2.5}I_{7.5}$, A_5I_5, $A_{7.5}I_{2.5}$, $A_{10}I_0$. The precursor solution was prepared by dissolving 0.29g zinc acetate dehydrate ($Zn(CH_3COO)_2.2H_2O$, Merck) in double distilled water added with few ml of acetic acid (CH_3COOH). The acid stabilized the solution and also prevented the precipitation of zinc hydroxide ($Zn(OH)_2$). A dopant of 0.009M (Al/In or Al and In, with an overall concentration of 0.009M) was added to the solution, so that 3 mol% doping was achieved. The raw materials for dopants were aluminium nitrate ($Al(NO_3)_3$; Merck and indium (III) acetate ($In(C_2H_3O_2)_3$; AlfaAesar. All the chemicals used were of analytical grade. The resulting solution was stirred with a magnetic stirrer at room temperature for 30 min. Prior to the deposition, the substrates were cleaned as described in chapter 3; section 3.2.2.

4.2.2 Thin film preparation using spray coater

The nitrogen was used as a carrier gas for spray coating, and it was allowed to pass through the spray gun along with the solution at a flow rate of 1.5 ml/min. The substrate was kept at a temperature of 450°C throughout the coating, and the nozzle to substrate distance used was 18cm. The coated films were finally annealed in the reduced atmosphere with N_2+ H_2 gas in the ratio 95:5 for 30min at 400°C to improve the carrier concentration. The flow chart for thin film preparation using spray coater is shown in Fig.4.1.

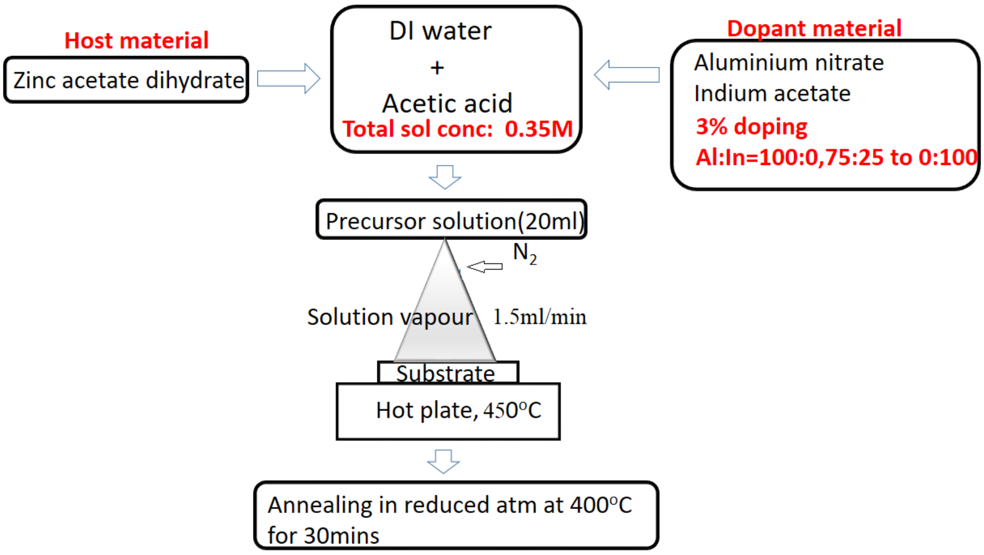

Figure 4.1: Flow chart for thin film deposition using spray coater

4.3 Structural properties

The structural studies were carried out by employing the Rietveld refinement technique[1, 2] using the XRD data with the help of General Structure Analysis System (GSAS) software, using $P6_3mc$ space group. The XRD pattern along with the Rietveld refined data are shown in Fig.4.2. As seen in the figure, the observed and calculated profiles are closely matched for all films. It was also observed that the peaks were corresponding to the Bragg 2θ positions for $P6_3mc$ space group (ICDD pdf #36-1451). Parameters such as atom position (u), lattice parameter, scale factors and shape parameters were considered as free parameters during fitting. Quality of the fitted experimental data was assessed by computing the goodness of fit (χ^2) and profile factor (R_P). The c-axis oriented growth of ZnO film seen in Fig.4.2. has no significant change when doped with Al; however, changes in orientation was observed with further increase in the concentration of In from 25 to 100%. The lattice constants of doped as well as co-doped ZnO films showed a small deviation with respect to undoped ZnO film as seen in Table.4.1. According to the Vegard's law, change in lattice constants(represented as Δa and Δc) due to doping is mainly because of different ionic radii of the host and dopant materials[4]. In addition, it also indicates the substitution of dopants in the host lattice. The decrease in the value of lattice constants of $A_{10}I_0$ may be because of the substitution of Al in the Zn lattice, while the increase in lattice constant may be due to doping with In (A_0I_{10}). As mentioned in section 3.4 of chapter 3, the ionic radius of Al is less (0.057nm) and In is more (0.080nm) compared to the ionic radius of the host Zn (0.074nm) atom.

Table 4.1: Lattice constants extracted from Rietveld refinement using XRD data

Sample	χ^2	Lattice constants(A^0) a=b	c	Δa (A^0)	Δc
ZnO	1.308	3.250	5.205		
$A_{10}I_0$	1.456	3.249	5.204	0.001	0.001
$A_{7.5}I_{2.5}$	1.321	3.251	5.204	0.001	0.001
A_5I_5	1.997	3.255	5.206	0.005	0.001
$A_{2.5}I_{7.5}$	1.451	3.256	5.204	0.006	0.001
A_0I_{10}	1.479	3.258	5.216	0.008	0.011

The unit cell volume obtained after the refinement, and the Zn-O bond length calculated from refined data are listed in Table.4.2. The average crystallite size (D) and strain calculated using the Williamson-Hall method[3] are also tabulated Table.4.2. The bond length along c-axis is calculated by finding u×c (extracted from Rietveld refinement), where u is the relative shift of the anionic sub-lattice with respect to the cationic sub-lattice in the z direction and c is the lattice parameter. In the other direction, the bond length is defined as $\frac{a^2}{3} + (\frac{1}{2} - u)^2c^2$ [1].

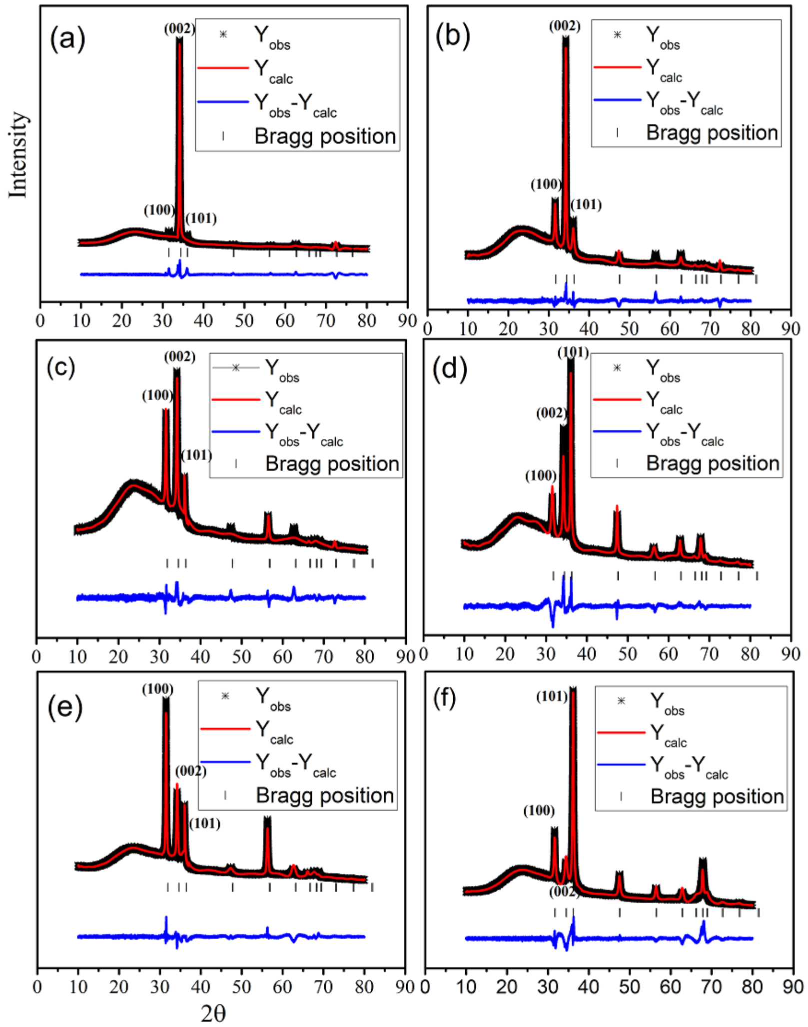

Figure 4.2: Rietveld refinement of XRD data of (a)ZnO, (b)$A_{10}I_0$, (c)$A_{7.5}I_{2.5}$, (d)A_5I_5, (e)$A_{2.5}I_{7.5}$ and (f)A_0I_{10}.The black curves represent experimental data, the red line is the calculated fit, vertical lines are the positions of refined phase reflections and the blue line is the difference line between experimental and fitted data.

The increased deviation observed in the case of In doped ZnO may be because of the more number of substituted In ion in Zn site. For co-doped films, a large shift was observed for the lattice parameter ‘a’ and its value was found to increase with In concentration indicating that In was more favoured to substitute for Zn in ZnO lattice. In addition, cell volume was also found to increase when In is introduced in the lattice and this can be understood using the equation $V = 0.866a^2c$ for the hexagonal system[5]. It could be easily seen that noticeable bond length change was observed for A_0I_{10}, which was increased from 1.972 to 1.982 when doped with In. The equal bond length along and perpendicular to 'c' axis also confirm the symmetric structure of A_0I_{10} film. Moreover, change in 'u' value compared with undoped ZnO is observed only after the Al:In ratio of 2.5:7.5. The change beyond a specific Al:In ratio confirms the presence of active dopants in the Zn site. The crystallite size is observed to decrease from 38nm to 23nm when In is used as dopant or co-dopant in the ZnO film. However, the crystallite size for $A_{10}I_0$ was found to increase because of Al dopants.

Table 4.2: Structural parameters of doped and co-doped ZnO thin films, estimated from XRD data

Sample	Cell volume	Bond length		u	D(nm)	Strain
	47.61	along c	⊥ to c		± 1nm	$\times 10^{-3}$
		1.972	1.979	0.379		
ZnO	47.611	1.972	1.979	0.379	38	1.24
$A_{10}I_0$	47.573	1.972	1.979	0.379	48	1.64
$A_{7.5}I_{2.5}$	47.630	1.973	1.978	0.380	24	0.51
A_5I_5	47.766	1.978	1.980	0.380	24	0.59
$A_{2.5}I_{7.5}$	47.778	1.978	1.980	0.380	25	0.44
A_0I_{10}	47.946	1.982	1.982	0.380	23	0.47

4.4 Morphological studies

Microscopic images from scanning electron microscopy were utilized to analyse the crystal morphology of the films.

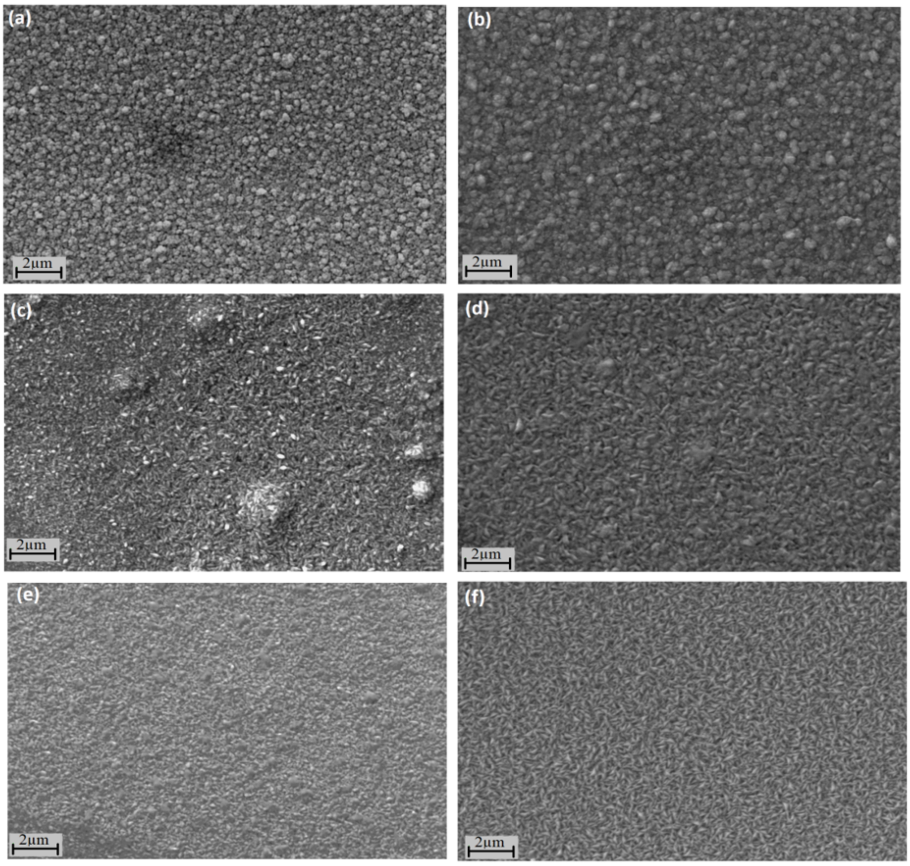

Figure 4.3: SEM images of the films; (a)ZnO, (b)$A_{10}I_0$, (c)$A_{7.5}I_{2.5}$, (d)A_5I_5, (e)$A_{2.5}I_{7.5}$ and (f)A_0I_{10}

Granular like structures of the films of ZnO and $A_{10}I_0$ were found to change to platelet like structures with the addition of indium, as seen in Fig.4.3. Edinger et al[6] reported a similar structure for water-based deposited In doped ZnO films. A dense clump of crystallites in $A_{7.5}I_{2.5}$ and A_5I_5 films as shown in Fig.4.3.c may be because of the remaining Al atoms, which are not substituted in the lattice showing a change in $A_{2.5}I_{7.5}$, where Al concentration is minimum. The unsubstituted Al atoms might have converted to Al_2O_3, which would deteriorate the electrical properties[7] as discussed in the next section. The surface of A_0I_{10} film is uniform and dense with average grain length of 150 nm. The relatively uniform smooth morphology of $A_{2.5}I_{7.5}$

and A_5I_5 indicates that when dopants with different ionic radii interact with the ZnO lattice, In ion, having ionic radius relatively close to Zn is more preferred.

4.5 Electrical Properties

The effect of structural deviation on the electrical properties of the films were studied in detail. Table.4.3 illustrates the summary of carrier concentration, mobility and resistivity with respect to the Al:In ratio, measured using hall effect, before (BH) and after (AH) H_2 annealing. The role of intrinsic defects and extrinsic dopants in enhancing the electrical properties of the films were analysed from the data given in Table 4.3. Before annealing in reduced atmosphere, the substitution of external dopants resulted in increasing the free carriers in ZnO, in addition to the contribution from intrinsic defects. The external dopants substitute trivalent atom in place of a divalent atom, which results in one extra free electron[8, 9]. After annealing in the reduced atmosphere, the electrical properties of all films are improved further, mainly because of the creation of more oxygen vacancies[8, 9]. The analysis on the effect of dopants in the electrical behaviour of the films revealed an increased carrier concentration and increased mobility in the order $A_{10}I_0$, $A_{7.5}I_{2.5}$, A_5I_5, $A_{2.5}I_{7.5}$ and A_0I_{10}. This shows that In is more substituted than Al in the Zn site. If the Al atoms were not substituted in the Zn site, then there were chances of forming Al_2O_3, which would result in increasing the resistivity of the films[7, 10]. According to Karaagac et al[10], the dopants that are not substituted can act as interstitials in the lattice or may form agglomerates at grain boundaries as trapping or scattering sites, leading to an increase in the resistivity. The small free carrier density and mobility exhibited by Al doped and co-doped ZnO films and the increasing trend with decreasing Al content show that the Al atoms are not completely substituted in the Zn sites.

For doped materials, the energy needed to activate a dopant is defined as the activation energy E_a and the dopants resulted in large carrier density of host lattice will have minimum E_a. The increase in carrier density and mobility with increase in the concentration of In indicate that this ion is the most activated dopant in comparison with Al[11], which, in turn, shows that the energy needed to activate In dopant is less compared to the Al dopants. To get more clarification, these samples are considered for elemental analysis using XPS and to further clarify the free electron density fano resonance fitting of Raman mode(A_1(LO)) of these films are also studied.

Table 4.3: Carrrier concentration and mobility before and after hydrogen annealing

	Carrier concentration $\times 10^{20}/cm^3$		Mobility cm^2/Vs	
	BH	AH	BH	AH
ZnO	0.003	0.057	0.33	1.011
$A_{10}I_0$	0.099	0.37	0.59	3.62
$A_{7.5}I_{2.5}$	0.12	0.812	0.624	5.42
A_5I_5	0.721	3.211	0.934	9.46
$A_{2.5}I_{7.5}$	0.851	6.23	1.69	11.7
A_0I_{10}	0.997	8.921	2.36	13.7

4.6 Elemental composition studies

4.6.1 XPS peak study of host elements(Zn and O)

Fig.4.4 shows the XPS spectra of Zn $2p_{3/2}$, Zn $2p_{1/2}$ of doped and co-doped ZnO films, and the corresponding binding energy peaks are tabulated in Table.4.4. The Zn 2p doublet peak of ZnO film is usually observed at 1021.3 ±0.1 eV and 1044.5± 0.1eV respectively for Zn $2p_{3/2}$ and Zn $2p_{1/2}$ [12]. In this study, the Zn $2p_{3/2}$ peak is symmetric, and binding energy observed is less than that of bulk ZnO (1022.4eV) [12]. This indicates that most of the Zn is in the oxygen-deficient Zn^{2+} valence state in the lattice[12–14]. Islam et al studied the effect of dopants in the shifting of the binding energy of Zn 2p peaks[14]. According to them, increasing the dopant concentration in the film results in shifting of binding energy to higher energy. Park et al observed similar behaviour in indium and gallium doped ZnO nanorods[15]. The shift was explained based on the electro-negativity (χ) of Zn (χ=1.65), In (χ=1.78) and Ga (χ =1.81). The higher electro-negativity of In or Ga than Zn results in lower valence electron density of 'Zn' in Zn-O-In or Zn-O-Ga than in Zn-O-Zn. This results in weakening the screening effect of Zn and the consequent increase of the binding energy of Zn 2p for doped samples[15,16]. In the present work, the dopants have larger (In) and smaller (Al, χ=1.61) electronegativities than that of Zn, and hence a different effect on the binding energy can be expected. The difference in electronegativity of atoms with ionicity was explained by Wang et al[17]. According to them, the greater the difference in electronegativity of two atoms, the stronger will be the polar bond. Also, the atom having more electronegativity will position at the negative pole.

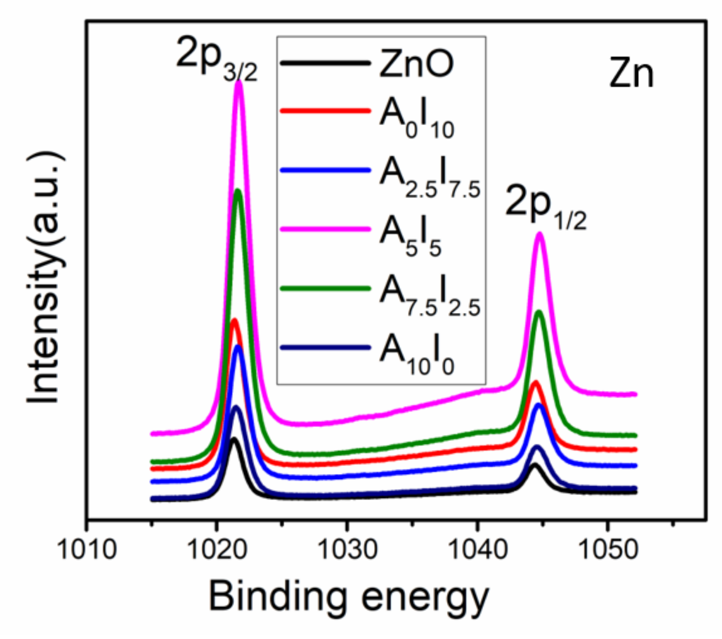

Figure 4.4: XPS spectra of Zn 2p doublet consisting of higher binding energy $2p_{1/2}$ and lower binding energy $2p_{3/2}$

In this work, the electronegativity difference between Zn-O, In-O, Al-O are 1.79, 1.66 and 1.83 respectively. The high bond polarity between Al-O indicates more ionicity between these atoms [17]. In addition to this, compounds with a higher level of ionicity can significantly lower their energies by increasing the coordination number. Hence a redshift in binding energy can be expected for aluminium doped film compared to films with other dopants like In or Ga. In the case of the co-doped films, the binding energy seems larger than that of the doped Al/In thin films. This indicates that other factors also need to be considered along with the electronegativity of dopants. One factor may be the presence of more zinc ions bonded to oxygen, which reflects the lack of oxygen deficiency in these films[12]. The binding energy of oxygen-deficient Zn is lower than that of the bulk ZnO[12]. Hence, the high binding energies of the films $A_{2.5}I_{7.5}$, A_5I_5, and $A_{7.5}I_{2.5}$ show less chance for defect-related improvement in the electrical properties of these films. The study on structural and electrical properties of Al/In doped and co-doped ZnO films showed that indium was more favoured to substitute in ZnO lattice than Al. The better electrical properties obtained were in accordance with the increase in the relative concentration of indium in the co-doping. The dependence of the crystallite size and the significant difference in the intensity of the peaks were also analysed. The relative intensity of the undoped ZnO film was less compared with the doped/co-doped films. As seen in the figure, the Zn peaks of A_5I_5 are more intense than those of ZnO. For smaller crystallites, the number of activated ions at the surface increases and thus results in high intensity. The average crystallite size of the undoped ZnO film decreased when we added the co-dopants were previously calculated using the William-son hall equation. Moreover, all the films possessed smaller grain size compared with ZnO, and hence resulted in high intensity than Zn peaks.

Table 4.4: Peak position of Zn 2p from the XPS spectra.

Sample	Zn $2p_{3/2}$	Zn $2p_{1/2}$
	1021.3 ± 0.1	1044.5 ± 0.1
ZnO	1021.3	1044.4
A_0I_{10}	1021.5	1044.6
$A_{2.5}I_{7.5}$	1021.6	1044.7
A_5I_5	1021.7	1044.8
$A_{7.5}I_{2.5}$	1021.7	1044.8
$A_{10}I_0$	1021.2	1044.6

Fig.4.5. shows the Gaussian-Lorentz fitting and deconvoluted peak assignment of the O 1s spectra of samples. Generally, the asymmetric peaks of oxygen are deconvoluted into three peaks as; O_1 oxygen combined with cations in a stoichiometric oxidation state with low binding energy. The O_2, the medium binding energy ascribed for O^{2-} ions bonded to nonstoichiometric oxidized cations. i.e., for those cations having their oxidation state less than that of their chemical formula. These cations are responsible for maintaining the charge balance in the structure. Thus, O_2 corresponds to oxygen in the oxygen-deficient region and can be used for indirect measurement for the oxygen vacancies. The O_3 peaks with relatively high binding energy represent the specific chemisorbed oxygen, such as in H_2O and CO_3[18]. The binding energy of O_1, O_2 and O_3 peaks at 530.5, 531.5 and 532.4 (as seen in Fig.4.5) respectively are compared with the reported values shows that there was no such noticeable deviation[18]. The difference in the area of the O_1 O_2 and O_3 peaks (Fig.4.6) showed that O_1 peak is relatively more intense than O_2 and O_3 peaks. This confirmed the presence of more stoichiometric Zn-O bonds compared with vacant or chemisorbed oxygen. The second dominant peak was O_2 which quantifies the oxygen vacancies in these films[8,15,19–22].

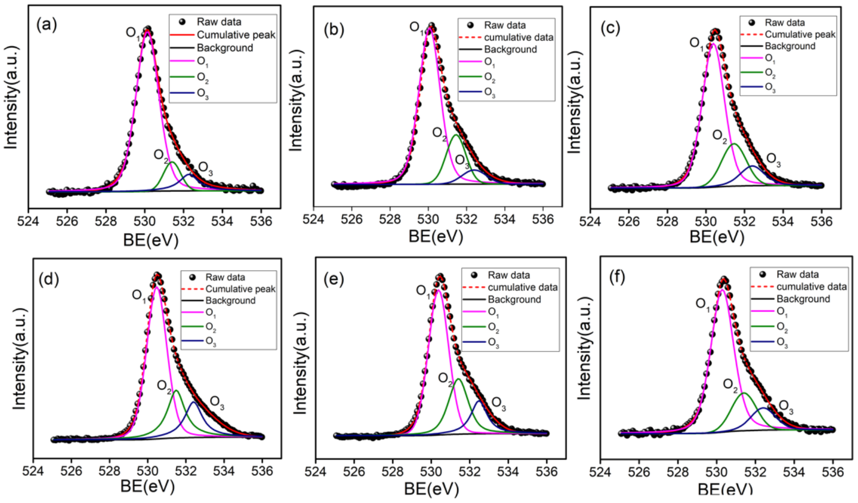

Figure 4.5: Asymmetric O1s peak deconvoluted to O_1, O_2, O_3 of (a)ZnO, (b)A_0I_{10}, (c)$A_{2.5}I_{7.5}$, (d)A_5I_5, (e)$A_{7.5}I_{2.5}$ and (f)$A_{10}I_0$

A relatively higher O_2 peak area was observed for co-doped ZnO, but it is observable in other peaks such as O_1 and O_3 as well. We have also observed that due to small crystallite size of co-doped ZnO films, a relatively higher intensity than Zn was observed. This crystallite size difference also may result in increasing intensity of O peaks in these film. Thus a relatively high peak area was observed for A_0I_{10}, $A_{2.5}I_{7.5}$, A_5I_5, $A_{7.5}I_{2.5}$. Thus the quantification of the oxygen vacancies in the films were calculated using the ratio of peak area of O_2 to O_{total}. And the obtained values respectively for ZnO, A_0I_{10}, $A_{2.5}I_{7.5}$, A_5I_5, $A_{7.5}I_{2.5}$, $A_{10}I_0$, are 0.1, 0.2, 0.2, 0.2, 0.2 and 0.2. This shows that the oxygen vacancies created during the post-deposition heat treatment in the reduced atmosphere of all films are same.

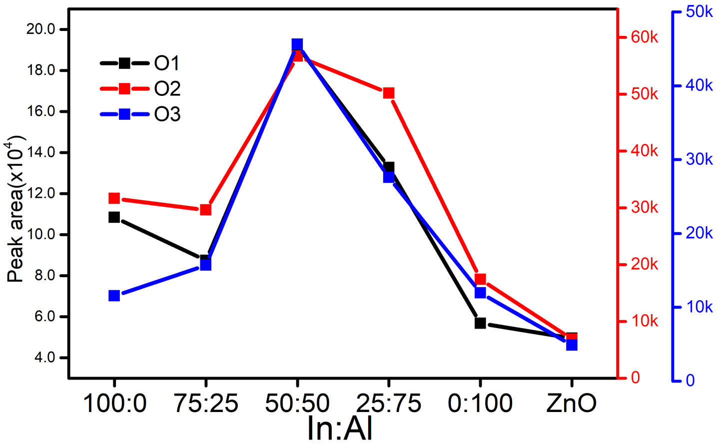

Figure 4.6: Variation of O_1, O_2 and O_3 peak area with co-doping ratio of ZnO thin films

4.6.2 XPS peak study of dopants (In and Al)

The contribution of the dopant concentration to electrical properties was investigated in detail as follows.

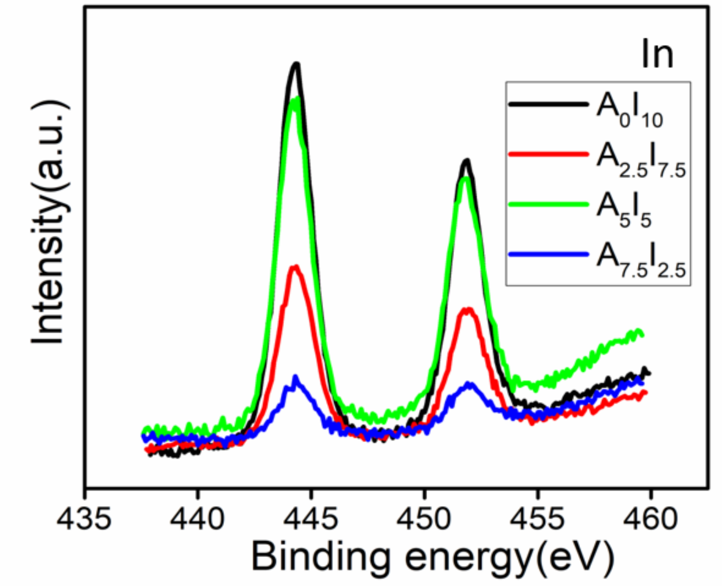

Figure 4.7: In 3d doublet peaks of XPS spectra consisting of higher energy $3d_{3/2}$ and lower energy $3d_{5/2}$

Fig.4.7 shows the In 3d spectra of the samples. The peak positions are listed in Table.4.5. The variation of the intensity of In 3d peaks with the quantity of indium in the sample can be seen in the figure. A relatively higher intensity is observed for the film A_0I_{10}, which decreases for the films $A_{2.5}I_{7.5}$, A_5I_5 and $A_{7.5}I_{2.5}$, with respect to the indium concentration. On the other hand no obvious shift is observed for the binding energy with indium concentration, as seen in the figure.

Fig.4.8. shows the Al 2p peaks and peak positions are tabulated in Table.4.5 and are observed only for the films $A_{10}I_0$, $A_{7.5}I_{2.5}$, and A_5I_5; the peaks could not be resolved for the film $A_{2.5}I_{7.5}$. Moreover the resolved XPS peaks of aluminium compared with indium again showed that Al substitution was minimum in ZnO lattice. The electrical analysis also showed the incorporation of more In^{3+} in the Zn site than Al^{3+} in the these films. This may be due to the agglomeration of crystallites in the Al doped ZnO films. The morphological analysis using SEM also confirmed the presence of clusters in Al doped films.

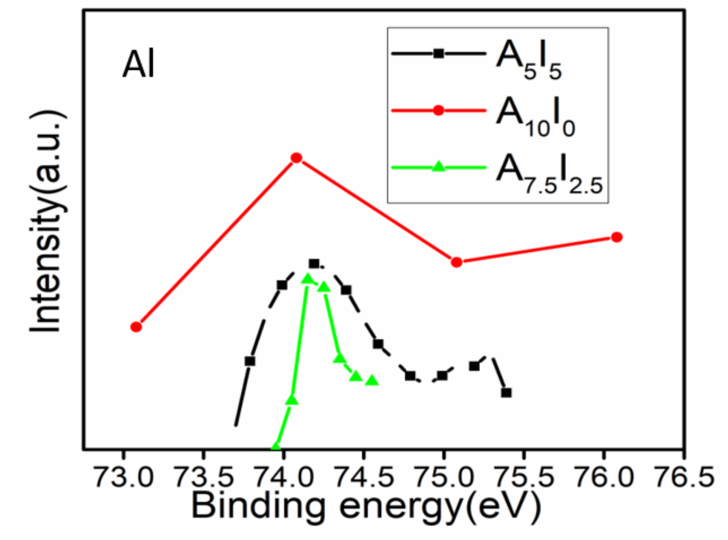

Figure 4.8: XPS spectra of Al 2p peaks

Table 4.5: Peak positions of In 3d and Al 2p from the XPS spectra.

Sample	A_0I_{10}	$A_{2.5}I_{7.5}$	A_5I_5	$A_{7.5}I_{2.5}$	$A_{10}I_0$
In $3d_{5/2}$	444.3	444.4	444.4	444.3	-
In $3d_{3/2}$	452.0	452.0	452.4	452.4	-
Al $2p_{3/2}$	-	-	74.0	74.2	74.2

For the quantitative analysis of the presence of indium, aluminium, zinc and oxygen in the surface of the film, elemental composition analysis was carried out using XPS Peak FIT using the peak area. Table.4.6. gives a summary of the surface chemical composition of Zn and the dopants in the films. The oxygen concentration was found to be less than that of Zn indicating that oxygen vacancies are formed during the annealing in reduced atmosphere. Moreover the higher concentration of the dopant In compared to Al can also understand from Table.4.6.

Table 4.6: Elemental percentage composition of Zn, O, In and Al extracted using XPS PEAKFIT software

Sample	Zn(%)	O(%)	In(%)	Al(%)
$A_{10}I_0$	84.1	15.6		0.2
$A_{7.5}I_{2.5}$	84.0	15.7	0.2	0.1
A_5I_5	80.8	16.5	2.58	0.2
$A_{2.5}I_{7.5}$	80.24	16.02	3.72	
A_0I_{10}	75.18	17.22	7.58	

4.7 Raman studies

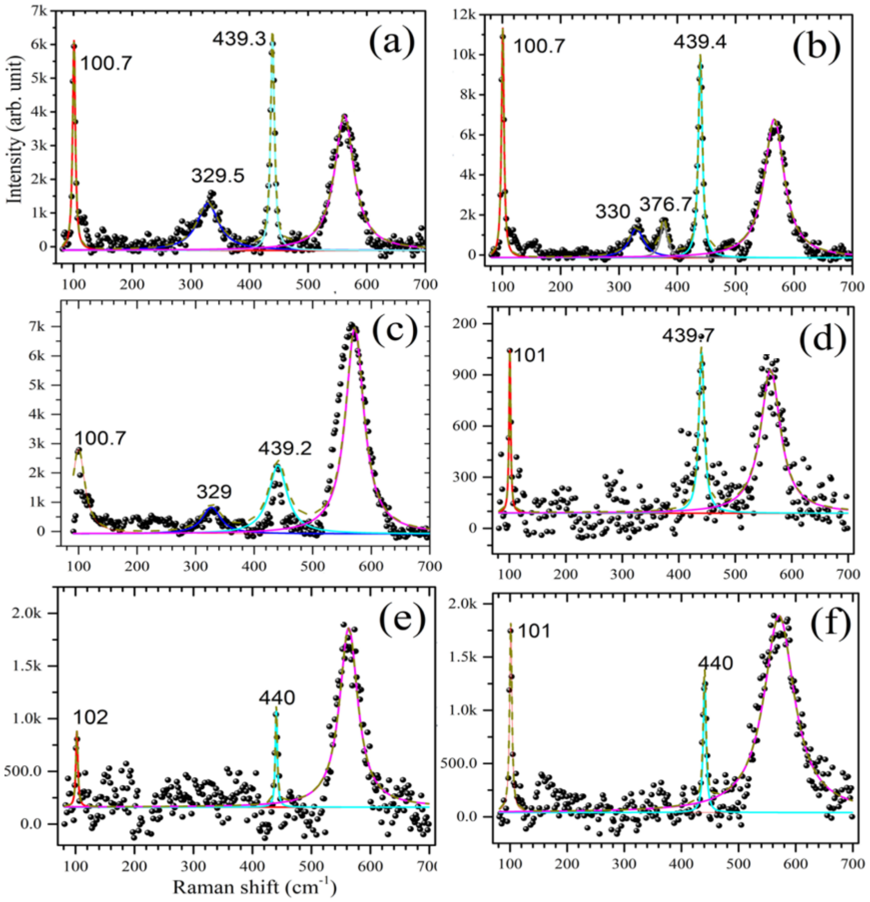

Figure 4.9: Raman spectra of the films(a)ZnO, (b)$A_{10}I_0$, (c)$A_{7.5}I_{2.5}$, (d)A_5I_5, (e)$A_{2.5}I_{7.5}$ and (f)A_0I_{10}

Raman spectroscopy was used to further analyse the structural properties and to correlate the free carrier density of films obtained in hall measurement with the fano fitting of Raman mode. The Fig.4.9. shows the Raman spectra of undoped ZnO, Al doped ZnO($A_{10}I_0$), Al-In co-doped ZnO ($A_{7.5}I_{2.5}$, A_5I_5, $A_{2.5}I_{7.5}$) and In doped ZnO(A_0I_{10}). ZnO shows hexagonal wurtzite structure belonging to the space group C^4_{6V} and group theory predicts modes such as E_2(low), E_2(high), A_1(TO), A_1(LO), E_1(TO) and E_1(LO) in ZnO.

The non-polar E_2(low) and E_2(high) modes near to 101 cm^{-1} and 440 cm^{-1}, correspond to symmetry allowed modes of wurtzite ZnO with minimum electronic contribution and as seen in the figure these peaks are more intense compared to the other modes. Ghimbeu et al[23] reported that the intense E_2 modes represent high crystallinity of the films. The small shift observed in the positions of these peaks when doped is negligible. The frequency at 330 cm^{-1} originates from the overtone phonon (E_2(high)-E_2(low)) and is not clearly observed for the films $A_{7.5}I_{2.5}$, $A_{2.5}I_{7.5}$ and A_0I_{10}.

The peak at 380 cm^{-1} is A_1(TO) mode and was observed only for the film $A_{10}I_0$. The peak position of A_1(LO) mode in doped ZnO is observed to be different from that of the undoped ZnO. A gradual (up to 10 cm^{-1}) increment towards high frequency side along with asymmetric broadening was observed when Al:In doping ratio changed from 10:0 to 0:10. For heavily doped n-type materials ($10^{20}/cm^3$), there are chances for Raman active inter-conduction-band transitions, which interfere with the zone centre optical phonon to produce fano-type asymmetric phonon line shape due to discrete-continuum interaction[24]. The fanoline shape function is given as

$$I = A\frac{(q-\epsilon)^2}{(1+\epsilon^2)} \tag{4.1}$$

where $\epsilon = \frac{\omega-\omega_o}{\gamma}$, A is amplitude, ω_o is the phonon frequency, q is the asymmetric parameter and γ is the half width parameter.

The possibilities of fano-fitting of the asymmetric broadened A_1(LO) peak of doped films is explored as shown in Fig.4.10 and the fitting is compared with the line shape of the Lorentz fitted ZnO film. The A_1(LO) mode of ZnO fitted well to Lorentz function, as seen in Fig.4.10a. On the other hand, the fano fit was also not satisfactory for $A_{10}I_0$ and $A_{7.5}I_{2.5}$. It may be because of relatively low carrier density and asymmetric line shape in these films. At the same time, the films A_5I_5, $A_{2.5}I_{7.5}$ and A_0I_{10} having carrier density ($10^{20}/cm^3$) exhibited a better fitting with fano line shape than the Lorentz line shape function. This shows that the Raman analysis of these films were in consistent with the hall measurement described before.

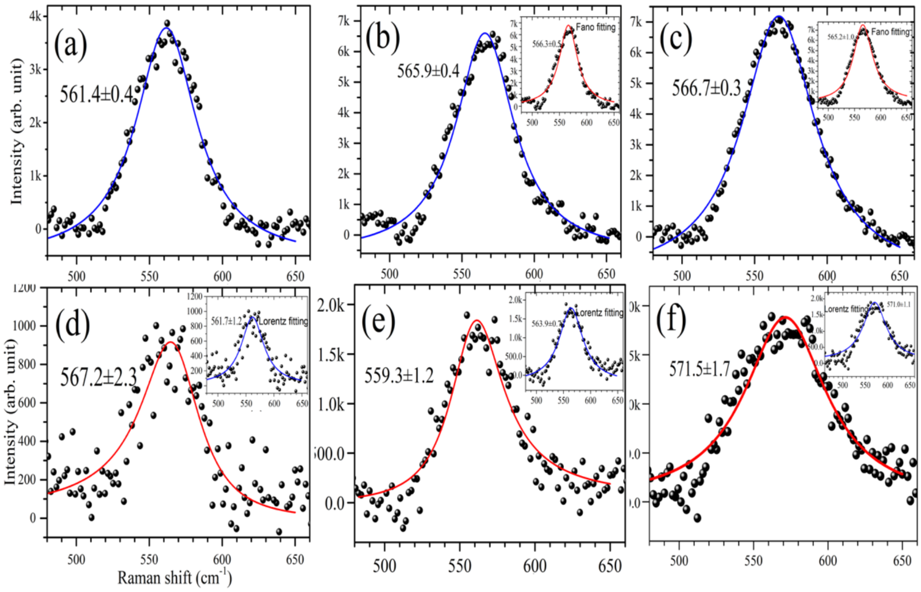

Figure 4.10: Lorentz fitting of the films (a)ZnO, (b)$A_{10}I_0$, (c)$A_{7.5}I_{2.5}$ and Fano fitting of (d)A_5I_5, (e)$A_{2.5}I_{7.5}$ and (f)A_0I_{10}. Inset figures of (b), and (c) show the Fano fitting and (d-f) show the Lorentz fitting of the films

4.8 Optical properties

4.8.1 Photoluminescence (PL) studies

PL spectra have been used to elucidate the band structure of these thin films upon variation in doping ratio. Fig.4.11 depicts the PL spectra of the doped and co-doped films. ZnO exhibits two emission bands; one is UV emission, dominated by recombination of bound and free excitons and their LO (longitudinal optical) phonon replicas, and the other one is in visible region[25–30]. The figure shows the UV emission peak corresponding to near band edge (NBE) emission at 380nm and blue emission near to 400nm. According to Cao et al[31] the emission near to 400 nm is due to exciton recombination between the interstitial Zn atom (shallow donor level) and the valence band. Both peaks exhibited small red-shift with increase in the number of free electrons.

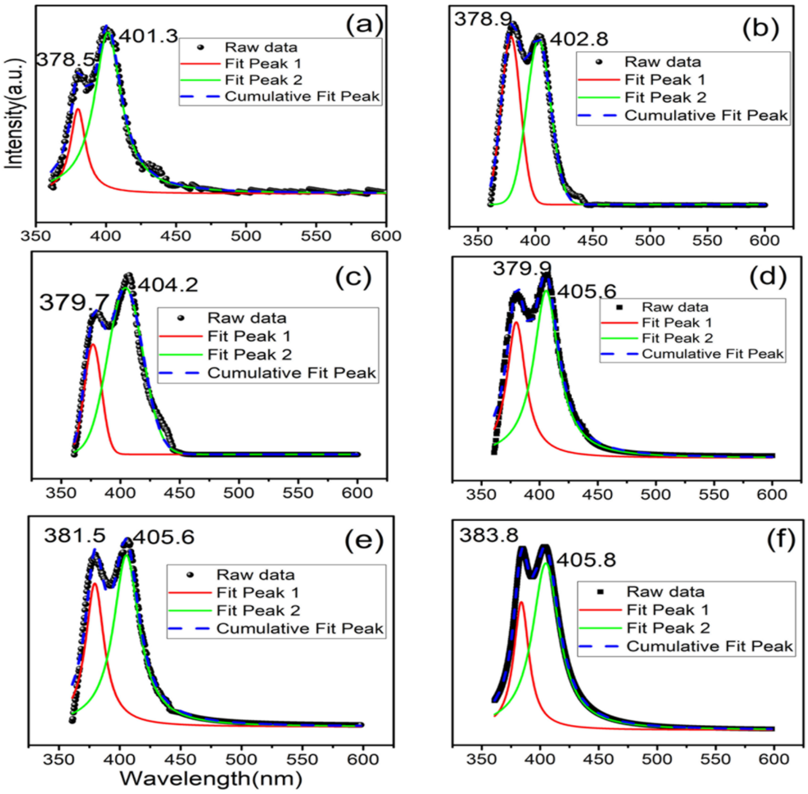

Figure 4.11: PL peaks of the films for the excitation wavelength of 320 nm;(a)ZnO, (b)$A_{10}I_0$, (c)$A_{7.5}I_{2.5}$, (d)A_5I_5, (e)$A_{2.5}I_{7.5}$ and (f)A_0I_{10}

In the absence of the donor atoms, these vacancy sites will attribute to non-radiative transitions, where the trap recombination rate is proportional to the number of traps (N_T) and holes (p). If N_T is the same for all films, radiative transition enhances with an increase in free electron concentration[27, 28]. The absence of visible emissions decreases the possibility of transitions at lower energies[27, 29]. Makino et al.[27] observed shift and change in the intensity of the NBE peak with a change in carrier density in Ga doped ZnO. If the thin films have oxygen or Zn vacancies, the defects trap electrons result in two types of defect donor levels, at 0.2-0.3 eV and 0.7-0.8 eV below the conduction band minimum. The former is called shallow donor level and the latter is the deep acceptor level[30, 32]. There are several reports on the emissions at a deep level, such as green luminescence, but its nature is not well understood yet[33, 34]. The PL analysis confirmed the absence of deep emissions and indicates that there are less likely chances of transitions within the bandgap when the material interacts with light for plasmonic applications.

4.8.2 Urbach energy calculation

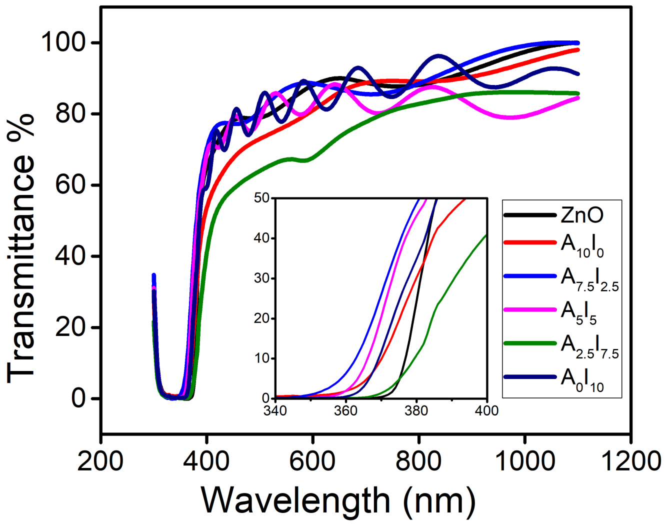

Figure 4.12: Optical transmittance spectra; inset shows the urbach tail below bandgap energy

Fig 4.12 shows the transmittance spectra of ZnO, $A_{10}I_0$, $A_{7.5}I_{2.5}$, A_5I_5, $A_{2.5}I_{7.5}$, and A_0I_{10} films in the visible region. The difference in the average transmittance of the films can be attribute to the optical absorption due to the formation of localized states near the conduction band minimum. Thus resulted in a tail for transmission spectra below 400nm defined as urbach tail[35–37]. This was discussed detail in chapter 3; section 3.6.2.

Table 4.7: Fitting parameters of ln $(\alpha) = b_0+(\mathrm{h}\nu)b_1$ together with R^2 value of linear regression analysis.(Recriprocal of b_1 is E_u)

Sample	b_0	b_1	E_u	R^2
ZnO	8.27	0.97	1.03	0.54
$A_{10}I_0$	7.25	1.27	0.79	0.51
A_1I_9	5.70	1.66	0.60	0.53
A_3I_7	6.38	1.48	0.68	0.52
A_5I_5	8.34	1.04	0.96	0.54
A_0I_{10}	7.40	1.201	0.83	0.52

Considering the equation (3.9) in chapter 3 and using the linear least square fit of the experimental absorption data, $\mathrm{E_u}$ was calculated and is tabulated in Table.4.7. The change in $\mathrm{E_u}$ was in agreement with the change in absorption band edge and hence bandgap, as shown in inset of Fig.4.12. The blue shift of absorption band edge shows the less effect of defect states in the films, where the value of $\mathrm{E_u}$ quantifies the defects present in the films[36–38].

4.8.3 Band gap determination

The bandgap of the films was estimated using the Tauc plot[39] and is shown in Fig.4.13. The bandgap of the doped and co-doped films showed a blue-shift compared to undoped ZnO sample. The blue-shift may be due to an increase in free electron concentration as a result of doping. These donor electrons occupy the states at the bottom of the conduction band. Higher energy is needed to make the vertical transition from the valence band to states with fermi momentum in the conduction band. This bandgap widening is generally seen in heavily doped wide bandgap semiconductors due to the suppression of low energy transitions and is called Burstein-Moss (BM) band filling effect[40].

In this work, the blue-shift observed initially were red-shifted and then again were blue-shifted. The sudden band gap narrowing (BN) after a certain carrier density was explained by Kim et al[41]. The BN has been attributed to the merging of donor and conduction bands indicating semiconductor to metal transition. The BN effect observed by Kim et al[41] and Sernelius et al[42] were beyond $n=5\times 10^{19}/cm^3$ for IZO and $4.54\times10^{20}/cm^3$ for AZO. The particular carrier density after which the shift has been observed is the Mott critical density(n_o), which is inversely proportional to the Bohr radius of dopant[41, 42].

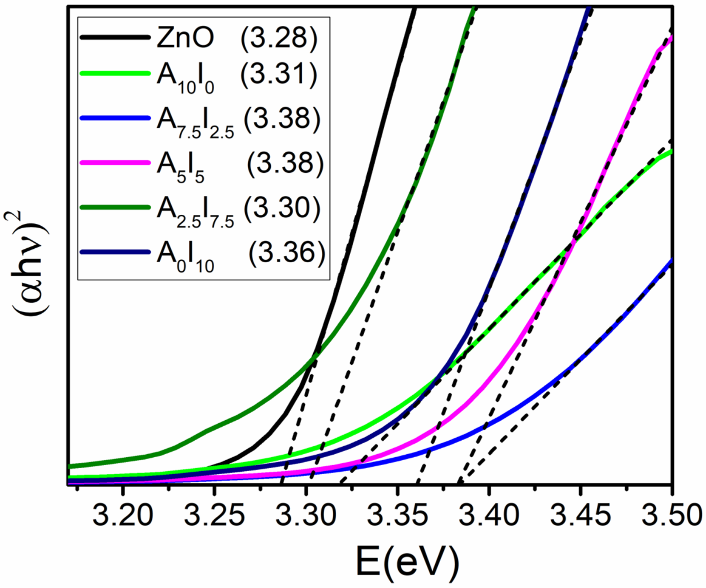

Figure 4.13: Estimation of the bandgap of doped and co-doped ZnO films using Tauc relation.

In this study, the Mott critical density was observed to be at $n=3.21\times10^{20}/cm^3$ for the co-doped film, which was between the n_o value observed for the IZO and AZO films. In addition, the dependence of bandgap shift with a carrier concentration of n-type ZnO was studied by Lu et al[40]. According to these authors, the carrier concentration and bandgap follow the BM effect initially will undergo the BN effect, consistent with the Mott criterion, and then again shows the blue-shift due to band renormalisation(BR) in a different rate[40]. These three effects can be seen in the films in this study, in such a way that the films from $A_{10}I_0$ to A_5I_5 obey BM effect, the films from A_5I_5 to $A_{2.5}I_{7.5}$

exhibit BN effect and the films $A_{2.5}I_{7.5}$ to A_0I_{10} shows the BR effect. The changes observed in the bandgap with carrier density emphasize the importance of fano fitting and it also validates the electrical properties obtained by hall measurement.

4.9 Investigation of plasmonic properties in the films

4.9.1 Drude-Lorentz approach on doped -semiconductors

The influences of structural, electrical and optical parameters on plasmonic properties of these thin films were then studied. Here also Drude-Lorentz model described in chapter 3; section 3.7.1 was used to explain the optical response of free as well as bound electrons in the film. As discussed in the previous chapter, one of the primary criteria for the excitation of surface plasmon resonance is the negative real permittivity (ϵ_1) of the material at the desired frequency. Fig.4.14a shows the negative permittivity of the films A_0I_{10}, $A_{2.5}I_{7.5}$ and A_5I_5 beyond the wavelengths 2137, 2214 and 2218 nm, respectively, which were simulated using the RefFIT software using eqn (3.11), chapter 3. Fig.4.14b shows the imaginary part of the permittivity values of these films and the inset image shows the fitted transmittance data using the fresnel equation[43]. The fitted values were tabulated in Table.4.8.

The importance of negative ϵ_1 is to understand the frequency up to which these films exhibit metal like behaviour. While ϵ_2 indicates the loss of these films in polarising the material. The ϵ_2 of all films are less than 1, which is very small compared to those of the conventional plasmonic materials in NIR. For the application of plasmonics in transformation optics (TO) the magnitude of ϵ_1 should be small and comparable with the value of ϵ_d(permittivity of dielectric) to balance the polarisation response from dielectric and metal components and to match the design requirements[44]. Moreover, in applications such as surface plasmon polariton (SPP) wave-guiding, a trade-off between ϵ_1 and ϵ_2 determines the better quality factor ($Q_{SPR} = \frac{\epsilon_1(\omega)^2}{\epsilon_2(\omega)}$) and hence good field penetration into the plasmonic material[43].

Table 4.8: Drude- Lorentz parameters fitted using RefFit

Sample	D-L parameters		
	ω_p eV	ω_o eV	γ eV
A_0I_{10}	0.01535	1.04535	0.15808
	0.00896	2.07190	071275
	0.20373	0.54363	0.02332
$A_{2.5}I_{7.5}$	0.03236	1.23984	3.40510
	0.00299	1.66300	0.01757
	0.23127	0.53094	0.01492
A_5I_5	0.0040	0.99972	0.04374
	0.02350	2.20382	0.02081
	0.42917	0.50560	0.00600

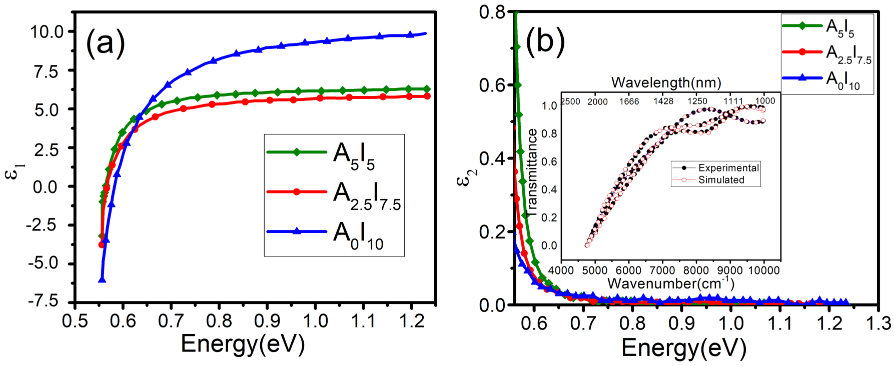

Figure 4.14: Estimation of (a) real part of permittivity ϵ_1 (b) imaginary part of permittivity ϵ_2; inset shows the D-L fitting of transmittance spectra.

4.9.2 Generation of SPR using 3 layer model

The suitability of doped and co-doped ZnO films for device performance by considering the quantitative analysis of real and imaginary values of permittivity on plasmonic properties was investigated theoretically by generating SPR spectra. Using a three layer model in prism geometry, where the thickness of prism and dielectric media was assumed to be zero, the SPR dip was generated by Winspall software. The field of reflectance of this multilayer model is defined as[45].

$$r_{pmd} = \frac{r_{pm} + r_{md}e^{2ikz_m d_m}}{1 + r_{pm} + r_{md}e^{2ikz_m d_m}} \tag{4.2}$$

where p, m and d denote prism, film and air, respectively. $\mathrm{d_m}$ is the thickness of the film and $\mathrm{k_{zm}}$ is the wave-vector of the film which is determined using the permittivity value extracted from DL equation.

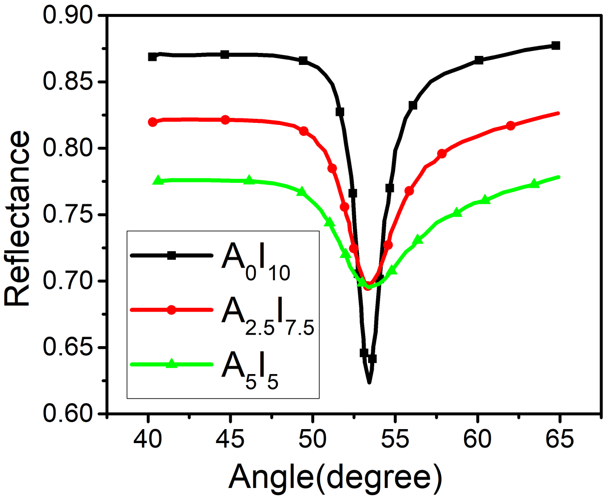

Figure 4.15: Simulated SPR using 3 layer model

The simulated SPR dips of A_0I_{10}, $A_{2.5}I_{7.5}$ and A_5I_5 based on Kretschmann configuration and using ϵ_1, ϵ_2 extracted from D-L approach are shown in Fig.4.15. A monochromator with wavelength 2200nm was chosen and the thickness values determined using tolansky method was used for the simulation. A noticeable change was observed for the FWHM and SPR minimum of the dip. The FWHM of A_5I_5 was 5.349^o, which decreased to 3.38^o for $A_{2.5}I_{7.5}$, and then to 1.915^o for A_0I_{10}. The mobility of these films, shown in Table 4.3, was found to vary in this fashion. Khamh et al[46] observed the broadening of the SPR band when the mobility of the films decreased[46]. They also added that in TCOs a pronounced change in the damping constant(γ) can be made by changing the mobility(μ). Since in plasmonics, the damping constant (γ) is related to ϵ_2 as ϵ_2=$\frac{\gamma\omega_p^2}{\omega(\omega^2+\gamma^2)}$), an increase in ϵ_2 results in increase in damping and this also may contribute to spectrally broader plasmons [46]. The film A_0I_{10} with comparatively larger mobility exhibited minimum value for ϵ_2 and showed a relatively small spectral broadening.

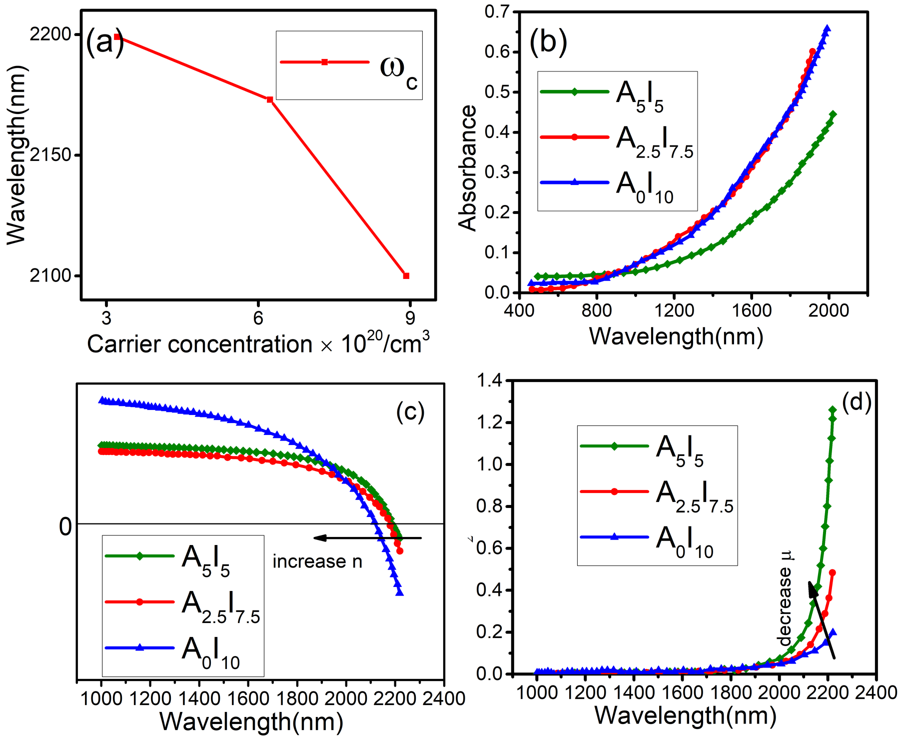

Figure 4.16: (a) Tuning of cross-over wavelength with carrier concentration, (b) SPR absorption, (c) and (d) dependence of the D-L model and material parameters

Fig.4.16a shows the variation of cross over frequency (ω_c) with the carrier density of the films. For doped semiconductors, ω_c describes the frequency at which the semiconductor to metal transition takes place, where the dependence of ω_c to plasma frequency (ω_p) was already described by Naik et al[43]. The increasing absorbance in NIR, shown in Fig.4.16b may be mainly because of the surface plasmon absorption; similar absorption observed for AZO and IZO nanocrystals at the NIR was already reported respectively by Buonsanti et al.[47] and Ghosh et al.[5]. The dependence of the D-Lmodel on carrier density (n), mobility μ are shown in Fig.4.16c and Fig.4.16d. The increase in the n value results in the shifting of cross over wavelength to the lower wavelength. On the other hand, an increase in μ decreases the loss of these plasmonic materials. This may be also due to the lack of lattice imperfections in the film, which does not create additional defect state in the films [45].

4.10 Summary

Al and In doped and co-doped ZnO films were prepared in a 3×1 inch substrate with different Al:In ratio using water as solvent by simple spray coating technique. The effect of ionic radii of dopants as well as their concentrations (Al:In) while substituting in Zn site were studied using X-ray diffraction. The Rietveld refinement studies revealed wurtzite structure for the films and showed the dependence of the ionic radii of the dopants on a structural parameter such as lattice constants, cell volume, bond length. SEM images were analysed to understand how the doping or co-doping and their ratios affect the grain shape, size and uniformity of films. The electrical properties of the films before and after annealing in the reduced atmosphere were studied. Enhancement in carrier concentrations was observed for all films due to the additional oxygen vacancies created during reduced atmosphere annealing. The differences in carrier densities of these films were validated using Raman line shape analysis with Fano and Lorentz fittings. The variation in the band gap energies of the films was estimated using Tauc's relation with respect to the carrier densities was in analogy with the findings from the Fano and Lorentz fitting, and thus confirmed a large number of free carriers for the films A_5I_5, $A_{2.5}I_{7.5}$ and A_0I_{10}. The absence of deep defects in the band gap of films was confirmed from the photoluminescence spectra of these films. Theoretical fitting using the Drude-Lorentz (D-L) model was utilized to extract the real and imaginary parts of the permittivity of the films. Films A_5I_5, $A_{2.5}I_{7.5}$ and A_0I_{10} having carrier density $10^{20}/\mathrm{cm}^3$ showed negative permittivity in near infrared (NIR). Tuning of cross over the frequency with carrier density in the NIR region was observed for these films. The surface plasmon resonance simulated using the permittivity values extracted from the D-L model showed the influence of mobility of the films on the broadening of the dip. The low loss exhibited by the films in the NIR region compared with conventional plasmonic material suggests the suitability of the films for plasmonic applications.

References

[1] V. Kumar, S. Kumari, P. Kumar, M. Kar, and L. Kumar, "Structural analysis by rietveld method and its correlation with optical propertis of nanocrystalline zinc oxide," *Adv Mater Lett*, vol. 6, no. 2, pp. 139–147, 2015.

[2] P. Prabeesh, I. P. Selvam, and S. Potty, "Structural properties of czts thin films on glass and mo coated glass substrates: a rietveld refinement study," *Appl. Phys. A*, vol. 124, no. 3, pp. 1–6, 2018.

[3] A. K. Zak, W. A. Majid, M. E. Abrishami, and R. Yousefi, "X-ray analysis of zno nanoparticles by williamson–hall and size–strain plot methods," *Solid State Sci.*, vol. 13, no. 1, pp. 251–256, 2011.

[4] A. R. Denton and N. W. Ashcroft, "Vegard's law," *Phys. Rev. A*, vol. 43, no. 6, p. 3161, 1991.

[5] S. Ghosh, M. Saha, and S. K. De, "Tunable surface plasmon resonance and enhanced electrical conductivity of in doped zno colloidal nanocrystals," *Nanoscale*, vol. 6, no. 12, pp. 7039–7051, 2014.

[6] S. Edinger, N. Bansal, M. Bauch, R. Wibowo, G. Újvári, R. Hamid, G. Trimmel, and T. Dimopoulos, "Highly transparent and conductive indium-doped zinc oxide films deposited at low substrate temperature by spray pyrolysis from water-based solutions," *J. Mater. Sci.*, vol. 52, no. 14, pp. 8591–8602, 2017.

[7] A. Singh, R. Mehra, A. Yoshida, and A. Wakahara, “Doping mechanism in aluminum doped zinc oxide films,” *J. Appl. Phys.*, vol. 95, no. 7, pp. 3640–3643, 2004.

[8] P. Nunes, E. Fortunato, and R. Martins, “Influence of the post-treatment on the properties of zno thin films,” *Thin Solid Films*, vol. 383, no. 1-2, pp. 277–280, 2001.

[9] J. Chang, W. Lin, and M.-H. Hon, “Effects of post-annealing on the structure and properties of al-doped zinc oxide films,” *Appl. Surf. Sci.*, vol. 183, no. 1-2, pp. 18–25, 2001.

[10] H. Karaagac, E. Yengel, and M. S. Islam, “Physical properties and heterojunction device demonstration of aluminum-doped zno thin films synthesized at room ambient via sol-gel method,” *J.alloy.compd*, vol. 521, pp. 155–162, 2012.

[11] S. Mondal, K. Kanta, and P. Mitra, “Preparation of al-doped zno (azo) thin film by silar,” 2008.

[12] G. Drewelow, A. Reed, C. Stone, K. Roh, Z.-T. Jiang, L. N. T. Truc, K. No, H. Park, and S. Lee, “Work function investigations of al-doped zno for band-alignment in electronic and optoelectronic applications,” *Appl. Surf. Sci.*, vol. 484, pp. 990–998, 2019.

[13] W. Yang, Z. Liu, D.-L. Peng, F. Zhang, H. Huang, Y. Xie, and Z. Wu, “Room-temperature deposition of transparent conducting al-doped zno films by rf magnetron sputtering method,” *Appl. Surf. Sci.*, vol. 255, no. 11, pp. 5669–5673, 2009.

[14] M. N. Islam, T. Ghosh, K. Chopra, and H. Acharya, “Xps and x-ray diffraction studies of aluminum-doped zinc oxide transparent conducting films,” *Thin Solid Films*, vol. 280, no. 1-2, pp. 20–25, 1996.

[15] G. C. Park, S. M. Hwang, J. H. Choi, Y. H. Kwon, H. K. Cho, S.-W. Kim, J. H. Lim, and J. Joo, “Effects of in or ga doping on the

growth behavior and optical properties of zn o nanorods fabricated by hydrothermal process," *Phys. Status Solidi A*, vol. 210, no. 8, pp. 1552–1556, 2013.

[16] X. Duan, C. Song, F. Yu, D. Yuan, and X. Li, "X-ray photoelectron spectroscopy studies of co-doped zno–ga2o3–sio2 nano-glass–ceramic composites," *Appl. Surf. Sci.*, vol. 257, no. 9, pp. 4291–4295, 2011.

[17] Y. Wang, T. Hou, S. Tian, S.-T. Lee, and Y. Li, "Influence of doping effect on zinc oxide by first-principles studies," *J. Phys. Chem. C*, vol. 115, no. 15, pp. 7706–7716, 2011.

[18] M. Chen, X. Wang, Y. Yu, Z. Pei, X. Bai, C. Sun, R. Huang, and L. Wen, "X-ray photoelectron spectroscopy and auger electron spectroscopy studies of al-doped zno films," *Appl. Surf. Sci.*, vol. 158, no. 1-2, pp. 134–140, 2000.

[19] H. Wang, S. Baek, J. Song, J. Lee, and S. Lim, "Microstructural and optical characteristics of solution-grown ga-doped zno nanorod arrays," *Nanotechnology*, vol. 19, no. 7, p. 075607, 2008.

[20] Y. Y. Kim, B. H. Kong, and H. K. Cho, "Vertically arrayed ga-doped zno nanorods grown by magnetron sputtering: The effect of ga contents and microstructural evaluation," *J. Cryst. Growth*, vol. 330, no. 1, pp. 17–21, 2011.

[21] D. Yoon, S. Yu, and J. Son, "Oxygen vacancy-assisted recovery process for increasing electron mobility in n-type basno 3 epitaxial thin films," *NPG Asia Mater.*, vol. 10, no. 4, pp. 363–371, 2018.

[22] Q. Gao, Y. Dai, C. Li, L. Yang, X. Li, and C. Cui, "Correlation between oxygen vacancies and dopant concentration in mn-doped zno nanoparticles synthesized by co-precipitation technique," *J. Alloys*, vol. 684, pp. 669–676, 2016.

[23] C. M. Ghimbeu, J. Schoonman, M. Lumbreras, and M. Siadat, "Electrostatic spray deposited zinc oxide films for gas sensor applications," *Appl. Surf. Sci.*, vol. 253, no. 18, pp. 7483–7489, 2007.

[24] M. Chandrasekhar, J. Renucci, and M. Cardona, "Effects of interband excitations on raman phonons in heavily doped n- si," *Phys. Rev. B*, vol. 17, no. 4, p. 1623, 1978.

[25] A. Mohanta, J. G. Simmons Jr, G. Shen, S. M. Kim, P. Kung, and H. O. Everitt, "Al doping in zno nanowires enhances ultraviolet emission and suppresses broad defect emission," *J. Lumin.*, vol. 211, pp. 264–270, 2019.

[26] R. K. Biroju, N. Tilak, G. Rajender, S. Dhara, and P. Giri, "Catalyst free growth of zno nanowires on graphene and graphene oxide and its enhanced photoluminescence and photoresponse," *Nanotechnology*, vol. 26, no. 14, p. 145601, 2015.

[27] T. Makino, Y. Segawa, S. Yoshida, A. Tsukazaki, A. Ohtomo, and M. Kawasaki, "Gallium concentration dependence of room-temperature near-band-edge luminescence in n-type zno: Ga," *Appl. Phys. Lett.*, vol. 85, no. 5, pp. 759–761, 2004.

[28] E. Schubert, I. Goepfert, W. Grieshaber, and J. Redwing, "Optical properties of si-doped gan," *Appl. Phys. Lett.*, vol. 71, no. 7, pp. 921–923, 1997.

[29] D. Meljanac, K. Juraić, V. Mandić, H. Skenderović, S. Bernstorff, J. R. Plaisier, A. Šantić, A. Gajović, B. Šantić, and D. Gracin, "The influence of thermal annealing on the structural, optical and electrical properties of azo thin films deposited by magnetron sputtering," *Surf. Coat. Technol.*, vol. 321, pp. 292–299, 2017.

[30] B. Jin, S. Im, and S. Y. Lee, "Violet and uv luminescence emitted from zno thin films grown on sapphire by pulsed laser deposition," *Thin solid films*, vol. 366, no. 1-2, pp. 107–110, 2000.

[31] B. Cao, W. Cai, and H. Zeng, "Temperature-dependent shifts of three emission bands for zno nanoneedle arrays," *Appl. Phys. Lett.*, vol. 88, no. 16, p. 161101, 2006.

[32] B. Guo, Z. Qiu, and K. Wong, "Intensity dependence and transient dynamics of donor–acceptor pair recombination in zno thin films grown on (001) silicon," *Appl. Phys. Lett.*, vol. 82, no. 14, pp. 2290–2292, 2003.

[33] P. Rodnyi and I. Khodyuk, "Optical and luminescence properties of zinc oxide," *Opt. Spectrosc.*, vol. 111, no. 5, pp. 776–785, 2011.

[34] A. Kohan, G. Ceder, D. Morgan, and C. G. Van de Walle, "First-principles study of native point defects in zno," *Phys. Rev. B*, vol. 61, no. 22, p. 15019, 2000.

[35] M. A. Basyooni, M. Shaban, and A. M. El Sayed, "Enhanced gas sensing properties of spin-coated na-doped zno nanostructured films," *Sci. Rep.*, vol. 7, no. 1, pp. 1–12, 2017.

[36] F. Anyaegbunam and C. Augustine, "A study of optical band gap and associated urbach energy tail of chemically deposited metal oxides binary thin films," *Dig J Nanometer Bios*, vol. 13, pp. 847–856, 2018.

[37] S. Schönau, F. Ruske, S. Neubert, and B. Rech, "Analysis of urbach-like absorption tails in thermally treated zno: Al thin films," *Appl. Phys. Lett.*, vol. 103, no. 19, p. 192108, 2013.

[38] B. Pejova, "The urbach–martienssen absorption tails in the optical spectra of semiconducting variable-sized zinc selenide and cadmium selenide quantum dots in thin film form," *Mater. Chem. Phys.*, vol. 119, no. 3, pp. 367–376, 2010.

[39] A. Singh, M. Kumar, R. Mehra, A. Wakahara, and A. Yoshida, "Al-doped zinc oxide (zno: Al) thin films by pulsed laser ablation.," *J. Indian Inst. Sci.*, vol. 81, no. 5, p. 527, 2001.

[40] J. Lu, S. Fujita, T. Kawaharamura, H. Nishinaka, Y. Kamada, T. Ohshima, Z. Ye, Y. Zeng, Y. Zhang, L. Zhu, *et al.*, “Carrier concentration dependence of band gap shift in n-type zno: Al films,” *J. Appl. Phys.*, vol. 101, no. 8, p. 083705, 2007.

[41] K. J. Kim and Y. R. Park, “Large and abrupt optical band gap variation in in-doped zno,” *Appl. Phys. Lett.*, vol. 78, no. 4, pp. 475–477, 2001.

[42] B. E. Sernelius, K.-F. Berggren, Z.-C. Jin, I. Hamberg, and C. G. Granqvist, “Band-gap tailoring of zno by means of heavy al doping,” *Phys. Rev. B*, vol. 37, no. 17, p. 10244, 1988.

[43] G. V. Naik, V. M. Shalaev, and A. Boltasseva, “Alternative plasmonic materials: beyond gold and silver,” *Adv. Mater.*, vol. 25, no. 24, pp. 3264–3294, 2013.

[44] P. R. West, S. Ishii, G. V. Naik, N. K. Emani, V. M. Shalaev, and A. Boltasseva, “Searching for better plasmonic materials,” *Laser Photonics Rev.*, vol. 4, no. 6, pp. 795–808, 2010.

[45] S. Rajak, J. Banerjee, and M. Ray, “Parametric influence of film thickness and incident angle on resonance spectra of pre-and post-annealed ga doped zno,” *J. Appl. Phys.*, vol. 125, no. 24, p. 243105, 2019.

[46] H. Khamh, E. Sachet, K. Kelly, J.-P. Maria, and S. Franzen, “As good as gold and better: conducting metal oxide materials for mid-infrared plasmonic applications,” *J. Mater. Chem. C*, vol. 6, no. 31, pp. 8326–8342, 2018.

[47] R. Buonsanti, A. Llordes, S. Aloni, B. A. Helms, and D. J. Milliron, “Tunable infrared absorption and visible transparency of colloidal aluminum-doped zinc oxide nanocrystals,” *Nano lett.*, vol. 11, no. 11, pp. 4706–4710, 2011.

Chapter 5

Investigation of plasmonic property in RF sputtered co-doped ZnO thin films

5.1 Overview

Plasmonic properties of Al and In co-doped ZnO films prepared using chemical deposition techniques were discussed in the previous two chapters. This chapter discusses the development of plasmonic co-doped ZnO thin film by a physical route, RF sputtering. Here the deposition are done at vacuum, and hence more crystallinity as well as material purity can be expected in the sputtered films. In this work also, we studied the structural, electrical and optical properties of co-doped ZnO by varying the co-dopant ratio of Al:In. Structural confirmation was done using the XRD and the rietveld refinement technique. The chances for Raman active inter-conduction band transitions occurring for heavily doped n type materials were examined for these films using fano resonance fitting. The defects within band gap were analysed with the help of PL studies. The Drude -Lorentz model was used for the theoretical prediction of the cross over wavelength, beyond which the material exhibits real negative permittivity. The surface plasmon resonance observed using the Kretschmann configuration was compared with the theoretical prediction provided by the model.

5.2 Sample preparation

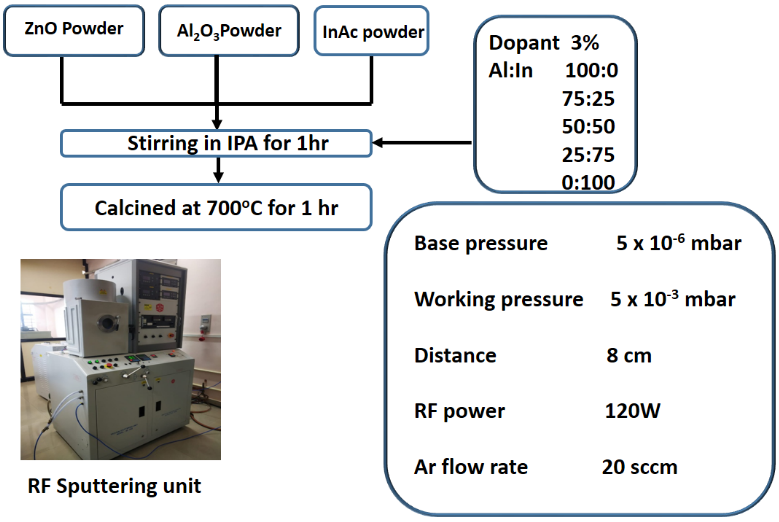

Figure 5.1: Thin film deposition using RF sputtering

5.2.1 Preparation of Al and In doped/co-doped ZnO powder

ZnO powder with co-dopants prepared by solid state route was used for fabricating films by RF magnetron sputtering. Analytical grade ZnO powder, Al_2O_3 powder (99.99%, Sigma Aldrich) and indium acetate powder (99.99% AlfaAesar) were used as the precursor salts to prepare co-doped ZnO powders by varying dopant ratios of Al and In. The powders in the Al: In ratios of 100:0, 75:25, 50:50, 25:75 and 0:100 were mixed thoroughly in an agate mortar in the presence isopropol alcohol for 1 hour. The overall dopant concentration in the powder was fixed to 3 percent. These powders were then calcined at 700°C for 3h. The flow chart for powder preparation is showed in Fig.5.1. For coating, 3×1 inch glass substrates were used and before coating, the substrates were cleaned as described in the section 3.2.2 of chapter 3.

5.2.2 Thin film preparation using RF sputtering

For sputtering, the base pressure was set to 5×10^{-6} mbar and the working pressure was to 5×10^{-3} mbar. The distance between target and substrate used is 8 cm and substrate is rotated at a rate of 10 rpm. Sputtering was done at room temperature for 1 hour. The sputtered film were named accordingly to their doping percentage as $A_{10}I_0$, $A_{7.5}I_{2.5}$, A_5I_5, $A_{2.5}I_{7.5}$, A_0I_{10}. The flow chart for thin film deposition is showed in Fig.5.1.

5.3 Structural properties

Structural studies were carried out by x-ray diffraction. Detailed structural studies were carried out further by Rietveld refinement technique[1, 2] using the XRD data with the help of General Structure Analysis System (GSAS) software, using $P6_3mc$ space group. The XRD patterns along with the Rietveld refinement results are shown in Fig.5.2. Black curve is the experimental pattern, red curve is the Rietveld fit, the black ticks (vertical lines) are the positions of phase reflection and the blue curve is the difference between observed and calculated intensities. As seen in the figure, the observed and calculated profiles are closely matching for all films. It is also observed that the x-ray diffraction peaks closely matched with those of the ICDD data of ZnO (ICDD pdf# 36-1451). Parameters such as atom position(u), lattice parameter, scale factors and shape parameters were used as the free parameters during fitting. Quality of the fitted experimental data was assessed by computing the goodness of fit (χ^2) and profile factor (R_P).The lattice constants of doped as well as co-doped ZnO films are tabulated in Table.5.1. The lattice strain is calculated using the difference between the lattice parameter values and ICDD data (represented as Δa and Δc), using the equation 3.5 given in Chapter 3. All films, irrespective of the co-dopant ratios, showed preferred (002) orientation. There is a small deviation for the lattice constants with respect to the ICDD data; however, no change with the variation of the co-dopant ratio was noticed. Since the deviations in lattice constants are minimum with respect to ICDD data, only a small strain and hence small

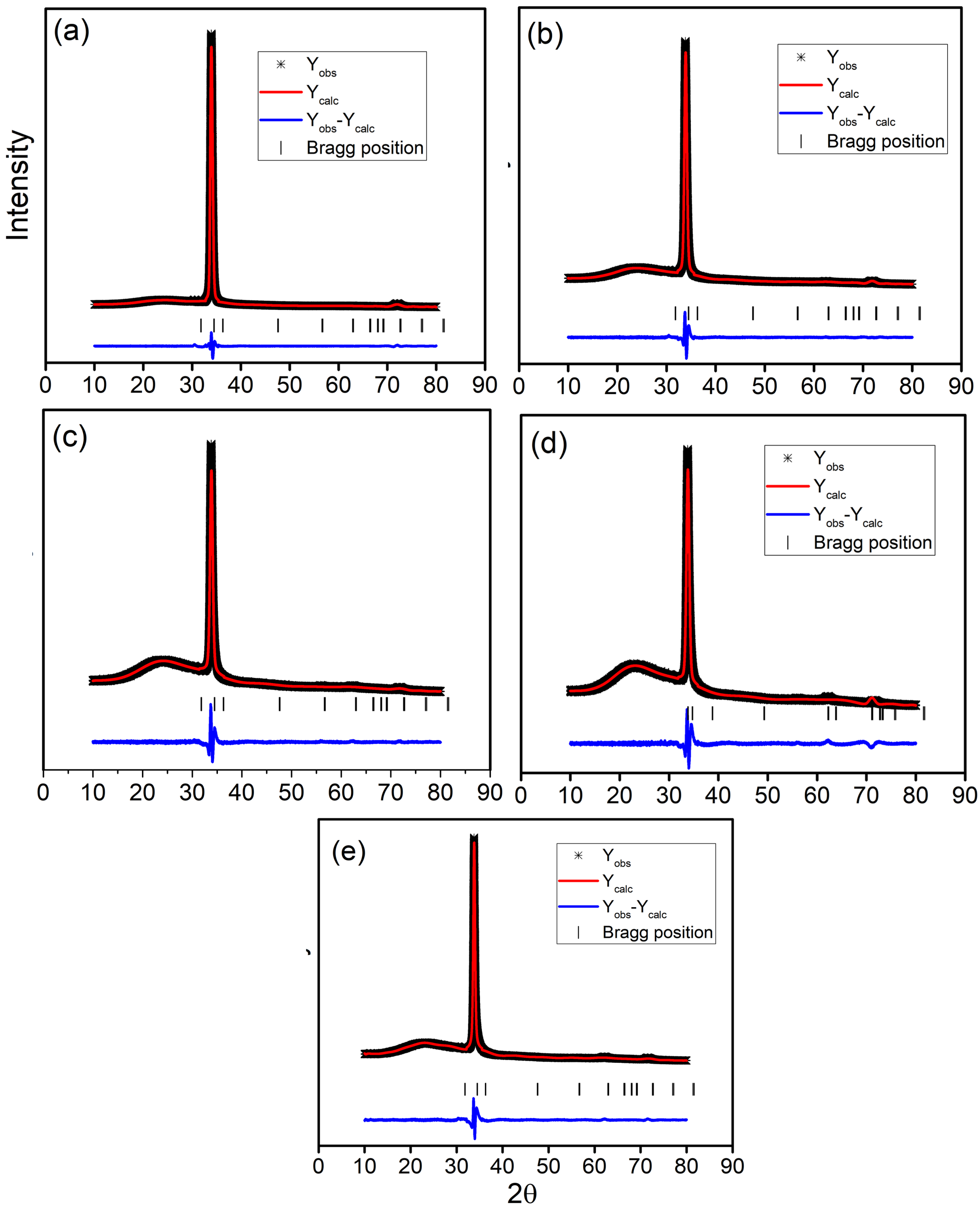

Figure 5.2: Rietveld refinement of XRD data of(a)$A_{10}I_0$, (b)$A_{7.5}I_{2.5}$, (c)A_5I_5, (d)$A_{2.5}I_{7.5}$ and (e)A_0I_{10}. The black curves represent experimental data, the red line is the calculated fit, vertical lines are the positions of refined phase reflections and the blue line is the difference line between experimental and fitted data.

stress, can be expected in these films [3, 4]. Compared with the films prepared by spin and spray coatings (described in chapter 3 and 4), the substitution of dopants in ZnO does not resulted in deviation in lattice constants. The expected change is due to difference in ionic radii of dopants and host lattice atom[5]. The unit cell volumes obtained after the refinement, the Zn-O bond length calculated from refined data were listed in Table.5.2. The bond length along c-axis is calculated by finding u×c, as described in the section 4.3 of the chapter 4. In the perpendicular direction, the bond length is defined as $[\frac{a^2}{3} + (\frac{1}{2} - u)^2 c^2]$ [1]. In addition, average crystallite size calculated using Debye Scherrer equation (eqn (3.3), Chapter 3) shows no noticeable change with change in co-doping ratio.

Table 5.1: Lattice constants and the strain of doped and co-doped ZnO thin films, estimated from XRD data

Sample	χ^2	Lattice constants(A^0) a=b	Lattice constants(A^0) c	Δa (A^0)	Δc (A^0)	Strain $\times 10^{-4}$
$A_{10}I_0$	1.52	3.249	5.206	0.001	0.001	1.9
$A_{7.5}I_{2.5}$	1.55	3.249	5.206	0.001	0.001	1.9
A_5I_5	1.24	3.249	5.206	0.001	0.001	1.9
$A_{2.5}I_{7.5}$	1.69	3.249	5.206	0.001	0.001	1.9
A_0I_{10}	1.98	3.249	5.206	0.001	0.001	1.9

In RF sputtering, due to RF power, sputtered particles possess kinetic energy and thus results in migrating to appropriate lattice sites. The RF power helps in the nucleation and growth, and consequently the crystallinity of the films is improved[6]. The (002) oriented growth for ZnO thin film by RF sputtering with large uniformity as well as crystallinity compared with other technique such as PLD, thermal evaporation was reported by Vyas et al[7].

The advantages of RF sputtered ZnO thin films over solution processed films are high purity, homogeneity, and the nanostructured feature of thin films[8, 9]. In chapter 4, the relatively minimum deviation of structural parameter of the film $A_{10}I_0$ was described mainly due to the unsubstituted Al dopants, which does not improved the carrier density upon doping. To see the behaviour in the sputtered films, the electrical properties of these films were carried out further, to understand the crystallinity as well as substitution of dopants in the ZnO lattice.

Table 5.2: Structural parameters of doped and co-doped ZnO thin films, estimated from XRD data

Sample	Cell volume	Bond length		u	D(nm)
	47.61	along c	⊥ to c		± 1nm
		1.972	1.979	0.379	
$A_{10}I_0$	47.59	1.978	1.976	0.380	19
$A_{7.5}I_{2.5}$	47.59	1.978	1.976	0.380	17
A_5I_5	47.59	1.978	1.976	0.380	18
$A_{2.5}I_{7.5}$	47.59	1.978	1.976	0.380	17
A_0I_{10}	47.59	1.978	1.976	0.380	19

5.4 Morphological studies

The surface morphology of the co-doped ZnO films was investigated by FE-SEM, and the images are shown in Fig.5.4. The films show dense, uniform and continuous morphology, and no cracks or holes were observed in the films. Particle size is observed to increase gradually in the films $A_{2.5}I_{7.5}$ and A_0I_{10}. This may be due to larger ionic radii of In dopant than that of Zn. Dopant dependent surface morphology due to the difference in the ionic radii with host atom have been reported earlier by Potter et al[11].

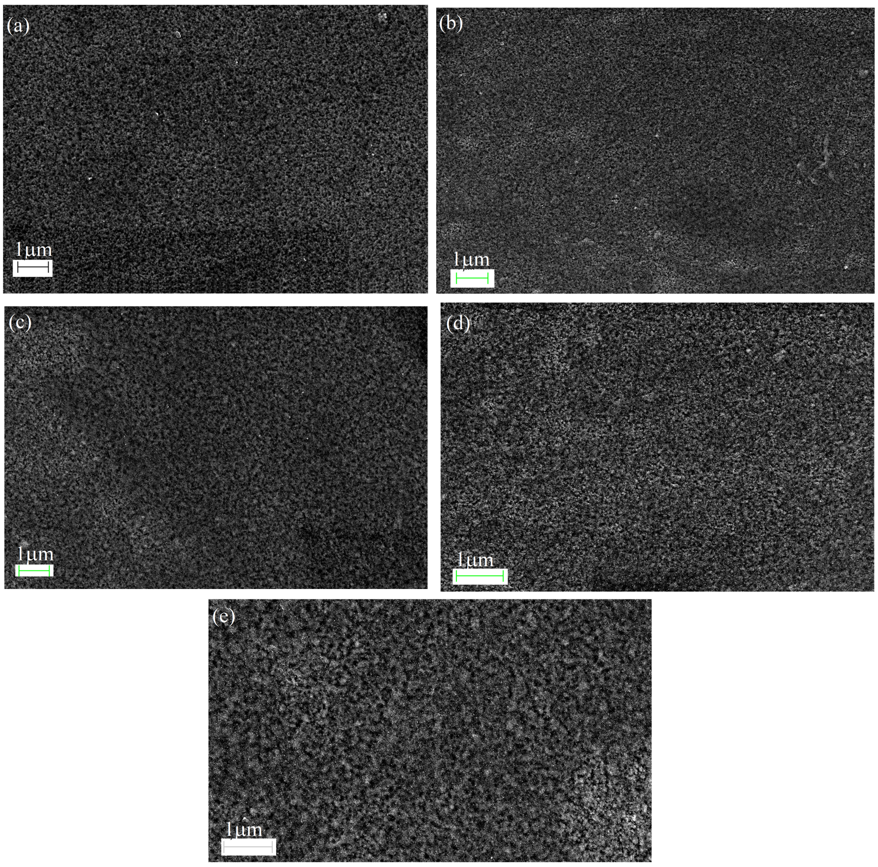

Figure 5.3: Surface morphology of (a) $A_{10}I_0$,(b)$A_{7.5}I_{2.5}$,(c)A_5I_5,(d)$A_{2.5}I_{7.5}$ and (e) A_0I_{10}

5.5 Electrical Properties

The summary of the electrical properties of the films investigated by hall measurement technique are shown in Fig.5.3. As seen, the carrier density of all films is in the order of $10^{20}cm^{-3}$, which is one of the criteria for a material to exhibit NIR plasmonics. In addition, the high carrier density confirms the well substitution of dopants in the ZnO lattice. The carrier density and mobility are varied in a similar fashion with the changes in Al:In. A relatively large carrier density and mobility are observed for the films $A_{10}I_0$ and $A_{7.5}I_{2.5}$. The relatively high mobility compared with the spray coated film shows the better crystallinity of the films. The mobility of the film have consequences in the broadening of SPR dip, larger the mobility smaller will be the broadening[10].

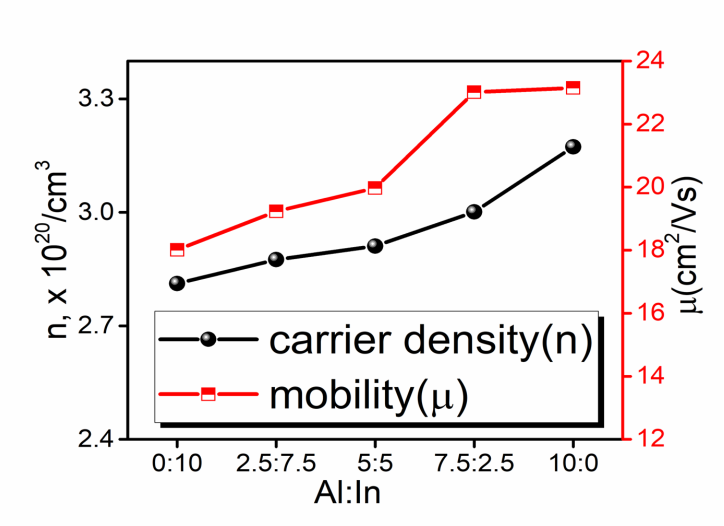

Figure 5.4: Variation of free carrier density and mobility of Al/In co-doped ZnO thin films

5.6 Raman studies

The micro-Raman spectra of the films were recorded to study the effect of co-dopant ratio on the Raman scattering of the ZnO thin films, and are shown in Fig.5.5. The Raman modes of the ZnO predicted are already described in the section 4.7 of chapter 4 of this thesis. Figure shows the characteristic raman modes of ZnO, E_{2L} and E_{2H}, observed near at 110 cm^{-1} and 450 cm^{-1}, respectively. The peak observed at 275 cm^{-1} may be assigned to B_1 mode, which is defined as silent mode[12]. This mode was not present in the Raman spectra of the spray coated co-doped ZnO films, described in Chapter 4, section 4.7 of this thesis.

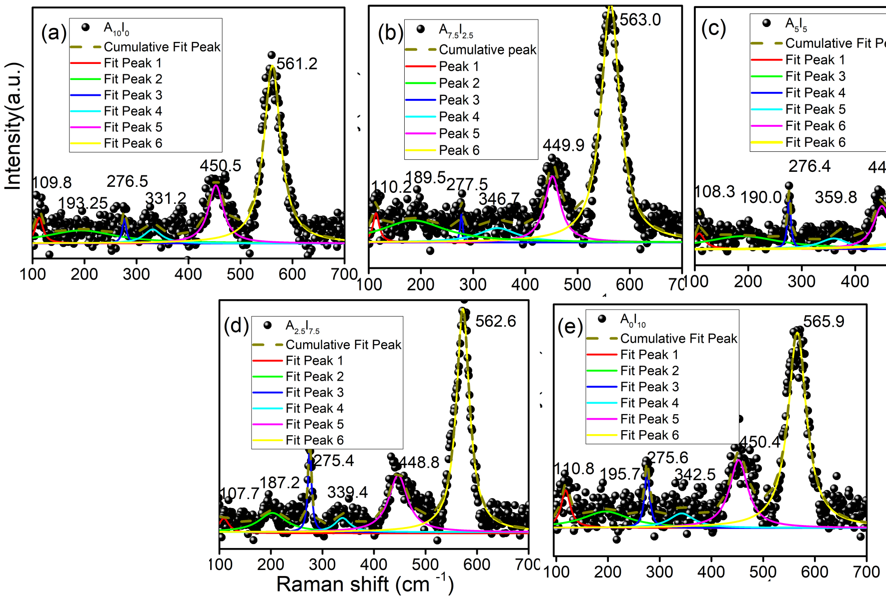

Figure 5.5: Raman spectra of the films(a) $A_{10}I_0$,(b)$A_{7.5}I_{2.5}$,(c)A_5I_5,(d)$A_{2.5}I_{7.5}$ and (e) A_0I_{10}

A possible origin of the silent B_1 peak can be attributed to the breakdown of the translational crystal symmetry imposed by defects and impurities[12]. The presence of second phonon scattering peaks were identified in these films near at 195 cm^{-1} and 330 cm^{-1} representing $2E_2$(low) and E_2(high)-E_2(low) respectively[13].

The chances for Raman active inter-conduction band transitions occurring for heavily doped n type materials were examined for these films. As described in the section 4.7 of the chapter 4 of this thesis, these types of transitions interfere with zone centre optical phonon will result in fano resonance scattering between the A_1(LO) mode and the conduction band electrons[14]. The Fano line shape function is given as

$$I = A\frac{(q-\epsilon)^2}{1+\epsilon^2} \tag{5.1}$$

where $\epsilon = \frac{\omega-\omega_0}{\gamma}$, A is amplitude, ω_o is the phonon frequency, q is the asymmetric parameter and γ is the half width parameter. The possibilities of fano-fitting of the asymmetric broadened A_1(LO) peak of doped films are explored, as shown in Fig.5.6. When the free electron concentration is large ($10^{20}/cm^3$), they will participate in the inelastic light scattering process, which result in the excitation to the higher energy levels in the conduction band. This scattering from the continuum channel can participate in fano resonance with the A_1(LO) phonon scattering. As seen in the figure, the A_1(LO) peak of all films fits well by fano line shape function. The influence of electronic raman on phonon scattering was determined by the parameter q. For a strong interference, q value will turn to low value[15]. The fitted q value for the films A_0I_{10}, $A_{2.5}I_{7.5}$, A_5I_5, $A_{7.5}I_{2.5}$, and $A_{10}I_0$ were 4.50, 4.46, 3.41, 2.54, and 2.51, respectively. The value of 1/q is referred as the coupling strength. For a bulk silicon, the inverse proportionality of free carrier density with q was reported [15]. Here also similar trend of varying q value with respect to carrier density was observed.

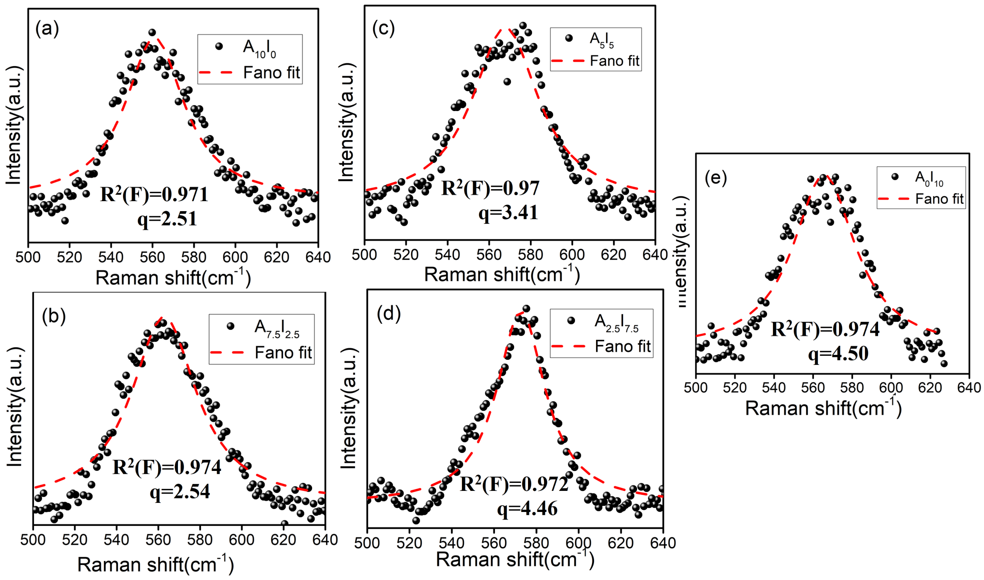

Figure 5.6: Fano fitting of the films(a)$A_{10}I_0$, (b)$A_{7.5}I_{2.5}$, (c)A_5I_5, (d)$A_{2.5}I_{7.5}$ and (e) A_0I_{10}

5.7 Optical properties

5.7.1 Photoluminescence (PL) studies

The room temperature PL spectra of the co-doped ZnO films are shown in Fig.5.7. The PL emissions of ZnO and doped ZnO are assigned to various defects present in the material such as oxygen vacancy (V_O), zinc vacancy (V_{Zn}), zinc interstitial (Zn_i), and oxygen interstitial (O_i). The emission near to 380nm is the near band emission occurs due to the excitonic recombination of bound and free excitons and their longitudinal optical phonon replicas[16–18]. Reports show that it is also possible for near band emission of ZnO to occur near to 400nm[19]. There is also the possibility of visible emission in ZnO, because of the radiative transitions between the valence band and the trap defects in the grain boundary, which is also reported near to 400nm [16–21]. In chapter 4, the NBE observed at 380nm and visible emission at 400nm, and differentiation of both emissions were discussed for spray coated co-doped ZnO thin films.

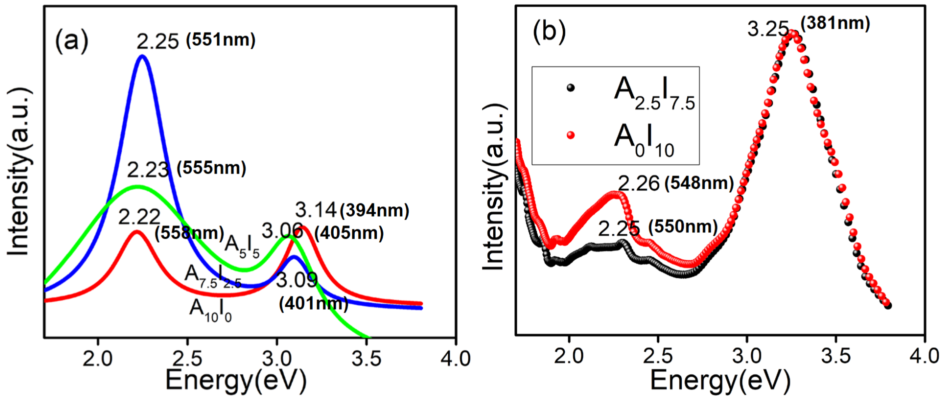

Figure 5.7: PL spetra of the films for the excitation wavelength of 320 nm;(a)$A_{10}I_0$, $A_{7.5}I_{2.5}$, A_5I_5 and (b) $A_{2.5}I_{7.5}$, A_0I_{10}

.

Figure shows the presence of emission near at 3.25 eV(381nm) for the films A_0I_{10} and $A_{2.5}I_{7.5}$ and this peak was shifted near to 3.14, 3.09 and finally to

3.06 eV for the films A_5I_5, $A_{7.5}I_{2.5}$ and $A_{10}I_0$, respectively (Fig.5.7a). The deconvolution of peaks showed the presence of only single peak, and thus can be assigned to NBE, which is found to shift to visible range when the co-dopant ratio was changed from $A_{2.5}I_{7.5}$ to A_5I_5. The reason for shifting of NBE peak can be explained using the second emission peak observed in visible region. The peak observed between 2.26 eV and 2.22 eV (near to 551 nm) is green emission, mainly due to radiative transition between oxygen vacancies and the valence band[22]. The dominancy of green emission was more in the films A_5I_5, $A_{7.5}I_{2.5}$, $A_{10}I_0$ compared with A_0I_{10} and $A_{2.5}I_{7.5}$(Fig.5.7b), which shows the presence of more oxygen vacancies in these films. The presence of large oxygen vacancies may be the reason for shifting of NBE emission to the lower energy. This in turn resulted in comparatively higher carrier density, when the Al: In was changed from 0: 10 to 10: 0.

5.7.2 Band gap determination

The average transmittance spectra of the films is shown in Fig.5.8a. All films possessed average transmittance >80%. Fig.5.8b shows the Tauc plot used to estimate the bandgap of the films[23]. As seen in Fig.5.8b, the band gap values were increased to 3.41, 3.44, 3.54, 3.61 and 3.65 eV, when the co-dopant Al: In ratios were changed in the ZnO films from 0: 10 to 10: 0, respectively. The variation in the bandgap of the films from A_0I_{10} to $A_{10}I_0$ is proportional to the free carrier density of the films, as seen in Fig.5.8c. Because of the high carrier density of all films, the variation of band gap with carrier density can explained on the basis of band renormalization effect (BR)[24]. Increasing band gap with carrier density can be explained both by BM and BR effects, as described in the section 3.6.1 of chapter 3 and section 4.8.3 of chapter 4. Based on these results and because of high carrier density ($>10^{20}/\text{cm}^3$) for all the sputtered films, BR effect is more appropriate in this case than BM.

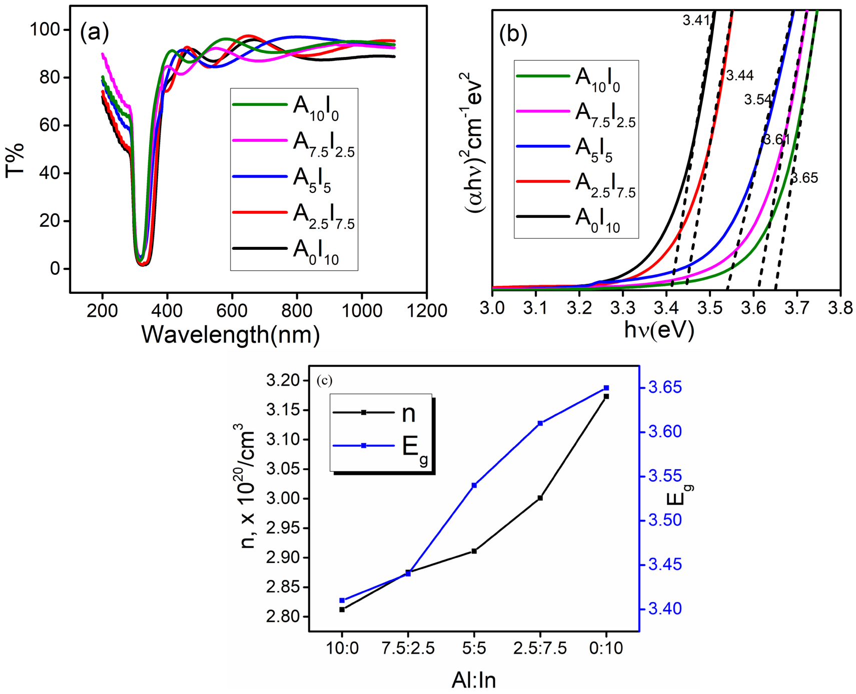

Figure 5.8: (a) Transmittance spectra, and (b) Tauc plot for estimating band gap of the co-doped ZnO films (c) Variation of carrier density and band gap with the change in co-dopant concentration

5.7.3 Urbach energy calculation.

The difference in the average transmittance of the films may be attributed to the optical absorption due to the formation of localized states near the conduction band minimum. This results in a tail for transmission spectra below 400nm, defined as urbach tail[25–27]. This is discussed detail in the section of 3.6.2 of the Chapter 3 of this thesis. Considering the eqn (3.9) in Chapter 3 and using the linear least square fit of the experimental absorption data, E_u was calculated and is tabulated in Table.5.3. The change in E_u was in agreement with the change in absorption band edge, and hence the bandgap, where E_u is the measure of the defects present in the films (Table 5.3)[26–28]. Thus, smaller E_u is observed for the films having larger bandgap.

Table 5.3: Fitting parameters of ln $(\alpha) = b_0+(\text{h}\nu)b_1$ together with R^2 value of linear regression analysis.(Recriprocal of b_1 is E_u)

Sample	b_0	b_1	E_u	R^2	E_g
$A_{10}I_0$	8.14	0.91	1.09	0.65	3.65
A_1I_9	7.79	0.90	1.10	0.69	3.61
A_3I_7	7.27	0.89	1.12	0.62	3.54
A_5I_5	7.14	0.86	1.15	0.64	3.44
A_0I_{10}	7.04	0.84	1.19	0.62	3.41

5.8 Investigation of plasmonic properties in the films

5.8.1 Drude-Lorentz approach on doped semiconductors

By using the D-L and Fresnel equations, real and imaginary parts of the dielectric functions were extracted [29, 30], as described in the section 3.7.1 of chapter 3. The fitted reflectance spectra and the simulated dielectric functions are shown in Fig.5.9. As seen in the figure, the films exhibit negative values for ϵ_1 near to 1350nm in the near infrared region. This indicates that these films are suitable for exciting surface plasmon resonance near to 1350nm. The exact cross over wavelength observed for $A_{10}I_0$ to A_0I_{10} respectively are 1333nm, 1340nm, 1351nm, 1360nm and 1365nm. The loss encountered while polarising the material is given by the imaginary part of the dielectric constant ϵ_2. The value of ϵ_2 in NIR estimated is tabulated in Table 5.4. It shows that the value of ϵ_1 is comparatively small compared to that of the conventional plasmonic materials.

Table 5.4: Imaginary part of the permittivity of the films of this study along with the data of conventional plasmonic materials

Material	ϵ_2	References
$A_{10}I_0$	0.3-3	This work
$A_{7.5}I_{2.5}$	0.3-3	This work
A_5I_5	0.3-3	This work
$A_{2.5}I_{7.5}$	0.3-3	This work
A_0I_{10}	0.3-3	This work
Ag	9-25	[31–33]
Au	5-10	[31–33]
TiN	10-40	[31–34]

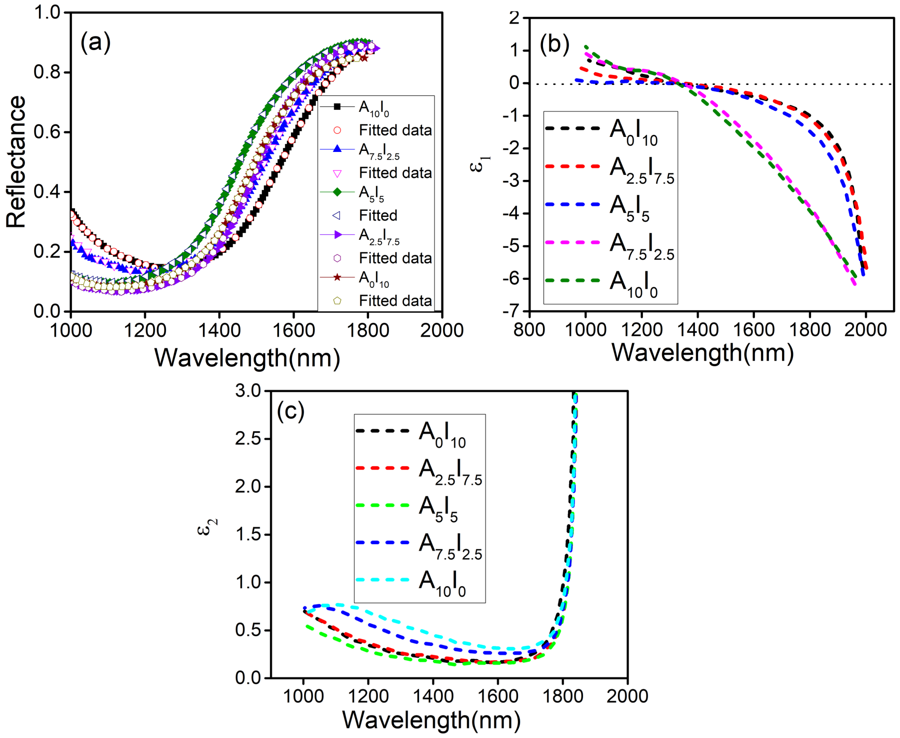

Figure 5.9: (a) Fitting of reflectance spectra and estimation of (b) real part of permittivity (ϵ_1), (c) imaginary part of permittivity (ϵ_2) using D-L equation of co-doped ZnO films

5.8.2 SPR using Kretschmann configuration

The setup used for generating SPR based on Kretschmann configuration is shown in Fig.5.10. The incident light coming out of the collimator will pass through a p polariser and illuminates the BK7 prism, as seen in the figure. The substrate coated with the co-doped film is kept on the prism using an index matching fluid. Evanescent wave penetrates through the prism and substrate, under the condition of total internal reflection. The refractive index and the critical angle of the BK7 prism for air(dielectric medium) are 1.57 (NIR) and 41.8^o, respectively. SPR was generated using the wavelength interrogation method and the incident angles selected were greater than the critical angle. The SPR generated by varying the incident angle based on wavelength interrogation is given in Fig.5.11.

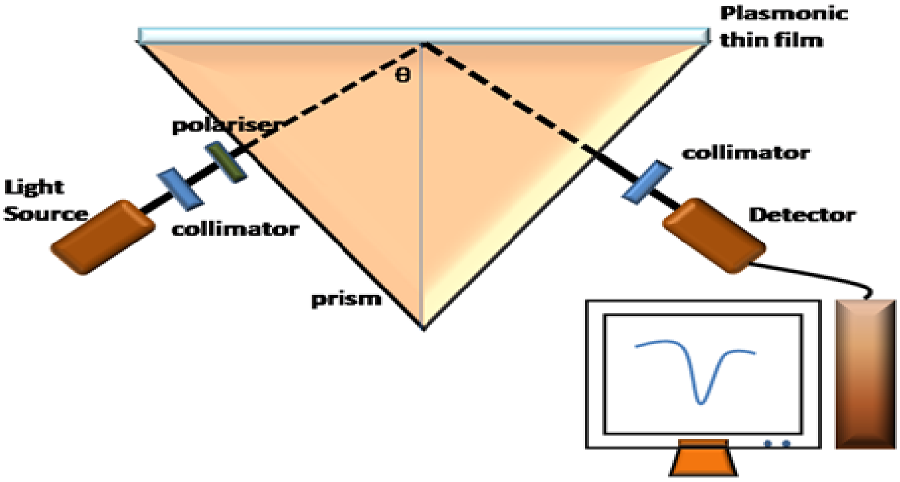

Figure 5.10: Kretschmann configuration for SPR generation

The resonance wavelength is found to shift to lower wavelength when the incident angle was changed to higher angles. However, the broadness of resonance dip is increased with the incident angle. A minimum resonance wavelength of around 1350 nm was observed for the films $A_{10}I_0$ and $A_{7.5}I_{2.5}$. The SPR observed were beyond 1350nm, as predicted by the D-L model. The observed SPR resonance of the films $A_{10}I_0$ and $A_{7.5}I_{2.5}$ are near to the telecommunication wavelength, and are thus suitable for communication applications. It can be seen that the high carrier density of ($10^{20}/\mathrm{cm}^3$) resulted in the excitation of SPR in the NIR.

The energy loss function (ELF) and the quality factor (Q_{SPP})[35] extracted using the equations described below are shown in Fig.5.12a.

$$ELF = -Im\frac{1}{\epsilon} = \frac{\epsilon_2}{\epsilon_1^2 + \epsilon_2^2} \tag{5.2}$$

$$Q_{SPP} = (\frac{1+\epsilon_1}{\epsilon_1})\frac{\epsilon_1^2}{\epsilon_2} \tag{5.3}$$

The function -Im ($1/\epsilon$) gives the energy loss and provides an indication of probability of surface plasmon resonance in the material[36]. A sharp maxima in this function is associated with the existence of plasma oscillations.

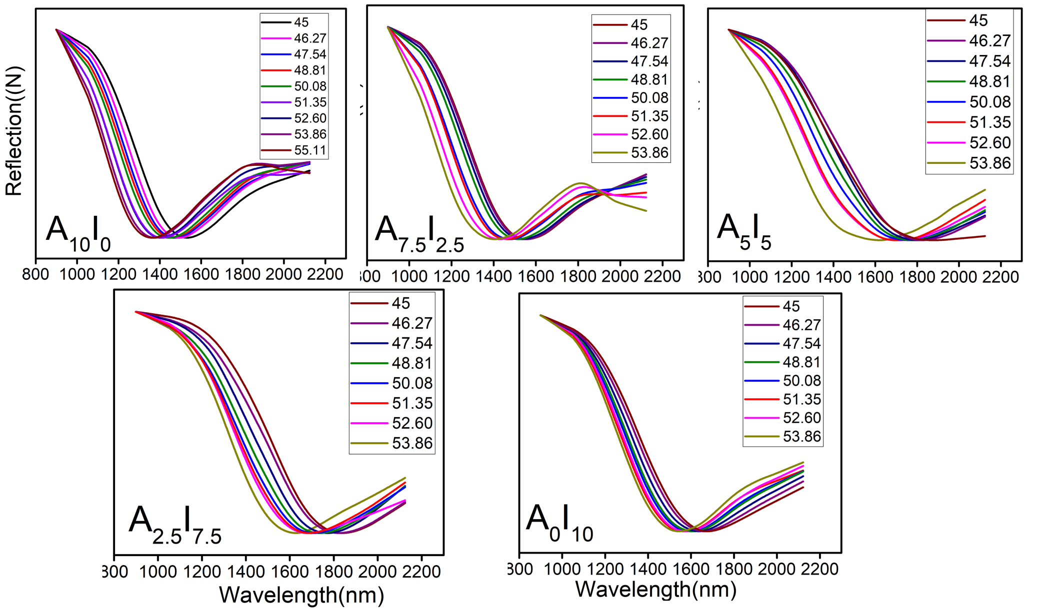

Figure 5.11: SPR generated based on wavelength interrogation method by Kretschmann configuration of the films

Fig.5.12a shows the energy loss function estimated from the real and imaginary parts of the permittivity extracted using the D-L equation as a function of wavelength in the near infrared region. As seen in the figure, the maxima observed at 1400nm in the region between 1200 and 1700nm indicates a large probability of surface plasmon resonance. The strong maximum is observed at $\epsilon_1 = 0$. The cross-over wavelength extracted from D-L equation is near to 1350nm, and the ELF spectra also indicated plasmonic resonance near to 1400nm.

A small redshift of ELF spectra is observed when Al: In changed from 10: 0 to 0: 10, which are in accordance with the red shift in cross over wavelength of these films. Another parameter is the quality factor or figure-of-merit, which is a term to compare the plasmonic performance of a material for different applications over a wide frequency region[30]. The loss in a material is an indicator of performance, which is described by ϵ_2. However, ϵ_1 is important in quantifying the overall material quantity in several devices and hence the quality factor for a plasmonic material is a function of both ϵ_1 and ϵ_2. Q_{SPP} shows an increasing nature beyond 1400 nm, which again indicates the suitability for NIR plasmonic applications of these films. Fig.5.12c shows the quality factors of the conventional plasmonic metals[30]. Due to the large negative permittivity, noble metals have large quality factor than other materials. The term in the eqn(5.3) can be simplified to ϵ_1^2/ϵ_2, and this indicates that the quality factor exhibits stronger dependence on real permittivity than the imaginary part of the permittivity. The quality factors of Ga doped ZnO and Al doped ZnO were reported as 1.01 and 2.3 respectively at 1500nm[30]. While comparing these with the results of the present study (Fig.5.12b), it is well understood that the obtained quality factors for the co-doped ZnO thin films are near to the reported values of conducting metal oxides.

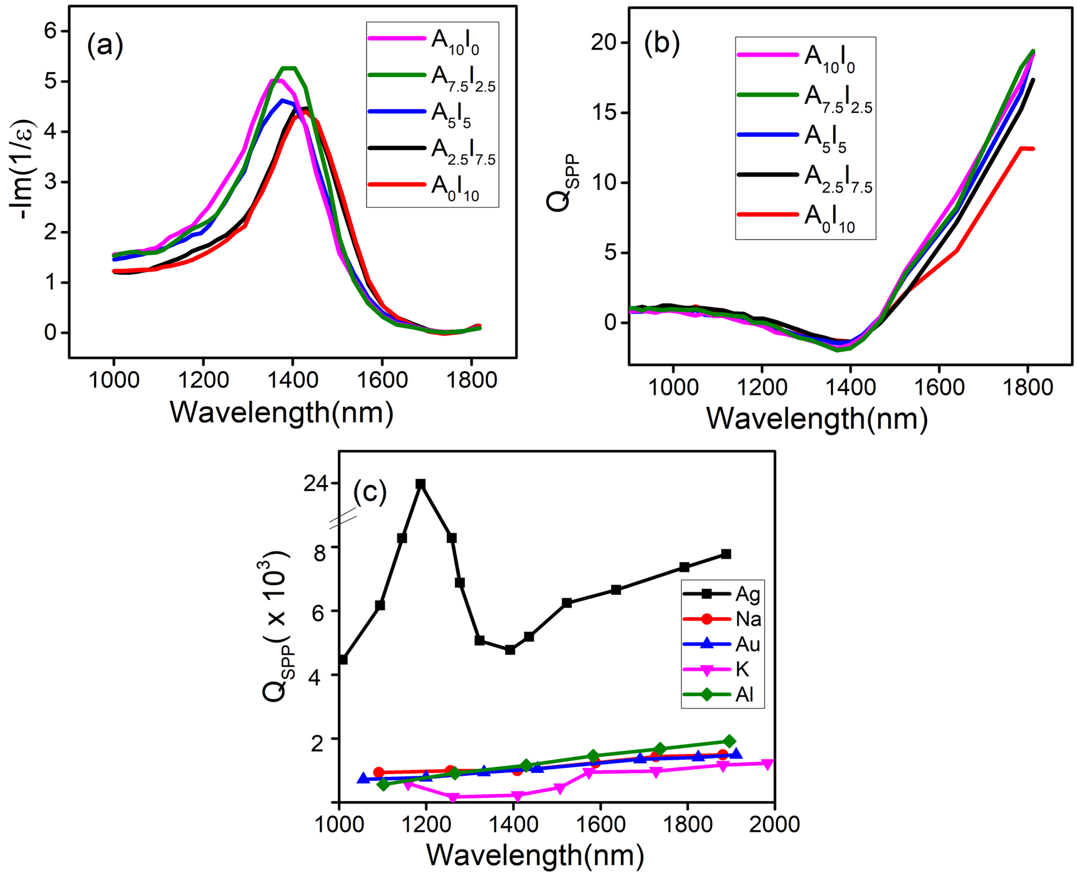

Figure 5.12: (a) Energy loss spectra, (b) quality factor (Q_{SPP}) of the co-doped ZnO films, and (c) reported quality factor of conventional plasmonic metals (redrawn from ref [30])

The full width at half maximum (FWHM) of the SPR dips of the films are shown in Fig.5.13. As seen in the figure, the SPR broadness increases with increasing incident angle. The relatively larger mobilities of the films $A_{10}I_0$ and $A_{7.5}I_{2.5}$ (near to 23 cm^2/Vs, Fig 5.3) may be reason for the relatively small FWHM observed (Fig.5.13) in these films. In addition, these films have relatively large carrier concentrations, and this may be the reason for observing SPR below the telecommunication wavelength.

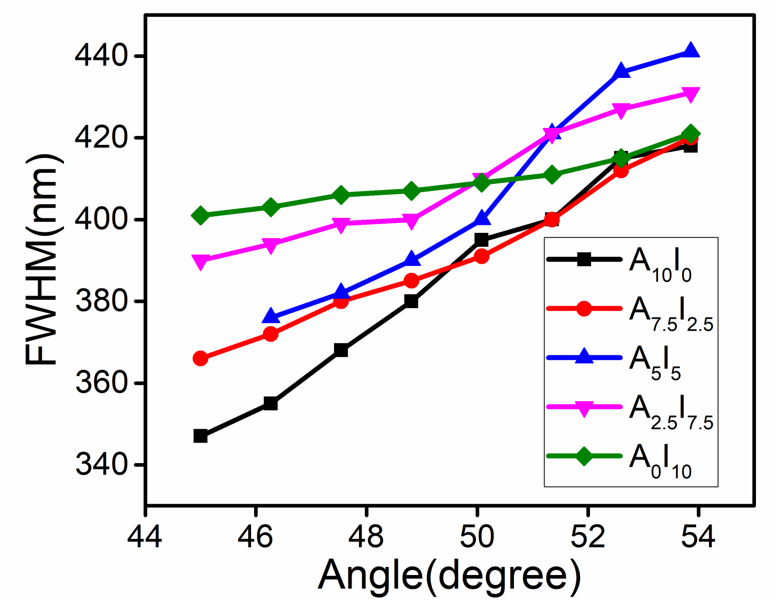

Figure 5.13: FWHM of the SPR dip of the films with varying incident angle in wavelength interrogation.

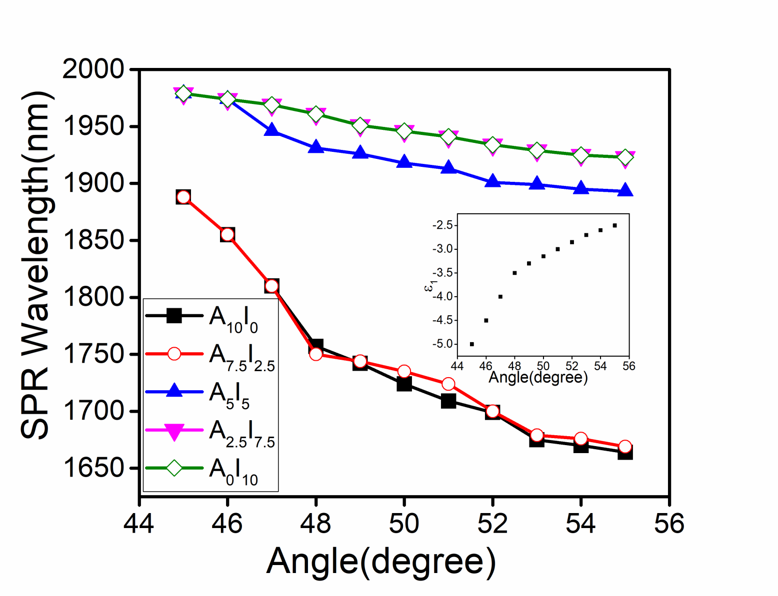

Figure 5.14: Variation of surface plasmon resonance wavelength with incident angle calculated. Inset shows the variation of ϵ_1 with incident angles estimated using equation 5.5.

The shifting of resonance wavelength to different regions can be accomplished by varying the incident angle for the co-doped films. The resonance condition of the SPR can be described by the equation below [37],

$$\frac{2\pi n_p}{\lambda} sin\theta = \frac{2\pi}{\lambda}\left(\frac{\epsilon_1 \epsilon_d}{\epsilon_1 + \epsilon_d}\right)^{\frac{1}{2}} \tag{5.4}$$

$$\theta = sin^{-1}\left(\frac{1}{n_p}\left(\frac{\epsilon_1 \epsilon_d}{\epsilon_1 + \epsilon_d}\right)^{\frac{1}{2}}\right) \tag{5.5}$$

where n_p is the refractive index of the prism; $\epsilon_1$and ϵ_d are the real part of the permittivity of plasmonic film and permittivity of the dielectric medium, respectively. Permittivity values were estimated using this equation for various angles of incidence used for the study, and the angle versus ϵ_1 curve is shown in the inset of Fig.5.14. The values for ϵ_d and n_p used were 1 and 1.57, respectively. The Fig.5.14 shows the surface plasmon resonance wavelength estimated at different angles of incidence.

As seen in the inset figure (Fig.5.14), when theta is increased from 45^o to 55^o, the associated change in ϵ_1 is from -5 to -2.5. The change in the values of real permittivity with respect to wavelength is already shown in 5.9b. Using Fig.5.14 (inset) and 5.9b, surface plasmon resonance wavelengths are estimated for different angles of incidence, and are shown in Fig.5.14, where the wavelengths corresponding to ϵ_1 value were obtained from Fig.5.9b. This shows that, when angle of incidence is increased, there is large chance for blue shift of the SPR wavelength. The SPR curve obtained using Kretschmann configuration is shown in Fig.5.15. Even if the range of SPR wavelength differ from calculated curve shown in 5.14, the blue shift of SPR with increase in incident angle is observed in both cases. The importance of the experimental demonstration is that the co-doping on ZnO have brought SPR behaviour in wide wavelength range from 1360 nm to 1830 nm, which indicates that these films are promising alternative plasmonic materials to metals for near infrared applications.

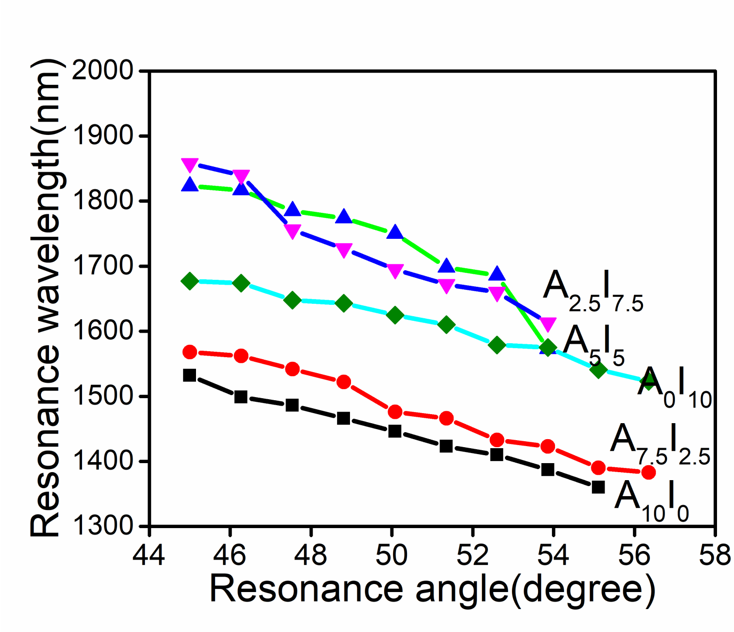

Figure 5.15: Variation of surface plasmon resonance wavelength with incident angle generated using the Kretschmann configuration.

5.9 Summary

In summing up of the present study, Al and In co-doped ZnO thin films were fabricated by RF sputtering using powder target, prepared by solid state route. Structural studies of the films by XRD and Raman spectra confirmed the hexagonal wurtzite structure for all samples. The free carrier densities of all films were of the order of $10^{20}/\mathrm{cm}^3$, required to exhibit plasmonic properties in NIR wavelength. The fano resonance fitting of A_1(LO) mode confirmed Raman active inter-conduction band transitions occurring for heavily doped n type materials. The near band and visible emissions due to oxygen vacancies further confirmed the n type doping in these films. The bandgap variations of the thin films were according to the BR effect. The real and imaginary parts of the permittivity extracted from the D-L equation predicted SPR in these film for wavelengths beyond 1350nm with relatively small loss comparing to conventional metals. SPR has been successfully generated in these films using the Kretschmann type prism configuration. The tuning of SPR wavelength in the telecommunication wavelength has been done by wavelength interrogation method. Co-doping of ZnO resulted in wide range of SPR behaviour for wavelengths from 1360nm to 1830 nm when the angle of incidence was changed from 45^o to 55^o.

References

[1] V. Kumar, S. Kumari, P. Kumar, M. Kar, and L. Kumar, "Structural analysis by rietveld method and its correlation with optical propertis of nanocrystalline zinc oxide," *Adv Mater Lett*, vol. 6, no. 2, pp. 139–147, 2015.

[2] P. Prabeesh, I. P. Selvam, and S. Potty, "Structural properties of czts thin films on glass and mo coated glass substrates: a rietveld refinement study," *Appl.Phys A*, vol. 124, no. 3, pp. 1–6, 2018.

[3] E. Ş. Tüzemen, H. Kavak, and R. Esen, "Influence of oxygen pressure of zno/glass substrate produced by pulsed filtered cathodic vacuum arc deposition," *Physic.B: Condens. Matt*, vol. 390, no. 1-2, pp. 366–372, 2007.

[4] Y. Wang, S. P. Lau, H. Lee, S. F. Yu, B. Tay, X. Zhang, K. Tse, and H. Hng, "Comprehensive study of zno films prepared by filtered cathodic vacuum arc at room temperature," *J. appl. phys.*, vol. 94, no. 3, pp. 1597–1604, 2003.

[5] A. R. Denton and N. W. Ashcroft, "Vegard's law," *Phys.revi. A*, vol. 43, no. 6, p. 3161, 1991.

[6] R. G. Waykar, A. S. Pawbake, R. R. Kulkarni, A. A. Jadhavar, A. M. Funde, V. S. Waman, H. M. Pathan, and S. R. Jadkar, "Influence of rf power on structural, morphology, electrical, composition and optical properties of al-doped zno films deposited by rf magnetron sputtering," *J. Mater. Sci: Mater. Electron*, vol. 27, no. 2, pp. 1134–1143, 2016.

[7] S. Vyas, P. Giri, S. Singh, and P. Chakrabarti, “Comparative study of as-deposited zno thin films by thermal evaporation, pulsed laser deposition and rf sputtering methods for electronic and optoelectronic applications,” *J.Electron. Mater.*, vol. 44, no. 10, pp. 3401–3407, 2015.

[8] Z. Li and W. Gao, “Zno thin films with dc and rf reactive sputtering,” *Mater. Lett.*, vol. 58, no. 7-8, pp. 1363–1370, 2004.

[9] N. Ekem, S. Korkmaz, S. Pat, M. Balbag, E. Cetin, and M. Ozmumcu, “Some physical properties of zno thin films prepared by rf sputtering technique,” *Int. J. of Hydrog. Energ.*, vol. 34, no. 12, pp. 5218–5222, 2009.

[10] H. Khamh, E. Sachet, K. Kelly, J.-P. Maria, and S. Franzen, “As good as gold and better: conducting metal oxide materials for mid-infrared plasmonic applications,” *J. Mater. Chem. C*, vol. 6, no. 31, pp. 8326–8342, 2018.

[11] D. B. Potter, M. J. Powell, I. P. Parkin, and C. J. Carmalt, “Aluminium/gallium, indium/gallium, and aluminium/indium co-doped zno thin films deposited via aerosol assisted cvd,” *J.Mater. Chem. C*, vol. 6, no. 3, pp. 588–597, 2018.

[12] V. Russo, M. Ghidelli, P. Gondoni, C. S. Casari, and A. Li Bassi, “Multiwavelength raman scattering of nanostructured al-doped zinc oxide,” *J. Appl. Phys*, vol. 115, no. 7, p. 073508, 2014.

[13] S. Guo, Z. Du, and S. Dai, “Analysis of raman modes in mn-doped zno nanocrystals,” *physica status solidi (b)*, vol. 246, no. 10, pp. 2329–2332, 2009.

[14] M. Chandrasekhar, J. Renucci, and M. Cardona, “Effects of interband excitations on raman phonons in heavily doped n- si,” *Phys. Rev. B*, vol. 17, no. 4, p. 1623, 1978.

[15] R. Gupta, Q. Xiong, C. Adu, U. Kim, and P. Eklund, “Laser-induced fano resonance scattering in silicon nanowires,” *Nano Lett.*, vol. 3, no. 5, pp. 627–631, 2003.

[16] A. Mohanta, J. G. Simmons Jr, G. Shen, S. M. Kim, P. Kung, and H. O. Everitt, “Al doping in zno nanowires enhances ultraviolet emission and suppresses broad defect emission,” *J.Lumin*, vol. 211, pp. 264–270, 2019.

[17] R. K. Biroju, N. Tilak, G. Rajender, S. Dhara, and P. Giri, “Catalyst free growth of zno nanowires on graphene and graphene oxide and its enhanced photoluminescence and photoresponse,” *Nanotechnology*, vol. 26, no. 14, p. 145601, 2015.

[18] T. Makino, Y. Segawa, S. Yoshida, A. Tsukazaki, A. Ohtomo, and M. Kawasaki, “Gallium concentration dependence of room-temperature near-band-edge luminescence in n-type zno: Ga,” *Appl. Phys. Lett.*, vol. 85, no. 5, pp. 759–761, 2004.

[19] M. Benhaliliba, C. Benouis, M. Aida, F. Yakuphanoglu, and A. S. Juarez, “Indium and aluminium-doped zno thin films deposited onto fto substrates: nanostructure, optical, photoluminescence and electrical properties,” *J. sol-gel sci. technol.*, vol. 55, no. 3, pp. 335–342, 2010.

[20] D. Meljanac, K. Juraić, V. Mandić, H. Skenderović, S. Bernstorff, J. R. Plaisier, A. Šantić, A. Gajović, B. Šantić, and D. Gracin, “The influence of thermal annealing on the structural, optical and electrical properties of azo thin films deposited by magnetron sputtering,” *Surf. Coat.Technol*, vol. 321, pp. 292–299, 2017.

[21] B. Jin, S. Im, and S. Y. Lee, “Violet and uv luminescence emitted from zno thin films grown on sapphire by pulsed laser deposition,” *Thin solid films*, vol. 366, no. 1-2, pp. 107–110, 2000.

[22] F. Leiter, H. Alves, A. Hofstaetter, D. Hofmann, and B. Meyer, “Rapid research notes-the oxygen vacancy as the origin of a green emission in

undoped zno," *Physica Status Solidi-B-Basic Research*, vol. 226, no. 1, p. R4, 2001.

[23] A. Singh, M. Kumar, R. Mehra, A. Wakahara, and A. Yoshida, "Al-doped zinc oxide (zno: Al) thin films by pulsed laser ablation.," *J. Indian Inst .Sci*, vol. 81, no. 5, p. 527, 2001.

[24] J. Lu, S. Fujita, T. Kawaharamura, H. Nishinaka, Y. Kamada, T. Ohshima, Z. Ye, Y. Zeng, Y. Zhang, L. Zhu, *et al.*, "Carrier concentration dependence of band gap shift in n-type zno: Al films," *J. Appl.Phys*, vol. 101, no. 8, p. 083705, 2007.

[25] M. A. Basyooni, M. Shaban, and A. M. El Sayed, "Enhanced gas sensing properties of spin-coated na-doped zno nanostructured films," *Sci. Rep*, vol. 7, no. 1, pp. 1–12, 2017.

[26] F. Anyaegbunam and C. Augustine, "A study of optical band gap and associated urbach energy tail of chemically deposited metal oxides binary thin films," *Dig.J.Nanomater.Biostruct.*, vol. 13, pp. 847–856, 2018.

[27] S. Schönau, F. Ruske, S. Neubert, and B. Rech, "Analysis of urbach-like absorption tails in thermally treated zno: Al thin films," *Appl.Phys. Lett.*, vol. 103, no. 19, p. 192108, 2013.

[28] B. Pejova, "The urbach–martienssen absorption tails in the optical spectra of semiconducting variable-sized zinc selenide and cadmium selenide quantum dots in thin film form," *Mater. Chem.Phys.*, vol. 119, no. 3, pp. 367–376, 2010.

[29] A. Kuzmenko, "Kramers–kronig constrained variational analysis of optical spectra," *Rev. sci. instrum.*, vol. 76, no. 8, p. 083108, 2005.

[30] P. R. West, S. Ishii, G. V. Naik, N. K. Emani, V. M. Shalaev, and A. Boltasseva, "Searching for better plasmonic materials," *Las.Photon. Revi*, vol. 4, no. 6, pp. 795–808, 2010.

[31] G. V. Naik, J. L. Schroeder, X. Ni, A. V. Kildishev, T. D. Sands, and A. Boltasseva, “Titanium nitride as a plasmonic material for visible and near-infrared wavelengths,” *Opt.Mater. Exp.*, vol. 2, no. 4, pp. 478–489, 2012.

[32] J. B. Khurgin and A. Boltasseva, “Reflecting upon the losses in plasmonics and metamaterials,” *MRS bullet.*, vol. 37, no. 8, pp. 768–779, 2012.

[33] G. V. Naik, V. M. Shalaev, and A. Boltasseva, “Alternative plasmonic materials: beyond gold and silver,” *Adv.Mater.*, vol. 25, no. 24, pp. 3264–3294, 2013.

[34] K. C. Maurya, V. M. Shalaev, A. Boltasseva, and B. Saha, “Reduced optical losses in refractory plasmonic titanium nitride thin films deposited with molecular beam epitaxy,” *Opt.Mater. Exp.*, vol. 10, no. 10, pp. 2679–2692, 2020.

[35] L. Chen, Y. Ran, Z. Jiang, Y. Li, and Z. Wang, “Structural, compositional, and plasmonic characteristics of ti–zr ternary nitride thin films tuned by the nitrogen flow ratio in magnetron sputtering,” *Nanomaterials*, vol. 10, no. 5, p. 829, 2020.

[36] S. Adachi and M. Takahashi, “Optical properties of tin films deposited by direct current reactive sputtering,” *J. Appl. Phys.*, vol. 87, no. 3, pp. 1264–1269, 2000.

[37] G. S. Mei, P. S. Menon, and G. Hegde, “Zno for performance enhancement of surface plasmon resonance biosensor: a review,” *Mater. Res. exp*, vol. 7, no. 1, p. 012003, 2020.

Chapter 6

Investigation of plasmonic property in DC sputtered TiN thin films

6.1 Overview

Plasmonic properties of Al and In co-doped ZnO films prepared by vacuum as well as non-vacuum based techniques were discussed in the previous three chapters. The suitability of these materials for NIR plasmonics applications were well described. This chapter discusses the development of plasmonic titanium nitride thin film for visible region, by a physical route, DC reactive sputtering. The ratios of argon and nitrogen gases were varied during sputtering to study the stoichiometric effect of Ti and N on the structural, optical and plasmonic properties of TiN thin films. As described in the section 1.4.4 of chapter 1, the non-stoichiometry of TiN thin films plays an important role in deciding the free carrier density in these films. The titanium nitride contains both Ti-Ti metallic bond and Ti-N covalent bond, and the free carrier concentration is found to be proportional to the concentration of titanium [1–3]. These films are suitable for visible plasmonic application, where the required carrier concentration can be achieved by coating titanium rich TiN thin films. XRD has been used for structural confirmation, and EDAX was used to estimate the elemental composition of the films. The Drude-Lorentz model was used for calculating the cross over wavelength. Surface plasmon resonance was generated using the Kretschmann configuration, and the SPR was observed in these films according to the theoretical calculation.

6.2 Sample preparation

6.2.1 Thin film preparation using DC sputtering

TiN thin films at different Ar:N_2 ratios were prepared using a DC magnetron reactive sputtering. A titanium target (99.995% pure) having a diameter of 2 inch and 3mm thickness was used for sputtering. Sputtering was done at DC power of 110W by varying the percentage of argon and nitrogen in the Ar:N_2 ratios of 95: 5, 90: 10, 85: 15, 80: 20, 75: 25. The samples were named according to this ratio. The distance between the substrate and the target is 80 mm. The base pressure was set to 5×10^{-6} mbar, and the working pressure used was 1.3×10^{-2} mbar. The target was pre-sputtered for 10 mins in order to remove the contaminants. Two separate flows of Ar and nitrogen (99.99% pure) gases were introduced into chamber to generate the plasma and to react with titanium metal, respectively. The substrate was rotated at 10 rpm for uniform film deposition. The deposition time was set to 1 hr and all the films were deposited at room temperature. Prior to the coating, the glass substrates were ultrasonicated successively in soap water, DI water, acetone and isopropyl alcohol for 15 mins, and finally dried in nitrogen flow.

6.3 Structural properties

The effect of changing Ar:N_2 ratio on the crystal structure of sputtered TiN films has been studied by x-ray diffraction. The XRD patterns of the films and the observed angle values were given in Fig.6.1 and in Table.6.1, respectively. The observed patterns were matched with the data of ICDD pdf #65-0965. A peak near to 43^o can be seen in the patterns, which is the characteristic (200) peak of TiN, and in addition to this, a weak (111) peak around at 37^o[4–7] was also observed for the films Ar:$N_2 = 75: 25$ and $80: 20$.

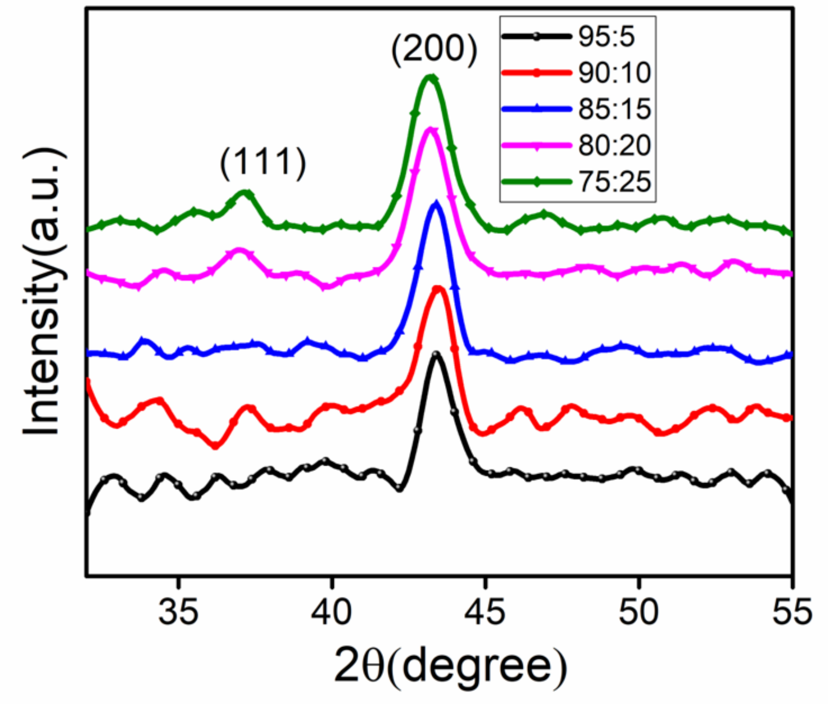

Figure 6.1: XRD data of TiN thin films fabricated with different ratios of Ar:N_2

The gradual apperance of (111) peak in 80:20 and 75:25 films may be due to the increased N_2 flow during sputtering. According to chang et al [4], increase in the nitrogen flow will dramatically change the crystalline structure of TiN. In addition chang et al[4] also observed that films prepared with Ar:N_2 = 70:30 and 60:40 were grown preferentially in the (111) orientation. However, in this study, the total gas flow rate was fixed to 20sccm; for a continuous plasma generation, 15sccm Ar is necessary, and thus limited the study to Ar/N_2 ratio of 75:25. Chang et al[4] also suggested that TiN films having (200) preferred orientation possess better plasmonic behaviour than the (111) oriented films. No other characteristic XRD peak of TiN existed in this pattern, as shown in Fig.6.1. From the analysis of XRD, it can be concluded that the films are of B1(cubic) structure, and the preferred orientation is along the (200) plane. The average crystallite size (D) for the films were calculated using the scherrer equation[6, 8] and are tabulated in

Table.6.1

$$D = \frac{0.9\lambda}{\beta cos\theta} \tag{6.1}$$

λ (=1.54060A°), the wavelength of x-ray used, β is FWHM of diffraction peaks in radian and θ is the incident angle expressed in degree. For cubic lattice, d_{hkl} in terms of lattice parameter 'a' can be written as[9]

$$\frac{1}{d_{hkl}^2} = \frac{h^2+k^2+l^2}{a^2} \tag{6.2}$$

The lattice constants calculated using the eqn 6.2 is also given in Table.6.1. The values are closely matching with the ICDD data (4.20 A°). A relatively small FWHM and hence larger crystallite size was observed for the films 75:25 and 80:20, which may be due to the presence of more nitrogen atom. According to Chen et al[6], nitrogen in TiN helps in nucleation and nuclei merging process of nitride, at the same time; and too much nitrogen may lead to more defects in the films. Hence, an optimized nitrogen content is always demanded in the TiN thin films for large free carrier concentration.

Table 6.1: Structural parameters estimated from XRD data of TiN films

Ar:N_2	2θ (111)	2θ (200)	d(A°) (2.12)	a (A°) 4.24	FWHM	Crystallite size(D nm)
95:5		43.4	2.07	4.14	0.017	7
90:10		43.5	2.08	4.14	0.018	7
85:15		43.4	2.07	4.16	0.018	8
80:20	37	43.2	2.09	4.18	0.021	8
75:25	37.1	43.2	2.09	4.18	0.021	9

6.4 Elemental analysis

The elemental compositions of the films were studied using EDAX spectra. The compositions estimated after applying absorption correction factor, as described in the section 2.3.3 of chapter 2 of this thesis, are tabulated in Table.6.2. As seen, all films are rich in titanium and the atomic percentage (and weight percentage) of nitrogen increases with increase in nitrogen of Ar:N_2.

The elemental mapping of nitrogen and titanium respectively are shown in Fig.6.2 and 6.3. The films showed uniform distribution of titanium and nitrogen, irrespective of the Ar-N_2 ratios. Dense mapping of titanium and nitrogen was also observed respectively for the films deposited with Ar:N_2 of 95:5 and 75:25. The values of x in nonstoichiometric TiN_x for the films deposited with Ar-N_2 ratios of 95:5, 90:10, 85:15, 80:20 and 75:25 were obtained to be 0.5, 0.67, 0.77, 0.80 and 0.82, respectively (Table.6.2).

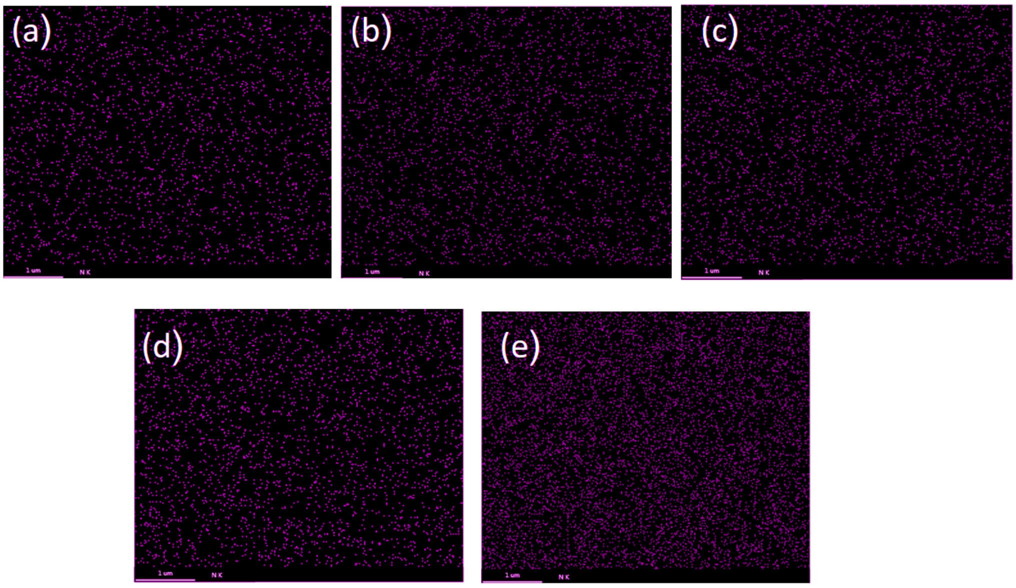

Figure 6.2: Elemental mapping of nitrogen in the films deposited with Ar/N_2 ratio of (a) 95:5, (b) 90:10, (c) 85:15, (d) 80:20 and (e)75:25

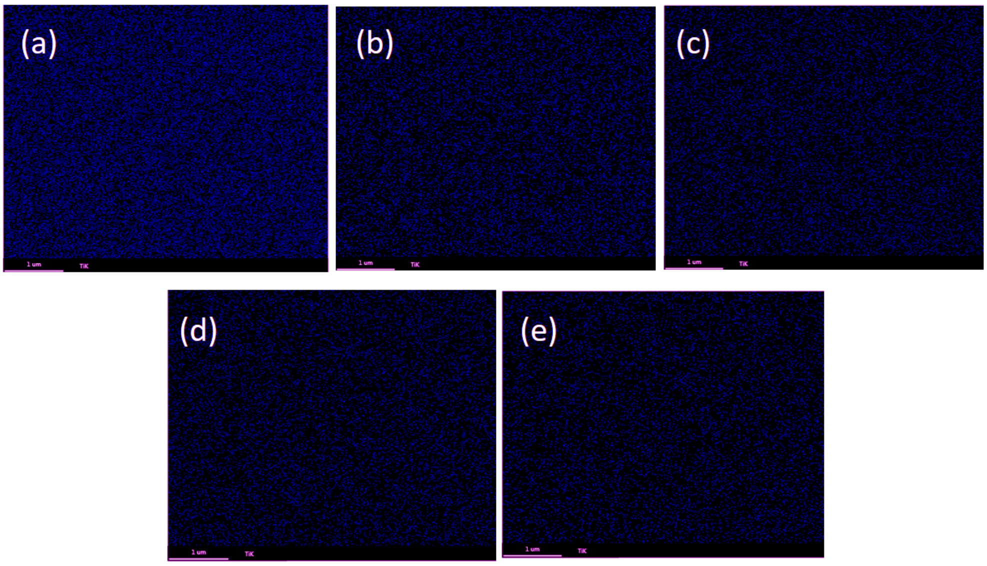

Figure 6.3: Elemental mapping of titanium in the films deposited with Ar/N_2 ratio of (a) 95:5, (b) 90:10, (c) 85:15, (d) 80:20 and (e)75:25

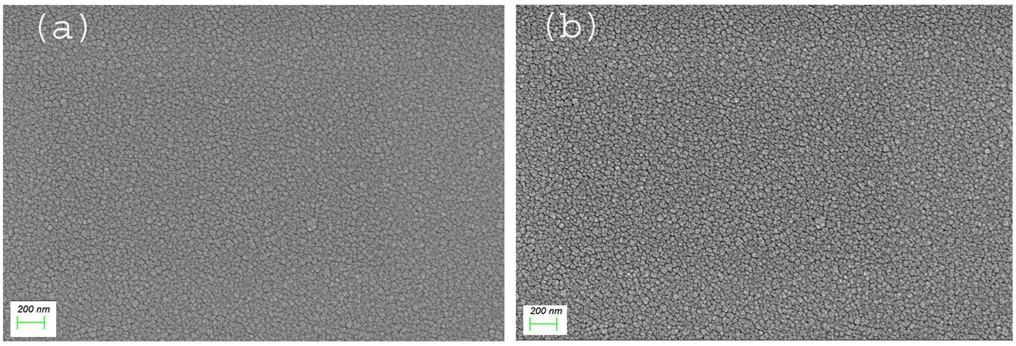

Figure 6.4: Surface morphology of TiN films deposited with Ar/N_2 ratio of (a) 95:5 and (b) 75:25

The surface morphology of TiN films coated with Ar/N_2 ratio of 95: 5 and 75: 25 were recorded by SEM is shown in Fig.6.4. As seen, the variation of Ar-N_2 ratio from 95: 5 to 75: 25 has no predominant effect in the uniformity as well as in the dense grain growth of TiN thin films.

Table 6.2: Elemental composition of the films determined from EDAX spectra

Ar:N_2	Wt%		At%		TiN_x
	N	Ti	N	Ti	
95:5	12.76	87.23	33.3	66.6	$TiN_{0.5}$
90:10	16.51	83.48	40.3	59.6	$TiN_{0.67}$
85:15	18.56	81.43	43.7	56.2	$TiN_{0.77}$
80:20	19.15	80.85	44.7	55.2	$TiN_{0.80}$
75:25	19.49	80.50	45.2	54.7	$TiN_{0.82}$

6.5 Optical properties

6.5.1 Band gap determination

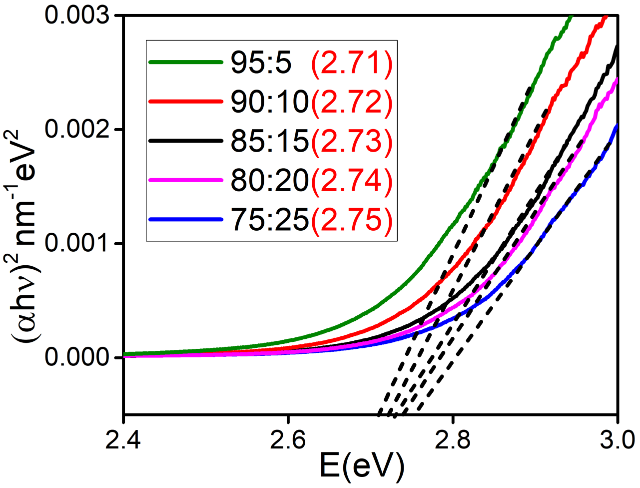

Figure 6.5: Estimation of bandgap using Tauc relation

The plots of $(\alpha h\nu)^2$ versus hν used to determine the bandgap of the TiN thin films[10, 11] coated with different Ar:N_2 ratios are shown in the Fig.6.5. A detailed description of Tauc plot was already discussed in the section 3.6.1 of the chapter 3 of this thesis. As seen in the figure, the bandgap of the TiN films showed a blueshift of 0.01eV in their bandgap when the Ar-N_2 ratio was changed from 95:5, 90:10, 85:15, 80:20 to 75:25. In a titanium metal due to presence of Ti-Ti metallic bond, they possess zero bandgap. But when nitrogen is reacted to Ti metal, covalent Ti-N bonds will appear and thus result in bandgap in TiN[1]. Hence, when the ratio of Ar-N_2 is changed from 95: 5 to 75: 25, due to the presence of more nitrogen atom in 75:25 film, and thus more Ti-N bond, there is a possibility of widening of bandgap, as showed in Fig.6.5. There are reports on widening of bandgap of TiN thin films when the nitrogen flow rate was increased. According to Mustapha et al[5], the obtained bandgap energies of TiN films fabricated by reactive DC sputtering at a substrate temperature of 300^oC increased from 3.72eV to 3.96eV when nitrogen is increased from 20% to 40%. Further increase in nitrogen percentage (nitrogen rich) resulted in decreasing the bandgap of these films, and this is explained on the basis of the increment in the grain sizes of films due to the substrate temperature. The bandgap of the TiN films observed are small compared to the reported values[5]. According to Kavitha et al[12], the bandgap observed for TiN thin film deposited at room temperature was 2.7eV. When the films are annealed at high temperature, its bandgap increased up to 3.7eV. In this work, the deposition of TiN was done at room temperature; and this may be the reason for the low bandgap observed for these films.

6.6 Investigation of plasmonic properties in the films

6.6.1 Extraction of dielectric function using D-L equation.

Fig.6.6a and Fig.6.6b represent the real and imaginary components of the permittivity extracted using the Drude-Lorentz (D-L) formula[13]. The extraction has been carried out using the refFit software[14]. The fitted parameters with D-L equation of the reflectance data is shown in Table.6.3, and the fitted graph is plotted in Fig.6.6c.

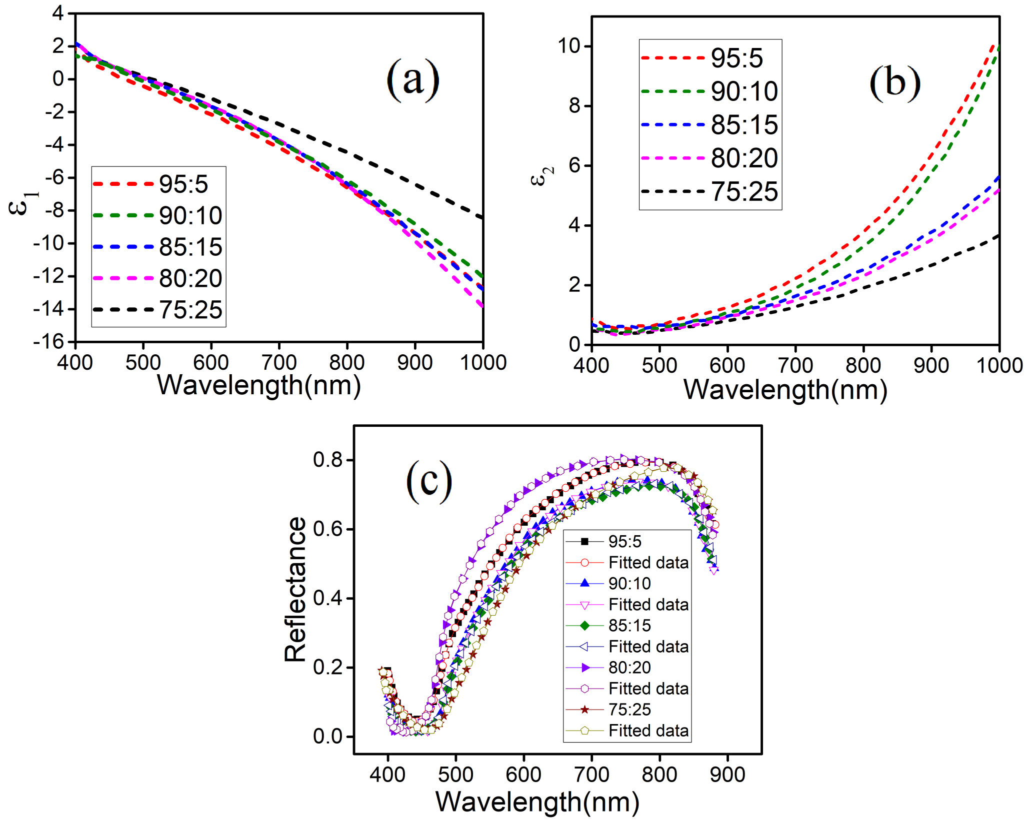

Figure 6.6: Real (a) and imaginary (b) of the permittivity of TiN thin films. Fitted reflectance spectra of the TiN films of different Ar-N_2 ratios(c).

The cross-over wavelength observed for all films were beyond 472nm, as seen in Table.6.4. The direct relation of cross-over wavelength with plasma wavelength has been described in the section 3.7.3 of the chapter 3 of this thesis. The carrier density (n) of the films is calculated as per the equation 6.3[15] and given in Table.6.4.

$$\omega_p^2 = \frac{ne^2}{m\epsilon_0} \tag{6.3}$$

According to Logothetidis et al[16] the electrical and optical properties of TiN are very much dependent on the nitrogen content in the material. The

Table 6.3: Fitting parameters of Drude-Lorentz equation for TiN thin films

Sample	D-L parameters		
	ω_p eV	ω_o eV	γ eV
95:5	1.312	3.117	0.487
	4.16	0.534	0.389
90:10	1.412	3.215	0.488
	5.13	0.632	0.382
85:15	1.523	3.212	0.452
	5.32	0.321	0.325
80:20	1.544	3.212	0.489
	5.36	0.336	0.369
75:25	1.593	3.365	0.414
	5.44	0.35	0.332

increase in nitrogen content results in more cation vacancy and behaviour of material will be more like dielectric[6]. Since the cross-over wavelength decreases with increase in square root of free carrier concentration (eqn 6.3), and the free carrier density in $\mathrm{TiN_x}$ is mainly due to Ti content, the change in the cross-over wavelength can be related to the change in the stoichiometry of TiN. Hence, when x in $\mathrm{TiN_x}$ increases, the cross-over wavelength increases, as shown in Fig.6.7.

Table 6.4: The cross-over wavelength and the carrier density calculated using eqn 6.3

Ar:N_2	$\lambda_c(nm)$	n ($\times\ 10^{21}/\mathrm{cm}^3$)
95:5	473	4.986
90:10	491	4.621
85:15	500	4.456
80:20	504	4.382
75:25	513	4.236

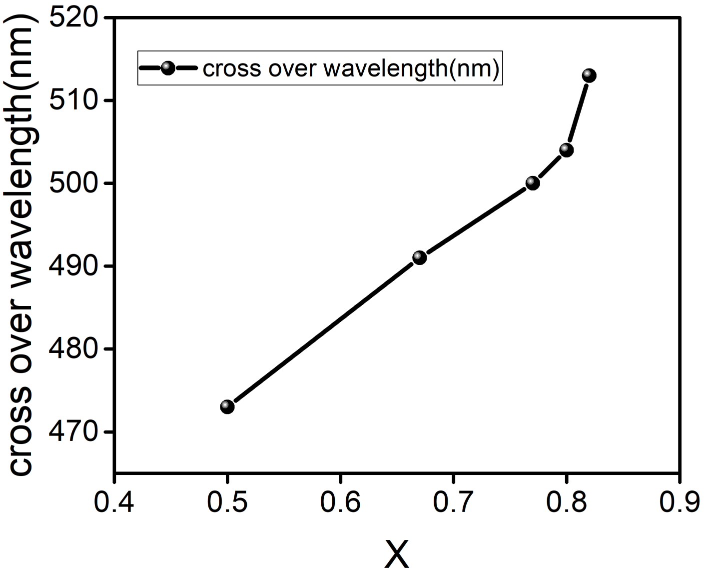

Figure 6.7: Variation of cross over wavelength with x in TiN_x film

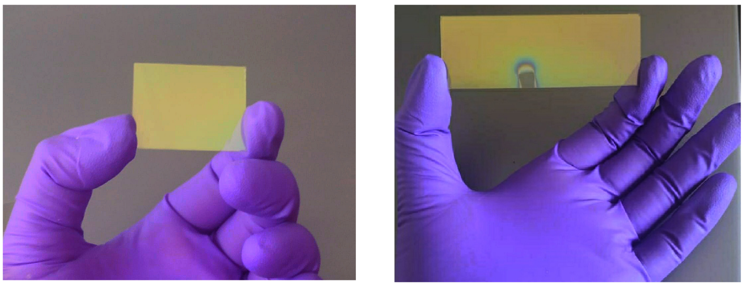

Figure 6.8: The images of the TiN films coated by DC magnetron sputtering on 1 x 1 inch and 3 x 1 inch glass substrates

The shift of cross over wavelength with respect to change in x of TiN was already reported by logothetidis et al[16]. For a stoichiometric TiN (x=1) film, the cross-over wavelength reported is near to 468nm and when x is increased further, the cross over frequency shifted to higher wavelength. The cross-over wavelength, thus, indicates the nature of stoichiometry of the TiN thin films. In the present study, shift in the cross-over wavelength to longer wavelength has been observed when the ratio of the Ar:N_2 was changed from 95: 5 to 75: 25. The shift is thus dependent on the changes in the stoichiometry of TiN, as confirmed through EDAX analysis. The TiN film prepared by DC magnetron sputtering exhibited different colour variations from light yellow to golden due to different nitrogen contents [17]. For x<1, the colour of the film is reported to be light yellow or metallic grey, and brownish yellow for over-stoichiometric films (x>1). The typical images of the TiN film coated with Ar:N_2 ratio of 95:5 are shown in Fig.6.8; the light yellow colour of the films confirm their sub-stoichiometric nature[16, 17].

The imaginary part of permittivity, ϵ_2 represented as loss is shown in Fig.6.6b. The ϵ_2 values of TiN and other nitrides along with gold and silver in the wavelength region 500-1000nm are tabulated and given in Table.6.5. The values of ϵ_2 for nitrides as well as gold/silver in the visible region are observed to be small, and thus exhibit low loss in visible region. In the case of TiN thin films, it is <18, and thus much low values for gold and silver. It is clear from the table that, low loss materials were achieved either by temperature-based deposition or by selecting oriented substrates. In this work, TiN thin films deposited at room temperature on glass substrate achieved low loss in visible region, which are thus comparable to the films deposited at higher substrate temperatures and on oriented substrates. Even if an increasing trend is observed in ϵ_2 (Fig.6.6b) for all TiN films, it is still small and comparable with films given in Table.6.5 [4, 18–22].

The other parameter used to characterise the plasmonic properties of the film is energy loss function (ELF) which is defined as[23–25],

$$ELF = -Im\frac{1}{\epsilon} = \frac{\epsilon_2}{\epsilon_1^2 + \epsilon_2^2} \tag{6.4}$$

Where ϵ_1 and ϵ_2 are the real and imaginary parts of permittivity ϵ. As described in the section 5.8.2 of Chapter 5, the function -Im $(1/\epsilon_1)$ is describing the energy loss and a sharp maxima in this function is associated with the existence of plasma oscillations. Fig.6.9a shows the energy loss function derived from the permittivity values extracted from D-L equation, as a function of wavelength in visible region.

Table 6.5: The imaginary parts of permittivity (ϵ_2) of nitrides, gold and silver in 500-1000nm.

Material	Substrate	Substrate temperature	Imaginary permittivity ϵ_2	reference
TiN(Ar%:N$_2$%)				
95:5	Glass	RT	0.5-10	This work
90:10			0.5-10	
85:15			0.5-5	
80:20			0.5-5	
75:25			0.5-3	
TiN	Sapphire	800	3-11	[18]
TiN	MgO	600	1-10	[19]
TiN(Ar:N$_2$)sccm				
4:6	Sapphire	300	3-8	[20]
2:8			3-10	
0:10			3-9	
4:6	Glass		8-18	
TiN	Quartz	RT	3-15	[1]
	HfO_2		3-11	
	Silicon		3-15	
TiN	MgO	250	4-14	[21]
TaN	Sapphire	800	10-20	[18]
HfN			3-30	
ZrN			2-15	
Au	-	RT	2	[18, 22]
Ag	-		0.2	

The figure shows a maxima between 400 and 700nm with a large probability around 500nm. In addition, the sharp maxima in surface energy loss spectra observes at $\epsilon_1 = 0$, where the probability of surface plasmon resonance is maximum[25]. In this study, the cross-over wavelength extracted from the D-L equation is near to the wavelength of 473nm; and the ELF spectra also shows a sharp maxima near to 500nm. This supports the value of the cross-over frequency extracted from D-L equation. The dependence of Ar:N_2 ratio during film coating on the position of maxima in the ELF function is also seen in Fig.6.9a.

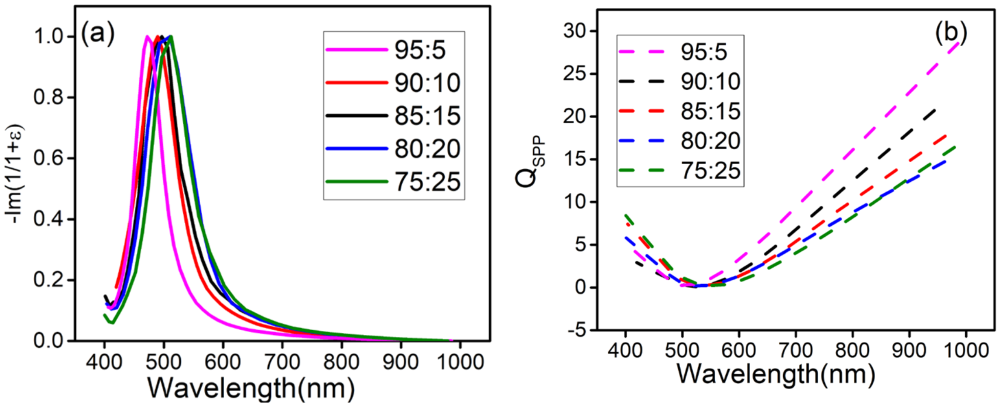

Figure 6.9: (a) Energy loss function and (b) quality factor of TiN thin films coated by sputtering with different Ar-N_2 ratios

As seen in the figure a redshift in the maxima is observed when the ratio was changed from 95:5 to 75:25. This can be related to the red shift of cross-over wavelength of these films provided by the D-L model. As discussed in the in the section 5.8.2 of Chapter 5, the performance of a plasmonic material over a wide frequency region is given by the quality factor, and it is defined as

$$Q_{SPP} = (\frac{1+\epsilon_1}{\epsilon_1})\frac{\epsilon_1^2}{\epsilon_2} \tag{6.5}$$

The Q_{SPP} of the conventional metals in visible region are near to 1000[26]. From the equation 6.5, it can be seen that the quality factor of the films depends on the real permittivity, and thus the relatively high quality factor of metals can be related to their high real permittivity. In the present study, the values of the real permittivity of all films are small comparing with that of the conventional metals, and thus the quality factor is of the order of one (Fig.6.9b). However, the increasing trend in the visible region shows the suitability of these films for visible plasmonic applications.

6.7 SPR generation using Kretschmann configuration

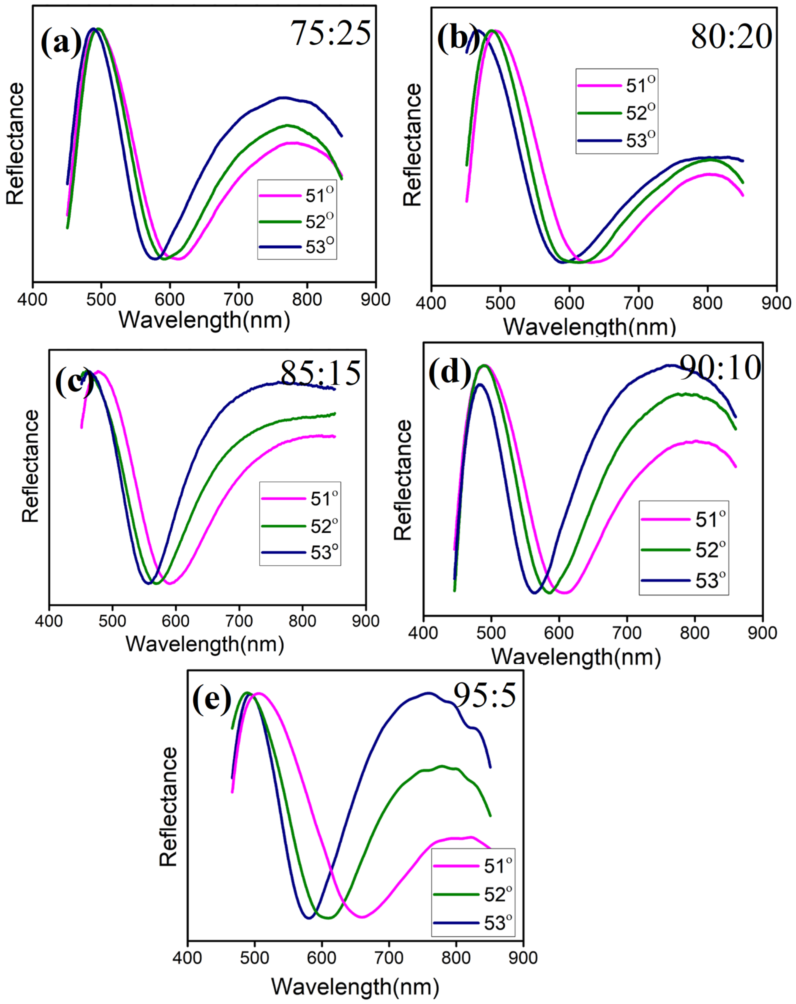

Figure 6.10: SPR generated for (a) 75:25 (b) 80:20, (c) 85:15 (d) 90:10 and (e) 95:5 TiN films based on wavelength interrogation by Kretschmann configuration

After carrying out theoretical studies, SPR was generated using the prism based Kretschmann configuration. The method to generate the SPR using prism type configuration is already described in the section 5.8.2 of the chapter 5 of this thesis. The sample is attached to the prism by using an index matching fluid. The SPR studies was done by wavelength interrogation method. The refractive index of the prism at visible region is 1.57 and the critical angle is 42^o for glass to air boundary. Three different angles greater than the critical angle, such as 51, 52 and 53 were selected for the generation of SPR using visible wavelength region, as seen in Fig.6.10. A shift to lower wavelength is observed when the angle of incidence is increased. The FWHM of the SPR dip is calculated and tabulated in Table.6.6. The FWHM of the films are found to decrease when the incident angle is increased. The films in the study exhibited FWHM of <135nm, and the minimum widths were observed for the films coated with Ar:N_2 ratios of 90:10 and 85:15 for an incidence angle of 53^o.

Table 6.6: Variation in FWHM of SPR with respect to incident angle

Ar:N_2	51^o	52^o	53^o
95:5	112	111	108
90:10	120	117	106
85:15	120	114	106
80:20	135	131	125
75:25	118	112	109

As described in the section 5.8.2 of the chapter 5, blue shift in the SPR dip is observed in response to the change in the incident angle from 45^o to 55^o, and this is associated with change in real permittivity from -5 to -2.5 (estimated using equation 5.5). The variation of real permittivity with change in angle of incidence from 51^o to 53^o is calculated in this case also, based on the same equation, and the angle versus ϵ_1 curve obtained is shown in the inset of Fig.6.11. The surface plasmon resonance wavelength estimated at different angles of incidence are shown in Fig.6.11, where the wavelengths corresponding to ϵ_1 value were obtained from Fig.6.6(a). As seen in the Fig.6.11, the SPR resonance conditions are obtained at various angles of incidence, where the values of ϵ_1 changes from -3 and -2.7. The change in the values of real permittivity with respect to wavelength is already shown in Fig.6.6(a). It is clearly understood that the SPR resonance have more chance to observe blue shift with increase in angle of incidence.

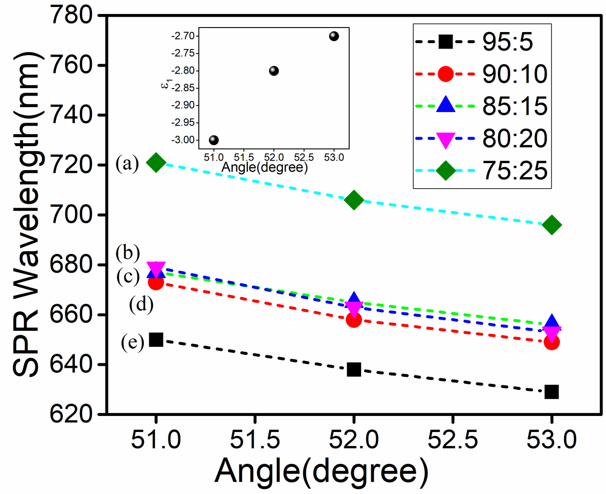

Figure 6.11: Variation of surface plasmon resonance wavelength in TiN films (a) 75:25 (b) 80:20, (c) 85:15 (d) 90:10 (e) 95:5 with estimated incident angle. Inset shows the variation of with incident angle calculated using eqn 5.5 described in Chapter 5.

The SPR wavelength versus incident angle curve drawn based on the experimental results done using Kretschmann method in wavelength interrogation is shown in 6.12. The figure indicates clearly that the SPR wavelength shifts to lower wavelengths with angle of incidence. Similar trend was observed in the theoretical curve in the Fig.6.11. Though the range of SPR wavelength observed experimentally differ from calculated curve, the blue shift of SPR wavelength with increasing incident angle is observed in both cases. The SPR dips of all films observed were beyond the cross-over wavelength estimated using the Drude-Lorentz equations. In addition, the shift in resonance wavelength is found to decrease with increase in the incident angle, as seen in Fig.6.12. This may be mainly due to the relatively small change in ϵ_1 when angle of incidence is changed from 52^o to 53^o, as seen in inset of Fig.6.11. In this work, based on the experimental demonstration, it is seen that the non-stoichiometry of TiN have brought SPR behaviour in wide wavelength range from 550nm to 655nm, which indicates that these films are promising plasmonic materials other than metals in visible plasmonic applications.

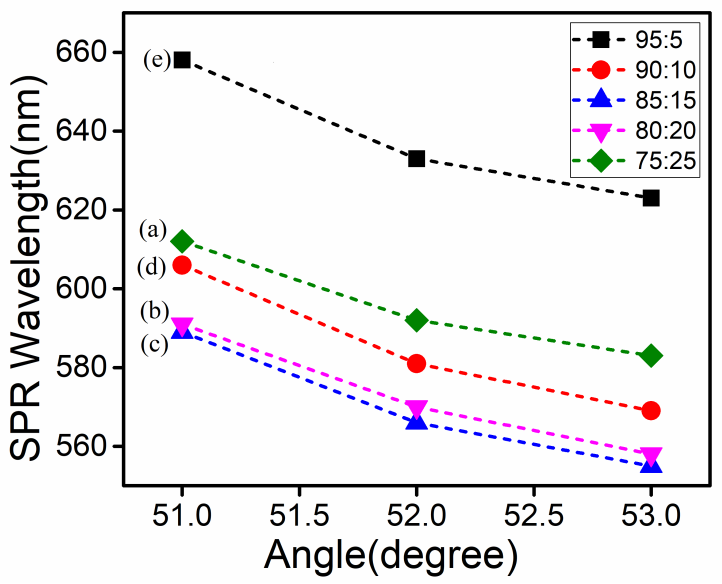

Figure 6.12: Change in resonance wavelength with respect to incident angle of various titanium nitride films (a) 75:25 (b) 80:20, (c) 85:15 (d) 90:10 (e) 95:5; SPR has been generated using Kretschmann configuration

6.8 Summary

In summing up of the present study, TiN thin films were fabricated by DC reactive sputtering by varying the Ar-N_2 ratio. Structural confirmation of the films was done by x-ray diffraction. The non-stoichiometric nature of the films were studied using the EDS spectra. The bandgap of the TiN films calculated using the Tauc relation showed a increasing trend with increase in nitrogen content in the films. The real and imaginary parts of the permittivity extracted from the D-L equation revealed SPR in these film for wavelengths near to 470 nm with loss comparable to the conventional plasmonic metals. The SPR has been successfully generated in these films using the Kretschmann configuration in wavelength interrogation method. The shift in SPR wavelength by changing the incident angle was studied in detail. The variation in the Ar-N_2 ratio resulted in wide range of SPR behaviour, for wavelengths from 550nm to 650nm, when the incident angle is changed from 51^o to 53^o.

References

[1] M. Solovan, V. Brus, E. Maistruk, and P. Maryanchuk, “Electrical and optical properties of tin thin films,” *Inorg. Mater.*, vol. 50, no. 1, pp. 40–45, 2014.

[2] J. Hojo, O. Iwamoto, Y. Maruyama, and A. Kato, “Defect structure, thermal and electrical properties of ti nitride and v nitride powders,” *J. Less-Common Met.*, vol. 53, no. 2, pp. 265–276, 1977.

[3] M. Delfino, J. Fair, and D. Hodul, “X-ray photoemission spectra of reactively sputtered tin,” *J. Appl. Phys.*, vol. 71, no. 12, pp. 6079–6085, 1992.

[4] C.-C. Chang, J. Nogan, Z.-P. Yang, W. J. Kort-Kamp, W. Ross, T. S. Luk, D. A. Dalvit, A. K. Azad, and H.-T. Chen, “Highly plasmonic titanium nitride by room-temperature sputtering,” *Scientific reports*, vol. 9, no. 1, pp. 1–9, 2019.

[5] N. Mustapha and Z. Fekkai, “Impact of nitrogen reactive gas and substrate temperature on the optical, electrical and structural properties of sputtered tin thin films,” *J.Mater.Sci.Mater.Electron*, vol. 31, no. 22, pp. 20009–20021, 2020.

[6] L. Chen, Y. Ran, Z. Jiang, Y. Li, and Z. Wang, “Structural, compositional, and plasmonic characteristics of ti–zr ternary nitride thin films tuned by the nitrogen flow ratio in magnetron sputtering,” *Nanomaterials*, vol. 10, no. 5, p. 829, 2020.

[7] E. Penilla and J. Wang, "Pressure and temperature effects on stoichiometry and microstructure of nitrogen-rich tin thin films synthesized via reactive magnetron dc-sputtering," *J Nanomater*, vol. 2008, 2008.

[8] U. Holzwarth and N. Gibson, "The scherrer equation versus the'debye-scherrer equation'," *Nat. Nanotechnol*, vol. 6, no. 9, pp. 534–534, 2011.

[9] M. O'Keeffe and B. G. Hyde, *Crystal structures.* Courier Dover Publications, 2020.

[10] F. Abeles, "Optical properties of solids," 1972.

[11] Z. Xie, X. Liu, P. Zhan, W. Wang, and Z. Zhang, "Tuning the optical bandgap of tio2-tin composite films as photocatalyst in the visible light," *Aip Adv.*, vol. 3, no. 6, p. 062129, 2013.

[12] A. Kavitha, R. Kannan, P. S. Reddy, and S. Rajashabala, "The effect of annealing on the structural, optical and electrical properties of titanium nitride (tin) thin films prepared by dc magnetron sputtering with supported discharge," *J. Mater. Sci. Mater. Electron.*, vol. 27, no. 10, pp. 10427–10434, 2016.

[13] G. V. Naik, V. M. Shalaev, and A. Boltasseva, "Alternative plasmonic materials: beyond gold and silver," *Adv. Mater.*, vol. 25, no. 24, pp. 3264–3294, 2013.

[14] A. Kuzmenko, "Kramers–kronig constrained variational analysis of optical spectra," *Rev. Sci. Instrum.*, vol. 76, no. 8, p. 083108, 2005.

[15] S. A. Maier, *Plasmonics: fundamentals and applications.* Springer Science & Business Media, 2007.

[16] S. Logothetidis, I. Alexandrou, and A. Papadopoulos, "In situ spectroscopic ellipsometry to monitor the process of tin x thin films deposited by reactive sputtering," *J. Appl. Phys.*, vol. 77, no. 3, pp. 1043–1047, 1995.

[17] S. Grosso, L. Latu-Romain, G. Berthomé, G. Renou, T. Le Coz, and M. Mantel, “Titanium and titanium nitride thin films grown by dc reactive magnetron sputtering physical vapor deposition in a continuous mode on stainless steel wires: Chemical, morphological and structural investigations,” *Surf. Coat. Technol.*, vol. 324, pp. 318–327, 2017.

[18] G. V. Naik, J. Kim, and A. Boltasseva, “Oxides and nitrides as alternative plasmonic materials in the optical range,” *Opt. Mater. Express*, vol. 1, no. 6, pp. 1090–1099, 2011.

[19] K. C. Maurya, V. M. Shalaev, A. Boltasseva, and B. Saha, “Reduced optical losses in refractory plasmonic titanium nitride thin films deposited with molecular beam epitaxy,” *Opt. Mater. Express*, vol. 10, no. 10, pp. 2679–2692, 2020.

[20] G. V. Naik, J. L. Schroeder, X. Ni, A. V. Kildishev, T. D. Sands, and A. Boltasseva, “Titanium nitride as a plasmonic material for visible and near-infrared wavelengths,” *Opt. Mater. Express*, vol. 2, no. 4, pp. 478–489, 2012.

[21] K. Hansen, M. Cardona, A. Dutta, and C. Yang, “Plasma enhanced atomic layer deposition of plasmonic tin ultrathin films using tdmati and nh3,” *Materials*, vol. 13, no. 5, p. 1058, 2020.

[22] P. B. Johnson and R.-W. Christy, “Optical constants of the noble metals,” *Phys. Rev. B*, vol. 6, no. 12, p. 4370, 1972.

[23] M. Creuzburg and H. Raether, “On the behavior of nuclear energy losses of electrons in alkali halides,” *Solid State Commun.*, vol. 2, no. 6, pp. 175–177, 1964.

[24] H. Philipp and H. Ehrenreich, “Optical properties of semiconductors,” *Phys. Rev.*, vol. 129, no. 4, p. 1550, 1963.

[25] S. Adachi and M. Takahashi, “Optical properties of tin films deposited by direct current reactive sputtering,” *J. Appl. Phys.*, vol. 87, no. 3, pp. 1264–1269, 2000.

[26] P. R. West, S. Ishii, G. V. Naik, N. K. Emani, V. M. Shalaev, and A. Boltasseva, “Searching for better plasmonic materials,” *Laser Photonics Rev.*, vol. 4, no. 6, pp. 795–808, 2010.